Modeling of Hybrid Nanolectronic Devices
for Quantum Information Processing

Andrea Maiani

**Modeling of Hybrid Nanoelectronic Devices for Quantum Information Processing**

# Modeling of Hybrid Nanoelectronic Devices for Quantum Information Processing

Andrea Maiani

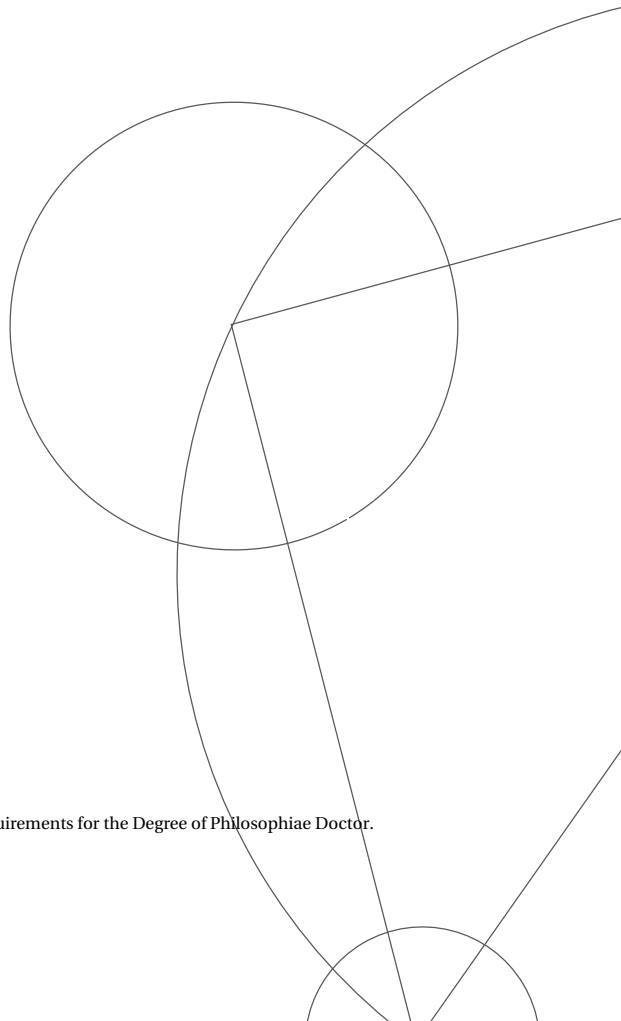Advisor :
Prof. Karsten Flensberg

Assessment committee :
Prof. Jens Paaske
Prof. Jeroen Danon
Prof. Ramón Aguado

Thesis submitted in partial fulfillment of the requirements for the Degree of Philosophiae Doctor.

**Modeling of Hybrid Nanoelectronic Devices for Quantum Information Processing**
Andrea Maiani
Copenhagen, March 2023.

Citation (APA):
Maiani, A. (2023). *Modeling of Hybrid Nanoelectronic Devices for Quantum Information Processing.* Niels Bohr Institute, Faculty of Science, University of Copenhagen.

Revised: March 20, 2023

## Abstract

Hybrid nanoelectronic devices offer a promising platform for developing quantum technologies by combining the macroscopic phase coherence of superconductors with the charge density control of semiconductor devices. This thesis focuses on modeling hybrid nanoelectronic devices and their applications in investigating topological phases of matter and quantum information processing.

The first part of the thesis introduces a novel orbital-free method for electrostatic modeling. This method significantly improves the precision of the density profile near interfaces while minimizing computational costs. Next, we use a symmetry-based approach to nonlocal conductance spectroscopy to investigate transport measurements in multiterminal devices. This approach can identify the direction of spin-orbit coupling and detect non-ideal effects.

The thesis then explores ferromagnetic hybrid heterostructures, which enable local control of effective magnetic fields by incorporating magnetic insulator insets. We examine the interplay of superconducting and ferromagnetic proximity effects and present a planar design for demonstrating topological superconductivity. We also show how this platform can be used to implement configurable $0$-$\pi$ Josephson junctions and how it can potentially realize nonsinusoidal current-phase relations.

Finally, the thesis investigates the application of junctions dominated by higher harmonics in superconducting qubits. We propose and study a coupling scheme for entangling to entangle parity-protected qubits with flux-tunable transmons in a heterogeneous quantum architecture.

## Resumé

Nanoelektroniske hybridenheder tilbyder en lovende platform for udvikling af kvanteteknologier ved at kombinere den makroskopiske fasekohærens af superledere med kontrollen af halvlederenheders ladningstæthed. Denne afhandling fokuserer på modellering af nanoelektroniske hybridenheder og deres anvendelser til at undersøge topologiske faser af stof og kvanteinformationsbehandling.

Den første del af afhandlingen introducerer en ny orbital-fri metode til elektrostatisk modellering. Denne metode forbedrer markant præcisionen af tæthedsprofilen nær grænseflader og minimerer samtidig beregningsomkostningerne. Dernæst bruger vi en symmetribaseret tilgang til ikke-lokal konduktansspektroskopi til at undersøge transportmålinger i multiterminale enheder. Denne tilgang kan identificere retningen af spin-banekoblingen og detektere ikke-ideelle effekter.

Afhandlingen udforsker derefter ferromagnetiske hybride heterostrukturer, der muliggør lokal kontrol af effektive magnetfelter ved at inkorporere magnetiske isolatorindsatser. Vi undersøger samspillet mellem superledende og ferromagnetiske nærhedseffekter og præsenterer et plant design til demonstration af topologisk superledning. Vi viser også, hvordan denne platform kan bruges til at implementere konfigurerbare $0$-$\pi$ Josephson forbindelser, og hvordan den potentielt kan realisere ikke-sinusformede strøm-fase-relationer.

Til sidst undersøger afhandlingen anvendelsen af forbindelser domineret af harmoniske svingninger af højere orden i superledende qubits. Vi foreslår og studerer et koblingsskema til sammenfiltring for at sammenfiltre paritetsbeskyttede qubits med flux-justerbare transmons i en heterogen kvantearkitektur.

# Acknowledgments

I am deeply grateful to all those who have supported me throughout the last three long and rewarding years of my Ph.D. Their unwavering support, encouragement, and guidance have been invaluable in shaping my academic and personal growth. I dedicate these lines to my mentors, colleagues, family, and friends who have been by my side throughout this journey.

I am deeply grateful to Karsten Flensberg for his guidance and support as my supervisor. His knowledge and expertise have been invaluable in helping me advance my studies and understand what really matters in a research project. Coming to Copenhagen to pursue my Ph.D. has been one of the best decisions I have made, and I am grateful to Karsten for making that possible. A special thank goes to the members of the assessment committee, Jens Paaske, Jeroen Danon, and Ramón Aguado, for taking the time to read and evaluate my thesis.

My heartfelt thanks go to the colleagues of the CMT section and the Center for Quantum Devices for creating a welcoming and supportive work environment. Despite the challenges of the pandemic, they made our office a pleasant place to work and spend time. In particular, I want to thank my officemates in room H.102, Gorm Steffensen, Fabian Jakubczyk, Benjamin Joecker, and Virgil Baran. I am especially grateful to Gorm for the countless stimulating conversations we had on a variety of topics that interspersed our physics sessions.

I am deeply grateful to the members of the "Italian invasion group", Lorenzo Maffi, Fabrizio Berritta, Matteo Wauters, and Michele Burrello, who, together with Ida Nielsen, have been fantastic travel companions. I also owe a debt of gratitude to Ida, who introduced me to rowing, which has been a fantastic addition to my life, and for her assistance with the Danish abstract of this thesis. Additionally, I am thankful to Fabrizio for his support in defending our common engineering background, and to Lorenzo for his tireless patience in explaining field theory concepts. I would like to reiterate my sincere appreciation to Benjamin, Fabrizio, and Ida for their invaluable assistance in proofreading this thesis. Their careful attention to detail and insightful feedback have undoubtedly enhanced the quality of this work.

A special mention is necessary for Waldemar Svejstrup and his trust in me as a master thesis mentor as well as his enthusiasm and friendship. It was a great honor, and I learned a lot in the process. I want to extend thanks to Andreas Pöschl and Alisa Danilenko. They have been amazing experimental collaborators, and I learned a lot from our discussions. I am also thankful to Samuel Escribano for joining forces in simulating ferromagnetic heterostructures.

I am especially grateful to Ruben Souto for his exceptional collaboration and support since the beginning of my Ph.D. and for being a fantastic mentor. I would also like to express my gratitude to Max Geier for spending time working together on scattering matrices and for helping me understand topological phases and their symmetries. I am deeply indebted to Constantin Schrade for his priceless mentorship during the second part of my Ph.D. Martin Leijnse, Saulius Vaitiekėnas, and Morten Kjaergaard were also pivotal in helping me learn and grow as a researcher, and I am grateful for the opportunity to work with them.

Finally, I could not have made it this far without the support of my family and the constant presence of my long-time friends. The greatest thank of all goes to my girlfriend, Elena, for always being there for me during challenging times and for celebrating successes together. Her unwavering love and patience mean the world to me. In addition, her help in choosing the best colors for my plots has been invaluable.

Thank you to all who have contributed to my Ph.D. in big and small ways. I am grateful for your support, encouragement, and friendship.

# List of abbreviations

| | |
|---|---|
| 2DEG | Two-Dimensional Electron Gas |
| ABS | Andreev Bound State |
| BCS | Bardeen–Cooper–Schrieffer |
| BdG | Bogoliubov-de Gennes |
| CBM | Conduction Band Maximum |
| CLA | Constant Landscape Approximation |
| CPR | Current-Phase relation |
| ETF | Extended Thomas-Fermi |
| MZM | Majorana Zero Mode |
| PHS | Particle-hole symmetry |
| PPQ | Parity-Protected superconducting Qubit |
| SAG | Selective-Area Growth |
| SOC | Spin-Orbit Coupling |
| SP | Schrödinger-Poisson |
| SPT | Symmetry-Protected Topological order |
| SQUID | Superconducting Quantum Interferometer Device |
| TF | Thomas-Fermi |
| TRS | Time-reversal symmetry |
| PDE | Partial Differential Equation |
| PPQ | Parity-Protected superconducting Qubit |
| VBM | Valence Band Minimum |
| VLS | Vapor-Liquid-Solid |
| vW | von Weizsäcker |
| ZBP | Zero-Bias conductance Peak |

# Contents

# Preface

Superconductivity is a fascinating phase of matter found in low-temperature electron systems. A small attractive interaction between electrons in a metal is enough to cause a phase transition that pairs all the electrons in the system, dramatically changing the physical properties of these materials. The most well-known features of this phase are the perfect electrical conductance and the expulsion of magnetic fields, known as the Meissner effect. These properties are fundamental for traditional applications of superconductors as powerful electromagnets. Another class of applications, like voltage standards, magnetometers, and qubits, are based on a different property of superconductors: their ability to maintain macroscopic phase coherence.

Over the decades, the number of materials that display a superconductive phase has increased significantly. Once considered an exotic phenomenon found in only a few materials, it is now observable in a wide range of substances, from basic elements that cover most of the periodic table to complex compounds. These unconventional superconductors opened the door for the discovery of more unconventional pairing, allowing for even more exotic physical phenomena.

One of the most fascinating phenomena in these exotic materials is the appearance of topological phases, where the material electronic structure changes in a way that is not detectable by local measurements. The clearest manifestation of such phases is the appearance of edge states that lives at the boundary with trivial regions or at the core of magnetic vortices. When these states appear at zero energy, they are known as Majorana zero modes, and they can be interpreted, to some extent, as a fraction of an electron. These peculiar excitations are associated with non-abelian anyons and ground-state degeneracies, meaning that exchanging the position of these excitations changes the state of the entire system. Such materials, therefore, have potential applications in quantum computing.

Scalable quantum information processors, capable of solving complex problems beyond the reach of classical computers, have been associated with huge promises of applications in fields such as chemistry, medicine, and finance, among others. However, the feasibility of these applications is not yet clear, leading some to advocate for focusing on quantum computer development first and worrying about applications later. Nevertheless, the quest for realizing a quantum computer has its own dignity independently of any applications, actual or potential. This is because, just as classical computers transformed our comprehension of the world at the macroscopic level, the journey of developing a quantum computer can broaden our understanding and provide a clearer and more comprehensive view of the universe's underlying

logic at the microscopic scale.

The biggest obstacle to this objective is the fragility of quantum information: any interaction with the noise in the environment irremediably destroys the delicate state of quantum bits. For this reason, in the last decades, intense research has been dedicated to developing new ideas about platforms and devices that protect quantum information in new ways. One possible approach is encoding quantum information using the aforementioned properties of topological superconductors. As a result, the so-called topological qubits are expected to be inherently resistant to environmental noise and other forms of decoherence.

Unfortunately, materials that exhibit stable and controllable intrinsic topological supercon- ductivity have yet to be discovered. Nature really wants to keep the exciting physics outside of the hands of curious researchers. For this reason, the idea of creating synthetic topological superconductivity by combining different materials has become a promising study area in the last decade. This approach involves creating *hybrid heterostructures* that can induce topolog- ical superconductivity in what looks like a "Hamiltonian alchemy" that mixes the different properties of the individual materials, like the macroscopic coherence of superconductors, the electronic controllability of semiconductors and sometimes even magnetic materials.

Despite tremendous effort, topological superconductivity in these devices is still disputed by some. The reason can be found in the difficulties in fabricating reproducible and control- lable devices and the high standard the community has set for what is considered conclusive evidence. However, the platform itself improved significantly over the years and is now ex- plored for other uses, ranging from new questions in basic science to applications to different quantum computing architectures, like protected superconducting qubits.

This dissertation represents the culmination of my years of research and studies at the Center for Quantum Devices from November 2019 to February 2023. It serves as a compre- hensive overview of my research in the fascinating field of hybrid quantum devices. Within its pages, I explore a range of topics, synthesizing the most significant findings while providing additional background material to contextualize my work. Undertaking this research has been an incredibly exciting and rewarding experience, allowing me to delve into a diverse array of materials, physical models, and methods. Given the breadth of subjects covered, I have chosen to present my findings in a unified format reflecting my learning pathway while at the Niels Bohr Institute. I hope that my work will contribute to the ongoing efforts in the exciting field of hybrid nanoelectronic devices. I am incredibly satisfied to have worked at the forefront between fundamental physics and technical development, a distinction that is often blurred and that I consider not particularly meaningful. After all, to keep discovering new stars, a better telescope is always necessary.

**Outline**

This Ph.D. thesis deals with several distinct aspects of hybrid quantum nanoelectronics. The thesis works as an introduction to the field of hybrid devices by integrating a summary of the major finding of my research activity with some additional background material.

- Chapter 1 introduces the theory of superconductivity, with a narrow focus on the aspects most useful for analyzing heterostructures. It discusses the main features of $s$-wave pairing, in particular with respect to the response to exchange fields. Then the focus moves to $p$-wave pairing and topological superconductivity. The second part of the chapter discussed superconductivity in heterostructures.

- Chapter 2 discusses electrostatic simulations of hybrid devices, presenting the work in [P3] concerning orbital-free approaches to the problem, and introducing the topic of spin-orbit coupling in semiconductors.

- Chapter 3 is an adaptation of Ref. [P4]. It presents the formalism for describing transport phenomena in hybrid heterostructures and presents the paper. The focus is on leveraging microscopic symmetries to find clever ways to combine the results of nonlocal tunneling conductance spectroscopy results and characterize spin-orbit coupling and non-ideal effects in hybrid devices.

- Chapter 4 deals with the extension of the hybrid heterostructure platform with ferromagnetic insets. After a brief introduction to the topic, the first part of the chapter discusses topological superconductivity and presents the major findings of papers [P1] and [P2]. In the second half of the chapter, Josephson junctions realized with this platform will be introduced, presenting the results of papers [P6] and [P7].

- Chapter 5 discusses an example application of such structures to superconducting qubits. After an introduction of generalized transmons, a coupling scheme able to entangle a conventional transmon and a parity-protected qubit is proposed. This chapter adapts Ref. [P5].

- Finally, the conclusion in Chapter 6 provides a comprehensive summary and an outlook of possible future developments in the field.

**Publications and the thesis author's contributions**

This thesis includes the results of the following articles, reformulated in a coherent and comprehensive manner. When they provide the most effective explanation of the concept, some passages have been quoted verbatim or minimally modified from the original sources.

1. *Topological superconductivity in semiconductor–superconductor–magnetic-insulator heterostructures*
   **Andrea Maiani**, Rubén S. Souto, Martin Leijnse, Karsten Flensberg
   Physical Review B, Vol. 103, No. 10 (March 2021) p. 104508, Ref. [P1].
   I was the primary contributor to scientific investigation, image preparation, and paper writing.

2. *Semiconductor-ferromagnet-superconductor planar heterostructures for 1D topological superconductivity*
   Samuel D. Escribano, **Andrea Maiani**, Martin Leijnse, Karsten Flensberg, Yuval Oreg, Alfredo L. Yeyati, Elsa Prada, Rubén S. Souto
   npj Quantum Materials, Vol. 7, No. 81 (August 2022), Ref. [P2].
   I contributed to the design of the project, interpretation of the results, and paper writing.

3. *Orbital-free approach for large-scale electrostatic simulations of quantum nanoelectronics devices*
   Waldemar Svejstrup, **Andrea Maiani**, Kevin Van Hoogdalem, Karsten Flensberg
   Semiconductor Science and Technology, Vol. 38, No. 4, p. 045004, Ref. [P3]
   I designed the project and provided support to the scientific investigation. I led the paper writing process.

4. *Conductance matrix symmetries of multiterminal semiconductor-superconductor devices*
   **Andrea Maiani**, Max Geier, Karsten Flensberg
   Physical Review B, Vol. 106, No. 10 (September 2022), p. 104516, Ref. [P4].
   I wrote the code, performed numerical simulations, and prepared the pictures. I am the main contributor to paper writing.

5. *Entangling Transmons with Low-Frequency Protected Superconducting Qubits*
   **Andrea Maiani**, Morten Kjaergaard, Constantin Schrade
   PRX Quantum, Vol. 3, No. 3 (August 2022) p. 030329, Ref. [P5].
   I have provided a major contribution to the scientific investigation, prepared the pictures, and contributed to the paper writing.

6. *Supercurrent reversal in ferromagnetic hybrid nanowire Josephson junctions*
   D. Razmadze, R. Seoane Souto, L. Galletti, **A. Maiani**, Y. Liu, P. Krogstrup, C. Schrade, A. Gyenis, C. M. Marcus, S. Vaitiekėnas
   Physical Review B, Vol. 107, No. 8, p. L081301, Ref. [P6].
   I provided important contributions to the interpretation of the results and to the magnetic modeling.

7. *Nonsinusoidal current-phase relations in semiconductor-superconductor-ferromagnetic insulator devices*
   **Andrea Maiani**, Karsten Flensberg, Martin Leijnse, Constantin Schrade, Saulius Vaitiekėnas, Ruben S. Souto
   arXiv:2302.04267, Ref. [P7].
   I designed the project and performed numerical simulations. I was the main contributor to picture preparation and paper writing.

# Superconductivity in heterostructures: an overture

*Quantum mechanics is an example of truth
that seems stranger than fiction,
but when you understand the math behind it,
it becomes a little more believable.*

*– Someone in an internet forum*

This chapter serves as an introduction to the microscopic theory of superconductivity. The subject is extremely vast, and it is possible to find several theories at different levels of approximation. For this reason, we will provide a succinct exposition that covers only the essential concepts necessary for understanding the research activity presented in this thesis. The chapter focuses more on the physical concept and will not cover the theoretical methods, in particular Green functions methods, as they are extensively covered in textbooks like Ref. [1, 2].

This thesis focuses on hybrid heterostructures, and one of the most suitable languages to discuss the physics in these systems is the Bogoliubov-de Gennes (BdG) method [3, 4] because it does not require any particular assumption about the length-scales of the phenomena described and can deal with both clean and disordered systems. The BdG method is introduced in Sec. 1.1, where we will make the relevant connection to its Green function counterpart by Gor'kov [5]. After having established the formalism, we will discuss two types of superconductors, the $s$-wave paired superconductor (Sec. 1.2) and the $p$-wave class (Sec. 1.3). For the former, the focus will be on the effect of exchange fields in the system, while the latter will be on the topological properties. After this introduction, Sec. 1.4 will present the proximity effect and will introduce some simple models to account for it. Sec. 1.5 will consider structures with multiple superconducting regions, the formation of Andreev bound states, and the Josephson effect. Finally, topological superconductivity in heterostructures is the subject of Sec. 1.6, and will conclude with an overview of experimental implementations of the idea.

## 1.1 Microscopic models for superconductivity

In this section, we will derive the mean-field approach to solve a generic attractive two-body potential between electrons in a single-band metal and show how this leads, under the necessary conditions, to the appearance of a superconducting phase. A formal derivation of the procedure can be found in many sources using a variety of methods, like by application of Wick theorem, a variational argument, or a Hubbard-Stratonovich transformation. Here we outline the main key steps inspired by Refs. [4, 6–9]. Next, we will introduce the main ideas behind the BdG method and its connection to the Gor'kov method. we will conclude the section with a brief introduction to the symmetry of the order parameter.

### Mean-field approximation

Let us consider a generic Hamiltonian $\mathcal{H}_0(\mathbf{r})$ for a free-electron in a single band in which we introduce an attractive two-particle interaction $\mathcal{V}_{\sigma\sigma'}(\mathbf{r}, \mathbf{r}')$ such that the complete Hamiltonian reads as

$$
\begin{aligned}
H = &\sum_{\sigma\sigma'} \int d\mathbf{r}\, \psi_\sigma^\dagger(\mathbf{r}) \mathcal{H}_{0,\sigma\sigma'} \psi_{\sigma'}(\mathbf{r}) \\
&+ \frac{1}{2} \sum_{\sigma\sigma'} \int d\mathbf{r}\, d\mathbf{r}'\, \mathcal{V}_{\sigma\sigma'}(\mathbf{r}, \mathbf{r}') \psi_\sigma^\dagger(\mathbf{r}) \psi_{\sigma'}^\dagger(\mathbf{r}') \psi_{\sigma'}(\mathbf{r}') \psi_\sigma(\mathbf{r})
\end{aligned}
\tag{1.1}
$$

where the sum runs over the spin degree of freedom $\sigma$ of the electron field $\psi_\sigma(\mathbf{r})$. This Hamiltonian supports a superconducting phase that is characterized by a non-zero anomalous single-particle correlator

$$
\rho_{\sigma\sigma'}^a(\mathbf{r}, \mathbf{r}') \equiv \langle \psi_\sigma(\mathbf{r}) \psi_{\sigma'}(\mathbf{r}') \rangle,
\tag{1.2}
$$

that is an indicator of the presence of pairing in the system.

It can be shown that we can decouple the interaction term in the Cooper channel by using the anomalous correlator as a mean field. Neglecting fluctuations, we can find the mean-field approximation using the following substitution

$$
\begin{aligned}
\psi_\sigma(\mathbf{r})\psi_{\sigma'}^\dagger(\mathbf{r}')\psi_{\sigma'}(\mathbf{r}')\psi_\sigma(\mathbf{r}) \rightarrow \Big[ &\langle\psi_\sigma^\dagger(\mathbf{r})\psi_{\sigma'}^\dagger(\mathbf{r}')\rangle\psi_{\sigma'}(\mathbf{r}')\psi_\sigma(\mathbf{r}) \\
+\psi_\sigma^\dagger(\mathbf{r})\psi_{\sigma'}^\dagger(\mathbf{r}')&\langle\psi_{\sigma'}(\mathbf{r}')\psi_\sigma(\mathbf{r})\rangle - \langle\psi_\sigma^\dagger(\mathbf{r})\psi_{\sigma'}^\dagger(\mathbf{r}')\rangle\langle\psi_{\sigma'}(\mathbf{r}')\psi_\sigma(\mathbf{r})\rangle \Big].
\end{aligned}
\tag{1.3}
$$

In principle, six other terms appear, three for the Hartree and three for the Fock channels. We neglect these as they are not essential for the superconducting phenomenology and, in general, can be reabsorbed in the chemical potential of the system.

The mean-field Hamiltonian then reads as

$$
\begin{aligned}
H_{\mathrm{MF}} = &\sum_{\sigma\sigma'}\int d\mathbf{r}\,\psi^\dagger(\mathbf{r})\mathcal{H}_{0,\sigma\sigma'}\psi(\mathbf{r}) \\
&+\frac{1}{2}\sum_{\sigma\sigma'}\int d\mathbf{r}\,d\mathbf{r}'\left(\Delta_{\sigma\sigma'}^*(\mathbf{r},\mathbf{r}')\psi_{\sigma'}(\mathbf{r}')\psi_\sigma(\mathbf{r}) + \psi_\sigma^\dagger(\mathbf{r})\psi_{\sigma'}^\dagger(\mathbf{r}')\Delta_{\sigma\sigma'}(\mathbf{r}',\mathbf{r})\right) \\
&-\frac{1}{2}\sum_{\sigma\sigma'}\int d\mathbf{r}\,d\mathbf{r}'\frac{\left|\Delta_{\sigma\sigma'}(\mathbf{r},\mathbf{r}')\right|^2}{\mathcal{V}_{\sigma\sigma'}(\mathbf{r}',\mathbf{r})}
\end{aligned}
\tag{1.4}
$$

where we defined the *pairing potential*

$$
\Delta_{\sigma\sigma'}(\mathbf{r},\mathbf{r}') = \mathcal{V}_{\sigma\sigma'}(\mathbf{r},\mathbf{r}')\rho_{\sigma\sigma'}^a(\mathbf{r},\mathbf{r}').
\tag{1.5}
$$

The second line in the mean-field Hamiltonian represents the process in which two electrons can be bound together and be absorbed by the condensate or vice versa. The last line is a constant term that is only relevant to describe the thermodynamic properties of the system and can be ignored when considering small excitations.

The mean-field Hamiltonian in Eq. 1.4 does not commute anymore with the number operator. This means that the ground state will mix states with a different number of electrons. This can lead to problems when considering isolated systems, but it is not of particular concern when considering open systems.

## Bogoliubov transformation and particle-hole symmetry

The Hamiltonian of the system is now quadratic in the field operator, but it contains anomalous terms, i.e., with a product of two creation or annihilation operators. These operators complicate diagonalizing the Hamiltonian and are the ones responsible for the breakdown of particle number conservation.

To eliminate the anomalous terms, we can use a Bogoliubov transformation, a linear transformation in which we define new fermionic operators $\{\gamma_n\}$ that are a linear combination of creation and annihilation operators

$$
\gamma_n = \sum_\sigma \int d\mathbf{r}\, u_\sigma^n(\mathbf{r})\psi_\sigma(\mathbf{r}) + v_\sigma^n(\mathbf{r})\psi_\sigma^\dagger(\mathbf{r})
\tag{1.6}
$$

where the coefficients $u$ and $v$ are called *coherence factor*. The above relation can be synthetically written by collecting all the degrees of freedom in a vector and the coherence factor in linear operators $\underline{u}$ and $\underline{v}$

$$[\gamma] = [\underline{u} \quad \underline{v}] \begin{bmatrix} \psi \\ \psi^\dagger \end{bmatrix} \tag{1.7}$$

where the matrix product is intended in a generalized sense as a sum over spin indices and an integral for the continuous space coordinates.

These operators are the creation and annihilation operators of the microscopic excitations of the condensate and are called Bogoliubov quasiparticles. By imposing preservation of the anticommutation relations for the newly defined operators, we obtain a linear transformation that reads as

$$\begin{bmatrix} \gamma \\ \gamma^\dagger \end{bmatrix} = \begin{bmatrix} \underline{u} & \underline{v} \\ -\underline{v}^\dagger & \underline{u}^\dagger \end{bmatrix} \begin{bmatrix} \psi \\ \psi^\dagger \end{bmatrix}, \qquad \begin{bmatrix} \psi \\ \psi^\dagger \end{bmatrix} = \begin{bmatrix} \underline{u}^\dagger & -\underline{v} \\ \underline{v}^\dagger & \underline{u} \end{bmatrix} \begin{bmatrix} \gamma \\ \gamma^\dagger \end{bmatrix}. \tag{1.8}$$

We determine the value coherence factors by requiring that this transformation diagonalize the Hamiltonian, i.e.

$$H_{\mathrm{MF}} = E_{\mathrm{g}} + \sum_n E_n \gamma_n^\dagger \gamma_n, \tag{1.9}$$

where $E_{\mathrm{g}}$ is the ground state energy while $E_n$ are the excitation energies. We can do that by rewriting the mean-field Hamiltonian as a quadratic form for the Nambu spinor $\Psi(\mathbf{r}) = \left( \psi_\uparrow(\mathbf{r}), \psi_\downarrow(\mathbf{r}), \psi_\uparrow^\dagger(\mathbf{r}), \psi_\downarrow^\dagger(\mathbf{r}) \right)$

$$H_{\mathrm{MF}} = \frac{1}{2} \int d\mathbf{r}\, d\mathbf{r}'\, \Psi(\mathbf{r})^\dagger \mathcal{H}_{\mathrm{BdG}}(\mathbf{r}, \mathbf{r}') \Psi(\mathbf{r}) + \frac{1}{2} \operatorname{tr} \mathcal{H}_0 - \frac{1}{2} \sum_{\sigma\sigma'} \iint d\mathbf{r}\, d\mathbf{r}'\, \frac{\left| \Delta_{\sigma\sigma'}(\mathbf{r}, \mathbf{r}') \right|^2}{\mathcal{V}_{\sigma\sigma'}(\mathbf{r}', \mathbf{r})} \tag{1.10}$$

where we defined the BdG Hamiltonian as

$$\mathcal{H}_{\mathrm{BdG}}(\mathbf{r}, \mathbf{r}') = \begin{pmatrix} \mathcal{H}_0(\mathbf{r}) \delta(\mathbf{r} - \mathbf{r}') & \Delta(\mathbf{r}, \mathbf{r}') \\ -\Delta^\dagger(\mathbf{r}', \mathbf{r}) & -\mathcal{H}_0^*(\mathbf{r}) \delta(\mathbf{r} - \mathbf{r}') \end{pmatrix}. \tag{1.11}$$

The excitation energies can be thus obtained by solving the Bogoliubov-De Gennes equation, that is, the eigenvalue equation for the BdG Hamiltonian

$$\int d\mathbf{r}'\, H_{\mathrm{BdG}}(\mathbf{r}, \mathbf{r}') \psi^n(\mathbf{r}') = E_n \psi^n(\mathbf{r}). \tag{1.12}$$

The eigenvectors $\psi^n = (u_\uparrow^n, u_\downarrow^n, v_\uparrow^n, v_\downarrow^n)$ can be interpreted as the wavefunction of Bogoliubov quasiparticles.

By applying the Bogoliubov transformation, we are doubling the dimension of the Hilbert space. This will result in a special symmetry featured by the BdG Hamiltonian called *particle-hole symmetry*. In general, a particle-hole symmetry $\mathcal{P}$ is antiunitary and anticommutes with the Hamiltonian

$$\mathcal{P} \mathcal{H}_{\mathrm{BdG}} \mathcal{P}^{-1} = -\mathcal{H}_{\mathrm{BdG}}. \tag{1.13}$$

In the basis adopted $\mathcal{P} = \tau_x \mathcal{K}$, where we introduced the Pauli matrix for the particle-hole space $\{\tau_i\}$, and $\mathcal{K}$ being the complex conjugation operator.

This fundamental property of superconductors has numerous consequences, and some will be evident when analyzing transport phenomena in Ch. 3. The most obvious consequence

is that the quasiparticle spectrum is symmetric around zero, and for each pair of eigenstates and eigenvalue $(E_n, \psi^n)$, there is a symmetric pair $(-E_n, \mathcal{P}\psi^n)$. We will label by positive $n$ all the positive eigenvalues.

The ground state energy in Eq. (1.9) can be written as

$$E_g = -\sum_{n>0} E_n + \frac{1}{2} \mathrm{tr}\,\mathcal{H}_0 - \frac{1}{2} \sum_{\sigma\sigma'} \iint \mathrm{d}\mathbf{r}\,\mathrm{d}\mathbf{r}' \frac{\left|\Delta_{\sigma\sigma'}(\mathbf{r},\mathbf{r}')\right|^2}{\mathcal{V}_{\sigma\sigma'}(\mathbf{r}',\mathbf{r})} \tag{1.14}$$

where the sum in the first term now runs on only half of the spectrum.

By solving the BdG equation, we have precise information about the system's excitation; however, we do not know much about the ground state. To express the new ground state, we start by the definition of the operators $\gamma_n$: since they are the excitations, the ground state $|\mathrm{GS}\rangle$ can be defined by the condition

$$\gamma_n |\mathrm{GS}\rangle = 0 \qquad \forall\, n > 0 \tag{1.15}$$

Starting from this definition, it can be shown that the ground state can be expressed as

$$|\mathrm{GS}\rangle = \frac{1}{\det^{1/4}(1 + S^\dagger S)} \exp\left[\frac{1}{2} \iint \mathrm{d}\mathbf{r}\,\mathrm{d}\mathbf{r}'\, \psi^\dagger(\mathbf{r}) S(\mathbf{r},\mathbf{r}') \psi^\dagger(\mathbf{r}')\right] |0\rangle \tag{1.16}$$

with the fermionic vacuum being $|0\rangle$, and $S = \underline{u}^{-1}\underline{v}$, that can be interpreted as the condensate wavefunction [8, 10]. With this definition, it is clear that $|\mathrm{GS}\rangle$ is a superposition of different states, each of them composed of a defined number of pairs.

With this picture of the ground state, it is now possible to better understand what kind of excitation is represented by Bogoliubov quasiparticles: a many-body state with a quasiparticle is a state with a single extra particle that cannot be absorbed in the condensate because it is lacking a partner. The symmetry around the Fermi level can be understood as the fact that one could read this state by both adding or removing an electron from the system.

When considering systems at finite temperatures and under the action of an external magnetic field, it is convenient to consider the free energy of the system. The general form of the free energy of a BdG system can be written as

$$\mathcal{F} = \langle H_{\mathrm{MF}}\rangle - TS + \int \mathrm{d}\mathbf{r} \frac{|\boldsymbol{\nabla}\times\mathbf{A}(\mathbf{r}) - \mathbf{B}^{\mathrm{e}}|^2}{2\mu_0} \tag{1.17}$$

where $T$ is the temperature, $S$ is the entropy, $\mathbf{A}$ is the magnetic vector field, $\mathbf{B}^{\mathrm{e}}$ is the external magnetic field and $\mu_0$ is the vacuum permittivity. Leveraging particle-hole symmetry, the free energy can be conveniently written as a function of the quasiparticle excitation energies as

$$\mathcal{F} = -k_{\mathrm{B}} T \sum_n \ln\cosh\left(\frac{E_n}{2k_{\mathrm{B}} T}\right) + \frac{1}{2} \mathrm{tr}\,\mathcal{H}_0 - \iint \mathrm{d}\mathbf{r}\,\mathrm{d}\mathbf{r}'\, |\Delta(\mathbf{r},\mathbf{r}')|^2 \mathcal{V}^{-1}(\mathbf{r}',\mathbf{r})$$
$$\int \mathrm{d}\mathbf{r} \frac{|\boldsymbol{\nabla}\times\mathbf{A}(\mathbf{r}) - \mathbf{B}^{\mathrm{e}}|^2}{2\mu_0} \tag{1.18}$$

By minimization of $\mathcal{F}$, one can obtain the BdG equations and the Maxwell equation for the current [8]. While by minimizing the free energy with respect to the pairing amplitude $\Delta$, instead, one obtains the gap equation that links the quasiparticle spectrum to the pairing potential. The gap equation reads as

$$\Delta(\mathbf{r},\mathbf{r}') = \mathcal{V}(\mathbf{r},\mathbf{r}') \sum_n u_n(\mathbf{r}) v_n^\dagger(\mathbf{r}') \tanh\left(\frac{E_n}{2k_{\mathrm{B}} T}\right). \tag{1.19}$$

**Connection with Gor'kov equations and its descendants**

A different approach for solving problems involving superconductivity is the Green function formalism introduced by Gor'kov [5]. This has a simple connection with the Hamiltonian BdG approach. To visualize it, let us define a (retarded) Green function

$$\mathcal{G}^R(\mathbf{r},\mathbf{r}',t,t') = \theta(t-t')\langle \Psi(\mathbf{r},t)\Psi^\dagger(\mathbf{r}',t')\rangle. \tag{1.20}$$

for the Nambu electron operators

$$\Psi(\mathbf{r},t) = \left(\psi_\uparrow(\mathbf{r},t),\, \psi_\downarrow(\mathbf{r},t),\, \psi_\uparrow^\dagger(\mathbf{r},t),\, \psi_\downarrow^\dagger(\mathbf{r},t)\right). \tag{1.21}$$

Other types of Green's function can be defined similarly.

This Green function has a nice block structure

$$\mathcal{G} = \begin{pmatrix} G & F \\ F^\dagger & \bar{G} \end{pmatrix} \tag{1.22}$$

where $G_{\sigma\sigma'}^R(\mathbf{r},\mathbf{r}',t,t') = \langle \psi_\sigma(\mathbf{r},t)\psi_{\sigma'}^\dagger(\mathbf{r}',t')\rangle$ is the normal Green's function of the system while $F_{\sigma\sigma'}(\mathbf{r},\mathbf{r}',t,t') = \langle \psi_\sigma(\mathbf{r},t)\psi_{\sigma'}(\mathbf{r}',t')\rangle$ is the anomalous component.

The connection with the BdG formalism is clear since the equation of motion for this function takes the form

$$\int d\mathbf{r}' \left[\omega - \mathcal{H}_{\text{BdG}}(\mathbf{r},\mathbf{r}')\right]\mathcal{G}(\mathbf{r}',\mathbf{r}'',\omega) = \delta(\mathbf{r}-\mathbf{r}'') \tag{1.23}$$

Note that the anomalous correlator, and consequently the pairing potential, can be written in terms of the anomalous Green function as

$$\Delta_{\sigma\sigma'}(\mathbf{r},\mathbf{r}') = \mathcal{V}_{\sigma\sigma'}(\mathbf{r},\mathbf{r}')\rho_{\sigma\sigma'}^a(\mathbf{r},\mathbf{r}') = \mathcal{V}_{\sigma\sigma'}(\mathbf{r},\mathbf{r}')\left[k_B T \sum_n F_{\sigma\sigma'}(\mathbf{r},\mathbf{r}',i\omega_n)\right] \tag{1.24}$$

where $\omega_n = \frac{(2n+1)\pi k_B T}{\hbar}$ are the Matsubara frequencies. All the other observables of the system can be obtained with standard expressions. For example, the density of states and the spin polarization can be written as

$$\rho_i(\omega) = \text{tr}\{\sigma_i G(\mathbf{r},\mathbf{r})\} \tag{1.25}$$

with $i \in \{0,x,y,z\}$.

The power of Gor'kov equations is not in its alternative solution strategy with respect to BdG equations (they are partial differential equations instead of a diagonalization problem) but rather in their nature as a first stepping stone of a hierarchy of approximation schemes. That can be used to address different situations on one side and to the possibility to describe more in detail the nature of the attractive interaction on the other.

The most common approximation scheme used for metallic superconductors that feature a high density of states is the Eilenberger equation [11]. These equations are the Green function counterpart of the Andreev approximation scheme of BdG equations, in which the equations are linearized in the neighbors of the Fermi surface. A second level of approximation can be applied by considering diffusive superconductors where diluted impurities scramble the motion of electrons. In this case, the behavior of the system is described by the Usadel equations [12].

The fundamental idea is that the band structure of the superconductor is not the most interesting characteristic of the system, and we want to simplify the description by getting rid of it. The first step is rewriting the Green function using a mixed Fourier transform

$$\tilde{\mathcal{G}}(\mathbf{r}, \mathbf{k}) = \int \mathcal{G}\left(\mathbf{r} + \frac{\mathbf{s}}{2}, \mathbf{r} + \frac{\mathbf{s}}{2}\right) e^{-i\mathbf{k}s}, \tag{1.26}$$

where we used the center of mass coordinate, $\mathbf{r}$, and the relative distance, $\mathbf{s}$, and then integrating over the normal state quasiparticle energy $\xi_{\mathbf{k}}$ to define the quasiclassical propagator

$$g(\mathbf{r}, \mathbf{e_k}) = \frac{1}{\pi} \int d\xi_{\mathbf{k}} \tilde{\mathcal{G}}(\mathbf{r}, \mathbf{k}) \delta\left(1 - \frac{\mathbf{k}}{|\mathbf{k}|} \cdot \mathbf{e_k}\right). \tag{1.27}$$

The equation of motion for this function is the Eilenberger equation. By further averaging over the direction of motion, the Usadel equation is obtained, that reads as

$$D\nabla \cdot (g\nabla g) - [\omega_n \tau_3 \sigma_0 + i\mathbf{h} \cdot \boldsymbol{\sigma} \tau_3 + (\Delta \tau_+ + \Delta^\dagger \tau_-) + \Sigma, g] = 0. \tag{1.28}$$

where $D$ is the diffusion constant, $\omega_n = 2\pi(2n+1)/T$ with temperature $T$ are the Matsubara frequencies, $\mathbf{h}$ is the exchange field, $\Delta$ is the order parameter and $\Sigma$ are additional self-energies. The equation needs to be complemented with the normalization constraint $g^2 = 1$. We recall that the diffusion constant is defined as $D = \frac{v_F \ell}{3}$, where $v_F$ is the Fermi velocity and $\ell$ is the elastic mean free path.

We swept several mathematical complications under the rug in this extremely synthetic account. A discussion of these can be found in the literature [13]. In this thesis, Usadel equations are just used to derive the phase diagrams shown in this chapter. Therefore we will not discuss them further.

## Symmetries of the order parameter

We now consider more in detail the pairing amplitude matrix. It is reasonable to assume that the attractive interaction depends only on the relative distance between the two electrons. However, since we deal with a structure that can feature an inhomogeneous pairing, e.g., a superconductor-semiconductor hybrid, we keep dependence on the center of mass coordinate $\mathbf{r}$, and we express the two-body interaction as

$$\tilde{\mathcal{V}}_{\sigma\sigma'}(\mathbf{r}, \mathbf{s}) = \mathcal{V}_{\sigma\sigma'}(\mathbf{r} + \mathbf{s}/2, \mathbf{r} - \mathbf{s}/2) \tag{1.29}$$

where we defined the relative distance $\mathbf{s}$.

We then consider the pairing potential in the same coordinate system, but we perform a Fourier transform in the $\mathbf{s}$ coordinate

$$
\begin{aligned}
\Delta_{\sigma\sigma'}(\mathbf{r}, \mathbf{k}) &= \int d\mathbf{s}\, \Delta_{\sigma\sigma'}(\mathbf{r} + \mathbf{s}, \mathbf{r} - \mathbf{s}) e^{i\mathbf{k}\cdot\mathbf{s}} \\
&= \int d\mathbf{s}\, \tilde{\mathcal{V}}_{\sigma\sigma'}(\mathbf{r} + \mathbf{s}, \mathbf{r} - \mathbf{s}) \rho_{\sigma\sigma'}^a(\mathbf{r} + \mathbf{s}, \mathbf{r} - \mathbf{s}) e^{i\mathbf{k}\cdot\mathbf{s}} \\
&= \frac{1}{\Omega^2} \iiint d\mathbf{s}\, d\mathbf{k}'\, d\mathbf{k}''\, \tilde{\mathcal{V}}_{\sigma\sigma'}(\mathbf{r}, \mathbf{k}') \rho_{\sigma\sigma'}^a(\mathbf{r}, \mathbf{k}'') e^{i(\mathbf{k} - \mathbf{k}' - \mathbf{k}'')\cdot\mathbf{s}} \\
&= \frac{1}{\Omega} \int d\mathbf{k}'\, \tilde{\mathcal{V}}_{\sigma\sigma'}(\mathbf{r}, \mathbf{k}') \rho_{\sigma\sigma'}^a(\mathbf{r}, \mathbf{k} - \mathbf{k}')
\end{aligned}
\tag{1.30}
$$

A good approximation is to assume a separation of length scales such that the pairing amplitude can be written as a product of two independent functions:

$$\Delta(\mathbf{r}, \mathbf{k}) \simeq \frac{\{f(\mathbf{r}), g(\mathbf{k})\}}{2} \tag{1.31}$$

where $f(\mathbf{r})$ describes the strength and phase of the order parameter and depends only on the center of mass coordinate, while $g(\mathbf{k})$ determines the type of pairing and depends only on the relative momentum. The curly braces denote an anticommutator, which is necessary to maintain the Hermiticity of the Hamiltonian.

Before going forward, we introduce a different basis for the Bogoliubov-De Gennes Hamiltonian to make the spin-rotation symmetry more evident. To do so, we apply a time-reversal symmetry operator $\mathcal{T} = U_{\mathcal{T}}\mathcal{K}$, with $U_{\mathcal{T}} = -i\sigma_y$ to the holes such that the particle-hole symmetry is $\mathcal{P} = i\tau_y\mathcal{T} = \sigma_y\tau_y\mathcal{K}$. In the new basis the spinor is $\Psi(\mathbf{r}) = \left(\psi, \mathcal{T}\psi^\dagger\right) = \left(\psi_\uparrow, \psi_\downarrow, -\psi_\downarrow^\dagger, \psi_\uparrow^\dagger\right)$ and the Bogoliubov-De Gennes Hamiltonian reads

$$\mathcal{H}_{\text{BdG}} = \begin{pmatrix} \mathcal{H} & \Delta' \\ \Delta'^\dagger & -\mathcal{T}H\mathcal{T}^{-1} \end{pmatrix}, \tag{1.32}$$

with $\Delta' = \Delta U_{\mathcal{T}}^\dagger$. Since this is the only basis we will use in the future, we drop the prime and simply refer to $\Delta$. In this basis, obtaining the Hamiltonian of holes is straightforward: we begin with the Hamiltonian for electrons and invert the signs of all terms that preserve time-reversal symmetry while leaving unaffected those that violate it.

The pairing matrix $\Delta$ determines what kind of pairs compose the condensate. Let us consider a homogeneous system for simplicity, such that $\Delta_\mathbf{k}$ is constant in space. It is insightful to decompose the pairing potential in its singlet ($d_0$), and triplet ($\mathbf{d}$) components

$$\Delta_\mathbf{k} = d_0(\mathbf{k})\sigma_0 + \mathbf{d}(\mathbf{k}) \cdot \boldsymbol{\sigma}. \tag{1.33}$$

The pairing potential is proportional to the anomalous correlator $\rho^a$, which is the expectation value of two fermion operators. For this reason, a symmetry constraint prescribes that the singlet component has to be even in $\mathbf{k}$, while the triplet component has to be odd in $\mathbf{k}$.

If we assume a spin-trivial electron Hamiltonian with a dispersion relation $\xi_\mathbf{k}$, the spectrum of the superconductor is given by

$$E_{\mathbf{k},j} = \pm\sqrt{\xi_\mathbf{k}^2 + \delta_{\mathbf{k},\pm}^2}, \tag{1.34}$$

where and $\delta_{\mathbf{k},\pm}^2$ are the eigenvalues of $\Delta_\mathbf{k}\Delta_\mathbf{k}^\dagger$. Using the $(d_0, \mathbf{d})$ vector introduced above, the modulus of the paring potential can be written as

$$\Delta_\mathbf{k}\Delta_\mathbf{k}^\dagger = \left(d_0^2(\mathbf{k}) + |\mathbf{d}(\mathbf{k})|^2\right)\sigma_0 + \mathbf{q}(\mathbf{k}) \cdot \boldsymbol{\sigma}, \tag{1.35}$$

with $\mathbf{q} = i(\mathbf{d} \times \mathbf{d}^*)$, while the eigenvalues of such matrix are

$$\delta_{\mathbf{k},\pm}^2 = \left(d_0^2(\mathbf{k}) + |\mathbf{d}(\mathbf{k})|^2\right) \pm \left|\mathbf{q}(\mathbf{k})\right|^2. \tag{1.36}$$

Systems with vanishing $\mathbf{q}$ are said *unitary*. They do not break time-reversal symmetry and do not show spin polarization. On the contrary, non-unitary states have a finite spin-polarization

aligned to the axis identified by **q**. For this reason, they are not favored in the absence of a magnetic field.

We can further classify the pairing amplitude by the order of the momentum operator. Most known superconductors are either *s*-wave or *d*-wave (order 0 or 2 in **k**). In contrast, the *p*-wave type pairing (order 1) is extremely rare. We will briefly discuss some properties of these pairings in the next sections.

## 1.2   *s*-wave superconductors

This section will briefly summarize the characteristics of the most common type of low-temperature superconductor, the *s*-wave superconductor. In this type of superconductor, Cooper pairs are formed by states of opposite momentum and spin. The type of two-body interaction potential takes the form

$$\tilde{\mathcal{V}}_{\sigma\sigma'}(\mathbf{r},\mathbf{s}) = V(i\sigma_y)\delta(\mathbf{s}) \rightarrow \mathcal{V}(i\sigma_y)(\mathbf{k},\mathbf{k}') = \frac{V}{\Omega}(i\sigma_y)\delta(\mathbf{k}+\mathbf{k}'), \tag{1.37}$$

and, consequently, the pairing potential is such $\Delta_{\mathbf{k}} = \Delta_0\sigma_0$.

Since the pairing potential is constant for all values of the relative momentum **k**, *s*-wave superconductors show an isotropic energy gap that is equal to the pairing potential. This is shown in Fig. 1.1 and can easily be seen in the dispersion relation obtained using Eq. 1.34, resulting in

$$E_k = \sqrt{\xi_{\mathbf{k}}^2 + \Delta_0^2}, \tag{1.38}$$

while the coherence factors are

$$u_k = \sqrt{\frac{1}{2}\left(1 + \frac{\xi_k}{E_k}\right)}, \quad v_k = \sqrt{\frac{1}{2}\left(1 - \frac{\xi_k}{E_k}\right)}. \tag{1.39}$$

Using Eq. (1.39) in the gap equation in Eq. (1.19), we can rewrite it as

$$\Delta_0 = \int d\mathbf{k}\,\mathcal{V}\frac{\Delta_0}{2E_{\mathbf{k}}}\tanh\left(\frac{E_n}{2k_B T}\right). \tag{1.40}$$

By solving it with standard renormalization trick [14], and comparing the result for zero and the critical temperature $T_c$ of the superconductor-metal transition, it is possible to derive the universal relation between the critical temperature and the pairing potential at zero temperature that read as

$$k_B T_c \simeq 1.764\,\Delta_0(T=0). \tag{1.41}$$

Moreover, thanks to Anderson theorem [15], non-magnetic weak disorder has negligible effects. The idea behind the theorem is that even when the impurities are included, and the momentum does not commute anymore with the Hamiltonian, there are still pairs of states at the same energy due to Kramers's degeneracy that can bond together and form Cooper pairs.

Another parameter able to drive a transition to the metallic phase is the magnetic field. For superconductors, like in many other materials, it is useful to distinguish between the orbital effects of a magnetic field **B**, that are due to the coupling between the momentum and the magnetic vector potential **A**, and spin effects of due to the coupling of the spin degree of
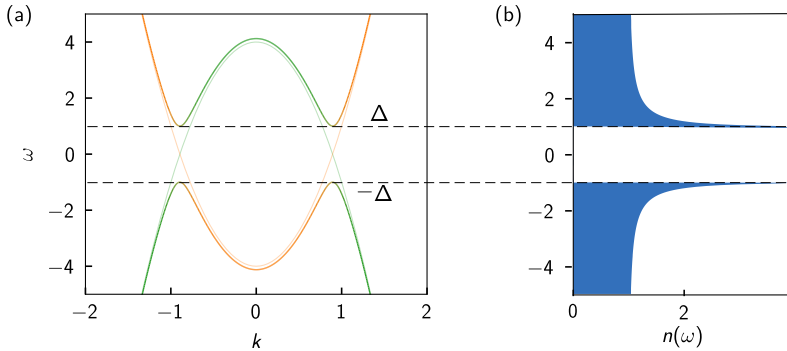
Fig. 1.1: **Dispersion relation and density of states of an $s$-wave superconductor.** (a) The $s$-wave pairing opens a gap in the spectrum at the Fermi surface. This is explained by the hybridization of the electron (orange curve) and hole (green curve) branches. (b) During the superconducting phase transition, the energy states that were previously situated within the gapped region in the normal phase are redistributed to the energy spectrum above the gap, resulting in the emergence of coherence peaks in the density of states.

freedom with the magnetic field. This distinction is crucial in understanding ferromagnet-superconductor heterostructures in Ch. 4.

To introduce the effect of an external field, let us consider a simple parabolic band for which the electron Hamiltonian reads as

$$\mathcal{H}_0 = \frac{\left(\mathbf{p} - e\mathbf{A}\right)^2}{2m} - g\mu_B \frac{\mathbf{S}}{\hbar} \cdot \mathbf{B}, \tag{1.42}$$

where the term in the brackets determines the orbital effects in the superconductor, with $e$ being the electron charge and $m$ the effective mass. The second term is the coupling with the spin degree of freedom $\mathbf{S}$ with the coupling strength given by the Landé g-factor and the Bohr magneton $\mu_B$. In order to include different types of spin-splitting fields, like the ones coming from a proximity-coupled ferromagnetic material, we rewrite the second part as generic Zeeman Hamiltonian

$$\mathcal{H}_Z = -\mathbf{h} \cdot \boldsymbol{\sigma} \tag{1.43}$$

where we call $\mathbf{h}$ an *exchange field*. For an external magnetic field $\mathbf{h} = g\mu_B \mathbf{B}/\hbar$.

Usually, the orbital effects are dominant, causing an immense variety of effects, including vortex physics in type-II superconductors. In the case of a type-I superconductor, the main effect is the Meissner effect which consists of the expulsion of the magnetic field from the bulk of the superconductor for fields that are below the so-called *thermodynamic critical field*. Above this value, the dissipationless supercurrent cannot keep up with the magnetic field, and superconductivity is suppressed. We can derive the thermodynamic critical field by considering the free energy density of a small region in the bulk in the presence of an external field $\mathbf{B}^e$. In the superconductor phase, there are two relevant contributions to the free energy in Eq. (1.17): the condensation energy that lowers the free energy and the magnetic field energy due to the difference between the external field $\mathbf{B}^e$ and the total magnetic field $\mathbf{B}$ that is null

due to the Meissner screening. In the normal state, both terms are zero, as shown in Fig. 1.2(a). The resulting free energy density difference between the two phases is given by

$$f_{SN} = -N_0 \frac{|\Delta|^2}{2} + \frac{B^2}{2\mu},$$

(1.44)

where $N_0$ is the density of states. The critical field at which the first-order superconductor-normal transition takes place is then obtained by the condition $f_{SN} = 0$ and results in the following expression

$$B_c = \sqrt{\mu N_0} |\Delta|.$$

(1.45)
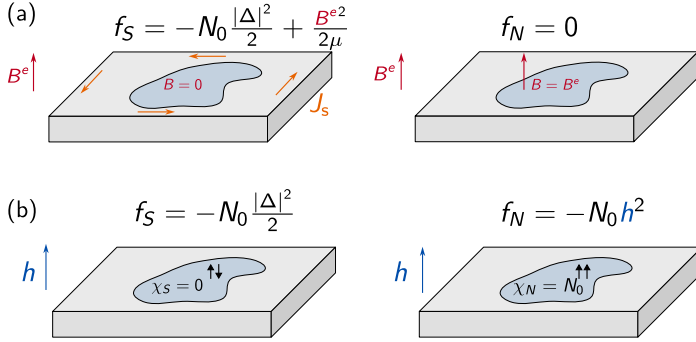


Fig. 1.2: **Critical fields in bulk superconductors.** (a) Calculation of the thermodynamic critical field. Since superconductors exhibit perfect diamagnetism, the magnetic field in the bulk is vanishing, giving a positive contribution to the energy equal to $|\mathbf{B}^e|^2/(2\mu)$ plus the condensation energy $-N_0|\Delta_0|^2/2$. Both terms are null in the normal phase. (b) Calculation of the paramagnetic critical field. The same idea can be applied to the evaluation of the paramagnetic limit. The condensation energy is negative and appears only in the superconductive phase, which is also characterized by a vanishing spin susceptibility, $\chi_S = 0$. In the normal phase, the spin susceptibility is proportional to the density of states, causing a negative contribution to the free energy equal to $-N_0 h^2$.

In the research presented in this thesis, the orbital effects are usually considered negligible, and we instead focus on the spin degree of freedom. This situation can be obtained when considering small superconductor samples with a very high thermodynamic critical field $B_c$ or when the superconductor is placed in contact with a ferromagnet that induces an exchange field in the material. Magnetism and *s*-wave superconductivity are competing phenomena. The competition between magnetism and *s*-wave superconductivity can be explained by their different microscopic origins: magnetism arises from the alignment of the spin of electrons in a material, while superconductivity results from the formation of Cooper pairs of electrons in a singlet state.

When we introduce a weak exchange field $h < \Delta_0$, this is unable to change the ground state of the system because of the energy gap. As a result, the static spin susceptibility of an *s*-wave superconductor is null at zero temperature [16]. The only effect of the exchange field is lifting the degeneracy of the excitation spectrum of the system since now, for each quasiparticle state,

one spin component has lower energy than the other. This causes the splitting of the coherence peaks shown in Fig. 1.3(a).

At the model level, the spectral properties of a spin-split $s$-wave superconductor can be deduced system can be calculated starting from Green's function in the wide-band limit

$$g^R_{\sigma\sigma'}(\omega) = -\frac{(\omega + i\eta + \sigma h)\tau_0 + \Delta\tau_x}{\sqrt{\Delta^2 - (\omega + i\eta + \sigma h)^2}}\delta_{\sigma\sigma'}, \tag{1.46}$$

where $h$ is the exchange field, and $\eta$ is known as the Dynes parameter and can be used to include pair-breaking scattering.
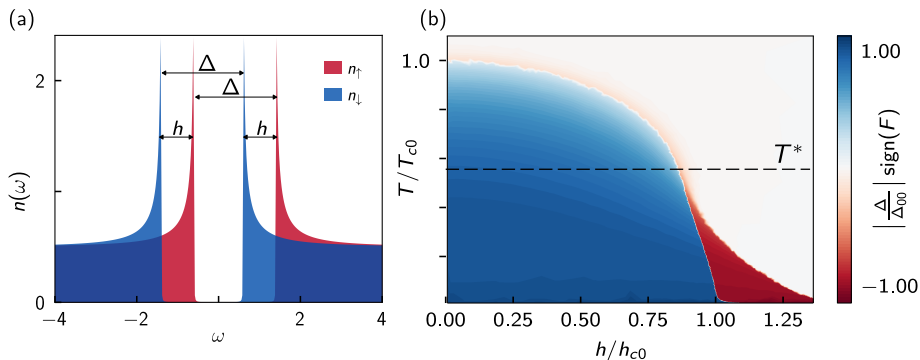


Fig. 1.3: **Properties of an exchange-split $s$-wave superconductor.** (a) Spin-resolved density of states of an $s$-wave superconductor with an exchange field $h = 0.5\Delta_0$. The coherence peaks appear split because quasiparticles with a spin aligned to the exchange field are favored with respect to the ones antialigned. Nevertheless, the ground state is unchanged for $h < h_{c0}$. (b) Phase diagram of a homogeneous $s$-wave superconductor calculated through self-consistent Usadel equations. At low-temperature, the pairing potential is almost unchanged until $h = h_{c0}$, where a first order first transition makes the superconducting phase metastable (red region). At $T = T^*$, the transition becomes of second order.

For the argument above, one could think that superconductivity persists as the ground state up to the closing of the gap for $h = \Delta_0$. However, this is not the case, and the critical line is actually located at a lower exchange field, as initially shown by Chandrasekhar [17] and Clogston [18]. In this case, what causes the transition to the normal state is Pauli paramagnetism. The reasoning is very simple and similar to the one used to derive the thermodynamic critical field. Let us consider a system without the Meissner effect. Considering the null spin-susceptibility, the difference between the free energy in the superconducting and normal state can be written as [19]

$$\frac{f_{SN}}{N_0} \simeq -\frac{|\Delta|^2}{2} + h^2 + \frac{\pi^2 T^2}{3}. \tag{1.47}$$

The critical line is then calculated as

$$h_{c0} = \frac{|\Delta|}{\sqrt{2}}, \tag{1.48}$$

which is known as the Chandrasekhar-Clogston limit or paramagnetic limit and does not depend on the density of states. At low temperatures, this first-order transition abruptly

brings the system to the normal metallic state. However, when the temperature overcomes $T^* = 0.556\,T_c$, the transition becomes of second order [20, 21]. The phase diagram of a spin-split superconductor is shown in Fig. 1.3(b).

In thin superconducting films, quantum confinement causes an increase in the superconducting pairing amplitude leading to a superconducting phase that survives under stronger exchange fields in absolute value. However, the Chandrasekhar-Clogston limit still holds in terms of Eq. 1.48 [22]. In making this consideration, we have assumed that $\Delta$ would remain homogeneous in space. Phases with inhomogeneous $\Delta$, so-called FFLO phases, have been predicted to appear at low temperatures for high-fields [23, 24]. However, these phases are very susceptible to disorder and negligible in most situations.

## 1.3   *p*-wave superconductors and topological superconductivity

We now move to a more exotic type of superconductor, namely one featuring *p*-wave pairing. In these superconductors, the pairs forming the condensate are in a triplet state, causing significantly different thermodynamic properties and excitation spectrum. For instance, equal-spin pairing superconducting phases (that are nonunitary) are not limited by Pauli paramagnetism. Therefore we could expect very high critical fields, provided the effect of the orbital diamagnetism can be reduced. Two important types of *p*-wave pairing are the chiral $p_x + i p_y$ superconductor, with $\mathbf{d} \propto \mathbf{e}_z(k_x + i k_y)$, and the helical $p_x + p_y$ superconductor, with $\mathbf{d} \propto k_x \mathbf{e}_x + k_y \mathbf{e}_y$. Both of them belong to the class of topological superconductors.

### A crash course in topological phases of matter

One of the most exciting features of *p*-wave superconductors is that they can support *topological phases*. Following Ref. [25], a topological phase of matter can be defined as a phase where the many-body ground-state wavefunction cannot be adiabatically connected to the atomic limit. This definition is not satisfactory in preciseness and completeness, but it will work fine to introduce the concept here. Topological superconducting phases are known for their *symmetry-protected topological order* (SPT order) [25–28]. This order occurs in systems with a quadratic Hamiltonian and is defined by a symmetry group $G$. The SPT phase is gapped, has short-range entanglement, and features topologically distinct phases that cannot be smoothly transformed into a trivial product state without breaking the symmetry group $G$ or closing the energy gap. Practically speaking, when transitioning between the trivial and topological regions of these systems, edge states are protected. These states are protected because no local perturbation that breaks translational symmetry can destroy them.

Based on this definition, it is evident that the symmetries that compose the group $G$ must be somewhat unconventional: we have to consider highly generic symmetries, like time-reversal symmetry or the particle-hole symmetry introduced for superconductors. These symmetries are special because they are represented by anti-unitary operators when acting on the single-particle Hilbert space. In a generalized setting, the relevant symmetries for SPT order are operators that belong to these three general classes:

- A *time-reversal symmetry* $\mathcal{T}$ is an anti-unitary operator that commutes with $\mathcal{H}$.

- A *particle-hole symmetry* $\mathcal{P}$ is an anti-unitary operator that anti-commutes with $\mathcal{H}$.

- A *chiral symmetry* $\mathcal{S}$ is a unitary operator which anti-commutes with $\mathcal{H}$.

When both time-reversal symmetry and particle-hole symmetry are present, a chiral symmetry can be defined as $\mathcal{S} = \mathcal{PT}$. It is important to note that although $\mathcal{P}$ and $\mathcal{S}$ anti-commute with the single-particle Hamiltonian, the two symmetries commute with the second-quantized Hamiltonian, as expected for a symmetry operator.

SPT phases can be classified by the symmetry group $G$ according to the Altland–Zirnbauer periodic table of topological invariants shown in Tab. 1.1. The table represents the absence of symmetries with 0. The presence of these symmetries is indicated by either +1 or −1, depending on whether the operator representing the symmetry is involutory or anti-involutory, indicating whether it squares to +1 or −1, respectively. The last three columns display the topological invariant that can classify the topologically distinct ground states as a function of symmetry class and spatial dimension $d$ [27, 29–31]. By virtue of the bulk-edge correspondence, by studying the bulk system Hamiltonian, which is a homogenous system with no boundaries, we can infer the existence and properties of topologically protected edge states, which occur at the boundaries of the material in a finite-size sample. The table is called periodic because it repeats with period 8 in $d$ for the real symmetry classes and period 2 for the complex ones (Bott periodicity).

| | $\mathcal{T}^2$ | $\mathcal{P}^2$ | $\mathcal{S}^2$ | $d = 0$ | $d = 1$ | $d = 2$ | $d = 3$ |
|---|---|---|---|---|---|---|---|
| A (unitary) | 0 | 0 | 0 | $\mathbb{Z}$ | - | $\mathbb{Z}$ | - |
| AIII (chiral unitary) | 0 | 0 | 1 | - | $\mathbb{Z}$ | - | $\mathbb{Z}$ |
| AI (orthogonal) | +1 | 0 | 0 | $\mathbb{Z}$ | - | - | - |
| BDI (chiral orthogonal) | +1 | +1 | 1 | $\mathbb{Z}_2$ | $\mathbb{Z}$ | - | - |
| D | 0 | +1 | 0 | $\mathbb{Z}_2$ | $\mathbb{Z}_2$ | $\mathbb{Z}$ | - |
| DIII | −1 | +1 | 1 | - | $\mathbb{Z}_2$ | $\mathbb{Z}_2$ | $\mathbb{Z}$ |
| AII (symplectic) | −1 | 0 | 0 | $2\mathbb{Z}$ | - | $\mathbb{Z}_2$ | $\mathbb{Z}_2$ |
| CII (chiral symplectic) | −1 | −1 | 1 | - | $2\mathbb{Z}$ | - | $\mathbb{Z}_2$ |
| C | 0 | −1 | 0 | - | - | $2\mathbb{Z}$ | - |
| CI | +1 | −1 | 1 | - | - | - | $2\mathbb{Z}$ |

Table 1.1: **Periodic table of topological invariants** The Altland-Zirnbauer classification of quadratic Hamiltonians divides the Hamiltonians into ten different classes depending on the presence of a time-reversal symmetry $\mathcal{T}$, a particle-hole symmetry $\mathcal{P}$, and a chiral symmetry $\mathcal{S}$, and whether these symmetries are involutory or anti-involutory [27, 29–31]. In the columns on the right, the topological invariant is provided for each class and dimension $d$.

**Spinless $p$-wave superconductor**

To explore the emergence of topological phases in $p$-wave superconductors, we examine a simplified model of a "spinless" superconductor in which one spin branch is inactive. We follow [32] and consider a system modeled by the BdG Hamiltonian

$$\mathcal{H} = \begin{pmatrix} \frac{\hbar k^2}{2m} - \mu & \Delta_p k \\ \Delta_p k & -\left( \frac{\hbar^2 k^2}{2m} - \mu \right) \end{pmatrix}, \tag{1.49}$$

that can be diagonalized using Eq. 1.34, resulting in

$$E = \pm\sqrt{\xi_k^2 + \Delta_p^2 k^2}\,. \tag{1.50}$$

The dispersion relation is shown in Figure 1.4(a) for various values of the chemical potential, $\mu$. Unlike the *s*-wave case, the spectral gap depends on the position of the Fermi surface. The gap is equal to $\sqrt{2m\mu}\Delta_p$ for positive $\mu$ and has a linear behavior of $E_g = -\mu$ for negative $\mu$. The gap closes at $\mu = 0$, indicating a quantum critical point between the weak-pairing ($\mu > 0$) and strong-pairing ($\mu < 0$) phases [33]. In the weak-pairing phase, the system, in the absence of pairing, is metallic, and the resulting superconducting phase is similar to the conventional *s*-wave paired system. In the strong-pairing phase, the system is more akin to a Bose-Einstein condensate and does not exhibit a Fermi surface.
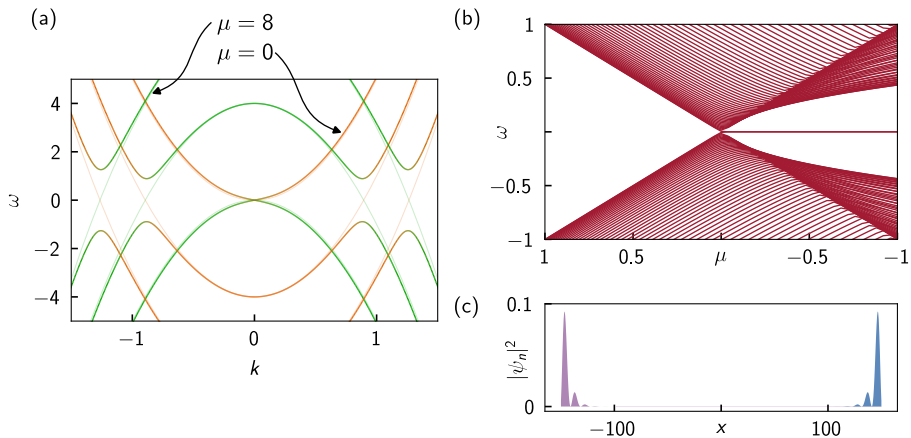


Fig. 1.4: *p***-wave superconductors.** (a) Dispersion relation of a 1D spinless p-wave supercon-ductor for $\mu = 0, 2, 4, 8$. It is possible to note how the size of the spectral gap depends on the Fermi momentum. The color scheme is the same as Fig. 1.1. (b) Spectrum of a finite length $L = 300$ wire spinless p-wave superconductor for varying $\mu$. At $\mu = 0$ the gap closes and reopens in the topological phase, marked by the appearance of MZMs. (c) Wavefunction of MZMs in the same system for $\mu = -0.6$. Parameters: $m = 0.1$, $\Delta = 1$

The BdG Hamiltonian considered here implicitly breaks time-reversal symmetry, as it only considers one spin component. As a result, the system belongs to class D of the topological classification and is characterized by a topological invariant $\mathbb{Z}_2$. This suggests that the two phases are topologically distinct. To confirm this, we will examine the presence of edge states, which will reveal which of the two phases is topologically nontrivial.

To begin, we note that when $m$ approaches infinity, the structure of the matrix $\mathcal{H}_{\text{BdG}} = \Delta_p k \tau_x - \mu \tau_z$ becomes equivalent to a one-dimensional Dirac Hamiltonian with the chemical potential playing the role of "mass". For this reason, we can expect to see a zero energy Jackiw-Rebbi bound-state on mass kinks. We can prove its existence by considering a chemical potential profile $\mu(x)$ with a soliton kink such that $\mu(-\infty) < 0$ and $\mu(+\infty) > 0$. We search for

zero-energy solutions using the ansatz

$$\psi_M(x) = \exp\left(-\frac{1}{\Delta}\int_{-\infty}^{+\infty}\mu(x')\,\mathrm{d}x'\right)\binom{u}{v} = \gamma(x)\binom{u}{v} \tag{1.51}$$

where $u$ and $v$ are complex coefficients and $\gamma$ is real valued. The resulting eigenvector equation is

$$\mathcal{H}\psi_M = \begin{pmatrix} -\mu(x) & i\mu(x) \\ i\mu(x) & \mu(x) \end{pmatrix}\binom{u}{v} = 0, \tag{1.52}$$

which has solution $v = iu$. By taking $u = (1+i)/2$ we can write the quasiparticle state as

$$\psi_M = \gamma(x)\frac{[\psi(x) + \psi^\dagger(x)] + i[\psi(x) + \psi^\dagger(x)]}{2}. \tag{1.53}$$

The localized fermionic excitation $\psi_M$ is its own antiparticle, that is the definition of a Majorana zero mode (MZM). It is a localized bound state, and it does not propagate. Therefore the two phases separated by the mass kinks are topologically distinct. Let us now consider the system with a finite electron mass $m$ and adiabatically increase $\Delta_p$ from 0: when $\mu < 0$, $\Delta_p > 0$, the system remains gapped; thus, the trivial insulator phase at $\Delta = 0$ and the strong-paired superconductive phase are adiabatically connected and belong to the same topological sector. The weak-paired superconducting phase, instead, cannot be connected to this sector for $\Delta \neq 0$ without closing the spectral gap.

Similar conclusions can also be drawn by numerically diagonalizing a finite-length 1D $p$-wave superconductor Hamiltonian, as shown in Fig 1.4(b). As the chemical potential is increased, the gap closes linearly with respect to $\mu$ and reopens in the topological phase. A pair of zero-energy modes can be observed in the topological phase, and their localized wavefunction is illustrated in Fig 1.4(c).

An alternative model for understanding the appearance of MZMs at the boundary between the topological and trivial region of a spinless $p$-wave superconductor is the discretized model introduced by Kitaev [34]. The Kitaev model has been used as an introductory toy model in many subsequent reviews like Refs. [35–40]

The model can be represented by the following Hamiltonian:

$$H = -\mu\sum_{i=1}^{N} c_i^\dagger c_i - \sum_{i=1}^{N-1} tc_i^\dagger c_{i+1} + \Delta c_i c_{i+1} + \text{h.c.} \tag{1.54}$$

where $\mu$ is the chemical potential, $t$ is the hopping amplitude and $\Delta$ is the pairing potential. The pairing potential acts on different sites that is the discrete equivalent to $p$-wave pairing. Indeed, by setting $t = \hbar^2/(2ma^2)$ and $\Delta = \Delta_p/(2a)$ the Kitaev model is just the discretized version of the Hamiltonian in Eq.(1.49) on a grid with spacing $a$.

To reveal the Majorana physics, we will rewrite the Hamiltonian in terms of new operators, $\gamma_{m,i}$ where $m \in \{1,2\}$, defined as follows:

$$c_i = \frac{1}{2}(\gamma_{1,i} + i\gamma_{2,i}), \quad c_i^\dagger = \frac{1}{2}(\gamma_{1,i} - i\gamma_{2,i}). \tag{1.55}$$

We show schematically this transformation in Fig. 1.5(a).

These operators are Majorana fermions because they satisfy the following defining properties

$$\{\gamma_{mi}, \gamma_{nj}\} = 2\delta_{ij}\delta_{nm}, \qquad \gamma_{mi}^{\dagger} = \gamma_{mi}. \tag{1.56}$$

This transformation makes it clear why Majorana fermions are often described as the real and imaginary parts of the composite complex operator that is a conventional fermion. One implication of the self-adjointness of the Majorana operators is that these excitations carry both zero energy and spin.

Rewritten in terms of the Majorana operators, the Kitaev Hamiltonian takes the form

$$H = -\frac{\mu}{2}\sum_{i=1}^{N}(i\gamma_{1,i}\gamma_{2,i} + 1) + \frac{i}{2}\sum_{i=1}^{N-1}\left[(\Delta + t)\gamma_{2,i}\gamma_{1,i+1} + (\Delta - t)\gamma_{1,i}\gamma_{2,i+1}\right]. \tag{1.57}$$
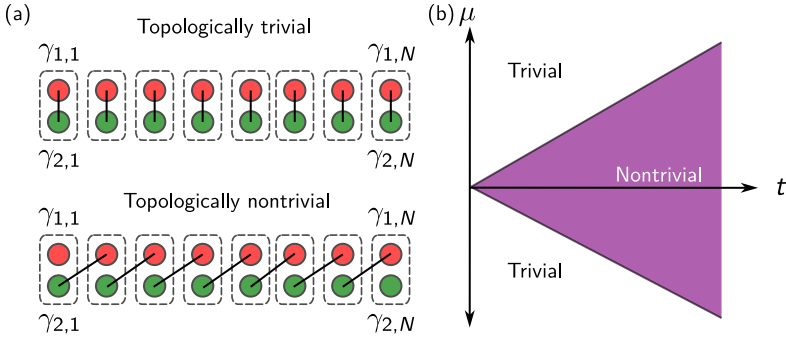


Fig. 1.5: **Kitaev chain** (a) Pictorial representation of the Kitaev chain in the topologically trivial and nontrivial phases. (b) Topological phase diagram of the Kitaev chain.

We will focus on limiting cases to understand the physical meaning of all the terms. The insulator limit is given by $\Delta = t = 0$ with $\mu < 0$. In this case, the chain consists of uncoupled sites:

$$H = -\mu\sum_{i=1}^{N}c_i^{\dagger}c_i = -\frac{\mu}{2}\sum_{i=1}^{N}(i\gamma_{1,i}\gamma_{2,i} + 1). \tag{1.58}$$

The two Majorana operators corresponding to a physical electron are paired in the same site. The system is fully gapped, and adding an electron cost a finite energy $-\mu$. This phase is topologically trivial and does not host any MZMs. This situation is depicted in the top panel of Fig. 1.5(a).

The next case we consider is $\Delta = t$ and $\mu = 0$. In this case, the Hamiltonian reduces to

$$H = it\sum_{i=1}^{N-1}\gamma_{2,i}\gamma_{1,i+1}, \tag{1.59}$$

The Majorana operators belonging to neighboring sites are paired in a Dirac fermion, as depicted in the bottom panel of Fig. 1.5(b). Therefore, it is insightful to rewrite the Hamiltonian

given in terms of new nonlocal fermionic operators

$$d_i = \frac{1}{2}(\gamma_{2,i} + i\gamma_{1,i+1}), \quad d_i^\dagger = \frac{1}{2}(\gamma_{2,i} - i\gamma_{1,i+1}). \tag{1.60}$$

The result is

$$H = 2t \sum_{i=1}^{N-1} \left( d_i^\dagger d_i - \frac{1}{2} \right). \tag{1.61}$$

As such, we see that the bulk of the system is still gapped, i.e., adding a fermion of type $d$ costs finite energy $2t$. However, the two Majorana operators $\gamma_{1,1}$ at the left end of the chain and $\gamma_{2,N}$ at the right end of the chain do not enter the Hamiltonian at all. This implies $[H,\gamma_{1,1}] = [H,\gamma_{2,N}] = 0$, i.e., the two outermost sites of the chain now host two isolated zero-energy modes satisfying the Majorana property $\gamma_{1,1} = \gamma_{1,1}^\dagger$, $\gamma_{2,N} = \gamma_{2,N}^\dagger$ as shown in Fig. 1.5(a).

The two MZMs can be combined to form a single nonlocal fermionic zero mode:

$$d_0 = \frac{1}{2}(\gamma_{1,1} + i\gamma_{2,N}), \quad d_0^\dagger = \frac{1}{2}(\gamma_{1,1} - i\gamma_{2,N}). \tag{1.62}$$

Since the constituent MZMs are localized at opposite ends of the chain, this fermionic zero mode is delocalized. Furthermore, this non-local fermionic state can be occupied or unoccupied without any energy cost, resulting in two degenerate ground states that differ in their fermion number. This is a distinct feature of the topological phase in comparison to conventional superconductors, where the ground state is non-degenerate and made up of a combination of states with even numbers of particles. Additionally, because of the non-local nature of the MZMs, it is impossible for any local perturbation to change the ground state.

While the above discussion focused on two limiting cases corresponding to the fully dimerized situations shown in Fig. 1.5, the qualitative properties of the trivial and nontrivial phase also persist if one deviates from these fine-tuned points, resulting in the phase diagram in Fig. 1.5(b). Indeed, the number of MZMs at a given end of the chain is directly related to a topological invariant, meaning that it is robust under continuous changes of the system parameters as long as the bulk spectral gap remains open and none of the protecting symmetries is broken.

## Non-abelian anyons and topological quantum computing

The presence of a two-fold ground state degeneracy and, in particular, the nonlocal nature of the zero-energy mode in this simple one-dimensional system provides the first element to explain the attractiveness of topological superconductors to encode quantum information. The core idea is that the protection against local perturbations makes it possible to envision qubits with extremely long coherence time.

To understand the possibility of manipulating the information in a protected way, it is necessary to introduce the non-Abelian exchange statistics of MZMs. Exchanging two anyons (MZMs) is represented by a non-trivial unitary acting on the degenerate ground-state subspace. These unitaries form a non-commutative group, hence the adjective non-abelian.

Non-abelian exchange statistics are more clearly explained for a different topological superconductor: the previously mentioned $p_x \pm i p_y$ paired state. In the two-dimensional case, this topological superconductor is characterized by a $\mathbb{Z}$ topological invariant. Indeed, an arbitrary number of MZMs can appear at the center of half-quantum vortices [41] since

the pairing amplitude is suppressed at the center of the vortex, which acts as a trivial region embodied in a topological superconducting one. In the presence of $N$ MZMs, the ground-state is $2^N$-fold degenerate. By bringing two vortices close to each other, the two MZMs can interact and form a fermionic degree of freedom with a definite occupation. Note, however, there is no prescribed way to pair (*fuse*) the MZMs [42].

A MZM-carrying vortex behaves as a non-abelian anyon as its exchange statics differs from the usual bosonic and fermionic ones. It is possible to change the state of a system by exchanging the position of vortices in a precise order, also called braiding. The dependence of the outcome on the path can be explained considering the 2+1D nature of the system: exchanging the position of the non-abelian anyons creates knots in the worldlines of the vortices that cannot be disentangled.

For practical application, it is necessary to translate the idea from vortices to two-dimensional systems comprised of several one-dimensional ones. The strategy to define a qubit is using four MZMs and fixing the total parity of the system in what is called a Majorana box qubit. This type of qubit has some limitations: only Clifford gates are realizable by braiding operations, and entangling two-qubit gates have to be realized in a non-protected way. Majorana-based qubits are advantageous because they keep quantum information encoded in delocalized fermionic states and are expected to be robust against most sources of decoherence. However, processes that change the total parity of the system, known as quasiparticle poisoning, involve a single MZM and cannot be suppressed by keeping them physically separated [35]

## 1.4   From Andreev reflection to the proximity effect

In the previous section, we discussed the unique properties of a $p$-wave superconductor, but few materials naturally exhibit a $p$-wave order parameter. Therefore, researchers have turned to an alternative approach: creating synthetic materials that exhibit the desired properties through the use of the *proximity effect.*

The proximity effect occurs when a superconducting material transfers some of its properties to adjacent non-superconducting material, leading to the formation of a proximity-induced superconducting gap. The phenomenon results from the coherent tunneling of Cooper pairs between the two materials. It can be explained by the penetration of the superconducting order parameter into the non-superconducting material, which decays exponentially with distance from the interface [43]. An alternative explanation involves Andreev reflection, a scattering event in which an electron coming from a normal metal is back-reflected as a hole [44, 45]. The scattering picture of Andreev reflection is anticipated in Fig. 1.6 and will be expanded in detail in Ch. 3.

A tunneling model for treating the proximity effect was introduced by McMillan [46]. In the following, we sketch a simplified version of the proof neglecting higher-order effects, like the back-action of the normal metal on the superconductor and the self-consistency of the pairing potential. Let us consider a simple system described by the Hamiltonian

$$H = H_N + H_{Sc} + H_T \tag{1.63}$$

that is the sum of a metal, $H_N$, superconductor, $H_{Sc}$, and tunneling $H_T$ terms.

We consider a simple $s$-wave superconductor described by

$$H_{Sc} = \sum_{\mathbf{k}} \xi_{\mathbf{k}} c_{\mathbf{k}}^\dagger c_{\mathbf{k}} + \Delta^\dagger c_{\mathbf{k}}(i\sigma_y) c_{-\mathbf{k}} + \text{H.c.}, \tag{1.64}$$
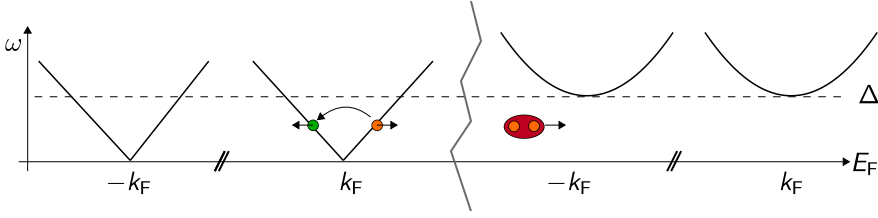
Fig. 1.6: **Sketch of Andreev reflection**. The diagram illustrates the process of Andreev reflection in momentum space. A right-moving electron in the metal (shown in orange), with an energy below the superconducting gap, collides with the superconductor-metal interface and is reflected as a left-moving hole (shown in green). This process generates an additional Cooper pair in the superconductor, which is absorbed by the condensate.

where $c_{\mathbf{k}}$ ($c_{\mathbf{k}}^{\dagger}$) are the electron annihilation (creation) operator in the superconductor, while the tunneling term is

$$H_{\mathrm{T}} = -\sum t\psi^{\dagger}(\mathbf{r})c_k + \text{H.c.}. \tag{1.65}$$

with $\psi_{\mathbf{k}}$ being the electron annihilation operator in the proximitized material.

In writing the tunneling Hamiltonian, we have neglected any possible complication in the tunneling amplitudes that are assumed constant. This can be justified in the limit of dirty interfaces, where momentum conservation is absent.

The proximity effect is derived by considering the renormalization of the normal metal Greens function

$$G_N^{-1}(\omega) = \omega\tau_0 - \mathcal{H}_{\mathrm{N}}\tau_1 - \Sigma(\omega), \tag{1.66}$$

where $\Sigma$ is a complex self-energy due to the tunneling of electrons in the superconductor. The self-energy reads as

$$\Sigma(\omega) = t^2 \int d\mathbf{k}\, G_{\mathrm{Sc}}(\mathbf{k},\omega) = -t^2 \int d\mathbf{k}\, \frac{\omega\tau_0 - \xi_{\mathbf{k}} - \Delta\tau_x}{\omega^2 - \xi_{\mathbf{k}}^2 - \Delta^2} \tag{1.67}$$

Performing the integral over the momentum in the wide-bandwidth approximation results in the following self-energy

$$\Sigma(\omega) = \gamma \frac{\omega\tau_0 + \Delta\tau_x}{\sqrt{\Delta^2 - \omega^2}}, \tag{1.68}$$

where we defined the coupling constant $\gamma = \pi t^2 N_0$ with $N_0$ being the normal state density of states at the Fermi level in the superconductor.

The final result is

$$G_{\mathrm{N}}^{-1} = \omega Z(\omega) + \mathcal{H}_{\mathrm{N}} + \frac{\gamma\Delta\tau_x}{\sqrt{\Delta^2 - \omega^2}}, \tag{1.69}$$

where the quasiparticle weight is defined as

$$Z(\omega) = 1 - \frac{\gamma}{\sqrt{\Delta^2 + \omega^2}}. \tag{1.70}$$

For the sake of simplicity, we ignore the effect of $Z(\omega)$, as it mainly describes the hybridization of the quasiparticles in the semiconductor with states of the superconductors and it

renormalizes the energy scale. We focus, instead, on the last term that defines an effective pairing potential

$$\tilde{\Delta}(\omega) = \frac{\gamma \Delta}{\sqrt{\Delta^2 - \omega^2}}.$$ (1.71)

that appears in the proximitized metal due only to the proximity to the superconductor. It introduces an energy gap in the spectrum and makes the system superconducting as well. Interestingly, at low energy ($\omega \ll \Delta$), the induced pairing potential is only proportional to the coupling, $\mathcal{H} \simeq \gamma$, while, for $\omega \gg \Delta$ the self-energy turns purely imaginary, and it represents the escape of highly-energetic quasiparticles in the superconductor. For simplicity, the energy dependence in the effective Hamiltonian is neglected in many analyses, and a constant induced pairing potential is considered when analyzing superconducting heterostructures, albeit different from the bulk value. This approximation is usually called the *weak-coupling* limit, while the *moderate-coupling* limit consists of including the complete self-energy in the effective Hamiltonian. The *strong-coupling* limit, instead, requires taking into account explicitly the superconductor in a complete BdG model and is usually needed for a realistic treatment of the disorder.

For what concerns the superconductor, the main effect on the density of states is the softening of the gap due to the difference between the induced gap and the parent superconductor gap values. More precise analysis of the proximity-coupled systems brings to renormalization of all the quantities involved in the low-energy effective model of a semiconductor [47].

## 1.5 Andreev bound states and Josephson effect

Another consequence of Andreev reflection is the formation of subgap states, called Andreev Bound States (ABS), in junctions where a non-superconducting layer is sandwiched between two gapped superconductors. The intuitive scattering picture that explains this effect is displayed in Fig. 1.7(a). The combination of two consecutive reflections at two different superconducting interfaces can create a closed loop that brings an electron-like quasiparticle back at the beginning of the coherent process, forming a bounded quasiparticle with an energy lower than the superconducting gap of the leads.

A widespread model to describe ABSs in metallic junctions is Beenakker's model [48]. Under the assumption that the scattering matrix of the normal region is weakly dependent on the quasiparticle energy for $\omega < \Delta$. The junction shows an ABS spectrum

$$\varepsilon_n = \Delta \sqrt{1 - T_n \sin^2\left(\frac{\phi}{2}\right)},$$ (1.72)

where $T_n$ are the transparencies of the transmission modes of the metallic central region while $\phi$ is the phase difference between the two superconducting leads. An extension of this model to junctions with exchange fields is presented in Appendix E.

In the process, the two Andreev reflections induce a Cooper pair transfer between the two superconducting leads, causing a dissipationless supercurrent to flow in the structure: the Josephson current. We conclude this section by deriving a general expression that links the quasiparticles spectrum to the supercurrent that flows in a junction. We consider a very generic system

$$H = H_{\mathrm{C}} + H_{\mathrm{Sc}} + H_{\mathrm{T}}$$ (1.73)
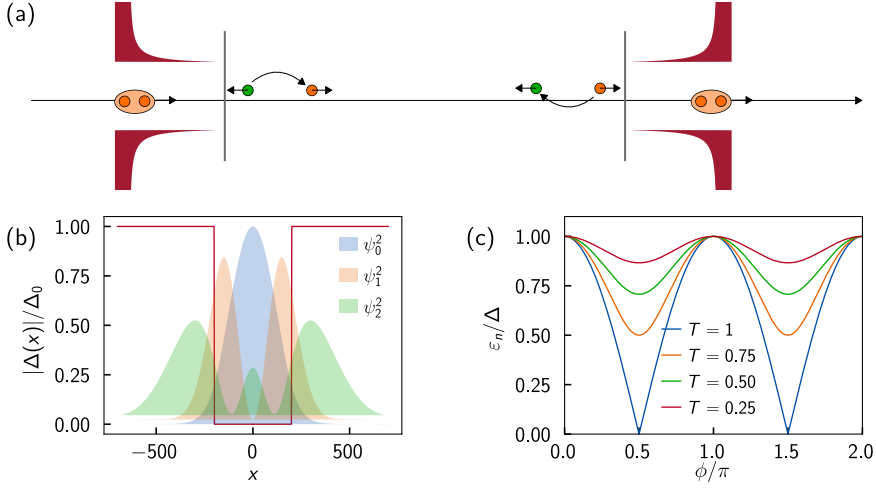
Fig. 1.7: **ABS and Josephson effect in superconductor-normal metal-superconductor junctions.** (a) Sketch of the formation of an ABS in a superconductor-normal metal-superconductor junction as an effect of consecutive Andreev reflections at two superconductor interfaces. (b) The three lowest ABSs in a simple superconductor-normal metal-superconductor junction with $t = 1$, $\Delta_0 = 2 \times 10^{-4}$, $\mu = 0$ at a phase difference equal to $\pi$. (c) ABS energy in Beenakker's model for various transparencies.

where $H_C$ is the Hamiltonian of the central region of a superconducting device, $H_{Sc}$ is the Hamiltonian of the superconducting terminals, and $H_T = \sum H_{T,i}$ is the tunneling Hamiltonian connecting the central region to the superconducting terminals labeled by $i$. This reads as

$$H_{T,i} = \sum_{n,p} \left( t_{i,np} d_n^\dagger \tau_z c_{p,i} + t_{i,np}^* c_{p,i}^\dagger \tau_z d_n \right), \tag{1.74}$$

where we use electron Nambu operator $d_n = (d_{n\uparrow}, d_{-n\downarrow}^\dagger)$ for the central region, and $c_{ip} = (c_{ip\uparrow}, d_{i-p\downarrow}^\dagger)$ for the all the leads. Here $-n$ means the time-reversed orbital of $n$, $\tau_j$ are the Pauli matrices in electron-hole space.

The tunneling matrix elements between the different regions are denoted by $t$. Note that we include the phase differences in the hopping amplitudes by a gauge transformation that moves the phase difference to the tunneling

$$c_{ip} \rightarrow c_{ip} e^{i\frac{\phi_i}{2}} , \, t_{ip} \rightarrow t_{ip} e^{i\frac{\phi_i}{2}} . \tag{1.75}$$

The charge operator reads $q = -e\tau_z$, therefore we can write the current through lead $i$ as

$$I_i = \dot{q}_i = ie \sum_{kn} \left( t_{i,np} c_{ip}^\dagger \tau_z d_{i,n} - t_{i,np}^* d_{i,n}^\dagger \tau_3 c_{ip} \right), \tag{1.76}$$

and we can rewrite the current in terms of the tunneling Hamiltonian as

$$I_i = 2e \frac{\partial H_T}{\partial \phi_i} . \tag{1.77}$$

The expected value is then

$$\langle I_i \rangle = 2e \left\langle \frac{\partial H_T}{\partial \phi_i} \right\rangle = 2e \frac{1}{Z} \operatorname{tr}\left[ e^{-\beta H} \frac{\partial H_T}{\partial \phi_i} \right] =$$
$$2e \frac{-1}{\beta Z} \operatorname{tr}\left[ \frac{\partial e^{-\beta H}}{\partial \phi_i} \right] = 2e \frac{-1}{\beta} \frac{\partial \ln Z}{\partial \phi_s} = 2e \frac{\partial F}{\partial \phi_i}, \tag{1.78}$$

where $F(\{\phi_i\})$ is the free energy of the system. The phase derivation can not simply be pulled out of the expectation value because the wave function depends on the phase difference. The function $F(\phi)$ is also called *Josephson potential* or *phase dispersion relation*, and it determines the currents and the energy of the system depending on the phases applied to the terminals.

Applying this formula to Beenakker's results gives the famous expression of the supercurrent

$$I(\phi) = \frac{e\Delta^2}{2\hbar} \sin(\phi) \sum_n \frac{T_n}{\epsilon_n} \tanh\left( \frac{\epsilon_n}{2k_B T} \right). \tag{1.79}$$

The function $I(\phi)$ is called *current-phase relation* (CPR) and is the characteristic used for the lumped-element description of Josephson junctions. The maximum current that can flow in a Josephson junction in the two directions is called critical current,

$$I_{c,+} = \max I(\phi), \quad I_{c,-} = \min I(\phi). \tag{1.80}$$

When a current bias is applied above the critical current, the junction turns to the normal, resistive state.

In real-world Josephson junctions, parasitic effects such as resistive and capacitive elements, as well as noise, can lead to hysteresis around the critical current ($I_c$). This can manifest as a superconducting-resistive transition at the switching current ($I_{sw}$), and a resistive-superconducting transition at the retrapping current ($I_{rt}$). It is worth noting that these currents may differ from the critical current ($I_c$).

## 1.6 Topological superconductivity in hybrid heterostructures

The proximity effect provides an alternative way to create synthetic topological superconductivity by combining proximity-induced conventional superconductivity, with a material that has lifted spin-degeneracy due to spin-orbit coupling and an additional mechanism that breaks Kramer degeneracy. One of the earliest works in this direction was by Gor'kov and Rashba, who demonstrated that a 2DEG with Rashba spin-orbit coupling could produce a mixture of singlet and triplet pairing [49]. This idea was further developed by Fu and Kane, who proposed using topological insulators to create synthetic topological superconductivity [50]. A major breakthrough was the realization that simpler semiconductors with a strong Rashba effect and a magnetic field could also be used to achieve 1D topological superconductivity [51, 52], 2D $p_x + i p_y$ superconductors [53] or MZM in artificial vortex cores [54].

To illustrate the idea, here we will focus on the BdG Hamiltonian

$$\mathcal{H} = \left[ \left( \frac{\hbar^2 (k_x^2 + k_y^2)}{2m^*} - \mu \right) \sigma_0 + \alpha_z (k_x \sigma_y - k_y \sigma_x) \right] \tau_z + \Delta \sigma_0 \tau_x + h \sigma_z, \tag{1.81}$$

usually referred to as the Lutchyn-Oreg model. This Hamiltonian describes a 2DEG with effective mass $m^*$, a Rashba spin-orbit coupling[1] $\alpha_z$, and a Zeeman splitting $h_z$. The semiconductor is proximitized by a s-wave superconductor with pairing potential $\Delta$, here described in the weak coupling limit.

We start by discussing the property of the normal state Hamiltonian obtained by setting $\Delta = 0$. The Hamiltonian is diagonalized by the unitary

$$U_{\text{hx}} = \exp\left(-\frac{i\theta}{2}\tau_z \mathbf{n} \cdot \boldsymbol{\sigma}\right) = \cos\left(\frac{\theta}{2}\right) - i\tau_z \sin\left(\frac{\theta}{2}\right)\mathbf{n} \cdot \boldsymbol{\sigma}, \qquad \mathbf{n} = \frac{\mathbf{e}_z \times \mathbf{k}}{k}, \qquad (1.82)$$

that can be seen as a rotation of the spin degree of freedom locally in momentum space. The rotation angle is defined by

$$\sin\theta = \frac{k\alpha}{\sqrt{\alpha^2 k^2 + h_z^2}}, \qquad \cos\theta = \frac{h}{\sqrt{\alpha^2 k^2 + h_z^2}} \qquad (1.83)$$

In this basis, the Hamiltonian is diagonal and reads as

$$U_{\text{hx}}\mathcal{H}U_{\text{hx}}^\dagger = U_{\text{hx}}\mathcal{H}_{\text{LO}}U_{\text{hx}}^\dagger = \left(\frac{\hbar^2 k^2}{2m^*} - \mu\right)\sigma_0 \tau_z - \sqrt{\alpha^2 k^2 + h_z^2}\tau_0 \sigma_z, \qquad (1.84)$$

and the eigenvectors form the so-called helical basis

$$\begin{pmatrix} |e_{+,\mathbf{k}}\rangle \\ |e_{-,\mathbf{k}}\rangle \\ |h_{-,-\mathbf{k}}\rangle \\ |h_{+,-\mathbf{k}}\rangle \end{pmatrix} = U_{\text{hx}}(\mathbf{k}) \begin{pmatrix} +\left|e_{\uparrow,\mathbf{k}}\right\rangle \\ +\left|e_{\downarrow,\mathbf{k}}\right\rangle \\ -\left|h_{\downarrow,-\mathbf{k}}\right\rangle \\ +\left|h_{\uparrow,-\mathbf{k}}\right\rangle \end{pmatrix}. \qquad (1.85)$$

We first focus on the $\Delta = 0$ case and select the electron sector, $\tau = +1$. The dispersion relation is shown in Fig. 1.8 for various cases. Fig. 1.8(a) shows a 2DEG with strong Rashba spin-orbit coupling. The system features two bands with spin-momentum locking. Meaning that for each point in the Brillouin zone, there is a preferred spin direction that commutes with the Hamiltonian. Time-reversal symmetry is preserved, and therefore, Kramers's degeneracy holds. The introduction of a magnetic field in an in-plane direction opens the gap at $\mathbf{k} = 0$. However, the two bands still intersect as there exists a direction for which the Zeeman term commutes with Rashba one, as shown in Fig. 1.8(b). Finally, in case the magnetic field is oriented out-of-plane, a gap opens between the two bands for any point in the Brillouin zone. Notably, for $h > \mu$ the upper band is gapped out, and the low-energy physics is dictated entirely by the low-energy band. This phase is called *helical liquid*.

We now introduce the superconducting pairing in the picture by setting $\Delta \neq 0$. In the helical basis defined above, the Hamiltonian reads as

$$U_{\text{hx}}\mathcal{H}_{\text{LO}}U_{\text{hx}}^\dagger = \left(\frac{\hbar^2 k^2}{2m^*} - \mu\right)\sigma_0 \tau_z - \sqrt{\alpha^2 k^2 + h_z^2}\tau_0 \sigma_z +$$
$$\frac{k_x \alpha_z \Delta}{\sqrt{h_z^2 + k_x^2 \alpha_z^2}}\tau_y \sigma_y + \frac{h_z \Delta}{\sqrt{h_z^2 + k_x^2 \alpha_z^2}}\tau_x \sigma_0. \qquad (1.86)$$

---

[1]We use a Rashba-type spin-orbit coupling because it is the most common type of spin-orbit coupling in these devices, and has some nice properties we will discuss later. Note, however, how any type of linear spin-orbit coupling would work as well.
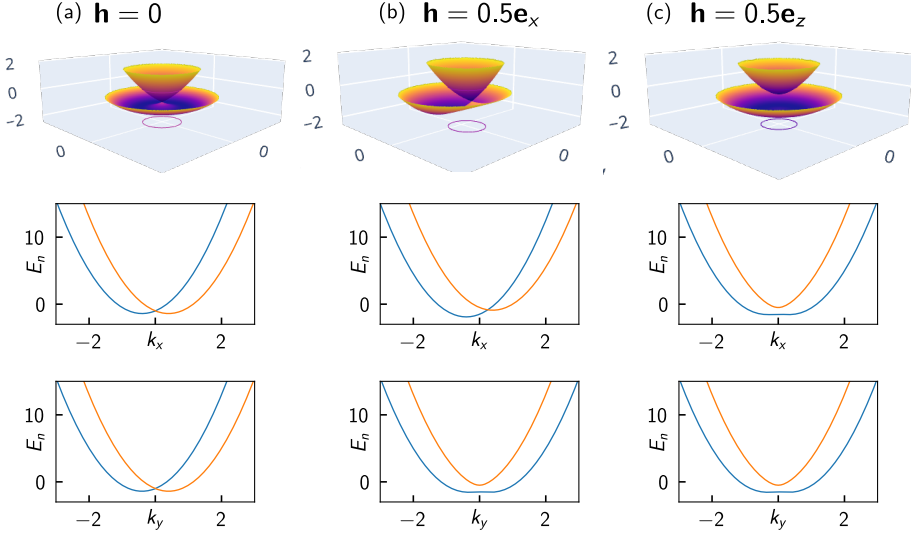
**Fig. 1.8: Dispersion relation of a Rashba semiconductor in presence of a spin-splitting field.**
(a) Dispersion relation for $\mathbf{h} = 0$. The action of the Rashba field is lifting the spin degeneracy displacing the two parabolic bands, and introducing spin-momentum locking. The two bands have opposite helicity. (b) Dispersion relation for $\mathbf{h} \neq 0$ oriented in plane. If the magnetic field lies in-plane, there is a direction in momentum space for which the spin-orbit coupling term commutes with the magnetic field. (c) Dispersion relation for $\mathbf{h} \neq 0$ oriented out-of-plane. In this case, the two bands split for all points in momentum space. And for $h > \mu$ the system can be tuned to the helical phase.

Notably, the singlet pairing in the spin basis has now split into two terms. The first term in the second line of Eq. (1.86) represents a triplet component, while the second term in the same line is the remaining singlet pairing.

For a high enough $h$, the $+$ band is gapped out, and we can project on the reduced basis $\{|e_{-\mathbf{k}}\rangle, |h_{-\mathbf{k}}\rangle\}$ to obtain

$$\tilde{\mathcal{H}} = \left(\frac{\hbar^2 k^2}{2m^*} - \mu + \sqrt{\alpha^2 k^2 + h_z^2}\right)\tau_z + \frac{k_x \alpha_z \Delta}{\sqrt{h_z^2 + k_x^2 \alpha_z^2}}\tau_y. \tag{1.87}$$

This Hamiltonian looks very similar to what we desire. Indeed, it represents a single spin with a triplet pairing, that, for low enough momenta, is of $p$-wave type. With the knowledge about the presence of a $p$-wave type pairing, we now consider the full Hamiltonian, which has a spectrum given by

$$E^2 = \xi_k^2 + h^2 + \Delta^2 + (\alpha_z k_x)^2 \pm 2\sqrt{\Delta^2 h^2 + h^2 \xi_k^2 + \xi_k^2 (\alpha_z k_x)^2} \tag{1.88}$$

with $\xi_k = \frac{\hbar^2 k_x^2}{2m^*} - \mu$. The system is always gapped at finite momentum as long as $\alpha_z \neq 0$. The special point $\mathbf{k} = 0$ instead, undergoes a gap closing and reopening for $h^2 = \Delta^2 + \mu^2$, as shown in Fig. 1.9 where $h^2$ is varied from 0 to values bigger than $\Delta^2 + \mu^2$.
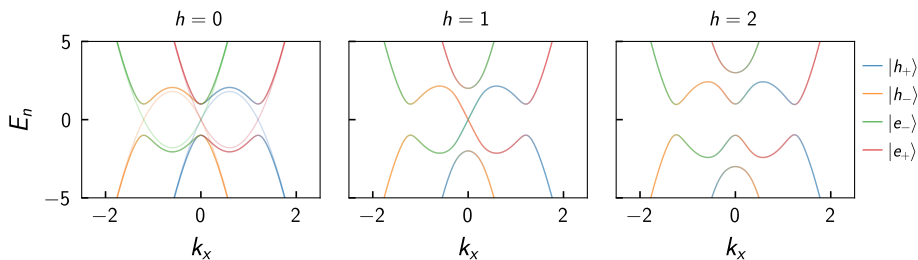
Fig. 1.9: **Dispersion relation of the Lutchyn-Oreg model.** The plot shows the dispersion relation for the Lutchyn-Oreg model for $\mu = 0$ and $\Delta = 1$. The Zeeman term $h$ is varied from 0 to values bigger than $\Delta$. In the second plot, the splitting of the bands can be observed, together with the gap closing at $\mathbf{k} = 0$. At higher $h$, the gap reopens in the topological phase.

We finally need to prove that this point is a topological quantum phase transition separating a trivial and a topological state. To do so, we will resort to a topological invariant, and we will consider a 1D or quasi-1D wire. Because of the presence of the particle-hole symmetry $\mathcal{P}$, we can define a transformation $U_M$ to the Majorana basis. This is defined as the basis where the particle-hole symmetry is just the complex conjugation operator

$$U_M \mathcal{P} U_M^\dagger = \mathcal{K}. \tag{1.89}$$

For the basis of time-reversed holes, the transformation read as

$$U_M = \begin{pmatrix} 1 & 0 & 0 & -1 \\ i & 0 & 0 & i \\ 0 & 1 & 1 & 0 \\ 0 & i & -i & 0 \end{pmatrix}. \tag{1.90}$$

In this basis, the Hamiltonian can be written as follow

$$\mathcal{H} = \frac{i}{2} M, \tag{1.91}$$

where $M$ is real and skew-symmetric. This allows for calculating the Pfaffian invariant defined as

$$\mathcal{Q} = \text{sgn}\left[ \frac{\text{Pf}M(k_z = 0)}{\text{Pf}M(k_z \to +\infty)} \right], \tag{1.92}$$

The sign of this Pfaffian divides the set of all gapped quadratic forms of Majorana fermions into two inequivalent classes [34].

An ideal 1D wire belongs to the BDI class because other than the particle-hole symmetry, it features an additional time reversal symmetry $\mathcal{A} = \sigma_0 \tau_0 \mathcal{K}$, that is involutory $\mathcal{A}^2 = +1$, and also a chiral symmetry $\mathcal{S} = \mathcal{P}\mathcal{A} = \sigma_2 \tau_2$. One-dimensional BDI systems are characterized by a topological invariant $W_\mathbb{Z}$ that counts the number of MZM.

Since all BDI systems also belong also to the D class, we can use the topological invariant for the D class that, for dimension $d = 1$, is the $W_{\mathbb{Z}_2}$ [55]. The two invariants are related by

$$W_{\mathbb{Z}_2} = (-1)^{W_\mathbb{Z}} \tag{1.93}$$

Luckily, $W_{\mathbb{Z}_2} = \mathcal{Q}$ defined above [34].

Applying the topological invariant just defined to the Hamiltonian in Eq. (1.81), considering that the kinetic energy dominates for large $k_z$, the Hamiltonian approaches the one for quasi-free electrons, which have Pfaffian $\mathrm{Pf} M(k_z \to \infty) = 1$, i.e., is in the trivial state. We finally proved that the topological phase is defined by the paraboloid

$$h^2 > \Delta^2 + \mu^2 . \tag{1.94}$$

A quasi-1D system still belongs to the BDI class as long as the transversal spin-orbit coupling is absent. In case of transversal spin-orbit coupling, both the time-reversal symmetry $\mathcal{A}$ and the chiral symmetry $\mathcal{S}$ are broken, and the system is brought in the D class. Physically means that transversal spin-orbit coupling couples the MZMs at the end of the wires, which becomes gapped, leaving at maximum one zero energy state [55].

As an external magnetic field increases, the system undergoes a topological quantum phase transition characterized by the closing and reopening of the superconducting gap. In the topological regime, sufficiently long wires feature zero-energy Majorana bound states at the ends.

## Experimental realizations

We have shown how a low-density superconductor with strong spin-orbit coupling and an exchange field can have topologically distinct phases. However, a material with such characteristics has not yet been found in nature. A different approach is leveraging proximity effects to combine together the different elements and generate synthetic topological superconductivity. Hybrid superconductor-semiconductor heterostructures have emerged as a potential platform for this purpose [56, 57].

The semiconductor act as a host material with a controllable, low-density of electrons and a potentially high $g$ factor. A superconducting pairing potential can be introduced in the structure by coupling it with a conventional superconductor. Following this idea, different hybrid semiconductor-superconductor platforms have been proposed to exhibit topological superconductivity. The first experiments concerned nanowire structures with evaporated superconductors [58–62].

The positive results of the first generation of these experiments triggered a considerable effort to improve the fabrication technology, which resulted in the development of epitaxial, highly transparent interfaces for compatible materials. Moreover, improvement in the fabrication of semiconductor structures has consistently reduced the disorder in the devices, which can now reach high mobility. In the second generation of experiments, several variations of nanowire structure have been tested, starting from vapor–liquid–solid (VLS) [63–65], to selective-area-grown (SAG) wires [66], and two-dimensional electron gas (2DEG) systems [67–72]. A variation of this idea that involves using a ferromagnetic insulator as the source of spin-splitting has emerged in recent years [73]. These systems will be the subject of Ch. 4.

# 2

## Electrostatic landscape and spin-orbit coupling

The reason for the advent of hybrid superconductor-semiconductor devices lies in two fundamental properties of semiconductors: the low charge carrier density and the strong spin-orbit coupling present in many compounds. Both the density and the spin-orbit coupling strength are tunable through electrostatic control, which is, therefore, a fundamental aspect in the design of hybrid devices. This chapter delves into these two properties of hybrid superconductor-semiconductor devices. In Sec. 2.1, we will introduce the most common methods of electrostatic modeling in hybrid devices: the Schrödinger-Poisson (SP) and the Thomas-Fermi (TF) approach to the problem. The TF approach will be presented as an example of an orbital-free theory of the electron gas, allowing for the introduction of more precise extensions that are the focus of paper [P3]. While in Sec. 2.2, we will introduce spin-orbit coupling in semiconductor heterostructures and explore how it can be manipulated through geometry and electric fields in nanostructures.

## 2.1 Simulation of the electrostatic landscape

The possibility of using electric fields to manipulate the properties of hybrid devices is a key feature of these systems. The low-density regime of semiconductor regions makes the electron gas highly responsive to changes in the electrostatic landscape, allowing for easy and reliable control through capacitively coupled gates. However, understanding the precise relationship between the potential applied to the metallic gates and the electrochemical potential is a complex task, with several factors contributing to the challenge. Some of the major complications in modeling the electrostatic behavior are the following:

1. **Band alignment.** A fundamental parameter of electrostatic simulations of heterostructures is the energy offset of the band structures of each material in the structure. These parameters are difficult to evaluate from experiments and even to define theoretically, yet, the results of the simulations depend heavily on them.

2. **Interface physics.** The interface between two different materials can host dangling bonds, dislocations, midgap states, and other defects that can significantly impact surface physics. These properties depend not only on the materials at the two sides of the interface, but also on the fabrication details of the structure.

3. **Fixed charge.** Precise simulations require modeling fixed charges that may be present in the structure, such as doping or fixed surface charge. This charge can depend on the fabrication process and can also cause hysteretic behavior if it escapes traps in rare events.

Even without considering the model-level complications, electrostatic simulations are complex and potentially nonlinear problems that involve simulating an interacting electron liquid in complicated geometries and boundary conditions. The electrostatic problem can be expressed in two ways. The first method starts with the non-interacting electrons problem and introduces the calculation of the electrostatic field, resulting in a Shrödinger-Poisson (SP) formulation. The second method begins from a perspective similar to density-functional theories, where an energy functional for the interacting electron fluid is sought. This section introduces both methods by considering the simplest case of direct bandgap semiconductors

with electron accumulation. For low densities, we can assume that the electrons in the semi-conductor are close to the $\Gamma$ point and can be reliably described by a parabolic band. We only model the electron fluid and neglect the hole accumulation process. However, extending the method by including a hole fluid is straightforward.

Before proceeding, it is essential to define what is the objective of solving the electrostatic problem for a nanostructure. We are mainly interested in the electrostatic potential $\varphi$. This enters the low-energy continuum model both as a component of the electrochemical landscape and as a tuning parameter of the spin-orbit coupling. A secondary result is the local one-particle density $n(\mathbf{r})$. This can be used for other purposes, for example, as a parameter to generate a low-dimensional effective Hamiltonian. For example, one can be interested in projecting a 3D Hamiltonian on a 2D subspace to model a 2DEG device. This could be done by taking the weighted average of the parameters that enter the Hamiltonian. In any case, it is important to note that the precise calculation of the excitations spectrum or transport properties is not typically part of the electrostatic problem itself but is commonly resolved in later stages of the simulation pipeline [74].

**Schrödinger-Poisson formulation**

In the SP formulation, the electron fluid in the heterostructure can be described by an electron field $\psi(\mathbf{r})$ that is the ground state of the Hamiltonian

$$H = \int d\mathbf{r} \, \psi^{\dagger}(\mathbf{r}) \mathcal{H} \psi(\mathbf{r}) \tag{2.1}$$

where the quadratic Hamiltonian for a semiconductor with a simple band structure reads as

$$\mathcal{H} = \left[ \frac{\hbar^2}{2} \boldsymbol{\nabla} \cdot m^{-1} \boldsymbol{\nabla} + E_{\text{CBM}} - e\varphi \right] \tag{2.2}$$

where $m(\mathbf{r})$ is the effective mass, $E_{\text{CBM}}(\mathbf{r})$ is the conduction band minimum of the material, $e$ is electron charge, and $\varphi$ is the electrostatic potential. Here we have omitted spin-orbit fields for simplicity, as they are expected to play a minor role, but they can be straightforwardly included.

The electrostatic field that enters the single-particle Hamiltonian is a solution of the Poisson equation

$$\begin{cases} -\boldsymbol{\nabla} \cdot \varepsilon \boldsymbol{\nabla} \varphi = \rho_{\text{fx}} + \rho_{\text{m}} \\ \varphi(\partial \Omega_i) = V_i \qquad i \in G \end{cases} \tag{2.3}$$

where $\varepsilon(\mathbf{r})$ is the materials permittivity, $\rho_{\text{fx}}(\mathbf{r})$ is the fixed charge, and $\rho_{\text{m}}(\mathbf{r})$ is the mobile charge. Finally, the mobile charge is given by

$$\rho_{\text{m}}(\mathbf{r}) = -e\langle \psi^{\dagger}(\mathbf{r}) \psi(\mathbf{r}) \rangle = \sum_n |\psi_n(\mathbf{r})|^2 f(\omega_n / k_B T) \tag{2.4}$$

where $f$ is the Fermi-Dirac distribution, $k_B$ the Boltzmann constant, $T$ is the temperature, and $(\psi_n, \omega_n)$ are the single-particle eigenstates and eigenvalues of the quadratic Hamiltonian:

$$\mathcal{H} \psi_n = \omega_n \psi_n. \tag{2.5}$$

In this way, the Schrödinger problem in Eq. (2.5) and the Poisson problem in Eq. (2.3) are coupled together and must be solved self-consistently. Note that, in this case, the gauge

invariance of the Schrödinger equation plays a complicated role as $E_{\mathrm{CBM}}$ has an arbitrary offset that has to be chosen consistently with the applied voltage to the gates, $\{V_i\}$.

The choice of boundary conditions is peculiar for metallic parts in contact with semiconductors. These regions are part of the Schrödinger problem, the hybrid wavefunctions have finite support in both the semiconductors and the metallic domains, but they are excluded from the electrostatic problem as a Dirichlet boundary condition fixes the surface potential [74–76].

For what concerns Poisson's equation, we assume all metallic regions are described by ideal metals, and therefore the potential is constant in these domains. When a voltage bias $V_i$ is applied to region $\Omega_{\mathrm{M}_i}$, a Dirichlet boundary condition can be used that takes the form $\varphi(\partial\Omega_{\mathrm{M}_i}) = \delta\mu_i + V_i$ where $\delta\mu_i$ is a material-specific constant that models the Fermi energy difference between the metal in the region $\Omega_{\mathrm{M}_i}$ and the reference one. When $\Omega_{\mathrm{M}_i}$ is a floating island, the Neumann condition $\nabla_\perp\varphi(\partial\Omega_{\mathrm{M}_i}) = 0$ fixes the electric field to be normal to the surface. Precise calibration of the band-offsets $\delta_i$ requires a careful comparison of numerical simulations and experimental results [77].

The SP approach can be a computationally demanding task due to several numerical challenges. One of the main challenges is the diagonalization of a large matrix, which is required for the Schrödinger part of the problem when the system is discretized using many degrees of freedom. To address this, sparse methods, such as Arnoldi iteration, can be employed. These methods have a time complexity of $O(kN^2)$ for $k$ eigenvalues of an $N \times N$ matrix, compared to $O(N^3)$ for dense diagonalization. However, it is not always possible to accurately estimate the number of eigenvectors required in the first iterations, and even with this optimization, diagonalization remains a bottleneck for convergence. The second issue is in the nature of the segregated approach used in SP problems.

A self-consistent problem in which two different fields, described by distinct partial differential equations, are interconnected can be solved using a *monolithic* approach, also known as a *fully-coupled* method. This approach involves solving the partial differential equations as a single system of equations rather than breaking them into separate subproblems. In contrast, *segregated* (or *partitioned*) methods involve breaking the partial differential equations into separate subproblems that are solved independently, with the solutions of one equation being used as input for the other equation. The solution is found by iteratively solving one problem while keeping the other field frozen until a convergence criterion is met. In general, segregated/partitioned methods are simpler to implement but can be less accurate and may experience severe convergence issues. On the other hand, fully-coupled methods can be more accurate but also more computationally intensive.

Because of the nature of the Schrodinger problem, a straightforward monolithic approach is not easily implementable. Instead, the solution can typically be found only through iterative partitioned methods. The systems often operate in a low-density regime, making the electron gas highly sensitive to changes in the electrostatic landscape. This results in a strongly nonlinear problem that can cause severe convergence issues [78]. Additionally, the treatment of metallic regions in contact with semiconductors can also present a challenge, as hybrid wavefunctions have finite support in both regions but are excluded from the electrostatic problem, potentially leading to inconsistencies in the solution. Despite these challenges, the SP approach is a powerful method, but it requires significant computational resources and careful implementation to achieve accurate and reliable results.

**Orbital-free methods**

An alternative approach is one that follows more closely density functional theory. The key result of density functional theory is the Hohenberg-Kohn theorem states that the energy, and all other possible observable of a many-electron system, can be expressed as a functional of the density alone [79]. This means that the ground-state density itself can be found as the minimizer of the energy functional. In our case, we extend the energy functional to depend explicitly also on the electrostatic potential $\varphi$. This is due to the fact that the electric field in a device is not a solution of the free-space Poisson equation but is, instead, the solution of a complicated problem defined in a composite domain with non-trivial boundary conditions. It is worth noting that a functional theory that takes this form is not, strictly speaking, a density functional theory, as the electric potential is explicitly included and cannot be easily transformed into a functional of the electron density only. This is caused by metallic parts like gates or floating metallic islands. These modify the boundary condition of the electric potential equation such that the Poisson equation Green's function becomes a complicated object generally not expressible in an analytic form. Including explicitly the electric potential circumvents this problem.

When treating a closed system like an atom or a molecule, the minimization problem is characterized by the constraint on the number of electrons in the system. We do not have such a constraint in our case. The total number of electrons is not fixed, but actually one of the results we want to determine. Moreover, it can also take fractional values without causing particular concern in most cases.

The energy functional we consider looks as follows

$$E[n, \varphi] = K[n] + V[n] + U[\varphi] + \int_{\Omega} \mathrm{d}\mathbf{r}\, \rho \varphi, \tag{2.6}$$

where $K[n]$ is the kinetic energy functional of the electrons, $V[n]$ is the potential energy of the electron liquid, $U[\varphi]$ is the electrostatic field energy, and the last term is the coupling between the electrostatic field and the charge $\rho = \rho_{\mathrm{fx}} + \rho_{\mathrm{m}}$, which comprises the free electrons charge $\rho_{\mathrm{m}} = -en$ and the fixed charge of the system $\rho_{\mathrm{fx}}$. The computational domain $\Omega$ can be split into three different types of regions: metals, insulators, and semiconductors such that $\Omega = \Omega_{\mathrm{M}} \cup \Omega_{\mathrm{Sm}} \cup \Omega_{\mathrm{I}}$.

The electrostatic field energy takes the standard form

$$U[\varphi] = \int_{\Omega} \mathrm{d}\mathbf{r}\, \varepsilon \frac{\left\| \boldsymbol{\nabla} \varphi \right\|^2}{2}, \tag{2.7}$$

where $\varepsilon(\mathbf{r})$ is the permittivity, while the potential is

$$V[n] = \int_{\Omega_{\mathrm{Sm}}} \mathrm{d}\mathbf{r}\, [E_{\mathrm{CBM}} n + V_{\mathrm{ex}}(n)], \tag{2.8}$$

where $E_{\mathrm{CBM}}(\mathbf{r})$ is the conduction band minimum of the semiconductor that acts as local chemical potential. The exchange energy can be included within the local density approximation through the $V_{\mathrm{ex}}[n(\mathbf{r})]$ term, which we neglect as it gives minor contributions.

Finding precise kinetic energy functionals is the focus of much modern research [80–84]. There are two main approaches: the Köhn-Sham and the orbital-free methods.

In the Köhn-Sham approach, a fictitious system of non-interacting particles is introduced to evaluate the kinetic energy on the states of an auxiliary quadratic Hamiltonian [85]. This method is similar to the SP approach described before and thus requires the diagonalization of the Hamiltonian.

An alternative approach is represented by orbital-free methods that try to attack the problem by considering analytic expressions for the kinetic-energy functional that do not require the diagonalization of a Hamiltonian. These methods can be substantially less computationally demanding due to the fact that the solution algorithm is a simpler optimization problem.

**Thomas-Fermi method**

The simplest orbital-free method is the TF approximation. In this approximation, we assume the system has a high density of states such that the local density is well approximated by the expression for a free electron gas. The kinetic energy functional read as

$$K[n] = \int_{\Omega_{Sm}} d\mathbf{r}\, C_{TF}(\mathbf{r}) n^{5/3}(\mathbf{r}) \,, \tag{2.9}$$

where we defined the TF constant $C_{TF}(\mathbf{r}) = (3\pi^2)^{\frac{2}{3}} \frac{\hbar^2}{2m(\mathbf{r})} \frac{3}{5}$.

In this case, solving the electrostatic problem is equivalent to solving a nonlinear Poisson equation

$$-\nabla \cdot \varepsilon \nabla \varphi = \rho_{fx} - \frac{e}{3\pi^2} \left[ \frac{2m(E_{CBM} - e\varphi)}{\hbar^2} \right]^{\frac{2}{3}} \,,. \tag{2.10}$$

This functional is completely local, is exact for uniform systems, and holds as an approximation as long as the electron density is slowly varying in space. The validity of this assumption for a specific system can be checked through the *TF error*:

$$R_{TF} \equiv \frac{\|\nabla n(\mathbf{r})\|}{n(\mathbf{r}) k_F(\mathbf{r})} \,, \tag{2.11}$$

where $k_F(\mathbf{r}) = [3\pi^2 n(\mathbf{r})]^{1/3}$ is the Fermi wavelength. The TF approximation is valid in the limit $R_{TF} \ll 1$ [79]. This condition is never satisfied at interfaces with vacuum or insulators where the density goes abruptly to zero. Moreover, it has been demonstrated how the electron density near the interface with a metallic gate is also poorly estimated [75]. Nevertheless, the TF method is widely used in the community as the derived electrostatic potential is considered precise enough for the modeling needs, with a computational cost that is a fraction of the SP ones.

To understand the limitation of this method, we consider two simple but relevant geometries for 2DEG devices: a nanowire and a circular dot. For the 2DEG, we choose a semiconductor stack similar to the ones used in many modern experiments, for instance, Refs. [86, 87]. Fig. 2.1(a) display the schematic of a cross-section of a 2DEG nanowire. Two Au gates serve the purpose of depleting the areas next to the Al wire. The two Au gates and the Al wire are separated by HfO$_2$ dielectric. Fig. 2.1(b) shows the electron density in the system, simulated using a top gate voltage of $-3$ V with respect to the grounded Al wire while in Fig. 2.1(c) we plot the TF error as defined in Eq. (2.11). From this simulation, it is clear that the TF error does not satisfy $R_{TF} \ll 1$, and thus the electron density is varying too quickly in space to justify the use

of the TF approximation. This behavior is consistent when trying different top gate voltages. In Figs. 2.1(d)-(f), we simulate a quantum dot on the same semiconductor stack. We apply a voltage of $-0.25$ V to the outer gate and $0$ V to the inner gate. In Fig. 2.1(e) and (f), we show, respectively, the electron density in a plane located in the middle of the InAs layer and the TF error that approaches 1 at the boundary to the depleted region.
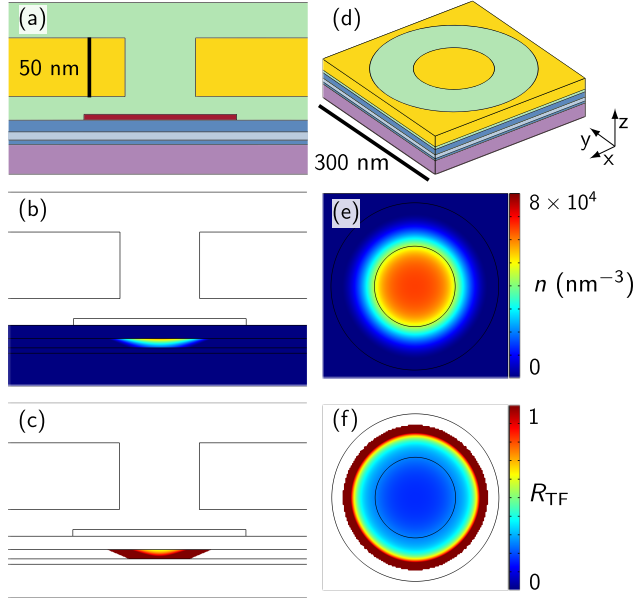


Fig. 2.1: **Electrostatic simulations of two example devices with the TF method.** The first row shows the sketches of a cross-section of a common 2DEG device (a) and a simple circular quantum dot (d). In both cases, the devices are built on top of a semiconductor stack (schematic given in Fig. 2.2) that provides the vertical confinement of electrons. The lateral confinement is controlled by Au gates (yellow), $HfO_2$ oxide (gray), and an Al wire (dark gray). (b) and (e) show the electron density from a TF simulation. (e) is plotted in the middle of the InAs well. (c) and (f) show $R_{TF}$.

**Extended TF method**

A step beyond the TF approximation is represented by gradient expansions of the kinetic energy functional in what is called *extended Thomas-Fermi* (ETF) method. By introducing gradient terms in the kinetic energy functional, the ETF method incorporates corrections to the electronic density due to quantum confinement while it preserves the scalability of a theory that can be expressed as a functional minimization problem. A systematic way to obtain such gradient expansion is through a semiclassical expansion of the free energy [88].

For testing purposes, we opted for the simplest model that goes beyond the homogeneous electron gas case of the TF method by incorporating the so-called von Weizsäcker (vW) correction [84, 88–90]. This term captures the energy cost of rapid variation of the density in space.

The kinetic energy functional reads as

$$K[n] = \int_{\Omega_{Sm}} d\mathbf{r}\, C_{TF}(\mathbf{r})\, n^{5/3}(\mathbf{r}) + \lambda_{vW} \frac{\hbar^2}{8m} \frac{\|\nabla n(\mathbf{r})\|^2}{n(\mathbf{r})}\,, \tag{2.12}$$

where $\lambda_{vW}$ is called vW parameter and $m$ is the effective mass.

To move from an optimization problem to a boundary value problem, we will use functional minimization. It is convenient to define the matter field $\psi = \sqrt{n}$ before proceeding. Note that $\psi$ is a real field defined as the square root of the density. It cannot be interpreted as a wavefunction as it does not carry information about the phases of the electrons. Therefore this theory cannot describe long-range interference effects, but it just includes a local correction to the electronic density due to quantum confinement effects. The functional derivative $\frac{\delta E}{\delta \varphi} = 0$ returns the Poisson equation while $\frac{\delta E}{\delta \psi} = 0$ returns a partial differential equation that has the form of a nonlinear Schrödinger equation. The system of coupled partial differential equations is then

$$\begin{cases} -\nabla \cdot \varepsilon \nabla \varphi = \rho_{fx} - e\psi^2\,, \\ -\frac{\hbar^2}{2} \nabla \cdot \left( \frac{\lambda_{vW}}{m^*} \nabla \psi \right) + \frac{5}{3} C_{TF} \psi^{7/3} + \left[ -e\varphi + E_{CBM} \right] \psi = 0\,. \end{cases} \tag{2.13}$$

In the literature, there has been much discussion on the value of the vW coefficient, $\lambda_{vW}$, which works as a weight of the gradient-dependent vW term. In the limit $\lambda_{vW} \to 0$, the TF method is recovered. In Ref. [91], the response function of a uniform system of independent fermions is investigated, and it is shown that $\lambda_{vW} = 1$ is valid in the limit of short-wavelength perturbations, whereas $\lambda_{vW} = 1/9$ is valid in the limit of long-wavelength perturbations. Other analysis pointed to the value of $\lambda_{vW} = 1/5$ as the most adequate [92]. In the following, we will treat $\lambda_{vW}$ as a parameter of the model and empirically select a value in the $[0, 1]$ interval that agrees with SP simulations in simple geometries.

We start with the problem of determining the optimal value of $\lambda_{vW}$ for the use case of nanoelectronic devices. We considered a 2D translational invariant metal-oxide-semiconductor device composed of a semiconductor heterostructure quantum well, an insulator layer, and a metallic top-gate as shown in Fig. 2.2(a). We study the electrostatic problem with the TF and ETF method with various $\lambda_{vW}$ and compare the results with a simulation done with the self-consistent SP method. The density per unit area is shown in Fig. 2.2(b).

To assess quantitatively the optimal value for the vW parameter, we introduce two metrics: the absolute difference of the density per unit area

$$\delta N \equiv \frac{|N_{vW} - N_{SP}|}{N_{SP}}\,, \tag{2.14}$$

where $N = \int n\, dx$ is the total number of electrons per unit area, and the quantity

$$(\delta n)^2 \equiv \int (n_{SP} - n_{vW})^2\, dx\,, \tag{2.15}$$

that takes into account the difference in the shape of the density profile. The results are shown in Fig. 2.2 (c). In general, we find that low values of $\lambda_{vW}$ in the interval $[0.05, 0.2]$ provide the best agreement with SP results. We then decided to elect $\lambda_{vW} = 1/9$ as the standard parameter because of the theoretical works also backing this choice [91].

(a)

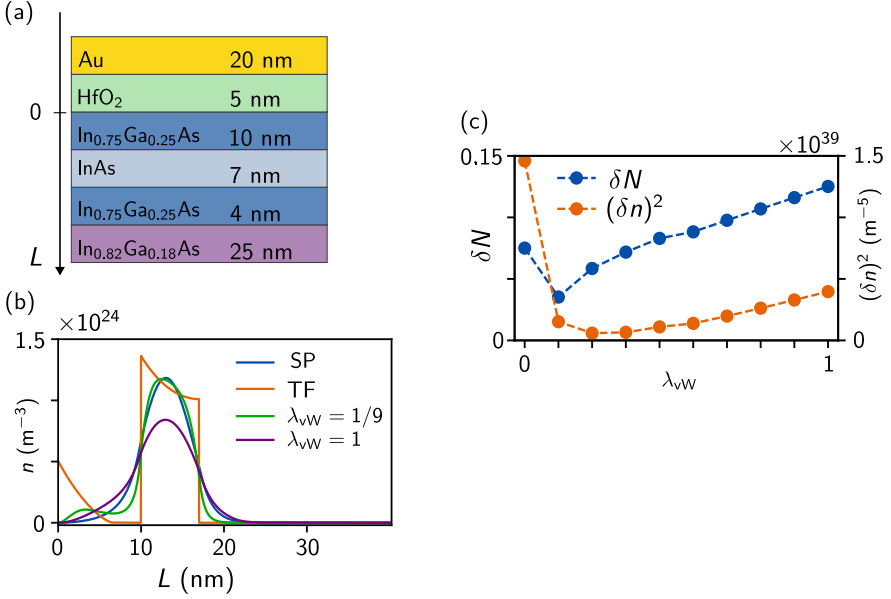| Au | 20 nm |
| HfO$_2$ | 5 nm |
| In$_{0.75}$Ga$_{0.25}$As | 10 nm |
| InAs | 7 nm |
| In$_{0.75}$Ga$_{0.25}$As | 4 nm |
| In$_{0.82}$Ga$_{0.18}$As | 25 nm |

(b)

(c)

Fig. 2.2: **Calibration of the $\lambda_{vW}$ parameter.** (a) shows a schematic of the simulated semiconductor stack inspired by the one used in [93] (not to scale). An Au gate (yellow) is separated from the four semiconducting layers by a layer of oxide (gray). (b) shows the results of TF, ETF (with various $\lambda_{vW}$), and SP simulations. (c) shows a comparison of different values of $\lambda_{vW}$, using the two metrics defined in Eqs. (2.14) and (2.15). For all simulations the built-in bias at the interface is 0.1 V.

Next, we simulated a quantum dot shown in Fig. 2.3 to test the ETF method for a complicated realistic 3D device. As a benchmark, we use the TF and the Schrödinger-Thomas-Fermi (STF) methods. By STF, we indicate the method for which the electrostatic field is calculated with the TF method, but then it is used as an input for a single Schrödinger step to calculate the single-particle state. STF is the most common approach in the field of hybrid devices. Here we fix the outer gate to $-0.35$ V and consider the number of electrons in the dot as a function of the inner gate voltage. The results can be seen in Fig. 2.3(c). Note that the device under consideration does not show a dot-like behavior as the charge increases almost linearly with the gate voltage, as expected for a 2D system. This suggests that the lateral confinement induced by the gate system is not able to strongly confine the electrons in this case.

We see that all the methods predict depletion in the semiconducting stack at $\sim -0.35$ V (the STF method predicts depletion until $\sim -0.2$ V), and as the inner gate voltage is increased, electrons start to accumulate in the stack. Of the three methods, the TF method generally predicts the largest number of electrons, while the STF method predicts the lowest. The ETF results are intermediate between the two. Even though the ETF and STF methods do not overlap for all voltages, the two methods seem to have great compliance in the moderate filling regime.

One important difference between the TF and ETF methods is that the TF method predicts

a steep jump in the differential capacitance $C(V) = \partial Q/\partial V$ as the voltage increases. This happens as electrons at particular voltages, corresponding to the conduction band minimum of the layers, start accumulating in a previously classically forbidden region. The ETF method, by allowing exponentially suppressed tails in the classically forbidden layers, prevents this from happening and is thus less prone than the TF method to show unphysical behavior. In the setup considered here, we can thus conclude that the ETF method is superior to the TF method for simulating the number of electrons and calculating elements of the capacitance matrix.
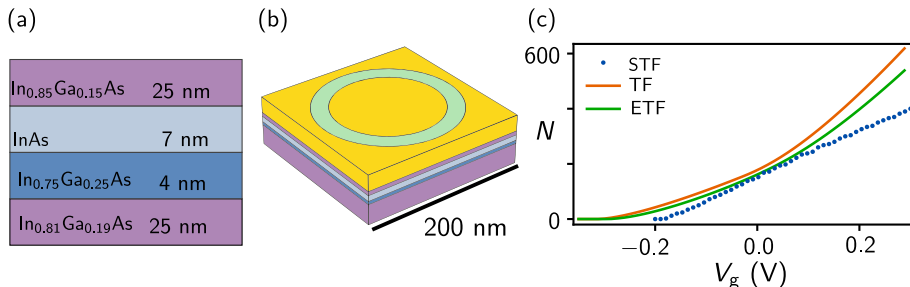


Fig. 2.3: **Electrostatic simulation of a quantum dot.** (a) shows the semiconducting stack (not to scale), (b) shows the simulated geometry, and (c) shows how electrons accumulate in the semiconducting stack as the inner gate voltage is increased.

The material properties used in this research work, including the band offset between semiconductors used to evaluate the conduction band minimum $E_{\text{CBM}}$, are shown in Tab. 2.1. In the results presented in this section, we have not considered the case of metal-semiconductor interfaces. The treatment of these interfaces in the context of the ETF method is not easy because of the huge difference in the density of electrons in the two classes of materials. An attempt to analyze the issue of such boundary conditions can be found in Appendix B.

| | $\varepsilon/\varepsilon_0$ | $m_{\text{eff}}/m_{\text{e}}$ | $E_{\text{CBM}}$ [eV] |
|---|---|---|---|
| $In_{0.75}Ga_{0.25}As$ | 14.76 | 0.035 | 0.00 (ref) |
| InAs | 15.15 | 0.026 | -0.205 |
| $In_{0.85}Al_{0.15}As$ | 14.39 | 0.038 | 0.079 |
| $In_{0.82}Al_{0.18}As$ | 14.23 | 0.041 | 0.136 |
| $In_{0.81}Al_{0.19}As$ | 14.18 | 0.042 | 0.155 |
| $HfO_2$ | 25.00 | 1.000 | 4.793 |

Table 2.1: **Material parameters used in the simulations.** For simulations using $In_{0.75}Ga_{0.25}As$ as the upper barrier we have $\delta\mu_i = 0$ eV, while for simulations using $In_{0.85}Al_{0.15}As$ we have $\delta\mu_i = -0.1113$ eV. The numerical values are taken from Refs. [74, 94–96].

To summarize, we investigated orbital-free methods for the solution of the electrostatic problem for nanoelectronic devices. We checked that the widespread Thomas-Fermi method, regarded as the simplest orbital-free method, is often applied outside its range of validity. The

most notable case of the approximation breakdown occurs at the interfaces with classically forbidden regions, like insulators, where the density of electrons has abrupt jumps.

To achieve a more accurate description of the density profile in these cases, we considered the extended Thomas-Fermi (ETF) method that includes the von Weizsäcker correction of the kinetic energy functional. This correction can significantly increase the precision of the density profile near interfaces.

We addressed the question of the optimal value of the $\lambda_{vW}$ parameter by studying a simple 2DEG system and found that the theoretically motivated value of $\lambda_{vW} = 1/9$ provides a good agreement also in the practical example cases considered. By applying the method to the simulation of realistic device geometries, we found that the ETF method provides density profiles closer to the ones calculated with the Schrödinger-Poisson method than the density profile provided by the TF method.

SP methods can be computationally expensive as they require explicit diagonalization of the Hamiltonian, whereas the predictive power of the TF method is poor due to the perfect local behavior of the energy functional. Therefore, the ETF method represents a good compromise in terms of computational speed and predictive power. orbital-free methods are an often neglected alternative for electrostatic simulations of nanoelectronic devices, which are useful to handle large systems since the problem can be nicely expressed in variational form and implemented on any finite element solver. The effect of finite-temperature and spin-orbit coupling can be straightforwardly included in the method [97, 98].

## 2.2 Spin-orbit coupling

A proper description of the spin-orbit interaction is crucial to predict the properties of a semiconductor heterostructure when proximitized by a superconductor, in particular in relation to the robustness of the topological phase. This section will give a brief account of the simplified models of spin-orbit coupling used in the field.

In general, spin-orbit coupling arises in the presence of a broken spatial inversion asymmetry. The cause of such symmetry breaking can be the lack of inversion symmetry in the crystal lattice; in this case, we refer to a *bulk inversion asymmetry* (BIA), In this case of *structural inversion asymmetry* (SIA), the absence is due to the geometry of the device.

The zincblende and wurtzite crystal systems are the most common for the III-V semiconductor compounds used in hybrid heterostructures as they are easy to grow and possess the smaller lattice mismatch with the commonly used superconductors [99]. For InAs, the zinc-blende corresponds to the (111) growth direction, while the wurtzite is found with the (0001) growth direction.

A proper description of the spin-orbit coupling in semiconductor devices requires the use of extended Kane models with up to 14 bands for zincblende crystals and eight bands for wurtzite ones [100]. Nevertheless, a simplified description involving only the conduction band is enough for many analyses.

This thesis considers III-V semiconductors that feature a direct bandgap around the $\Gamma$ point in the Brillouin zone. Under the assumptions of low temperature and density, we can take a parabolic approximation and write an effective Hamiltonian that reads as

$$\mathcal{H} = \frac{\hbar^2 \mathbf{k}^2}{2m} + \mathfrak{B}(\mathbf{k}) \cdot \boldsymbol{\sigma} \, , \tag{2.16}$$
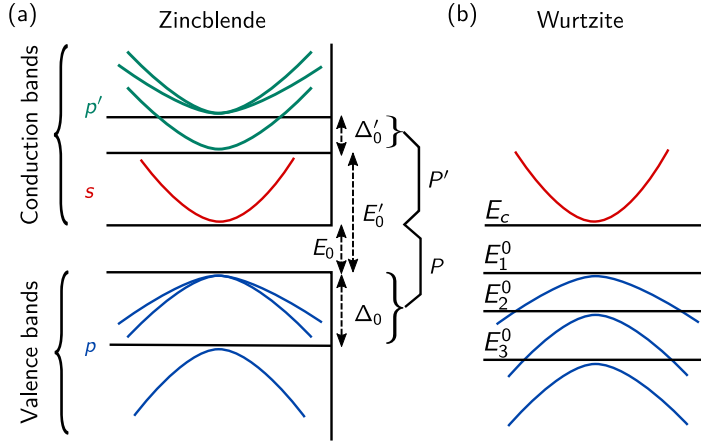
39

Fig. 2.4: **Band structure of a III-V semiconductor.** Sketch of the bandstructure and spin-orbit coupling parameters for a zincblende (a) and wurtzite (b) crystal of III-V semiconductors.

where $m$ is the effective mass, $\mathbf{k}$ is the crystal momentum, and the second term is the spin-orbit coupling. This is represented by the effective magnetic field $\mathfrak{B}(\mathbf{k})$, which is an odd function in $\mathbf{k}$ to satisfy time-reversal symmetry.

Using a third-order perturbation theory, it is possible to write the Rashba spin-orbit coupling as

$$B(\mathbf{k}) = \frac{\boldsymbol{\alpha}_R(\mathbf{r}) \times \mathbf{k} - \mathbf{k} \times \boldsymbol{\alpha}_R(\mathbf{r})}{2}, \tag{2.17}$$

where we defined the Rashba field

$$\boldsymbol{\alpha}_R(\mathbf{r}) = r_{41}^{6c6c} \nabla \varphi(\mathbf{r}) \tag{2.18}$$

that is proportional to the electric field $\nabla\varphi$, and the symmetrized product is used to guarantee the Herminicity of the Hamiltonian. The proportionality constant is given by

$$r_{41}^{6c6c} = \frac{eP^2}{3}\left[\frac{1}{E_0^2} - \frac{1}{(E_0+\Delta_0)^2}\right] + \frac{eP'^2}{3}\left[\frac{1}{(E_0-E_0')^2} - \frac{1}{(E_0-E_0'+\Delta_0)^2}\right], \tag{2.19}$$

where $E_0$ is the valence to the conduction band gap, $\Delta_0$ is the split-off gap in the semiconductor, $P$ and $P'$ are the coupling element (conduction to valence band coupling) corrected to take into account the material and crystal properties of the electron gas [100]. These coupling elements are sketched in Fig. 2.4.

A conduction-band model for the BIA-induced spin-orbit coupling in zincblende structures has been proposed by Dresselhaus [101] and takes the form

$$\mathfrak{B}(\mathbf{k}) = \gamma^{ZB}\begin{pmatrix} k_x(k_y^2 - k_z^2) \\ k_y(k_z^2 - k_x^2) \\ k_z(k_x^2 - k_y^2) \end{pmatrix}, \tag{2.20}$$

where $\gamma^{ZB}$ is the spin-orbit coupling parameter.

III-V wurtzite crystals, instead, have an anisotropic band structure near the $\Gamma$ point, so there is a need for two parameters for the effective mass tensor. The low-energy effective Hamiltonian can be written as

$$\mathcal{H} = \frac{\hbar^2}{2\,m_0} \left[ \frac{1}{m_\perp} \left( k_x^2 + k_y^2 \right) + \frac{1}{m_\parallel}\, k_z^2 \right] + \mathfrak{B} \cdot \boldsymbol{\sigma} \, . \tag{2.21}$$

The functional form of the spin-orbit field of the conduction electrons in bulk wurtzite III-V semiconductor is [102]

$$\mathfrak{B}(\mathbf{k}) = \left[ \alpha^{\mathrm{WZ}} + \gamma^{\mathrm{WZ}} \left( b k_z^2 - k_x^2 - k_y^2 \right) \right] \left( k_y, -k_x, 0 \right). \tag{2.22}$$

The Dresselhaus term is cubic and mixes different directions. For this reason, it gives considerable contributions to the Hamiltonian in quantum-confined nanostructures. In zincblende InAs, the Dresselhaus effect is usually negligible, while it can play an important role for the wurtzite crystal.

**Spin-orbit coupling in quantum confined system**

Before concluding this brief introduction of the spin-orbit coupling terms, we outline the main effects in quantum-confined structures. In this work, we only consider the linear terms in $\mathbf{k}$ in the Hamiltonian of Eq. (2.16), as they are the dominant ones at low densities.

To discuss the effects in 2DEGs, we now briefly introduce a minimal model, and later we discuss the possible origin of such spin-orbit coupling terms. Under the assumptions of low temperature and density, we can use a parabolic approximation and write an effective Hamiltonian that reads as

$$\mathcal{H} = \frac{\hbar^2 \mathbf{k}^2}{2m} + \mathfrak{B}(\mathbf{k}) \cdot \boldsymbol{\sigma} \tag{2.23}$$

where $m$ is the effective mass, $\mathbf{k} = (k_x, k_y)$ and the second term is the spin-orbit coupling.

If we consider only linear terms in the momentum, we can express the spin-orbit coupling as

$$\mathrm{B}(\mathbf{k}) \cdot \boldsymbol{\sigma} = \begin{pmatrix} \beta_w + \beta_d & \alpha_d - \alpha_{\mathrm{R}} \\ \alpha_d + \alpha_{\mathrm{R}} & \beta_w - \beta_d \end{pmatrix} \begin{pmatrix} k_x \\ k_y \end{pmatrix} \tag{2.24}$$

where we defined $\alpha_{\mathrm{R}}$ is a Rashba-type spin-orbit coupling, $\alpha_d$ and $\beta_d$ are Dresselhaus-like spin-orbit couplings, and finally $\beta_w$ is a Weyl-type spin-orbit coupling [103]. The spin texture in momentum space for a 2DEG with a spin-orbit coupling term of the various types is displayed in Fig. 2.5. In most common materials, $\alpha_d$ and $\beta_w$ are usually negligible.

The Rashba term has the same form as presented in the previous section since it is a SIA effect commonly found at 2D interfaces. At these interfaces, a surface dipole generates a strong electric field directed out of the surface. To obtain the linearized form of the Dresselhaous term, first-order perturbation theory can be applied to Eq. (2.20). For an electron gas confined in the $z$ direction, the result is

$$\mathfrak{B}(\mathbf{k}) = \gamma^{\mathrm{ZB}} \begin{pmatrix} k_x[k_y^2 - \langle k_z^2 \rangle] \\ k_y[\langle k_z^2 \rangle - k_x^2] \\ 0 \end{pmatrix} = \beta \left( -k_x \sigma_x + k_y \sigma_y \right) + o(\mathbf{k}^3) \tag{2.25}$$
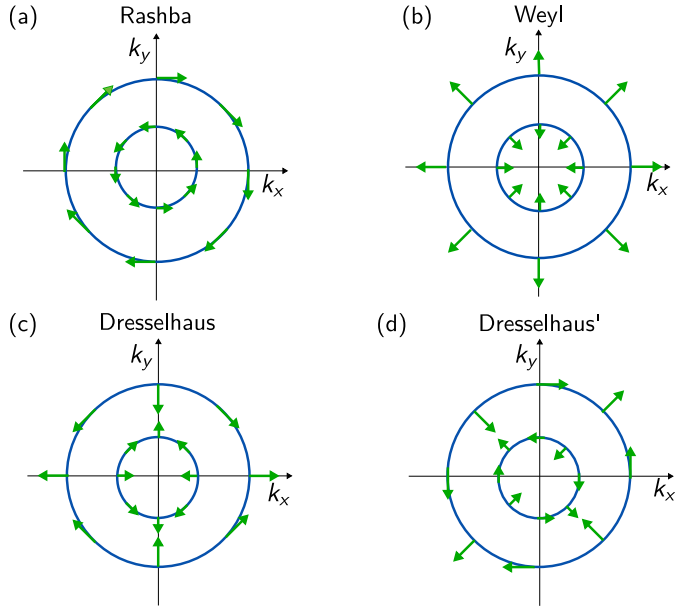
Fig. 2.5: **Spin textures in 2DEG with different types of spin-orbit coupling.** The picture sketches the spin texture of a 2DEG in momentum space caused by the presence of a Rashba spin-orbit coupling term (a), a Weyl term (b), a Dresselhaus (c), and a Dresselhaus' (d). This nomenclature is taken by Ref. [103]

with $\beta = \gamma^{\mathrm{ZB}} \langle k_z^2 \rangle$.

By applying the same procedure to a quasi-1D structure, confined also in the $y$ direction, we obtain the linear Dresselhaus term

$$\mathfrak{B}(\mathbf{k}) = \beta k_x \sigma_x, \qquad \beta = \gamma^{\mathrm{ZB}} \left[ \langle k_y^2 \rangle - \langle k_z^2 \rangle \right]. \tag{2.26}$$

The first-order approximation scheme we introduced treats spin-orbit coupling as a perturbation on top of the mode quantization induced by the geometry of the device. These can substantially modify the picture, in particular for the outer zone of the Brillouin zone. Moreover, we only mentioned the conduction band arbitrarily, ignoring some inter and intra-band coupling. These can quantitatively change the picture [104, 105].

# 3

# Transport in hybrid structures

In the previous chapters, we outlined the theoretical description of hybrid heterostructures physics. Now, we will establish the connection with the simplest type of experiments that can be conducted with these devices, namely transport measurements and, more specifically, tunneling spectroscopy.

Tunneling spectroscopy is a powerful tool for studying superconductor-semiconductor hybrid devices as it provides a clear signature for Andreev bound states (ABS). Nonlocal conductance spectroscopy is the natural extension of local two-probe spectroscopy and overcomes some of its limitations. Initially used in the context of the search for signatures of Cooper-pair splitting [106–110], this type of measurement has been recently considered in the context of topological superconductivity (TS) [111–113] leading to its use in experiments [114, 115], its inclusion in identification protocols for Majorana bound states (MBSs) in nanowires [116] and unconventional superconductors vortex cores [117], as well as for the characterization of chiral Majorana edge states in two-dimensional (2D) TS [118] and the helical gap in two-dimensional electron gases (2DEGs) [119]. Moreover, the same concept appears in experiments involving quantum dots to probe the non-equilibrium dynamics of quasiparticles [109, 110].

When an electron current flows across the device, aside from the electric charge current, energy and heat currents flow too. For this reason, the spectral features of the device, including peaks connected to the onset of the topological phase, can also be identified when analyzing the thermal conductance [120, 121]. Nevertheless, measurements of thermal transport require a very complex and delicate experimental setup. Easier experiments are the ones that study thermoelectric transport, where the system is driven out of equilibrium by using leads thermalized at different temperatures while the measured output is still a charge current. Thermoelectric measurements have been proposed as an additional tool to investigate subgap features and identify MBSs [122].

Motivated by recent experimental success in measuring multiterminal electric differential conductance [86, 87, 93, 107, 110, 114, 115, 123–125] and the need to characterize hybrid superconductor-semiconductor devices, we here extend the theory of multiterminal tunneling spectroscopy to extract additional information on the electronic and Andreev transmission processes from linear combinations of local and nonlocal differential conductance measurements at different bias voltage or magnetic fields. These linear combinations are derived using conditions that follow from quasiparticle-number conservation, microreversibility, and particle-hole conjugation in the presence of superconductivity. Further relations can be derived in the presence of geometrical symmetries, such as mirror symmetry, or less general Hamiltonian symmetries, like additional antiunitary symmetries.

For the specific case of a semiconductor nanowire proximity coupled to an $s$-wave superconductor, we show that the resulting symmetry relations of the conductance matrix can be used to identify the relative strength of Rashba versus Dresselhaus spin-orbit coupling (SOC). We furthermore show that these symmetry relations can be employed to identify signatures of deviations from the assumed symmetries, in particular, voltage bias-dependent electric potential landscapes and quasiparticle dissipation into environmental baths.

To achieve this objective, we discuss an extended version of the Landauer-Büttiker theory that accounts for bias-voltage-dependent electric potentials. These results are compared to the linear Landauer-Büttiker theory, where it is assumed that the potential landscape, in which the scattering occurs, does not depend on the bias voltages. We refer to this assumption as the *constant landscape approximation* (CLA).

Extensions of the CLA theory for both nonlinear electric conductance [126, 127] and ther-

moelectric conductance [128–130] have been considered before. Several previous works focused on the quadratic correction (in voltage bias) to differential conductance obtained by the method of characteristic potential, e.g. [127, 129, 131–134], that in practical applications relies on Thomas-Fermi approximation [134, 135]. This method is more suited for mesoscopic metallic devices with a high density of states, in which the finite-size effects can be neglected.

In the case of superconductor-semiconductor nanoelectronic devices, instead, the electrostatic potential can be a complicated function of the gate voltage that in general requires the solution of the complete Schrödinger-Poisson problem [P3, 75, 78, 136–139]. An initial characterization of finite-bias effects in the fully nonlinear regime was obtained by a combination of approximate analytic and numerical methods in Ref. [140].

In Sec. 3.1, we describe the general theory of nonlinear charge transport in multiterminal hybrid devices and the difference with CLA results. In Sec. 3.2, we show how fundamental symmetries such as microreversibility and particle-hole conjugation in the $S$ matrix generate conductance symmetries valid in CLA and how to use these to extract additional information on the transmission processes from the differential conductance matrix. As an example application, in Sec. 3.3 we demonstrate how these symmetries can be exploited to identify the spin-orbit direction in a semiconductor nanowire proximitized by a superconductor. Finally, in Sec. 3.4, with simple numerical simulations we show the effect of finite-bias deformation of the electrostatic potential and dissipation and discuss how violation of conductance symmetry can be used to distinguish between the two. We also illustrate an example of spin-orbit coupling characterization, and discuss how thermoelectric differential conductance can be used as a probe to avoid the finite-bias effect.
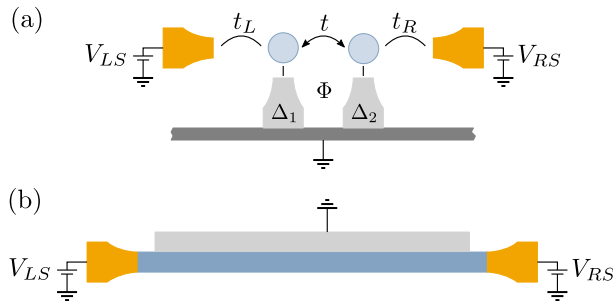


Fig. 3.1: **Examples of multiterminal hybrid devices** (a) double-dot Josephson junction, and (b) a spin-orbit coupled semiconductor nanowire (blue) proximitized by an $s$-wave superconductor (gray). The metallic contacts are depicted in yellow. All the superconductive leads are grounded.

## 3.1 Scattering transport theory

The Landauer-Büttiker formalism is a simple yet powerful technique to model transport phenomena. While usually employed in CLA, the nonlinear version can be constructed easily while paying attention to preserving the gauge invariance of the theory [127].

When the motion of quasiparticles is a coherent process and the interactions between quasiparticles beyond mean-field theory can be neglected, quasiparticle transport phenomena in a device are completely described by the single-particle scattering matrix $S$ that relates the probability amplitude of the incoming and outgoing quasiparticles in the leads. More specifically, the relation between the average currents and biases of a multiterminal device depends only on the transmission probability defined as

$$T_{\alpha\beta}^{\gamma\delta}(\varepsilon; P) \equiv \text{tr} \left| S_{\alpha\beta}^{\gamma\delta}(\varepsilon; P) \right|^2 , \tag{3.1}$$

where $S_{\alpha\beta}^{\gamma\delta}$ is the subblock of the scattering matrix that connects the channel of the incoming particles of type $\delta$ from lead $\beta$ to the channel of outgoing particles of type $\gamma$ in lead $\alpha$ for scattering events at energy $\varepsilon$. Since the device we are describing is a superconductor-semiconductor hybrid, the transmission matrix features a Nambu structure with particle and hole sectors, $\delta, \gamma \in \{e, h\}$. The transmission probabilities depend on the set of electric potentials applied to all the electrodes in the system $\{V_\eta\}$ and other external parameters like the applied magnetic field $\mathbf{B}$ and the pairing amplitude of superconductive leads $\{\Delta_\nu\}$. We denote the set of external parameters by $P = \{V_\eta\} \cup \{\Delta_\nu\} \cup \{\mathbf{B}\}$. In principle also the temperature of the leads can enter as a parameter of the system. For example, temperature could affect the size of the superconductive gap or induce charge accumulation in the semiconductor. We will neglect these effects as we are assuming that the temperature differences involved are much smaller than the critical temperature of the superconductor and are too small to induce a relevant change in the electrostatic potential landscape. Indeed, while voltage bias enters directly into the Poisson equation as boundary conditions, the temperature can enter the electrostatic problem only through charge accumulation.

A generic multiterminal system comprises a number of normal and superconductive terminals, suggesting a division of the $S$ matrix into subblocks as follows:

$$S = \begin{pmatrix} S_{NN} & S_{NS} \\ S_{SN} & S_{SS} \end{pmatrix} . \tag{3.2}$$

In this paper, we will consider the simplest case in which all the superconductive terminals are grounded together and we denote the voltage of the common superconductive lead as $V_S$.

If the system conserves the quasiparticle number, the $S$ matrix is unitary and it follows that

$$R_\alpha^{ee} + R_\alpha^{he} + \sum_{\beta \neq \alpha} \left( T_{\beta\alpha}^{ee} + T_{\beta\alpha}^{he} \right) = N_\alpha^e(\varepsilon) , \tag{3.3}$$

$$R_\alpha^{ee} + R_\alpha^{eh} + \sum_{\beta \neq \alpha} \left( T_{\alpha\beta}^{ee} + T_{\alpha\beta}^{eh} \right) = N_\alpha^e(\varepsilon) , \tag{3.4}$$

where we defined for clarity the reflection matrix $R_\alpha^{\gamma\delta} \equiv T_{\alpha\alpha}^{\gamma\delta}$ while $N_\alpha^e(\varepsilon)$ is the number of eigenmodes for electrons in lead $\alpha$. Note that, unless the density in the lead is so low to break particle-hole symmetry, $N_\alpha(\varepsilon) \equiv N_\alpha^e(\varepsilon) = N_\alpha^h(\varepsilon)$. Equation (3.3) represents the conservation of incoming quasiparticles from lead $\alpha$ while Eq. (3.4) is the same for outgoing quasiparticles. The conservation law breaks down when dissipation effects are included as they do not preserve the particle number. When restricted to energies below the smallest parent superconductor gap $\varepsilon < \min\{|\Delta_\nu|\}$, the matrices $S_{SS}(\varepsilon)$, $S_{SN}(\varepsilon)$, $S_{NS}(\varepsilon)$ are null and therefore a stronger relation holds where the sum over $\beta$ is restricted to the non-superconductive leads.

As mentioned above, in the superconductive version of the Landauer-Büttiker theory quasiparticle conservation takes the place of electron conservation for conventional devices. This implies that the electric charge is not explicitly conserved. Indeed, we can distinguish between the charge-conserving normal processes $T_{\alpha\beta}^{ee}$, and $T_{\alpha\beta}^{hh}$, and the non-charge-conserving Andreev processes $T_{\alpha\beta}^{eh}$, and $T_{\alpha\beta}^{he}$. The last two imply, respectively, the creation and the destruction of one Cooper pair in the superconductive leads.

A correct theory of nonlinear conductance of a multiterminal device needs to be gauge invariant. This means that the transmission probabilities are not changed by the addition of a constant offset to all the voltages and particle energy:

$$T_{\alpha\beta}^{\gamma\delta}(\varepsilon + \Delta E; \{V_\eta + \Delta E\}) = T_{\alpha\beta}^{\gamma\delta}(\varepsilon; \{V_\eta\}) \tag{3.5}$$

The easiest way to guarantee gauge invariance is to define a reference voltage. We define the superconductor lead to be our reference voltage and set $V_S = 0$. The first argument of the transmission function is then the energy of the scattering particle with respect to the superconductive lead chemical potential $\varepsilon = E_p + eV_S$. The parameters $V_{\alpha S}$ and $V_{\beta S}$ are the bias of the leads with respect to $V_S$. These biases, together with the voltage biases applied to the capacitively coupled gates, determine the electrostatic potential landscape in which the scattering events take place. Therefore, they enter here as parameters of the $S$ matrix as well as the transmission probability matrix.

## Currents

The nonlinear Landauer-Büttiker approach consists in first solving the electrostatic problem for the potential landscape given the applied biases. With the calculated potential landscape, the $S$ matrix for the scattering processes can be evaluated. Finally, once the static scattering problem has been solved, from the $S$ matrix all the transport properties of the system can be derived. In particular, we can use the transmission functions to determine the average currents in the nonequilibrium steady state. In this last step, the terminal biases $V_{\alpha S}$ appear again also as parameters of the distribution functions of the leads. The application of this approach for superconductive systems has been derived on several occasions [141–145], and in the most general formulation the average electric current through a lead $\alpha$ is then

$$
\begin{aligned}
I_\alpha^q(P) = {}& +\frac{e}{h} \int_{-\infty}^{+\infty} d\varepsilon \left[ f(\varepsilon - eV_{\alpha S}, \theta_\alpha) - f(\varepsilon, \theta_S) \right] \\
& \times \left[ N_\alpha - R_\alpha^{ee}(\varepsilon; P) + R_\alpha^{he}(\varepsilon; P) \right] \\
& - \sum_{\beta \neq \alpha} \frac{e}{h} \int_{-\infty}^{+\infty} d\varepsilon \left[ f(\varepsilon - eV_{\beta S}, \theta_\beta) - f(\varepsilon, \theta_S) \right] \\
& \times \left[ T_{\alpha\beta}^{ee}(\varepsilon; P) - T_{\alpha\beta}^{he}(\varepsilon; P) \right],
\end{aligned}
\tag{3.6}
$$

where $f(\varepsilon, \theta) = \left( 1 + e^{\varepsilon/k_B\theta} \right)^{-1}$ is the Fermi-Dirac distribution, and the parameters $\{\theta_\eta\}$ are the temperatures of the leads. We assumed for simplicity that the temperature of all the superconductive leads is equal to $\theta_S$. A similar expression can be written for the energy current $I_\alpha^\varepsilon$ while the heat current $I_\alpha^h = I_\alpha^\varepsilon + eV_{\alpha S} I_\alpha^q$ follows easily from the first law of thermodynamics [130].

We can write, for the $I^q$ and $I^h$ vectors of currents, the following differential relation with the voltages $V$ and temperatures $\theta$ vectors [129, 132, 146]:

$$\begin{pmatrix} \mathrm{d}I_\alpha^q \\ \mathrm{d}I_\alpha^h \end{pmatrix} = \begin{pmatrix} G_{\alpha\beta} & L_{\alpha\beta} \\ M_{\alpha\beta} & N_{\alpha\beta} \end{pmatrix} \begin{pmatrix} \mathrm{d}V_\beta \\ \mathrm{d}\theta_\beta \end{pmatrix} \tag{3.7}$$

where $G$ is the differential electric conductance, $N$ is the differential thermal conductance, while $L$ is the thermoelectric and $M$ is the electrothermal differential conductance.

An important observation about the charge current is that it does not satisfy Kirchhoff's current law. This is because the expression derived describes only the quasiparticle current while the supercurrent is not captured in this formalism. By imposing charge conservation, the net supercurrent flowing into the device is $I^s = -\sum_\alpha I_\alpha^q$. The net supercurrent can be evaluated as

$$I^s = -\frac{2e}{h} \sum_{\alpha\beta} \int_{-\infty}^{+\infty} \mathrm{d}\varepsilon \left[ f(\varepsilon - eV_{\beta S}, \theta_\beta) - f(\varepsilon, \theta_S) \right]$$
$$\times \left[ R_\beta^{he}(\varepsilon; P) + T_{\alpha\beta}^{he}(\varepsilon; P) \right]. \tag{3.8}$$

In the case of a single superconductive lead, this is equal to the supercurrent flowing into the device. In the case of multiple superconductive leads, instead, the supercurrent divides between the different superconductive leads.

**Constant landscape approximation**

In the CLA, the change in the potential landscape when a voltage bias is applied is neglected. We denote this by writing that $P = P_0$ where $P_0$ is the set of parameters at equilibrium. In this case, the CLA result for electrical conductance is

$$G_{\alpha\alpha} = G_0 \int_{-\infty}^{+\infty} \mathrm{d}\varepsilon \left[ -\partial_\varepsilon f(\varepsilon - eV_{\alpha S}, \theta_\alpha) \right]$$
$$\times \left[ N_\alpha - R_\alpha^{ee}(\varepsilon; P = P_0) + R_\alpha^{he}(\varepsilon; P = P_0) \right], \tag{3.9}$$

for local differential conductance, while for the nonlocal differential conductance we have

$$G_{\alpha\beta} = -G_0 \int_{-\infty}^{+\infty} \mathrm{d}\varepsilon \left[ -\partial_\varepsilon f(\varepsilon - eV_{\beta S}, \theta_\beta) \right]$$
$$\times \left[ T_{\alpha\beta}^{ee}(\varepsilon; P = P_0) - T_{\alpha\beta}^{he}(\varepsilon; P = P_0) \right], \tag{3.10}$$

where $G_0 = \frac{e^2}{h}$ is the conductance quantum and $\partial_\varepsilon f(\varepsilon, \theta) = -\frac{1}{2k_B\theta} \frac{1}{1+\cosh(\varepsilon/k_B\theta)}$.

A similar expression can be obtained for thermoelectric conductance. The local and nonlocal thermoelectric conductance reads as

$$L_{\alpha\alpha} = +L_0 \int_{-\infty}^{+\infty} \mathrm{d}\varepsilon \, k_B^{-1} \partial_\theta f(\varepsilon - eV_{\alpha S}, \theta_\alpha)$$
$$\times \left[ N_\alpha - R_\alpha^{ee}(\varepsilon; P = P_0) + R_\alpha^{he}(\varepsilon; P = P_0) \right] \tag{3.11}$$

and

$$
L_{\alpha\beta} = -L_0 \int_{-\infty}^{+\infty} d\varepsilon \; k_B^{-1} \partial_\theta f(\varepsilon - eV_{\beta S}, \theta_\beta)
$$
$$
\times \left[ T_{\alpha\beta}^{ee}(\varepsilon; P = P_0) - T_{\alpha\beta}^{he}(\varepsilon; P = P_0) \right],
\tag{3.12}
$$

where $L_0 = \frac{ek_B}{h}$ is the thermoelectric conductance quantum and we used the derivative of the distribution function with respect to temperature, that is $k_B^{-1}\partial_\theta f(\varepsilon, \theta) = -\frac{\varepsilon}{k_B\theta}\partial_\varepsilon f(\varepsilon, \theta)$. Note that since $\partial_\varepsilon f$ is an odd function of the energy, thermoelectric conductance is sensitive only to the antisymmetric component of the transmission spectrum of the device.

**Differential conductance in the nonlinear theory**

In principle, the average current given by Eq. (3.6) is exact for a non-interacting system if the potential landscape is calculated self-consistently from the set of parameters $P$. We do not attempt such a calculation here, since the devices treated often have a complicated three-dimensional geometry that cannot easily be reduced to a simple one-dimensional model when taking the electrostatic environment into account. Instead, in this section, we focus on general considerations, while in Sec. 3.4 we parametrize a potential landscape in a physically motivated way and look at differences with CLA results.

Evaluating the full derivatives of the charge current $I^q$ with respect to a terminal voltage bias we find that the electric differential conductance can be split into two parts

$$
G_{\alpha\beta}(\{V_\eta\}) = \frac{dI_\alpha^q}{dV_{\beta S}} = G_{\alpha\beta}^{(m)} + G_{\alpha\beta}^{(def)}
\tag{3.13}
$$

where the first term is the marginal contribution that reads as, i.e. for the local conductance,

$$
G_{\alpha\alpha}^{(m)} = +G_0 \int_{-\infty}^{+\infty} d\varepsilon \left[ -\partial_\varepsilon f(\varepsilon - eV_{\alpha S}, \theta_\alpha) \right] \left[ N_\alpha - R_\alpha^{ee}(\varepsilon; P) + R_\alpha^{he}(\varepsilon; P) \right].
\tag{3.14}
$$

This term can be interpreted as the fact that when evaluating the additional current carried by higher-energy states, the $S$ matrix has to be calculated using the potential landscape that takes into account the modified voltage bias. The second term accounts for the deformation of the $S$ matrix for the already filled channels due to the effect of the biasing itself. The deformation contribution reads as

$$
G_{\alpha\beta}^{(def)} = G_0 \int_{-\infty}^{+\infty} d\varepsilon \left[ f(\varepsilon - eV_{\alpha S}, \theta_\alpha) - f(\varepsilon, \theta_S) \right] \left[ -\frac{\partial R_\alpha^{ee}(\varepsilon; P)}{\partial V_{\beta S}} + \frac{\partial R_\alpha^{he}(\varepsilon; P)}{\partial V_{\beta S}} \right]
$$
$$
+ G_0 \int_{-\infty}^{+\infty} d\varepsilon \left[ f(\varepsilon - eV_{\beta S}, \theta_\beta) - f(\varepsilon, \theta_S) \right] \left[ -\frac{\partial T_{\alpha\beta}^{ee}(\varepsilon; P)}{\partial V_{\beta S}} + \frac{\partial T_{\alpha\beta}^{he}(\varepsilon; P)}{\partial V_{\beta S}} \right].
\tag{3.15}
$$

This correction is often neglected in previous works, e.g. Ref. [127]. The reason is that in the case of symmetric biasing $V_\alpha = V_\beta = V$ and fixed temperature $\theta_\alpha = \theta_\beta = \theta_S$, we can rewrite

$G_{\alpha\beta}^{(\text{def})}$ as

$$G_{\alpha\beta}^{(\text{def})}(V) = -G_0 \int_{-\infty}^{+\infty} d\varepsilon \left[ f(\varepsilon - eV, \theta_S) - f(\varepsilon, \theta_S) \right] \frac{\partial}{\partial V_\beta}$$

$$\times \left[ N_\alpha(\varepsilon) - R_\alpha^{eh}(\varepsilon; P) - R_\alpha^{he}(\varepsilon; P) - \sum_{\beta'} (T_{\alpha\beta'}^{eh}(\varepsilon; P) + T_{\alpha\beta'}^{he}(\varepsilon; P)) \right]. \tag{3.16}$$

Since $N_\alpha$ does not depend on the bias (it is a property of the leads) and all the other terms in the brackets are probabilities of Andreev's processes, it is clear that this quantity vanishes for non-superconductive devices. However, this contribution shows an interesting interplay between electrostatic behavior and superconductivity.

For example, let us consider a simple N-S junction. The differential conductance can be written as

$$G_{\alpha\alpha} = +2G_0 \int_{-\infty}^{+\infty} d\varepsilon \left[ -\partial_\varepsilon f(\varepsilon - eV_{\alpha S}, \theta_\alpha) \right] R_\alpha^{he}(\varepsilon; P)$$

$$+2G_0 \int_{-\infty}^{+\infty} d\varepsilon \left[ f(\varepsilon - eV_{\alpha S}, \theta_\alpha) - f(\varepsilon, \theta_S) \right] \frac{\partial R_\alpha^{he}(\varepsilon; P)}{\partial V_{\alpha S}}. \tag{3.17}$$

It is evident that in case $\frac{\partial R_\alpha^{he}(\varepsilon; P)}{\partial V_{\alpha S}} > 0$ the second term in the sum can overcome the first one, which is always positive, resulting in negative local differential conductance. A simple case of this can be when the coupling of the scattering region with the superconductor decreases with the bias [140, 147].

## 3.2 Conductance symmetries

In this section, we consider how the symmetries of the system manifest themselves first as symmetries of the $S$ matrix and, consequently, in the differential conductance matrix. We consider the ideal CLA case and, for this reason, we drop the biases as arguments in the $S$ matrix.

We choose the Nambu basis of time-reversed holes,

$$\Psi^T = (\psi, \mathcal{T}\psi)^T = \begin{pmatrix} \psi_\uparrow & \psi_\downarrow & -\psi_\downarrow^\dagger & \psi_\uparrow^\dagger \end{pmatrix}^T \tag{3.18}$$

where we have chosen for the time-reversal symmetry $\mathcal{T} = -i\sigma_y \mathcal{K}$, where $\mathcal{K}$ is the complex-conjugation operator, and therefore for the particle-hole symmetry $\mathcal{P} = i\tau_y \mathcal{T}$.

In the following analysis, we consider symmetric and antisymmetric linear combinations of the conductance matrix elements at opposite voltage bias and magnetic field. We have investigated all linear combinations. However, in the following, we only present the interesting cases in which the linear combination leads to a reduction in the number of terms.

### Particle-hole symmetry

If the system features particle-hole symmetry (PHS), the energy-resolved scattering matrix satisfies the following relation

$$S(\varepsilon) = \mathcal{P}S(-\varepsilon)\mathcal{P}^\dagger = \sigma_y \tau_y S^*(-\varepsilon)\sigma_y \tau_y. \tag{3.19}$$

This poses an additional constraint on Andreev transmission probabilities that read as

$$T_{\alpha\beta}^{\gamma\delta}(+\varepsilon) = T_{\alpha\beta}^{\bar{\gamma}\bar{\delta}}(-\varepsilon)\,, \tag{3.20}$$

where the overbar indicates that the index should be flipped $e \leftrightarrow h$.

This property of the transmission probabilities has a number of consequences on differential conductance. For example, in a system with a single normal terminal (e.g., an NS junction), or for a terminal that is completely isolated from others such that there are no propagating channels (normal or Andreev) connecting it to other leads, the reflection coefficients have to be energy symmetric below the gap. As a consequence, the conductance has to be a symmetric function of the voltage for ideal devices. For the same reason, in these cases the thermoelectric conductance is always exponentially suppressed for temperatures much smaller than the superconducting gap.

Dissipation, inelastic scattering, and coupling to other leads are known effects that break this symmetry of the transmission matrix [148–150] while finite-bias effects can lead to the break-down of the symmetry at conductance-matrix level [140, 151].

A generalization of this conductance-matrix symmetry for the multiterminal case can be obtained by considering the quantity

$$G_\alpha^{\text{sum}}(V) \equiv G_{\alpha\alpha}(V) + \sum_{\beta \neq \alpha} G_{\alpha\beta}(V)\,, \tag{3.21}$$

that is the sum of the local conductance at terminal $\alpha$ and the nonlocal conductances obtained measuring the current at $\alpha$ while applying a voltage bias to all the other normal leads. It follows that, as a consequence of Eq. (3.20),

$$G_\alpha^{\text{sum}}(V) = G_0 \int_{-\infty}^{+\infty} \mathrm{d}\varepsilon \left[ -\partial_\varepsilon f(\varepsilon - eV) \right] H_\alpha(\varepsilon)\,, \tag{3.22}$$

where we defined the quantity

$$\begin{aligned}
H_\alpha(\varepsilon) = R_\alpha^{he}(+\varepsilon) + R_\alpha^{he}(-\varepsilon) &+ \sum_{\beta \neq \alpha} \left[ T_{\alpha\beta}^{he}(+\varepsilon) + T_{\alpha\beta}^{he}(-\varepsilon) \right] \\
&+ \sum_\nu \left[ T_{\alpha\nu}^{ee}(+\varepsilon) + T_{\alpha\nu}^{eh}(+\varepsilon) \right].
\end{aligned} \tag{3.23}$$

The first two terms in $H_\alpha(\varepsilon)$ are explicitly symmetric in $\varepsilon$, while the last sum is null for $\varepsilon < \min|\Delta_\nu|$. Therefore, as a consequence,

$$G_\alpha^{\text{sa}}(V) \equiv G_\alpha^{\text{sum}}(V) - G_\alpha^{\text{sum}}(-V) = 0\,. \tag{3.24}$$

This relation is a generalization of the three-terminal case derived in Ref. [113]. This result has been derived for non-interacting systems in CLA, therefore, any deviation from zero in $G^{\text{sa}}$ can be used as a tool to inspect deviations from the CLA and the contributions of quasiparticle dissipation or Coulomb repulsion between quasiparticles. We will discuss these effects in Sec. 3.4.

We can split the local and nonlocal differential conductance into symmetric and antisymmetric components

$$G_{\alpha\beta}^{\mathrm{sym}}(V) \equiv \frac{G_{\alpha\beta}(V) + G_{\alpha\beta}(-V)}{2}, \tag{3.25}$$

$$G_{\alpha\beta}^{\mathrm{anti}}(V) \equiv \frac{G_{\alpha\beta}(V) - G_{\alpha\beta}(-V)}{2}. \tag{3.26}$$

It has been shown that one can extract the BCS charge, i.e. $\langle \tau_z \rangle$, of each ABS from the antisymmetric combination $G_{\alpha\beta}^{\mathrm{anti}}(V)$, given the ABSs are sufficiently separated in the spectrum [113].

A similar relation can be derived for thermoelectric differential conductance. Indeed, under the same conditions, we can define

$$L_{\alpha}^{\mathrm{sum}}(\theta) \equiv L_{\alpha\alpha} + \sum_{\beta \neq \alpha} L_{\alpha\beta} = L_0 \int_{-\infty}^{+\infty} d\varepsilon \, k_B^{-1} \partial_\theta f(\varepsilon, \theta) H_\alpha(\varepsilon). \tag{3.27}$$

Since $H_\alpha(\varepsilon)$ is an even function of $\varepsilon$ while $\partial_\theta f(\varepsilon)$ is an odd function, we have that $L^{\mathrm{sum}} \simeq 0$ for $k_B \theta \ll \min \Delta_\nu$. This holds, again, for non-interacting systems but only for temperatures low enough to exclude excitations of states above the parent gap. Since the thermoelectric conductance is connected to the antisymmetric part of the transmission spectrum, its sign at low temperature can be linked to the BCS charge $\langle \tau_z \rangle$ of ABSs, following a similar argument as for $G^{\mathrm{anti}}$ as presented in Ref. [113].

In the presence of dissipation, the previous transport symmetries do not hold. Here by dissipation, we mean the presence of a reservoir at the Fermi level that induces quasiparticle leakage. This can be due to various reasons, such as the presence of subgap states in the superconductor causing a softening of the gap or some other leakage mechanism that connects the scattering region to the common ground. A simple way to model quasiparticle leakage is by considering a fictitious lead $\beta'$ that is excluded when taking the calculation of $G_\alpha^{\mathrm{sum}}$. Focusing on energies below the gap, one finds that the antisymmetric part does not vanish but equals to

$$G_\alpha^{\mathrm{sa}}(V) = G_0 \int_{-\infty}^{+\infty} d\varepsilon \left[ -\partial_\varepsilon f(\varepsilon) \right] \left[ T_{\alpha\beta'}^{eh}(\varepsilon - eV) + T_{\alpha\beta'}^{ee}(\varepsilon - eV) \right.$$
$$\left. - T_{\alpha\beta'}^{eh}(\varepsilon + eV) - T_{\alpha\beta'}^{ee}(\varepsilon + eV) \right]. \tag{3.28}$$

A similar relation can be obtained for thermoelectric conductance. To assess in a more quantitative way the effect of dissipation later we will switch to numerical simulations (see Sec. 3.4).

### Microreversibility

The microreversibility of the scattering process is a consequence of global time-reversal symmetry and implies that, upon inversion of the time-reversal breaking fields and spin direction, the motion can be reversed[1]. As a consequence, the scattering matrix is equal to its transpose

$$S(\mathbf{B}, \Delta_\nu) = \mathcal{T} S(-\mathbf{B}, \Delta_\nu^*) \mathcal{T}^\dagger = \sigma_y S^T(-\mathbf{B}, \Delta_\nu^*) \sigma_y, \tag{3.29}$$

---

[1] Note that we are considering systems that do not break time-reversal symmetry internally.

which, expanding in particle and lead labels, becomes

$$S_{\alpha\beta}^{\gamma\delta}(\mathbf{B},\Delta_\nu^*) = \sigma_y \left[ S_{\beta\alpha}^{\delta\gamma}(-\mathbf{B},\Delta_\nu^*) \right]^T \sigma_y. \tag{3.30}$$

If we consider only non-spin-polarized leads, we can take the trace over the internal spin indices and get the following symmetry relation:

$$T_{\alpha\beta}^{\gamma\delta}(\varepsilon,\mathbf{B}) = T_{\beta\alpha}^{\delta\gamma}(\varepsilon,-\mathbf{B},\Delta_\nu^*). \tag{3.31}$$

Combining this relation with the one derived from particle-hole symmetry [Eq. (3.20)], we find that, for Andreev reflections and transmission coefficients,

$$T_{\alpha\beta}^{eh}(\varepsilon,\mathbf{B}) = T_{\beta\alpha}^{eh}(-\varepsilon,-\mathbf{B},\Delta_\nu^*). \tag{3.32}$$

This has implications both in the electric and thermoelectric nonlocal conductance.

The connection between microreversibility and thermoelectric quantities has been explored on general grounds both in theory [152, 153] and experiments [154]. In particular, microreversibility is the microscopic explanation of the Onsager-Casimir relations that lead to other transport symmetries in the charge, heat, and spin channels valid in linear response [155, 156].

Microreversibilty can be exploited to study separately normal and Andreev processes. To do so, we introduce two new quantities, $G^{\mathrm{ra}}$ and $G^{\mathrm{re}}$, both in the local and nonlocal versions, that we call *reciprocal conductances* and that can be extracted from the electric differential conductance matrix:

$$G_{\alpha\beta}^{\mathrm{ra}}(V,\mathbf{B}) \equiv G_{\alpha\beta}(V,\mathbf{B}) - G_{\beta\alpha}(+V,-\mathbf{B}) \tag{3.33}$$

$$G_{\alpha\beta}^{\mathrm{re}}(V,\mathbf{B}) \equiv G_{\alpha\beta}(V,\mathbf{B}) - G_{\beta\alpha}(-V,-\mathbf{B}) \tag{3.34}$$

By using microreversibility and particle-hole symmetry it is possible to show that

$$G_{\alpha\beta}^{\mathrm{ra}}(V,\mathbf{B}) = G_0 \int_{-\infty}^{+\infty} d\varepsilon \left[ -\partial_\varepsilon f(\varepsilon) \right] \left[ T_{\alpha\beta}^{he}(\varepsilon - eV,\mathbf{B}) - T_{\alpha\beta}^{he}(\varepsilon + eV,\mathbf{B}) \right], \tag{3.35}$$

$$G_{\alpha\beta}^{\mathrm{re}}(V,\mathbf{B}) = G_0 \int_{-\infty}^{+\infty} d\varepsilon \left[ -\partial_\varepsilon f(\varepsilon) \right] \left[ T_{\alpha\beta}^{ee}(\varepsilon - eV,\mathbf{B}) - T_{\alpha\beta}^{ee}(\varepsilon + eV,\mathbf{B}) \right], \tag{3.36}$$

where $G^{\mathrm{ra}}(V)$ is proportional to the antisymmetric part of the Andreev transmission probability while $G^{\mathrm{re}}(V)$ is proportional to the antisymmetric part of the normal electron transmission probability. For this reason, these two quantities can be used to analyze separately the two types of transport processes. Moreover, it can be verified from their definitions that these two quantities are the decomposition of the antisymmetric part of the local differential conductance:

$$G_{\alpha\beta}^{\mathrm{anti}} = G_{\beta\alpha}^{\mathrm{ra}} + G_{\beta\alpha}^{\mathrm{re}}. \tag{3.37}$$

The local versions, $G_{\alpha\alpha}^{\mathrm{re}}$ and $G_{\alpha\alpha}^{\mathrm{ra}}$ are proportional only to the antisymmetric part of the reflection probabilities. As mentioned before, if a lead is sufficiently isolated from the others such that there are no propagating channels connecting it to other leads, the reflection probabilities are bound to be energy-symmetric making the defined quantities null in absence of inelastic scattering.

The quantities (3.33), and (3.34) are the only symmetric or antisymmetric combinations of conductance matrix elements $G_{\alpha\beta}(V, \mathbf{B})$ that simplify to a difference of two transmission or reflection probabilities under the constraints imposed by unitarity [Eqs. (3.3) and (3.4)], particle-hole symmetry [Eq. (3.20)], and time-reversal symmetry [Eq. (3.31)]. Contrarily to PHS-derived conductance symmetries, the results in Eqs. (3.33) and (3.34) are not affected by dissipation since the derivation does not make use of the unitarity of the $S$ matrix.

Note that $\lim_{V \to 0} G^{\mathrm{ra}}(V) = 0$ in agreement with Onsager-Casimir relation. The vanishing of $G^{\mathrm{ra}}$ for normal (non-superconductive) devices can be explained as an extension of Onsager-Casimir relations beyond the linear-response regime.

## Additional antiunitary symmetry

Several widely used models in the context of proximitized devices, e.g., the Lutchyn-Oreg Hamiltonian describing a topological phase transition in a proximitized semiconductor nanowire [51, 52] satisfy an additional antiunitary symmetry $\mathcal{A} = U_{\mathcal{A}}\mathcal{K}$ aside from microreversibility that persists even in the presence of a Zeeman field. This symmetry implies additional constraints on the conductance matrix. In case the antiunitary symmetry is inherited from the normal state (i.e., it holds separately for electron and hole parts of the wavefunction), then the matrix $U_{\mathcal{A}}$ does not mix the particle-hole and lead indices. In this case, the symmetry condition for the scattering matrix can be written as

$$S(\mathbf{B}, \Delta_\nu) = U_{\mathcal{A}}^T S(\mathbf{B}, \Delta_\nu)^T U_{\mathcal{A}}^*. \tag{3.38}$$

As a consequence, the transmission probabilities satisfy the symmetry relations

$$T_{\alpha\beta}^{\gamma\delta}(\mathbf{B}, \Delta_\nu) = T_{\beta\alpha}^{\delta\gamma}(\mathbf{B}, \Delta_\nu), \tag{3.39}$$

The validity of this symmetry on the transmission probabilities is due to the block-diagonal structure of the unitary $U_{\mathcal{A}}$ combined with the definition of $T_{\alpha\beta}^{\gamma\delta}(\mathbf{B}, \Delta_\nu)$ in Eq. (3.1) that contains a trace over all single-lead indices that are present in the normal state.

In combination with PHS [Eq. (3.20)], we find

$$T_{\alpha\beta}^{\gamma\delta}(+\varepsilon, +\mathbf{B}, \Delta_\nu) = T_{\beta\alpha}^{\bar{\delta}\bar{\gamma}}(-\varepsilon, +\mathbf{B}, \Delta_\nu). \tag{3.40}$$

and, in particular for the Andreev transmission,

$$T_{\alpha\beta}^{eh}(+\varepsilon, +\mathbf{B}, \Delta_\nu) = T_{\beta\alpha}^{eh}(-\varepsilon, +\mathbf{B}, \Delta_\nu). \tag{3.41}$$

The combination with microreversibility in Eq. (3.31) instead gives

$$T_{\alpha\beta}^{\gamma\delta}(+\varepsilon, +\mathbf{B}, \Delta_\nu) = T_{\alpha\beta}^{\gamma\delta}(+\varepsilon, -\mathbf{B}, \Delta_\nu^*). \tag{3.42}$$

As a result, the *conductance magnetic asymmetry*, that we define as

$$G_{\alpha\beta}^{\mathrm{m}}(V, \mathbf{B}, \Delta_\nu) \equiv G_{\alpha\beta}(V, \mathbf{B}, \Delta_\nu) - G_{\alpha\beta}(V, -\mathbf{B}, \Delta_\nu^*). \tag{3.43}$$

vanishes.[2] Violations of this symmetry relation can be attributed to perturbations that break the antiunitary symmetry $\mathcal{A}$. This can be the result o, e.g., orbital effects or phase inhomogeneities.

---

[2]Note that for local quantities $G_{\alpha\alpha}^{\mathrm{m}} = G_{\alpha\alpha}^{\mathrm{ra}}$.

Similar considerations can be drawn for thermoelectric conductance. In the same fashion, we can define the *thermoelectric conductance magnetic asymmetry*

$$L_{\alpha\beta}^{\mathrm{m}}(V, \mathbf{B}, \Delta_\nu) \equiv L_{\alpha\beta}(V, \mathbf{B}, \Delta_\nu) - L_{\alpha\beta}(V, -\mathbf{B}, \Delta_\nu^*), \tag{3.44}$$

this quantity vanishes under the same assumptions.

Note that, in simpler systems like two-terminal metallic wires, the conductance is expected to be a symmetric function of the magnetic field. Therefore, the presence of a conductance magnetic asymmetry can be used as a probe of electron-electron interactions in the system [134]. In multiterminal superconductive devices instead, the symmetry is not expected even in the non-interacting system where the presence of the additional antiunitary symmetry is necessary to have a vanishing $G^{\mathrm{m}}$.

**Geometrical symmetries**

Geometrical symmetries of the device can also be exploited to build quantities that select only specific components of the transmission matrix. These can be useful in case the geometry of the system can be controlled to some degree of accuracy such that it may feature approximate geometrical symmetries.

For introducing a concrete example, let us consider a 2DEG wire like the one in Figs. 3.1(a) and 3.2(a). The wire is aligned along the $x$ direction, with two symmetric leads $L$ and $R$. Suppose the system is symmetric upon mirroring along the $x$ and $y$ directions, $\mathcal{M}_x$, and $\mathcal{M}_y$, and it features a rotation symmetry $\mathcal{R}_z(\pi)$. By using only $\mathcal{T}$, $\mathcal{P}$ and $\mathcal{M}_x$ symmetries we have

$$T_{RL}^{eh}(\varepsilon, B_x, B_y, B_z) \xrightarrow{\mathcal{T}\mathcal{P}\mathcal{M}_x} T_{RL}^{eh}(-\varepsilon, -B_x, B_y, B_z) \tag{3.45}$$

$$T_{RL}^{ee}(\varepsilon, B_x, B_y, B_z) \xrightarrow{\mathcal{T}\mathcal{M}_x} T_{RL}^{ee}(\varepsilon, -B_x, B_y, B_z) \tag{3.46}$$

and we can use this result to define new quantities similar to the reciprocal differential conductances, but with the advantage that is evaluated at only one lead and reversing only one component of the magnetic field

$$G_{LR}^{\mathrm{xa}}(V, \mathbf{B}) \equiv G_{LR}(V, B_x) - G_{LR}(V, -B_x), \tag{3.47}$$

$$G_{LR}^{\mathrm{xe}}(V, \mathbf{B}) \equiv G_{LR}(V, B_x) - G_{LR}(-V, -B_x). \tag{3.48}$$

By using Eqs. (3.45) and (3.46) it is possible to show that

$$G_{LR}^{\mathrm{xa}}(V, \mathbf{B}) = G_0 \int_{-\infty}^{+\infty} \mathrm{d}\varepsilon \left[-\partial_\varepsilon f(\varepsilon)\right] \left[T_{LR}^{he}(\varepsilon - eV, \mathbf{B}) - T_{LR}^{he}(\varepsilon + eV, \mathbf{B})\right] \tag{3.49}$$

$$G_{LR}^{\mathrm{xe}}(V, \mathbf{B}) = G_0 \int_{-\infty}^{+\infty} \mathrm{d}\varepsilon \left[-\partial_\varepsilon f(\varepsilon)\right] \left[T_{LR}^{ee}(\varepsilon + eV, \mathbf{B}) - T_{LR}^{ee}(\varepsilon - eV, \mathbf{B})\right], \tag{3.50}$$

Similarly, for the thermoelectric conductance, we have

$$L_{LR}^{\mathrm{x}}(\theta, B_x) \equiv L_{LR}(\theta, B_x) - L_{LR}(\theta, -B_x) \simeq 0. \tag{3.51}$$

Again, this quantity is exactly zero if we neglect the energies above the parent gap, and thus deviations at low temperatures can be directly linked to dissipation effects.

If a system featuring mirror symmetry satisfies an additional antiunitary symmetry as discussed in Sec. 3.2, then it follows that $G_{\alpha\beta}^{\mathrm{ra}} = 0$. In the absence of the additional antiunitary symmetry, the conductance symmetry $G_{\alpha\beta}^{\mathrm{ra}} = 0$ is present if the magnetic field lies in the plane orthogonal to the mirror symmetry axis. These properties can be used as an indication of whether the system satisfies mirror symmetry.

## 3.3 Additional antiunitary symmetry in a hybrid nanowire
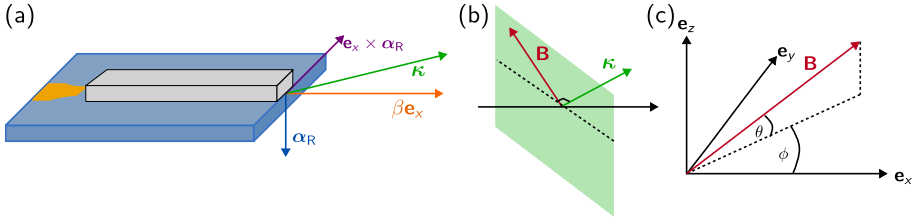


Fig. 3.2: **Sketch of a proximitized semiconductor nanowire with spin-orbit coupling.** In (a), using as a reference a simple 2DEG geometry, we introduce a Rashba field $\boldsymbol{\alpha}$ transverse to the nanowire direction $\mathbf{e}_x$ due to the interface electric field. The Rashba SOC manifests in a momentum-dependent spin splitting in the $\mathbf{e}_x \times \boldsymbol{\alpha}$ direction. A native Dresselhaus spin-orbit coupling can also be present; this acts as momentum-dependent $\mathbf{e}_x$ spin splitting. The combination of the two effects can be described by a generalized spin-orbit direction $\boldsymbol{\kappa}$ that defines an orthogonal plane shown in green in (b). When the magnetic field $\mathbf{B}$ lays in the orthogonal plane, the system features an additional antiunitary symmetry. In (c), we introduce a coordinate system to discuss the dependence of transport on the direction of the external magnetic field $\mathbf{B}$.

To introduce a concrete example application of the additional antiunitary symmetry discussed in Sec. 3.2, we now consider a quasi-1D semiconductor nanowire proximitized by a superconductor. An important question for these devices is the characterization of spin-orbit coupling. This can be achieved by leveraging the symmetry relations previously introduced.

We consider a system represented by the following low-energy effective Hamiltonian

$$\mathcal{H} = \left[ \frac{\hbar^2 \mathbf{k}^2}{2m^*} + V(\mathbf{r}) + \mathcal{H}_{\mathrm{SOC}} \right] \tau_z + \mathbf{b} \cdot \boldsymbol{\sigma} \tau_0 + \tilde{\Delta} \tau_x, \tag{3.52}$$

where $\mathbf{k} = -i\boldsymbol{\nabla}$ is the wavevector, $m^*$ is the effective mass, $V(x) = -\mu(x)$ is the potential landscape (which can include disorder), $\tilde{\Delta}$ is the proximity-induced pairing potential in the weak coupling limit, and $\mathbf{b}$ is the Zeeman spin splitting in the semiconductor. Finally, the spin-orbit coupling $\mathcal{H}_{\mathrm{SOC}} = \mathcal{H}_R + \mathcal{H}_D$ is the sum of the Rashba and the Dresselhaus term.

The Rashba interaction reads $\mathcal{H}_R = \mathbf{k} \times \boldsymbol{\alpha} \cdot \boldsymbol{\sigma}$ where the Rashba field $\boldsymbol{\alpha}$ is proportional to the electric field in the device. The Dresselhaus spin-orbit coupling arises from the lack of inversion symmetry of the material and can be written as $\mathcal{H}_D = \gamma_D \mathbf{l} \cdot \boldsymbol{\sigma}$. In zinc-blende crystals, the $\mathbf{l}$ vector components are $l_a = k_a(k_b^2 - k_c^2)$ where $(a, b, c)$ are cyclic permutations of the coordinates $(x, y, z)$ [104].

Here we consider a quasi-1D system in the $\mathbf{e}_x$ direction as shown in Fig. 3.2. For sufficiently thin wires with sufficiently energy-separated eigenmodes with different radial momenta, we can replace the radial momentum operators by their expectation values evaluated on the transverse eigenmode wave function $\mathbf{k} \simeq (k_x, \langle k_y \rangle, \langle k_z \rangle)$. Under this assumption, we can rewrite the Dresselhaus Hamiltonian as $\mathcal{H}_D = \gamma_D \sigma_x k_x \left[ -\langle k_z^2 \rangle + \langle k_y^2 \rangle \right] = \beta k_x \sigma_x$, while for the Rashba SOC, $\mathcal{H}_R = (\alpha_y \sigma_z - \alpha_z \sigma_y) k_x$, where a term $\langle \mathbf{k}_\perp \rangle \times \boldsymbol{\alpha}_\parallel \cdot \boldsymbol{\sigma}$ vanishes due to $\langle \mathbf{k}_\perp \rangle = 0$ for confined eigenmodes.

First, consider the case of pure Rashba spin-orbit coupling, i.e., $\gamma_D = 0$. The Hamiltonian satisfies an antiunitary symmetry when the magnetic field points within the plane spanned by the Rashba field $\boldsymbol{\alpha}$ and the direction of the wire. For $\boldsymbol{\alpha} = \alpha \mathbf{e}_z$, the antiunitary symmetry is complex conjugation, and the real-space Hamiltonian in Eq. (3.52) is real.

If the system features both Rashba and Dresselhaus spin-orbit coupling, the plane spanned by the magnetic fields that preserve an antiunitary symmetry is tilted. Without loss of generality, we choose a Rashba field perpendicular to the wire pointing along $z$, i.e., $\boldsymbol{\alpha}_\perp = \alpha_\perp \hat{e}_z$. We introduce a coordinate system for the magnetic field defined as $\mathbf{b} = b(\cos\theta\cos\phi, \cos\theta\sin\phi, \sin\theta)$ where $\theta$ is the elevation and $\phi$ the azimuth with respect to the wire direction. In this case, the spin-orbit coupling term reads $k_x(\alpha_\perp \sigma_y + \beta \sigma_x)$. A rotation $e^{i\phi_\kappa \sigma_z/2}$ in spin space by the angle $\tan\phi_\kappa = \frac{\beta}{\alpha_\perp}$ transforms $e^{-i\phi_\kappa \sigma_z/2} k_x (\alpha_\perp \sigma_y + \beta \sigma_x) e^{i\phi_\kappa \sigma_z/2} = k_x \sqrt{\alpha_\perp^2 + \beta^2}\, \sigma_y$. In this basis, spin-orbit coupling is real and the Hamiltonian satisfies $\mathcal{A} = \mathcal{K}$.

This antiunitary symmetry is preserved by a Zeeman field $\mathbf{b} = b_\perp \sigma_z + b_\parallel (\cos\phi_\kappa \sigma_x - \sin\phi_\kappa \sigma_y)$, such that $e^{-i\phi_\kappa \sigma_z/2} \left[ b_\perp \sigma_z + b_\parallel (\cos\phi_\kappa \sigma_x - \sin\phi_\kappa \sigma_y) \right] e^{i\phi_\kappa \sigma_z/2} = b_\perp \sigma_z + b_\parallel \sigma_x$ is real. Here, $\mathbf{b}_\perp$ is the component of the magnetic field parallel to $\boldsymbol{\alpha}_\perp$ and $\mathbf{b}_\parallel$ is the component pointing in the direction orthogonal to $\boldsymbol{\alpha}_\perp$ and $\beta\hat{x} + \alpha_\perp \hat{y}$. In other words, the combined Rashba and Dresselhaus spin-orbit coupling terms can be written as $\boldsymbol{\kappa} \cdot \boldsymbol{\sigma} k_x$ where $\boldsymbol{\kappa} = \mathbf{e}_x \times \boldsymbol{\alpha}_\perp + \beta\mathbf{e}_x$ is the generalized spin-orbit direction. The antiunitary symmetry is preserved by a Zeeman field $\mathbf{b} \cdot \boldsymbol{\kappa} = 0$. The plane spanned by the $\mathbf{b}$ vectors that satisfy the orthogonality condition can be identified by an angle $\phi_0 = \phi_\kappa + \pi/2$.

## 3.4 Numerical models

In this section, we introduce two numerical models to show examples of how microscopic symmetries of the systems manifest themselves in the transport properties. In both cases, we model the grounded leads in the system with the method of self-energies. This can be useful when the lead is a metal with high density compared to the scattering region as the self-energy takes the simple form of a local complex-valued potential. This is added to the Hamiltonian to generate an effective non-Hermitian energy-dependent Hamiltonian that can be studied with the scattering approach.

We consider the most general case of a grounded soft-gap superconductor that can be described by the Dynes superconductor model [157–159]. In the case of a superconductive lead with a high density of states, the intermediate coupling regime can be adequately described by the following local self-energy

$$\Sigma_\nu(\varepsilon, \mathbf{r}) = \gamma_\nu(\mathbf{r}) \frac{-(\varepsilon + i\Gamma_\nu)\tau_0\sigma_0 + \left(\Delta_\nu \tau_+ + \Delta_\nu^\dagger \tau_-\right)\sigma_0}{\sqrt{|\Delta_\nu|^2 \tau_0 \sigma_0 - [(\varepsilon + i\Gamma_\nu)\tau_0\sigma_0]^2}}\,, \tag{3.53}$$

where $\Delta_\nu = |\Delta_\nu| e^{i\phi_\nu}$ is the pairing amplitude with phase $\phi_\nu$ (that we assume constant in space), $\Gamma_\nu$ is the Dynes parameter that models pair-breaking scattering processes, the local coupling strength is $\gamma_\nu = \pi \mathcal{D}_\nu t_\nu^2$ with $\mathcal{D}_\nu$ being the density of states in the lead $\nu$, and $t_\nu$ is the interface hopping amplitude between the scattering region and the superconductive lead $\nu$. For a normal lead, this reduces to

$$\Sigma_n(\varepsilon, \mathbf{r}) = -i\gamma_n(\mathbf{r})\sigma_0\tau_0\,,\tag{3.54}$$

that is an imaginary potential that causes the decay of the quasiparticle wave function.

**Double-dot Josephson junction**

To study the effect of the additional antiunitary symmetry discussed in Sec. 3.2, we first consider a double-dot Josephson junction illustrated in Fig. 3.1. The effective Hamiltonian of the system is

$$\mathcal{H} = \begin{pmatrix} -\mu_1 & -t \\ -t & -\mu_2 \end{pmatrix} \tau_z \\ + \begin{pmatrix} 1 & 0 \\ 0 & 0 \end{pmatrix} \Sigma_1(\varepsilon) + \begin{pmatrix} 0 & 0 \\ 0 & 1 \end{pmatrix} \Sigma_2(\varepsilon)\tag{3.55}$$

where $\mu_i$ are the local chemical potentials in the dots, $t$ is the hopping amplitude between the dots, and $\Sigma_i$ are the local self-energies induced by the superconductive leads $i = 1,2$. The scattering matrix can be obtained by using the Weidenmüller formula (see, e.g., [160])

$$S(\varepsilon) = \mathbb{I} - 2\pi i W^\dagger \frac{1}{\varepsilon - \mathcal{H} + i\pi WW^\dagger} W\,,\tag{3.56}$$

where $W_i(E) \equiv \sqrt{\rho_i(\varepsilon)}\, t_i \Pi_i(\varepsilon)$ with $t_i$ the tunneling amplitude from the device to lead $i$, $\rho_i(\varepsilon)$ the density of states in lead $i$, and $\Pi_i(\varepsilon)$ the projector onto the eigenstates of lead $i$ at energy $\varepsilon$. In our model, we approximate the tunnel coupling between lead $L$ and dot 1 (lead $R$ and dot 2) by two energy-independent parameters, such that $W = \begin{pmatrix} w_L & w_R \end{pmatrix} \tau_z$.

When the phase difference between the two superconductive terminals $\phi_{12} = \phi_1 - \phi_2$ is zero or $\pi$, the system features the antiunitary symmetry $\mathcal{A} = \mathcal{K}$. As a consequence, the Andreev process probabilities are symmetric in the energy axis, i.e., $T^{eh}(\varepsilon) = T^{eh}(-\varepsilon)$, and $R^{eh}(\varepsilon) = R^{eh}(-\varepsilon)$. This can be verified by the zero in the conductance magnetic asymmetry $G^m$, as shown in the second column of Fig. 3.3.

The reciprocal conductance can also be used to verify the presence of a mirror symmetry of the device. A mirror symmetry $\mathcal{M}_x$ exchanges the two dots and reverses the sign of the phase difference $\phi_i \to -\phi_i$. The latter can be seen by noticing that the phase difference can be created by a magnetic field $B_z$ piercing a superconducting loop within the $x$-$y$-plane connecting to the two dots. This mirror symmetry implies a zero in the non-local reciprocal conductances $G^{ra}_{LR}$, $G^{ra}_{RL}$. Indeed, by calculating $G^{ra}_{LR}$ as a function of the dots' levels asymmetry $\delta\mu = (\mu_1 - \mu_2)/(\mu_1 + \mu_2)$ (see the rightmost column of Fig. 3.3), we verify the presence of a zero in $G^{ra}$ for $\delta\mu = 0$, that is when the system feature a mirror symmetry.

As a function of phase difference $\phi_{12}$, the symmetric configuration $\mu_1 = \mu_2$ exhibits a zero in the reciprocal conductances $G^{ra}_{LL}$, $G^{ra}_{LR}$ at $\phi_{12} = 0$ due to the mirror symmetry (c.f. the fourth column of Fig. 3.3). The zero in $G^{ra}_{LL}$, $G^{ra}_{LR}$ signals energy-symmetric Andreev reflection and transmission amplitudes [c.f. Eq. 3.33]. This mirror symmetry is broken at finite $|\phi_{12}| > 0$, including $\phi_{12} = \pi$, due to the different superconducting phase at the two dots.
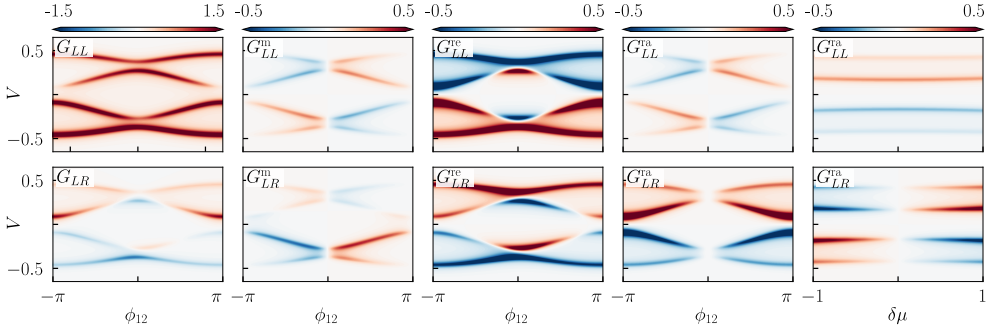
Fig. 3.3: **Conductance in double-dot Josephson junction.** The plots show the local conductance $G_{LL}$ and combinations $G_{LL}^{\mathrm{m}}$, $G_{LL}^{\mathrm{re}}$, $G_{LL}^{\mathrm{ra}}$ (top row, from left to right) and non-local conductance $G_{LR}$ and combinations $G_{LR}^{\mathrm{m}}$, $G_{LR}^{\mathrm{re}}$, $G_{LR}^{\mathrm{ra}}$ (bottom row, from left to right) in a double-dot Josephson junction as a function of the phase difference $\phi_{12} = \phi_1 - \phi_2$ for a symmetric configuration $\mu_1 = \mu_2$ (columns one to four). The rightmost column displays the reciprocal conductance $G_{LL}^{ra}$ for $\phi_{LR} = \pi/4$ as a function of the chemical potential asymmetry $\delta\mu = (\mu_1 - \mu_2)/(\mu_1 + \mu_2)$. The parameters used are $t = 0.2\,\mathrm{meV}$, $w_L^2 = w_R^2 = 0.01\,\mathrm{meV}$, $\mu_1 = \mu(1 + \delta\mu)$, $\mu_2 = \mu(1 - \delta\mu)$, $\mu = 0.10\,\mathrm{meV}$, $\gamma_1 = \gamma_2 = 0.3\,\mathrm{meV}$, $|\Delta_1| = |\Delta_2| = 1\,\mathrm{meV}$.

### Proximitized semiconductor nanowire

As an example of a three-terminal device, we consider the case of a semiconductor nanowire proximitized by an *s*-wave superconductor as shown in Fig. 3.4. We demonstrate how an antiunitary symmetry persisting at a finite magnetic field for specific directions can be employed to extract the ratio between Dresselhaus and Rashba spin-orbit coupling, as introduced in Sec. 3.3. We further study the effects of dissipation and voltage-bias-dependent potentials on the symmetry relations derived under CLA.

The Hamiltonian is similar to the one in Eq. (3.52), but here we treat the superconductive lead using the self-energy model

$$
\begin{aligned}
\mathcal{H}(\varepsilon) = & \left[ \frac{\hbar^2 k_x^2}{2m^*} + V(x) \right] \tau_z \\
& + \left[ (\alpha_y \sigma_z - \alpha_z \sigma_y) k_x + \beta k_x \sigma_x \right] \tau_z \\
& + \mathbf{b} \cdot \boldsymbol{\sigma} \tau_0 + \Sigma(\varepsilon),
\end{aligned}
\tag{3.57}
$$

where we take $m^* = 0.026 m_e$, consistent with an InAs nanowire, and $\Sigma(\varepsilon)$ is the superconductive lead self-energy as given in Eq. (3.53).

To include the effect of a finite bias, we model the deformation of the potential landscape in a simplified effective manner. Following an approach proposed by Ref. [140], we assume that the density of states in the superconductor shell is high enough to guarantee perfect screening of the electric field. This means that the potential drop falls entirely in the (depleted) barrier region. The case of imperfect screening is analyzed in Ref. [116].

To provide a gauge-invariant description of the potential landscape we select the voltage applied to the superconductor as the reference voltage $V_S = 0$ such that $\varepsilon = E_p - \mu_S = E_p + eV_S$

is the energy of the scattering particle. We define the left and right biases as $V_{LS}$ and $V_{RS}$. The other parameters that enter in the effective potential landscape are the chemical potential in the lead and the wire, that we define as $\mu_l = -e(V_l - V_S)$ and $\mu_w = -e(V_w - V_S)$, and the zero-bias barrier height $\Delta V_b = e(V_b - V_S)$. We assume the absence of built-in biases in the junction by considering a flat potential barrier at zero bias. The effect of the zero-bias barrier $\Delta V_b$ can be connected to a reduction of the coupling with the leads that causes a reduction of the height of the peaks and increased sharpness in the differential conductance. All these parameters are shown in the sketch of the landscape shown in Fig. 3.4. We modeled the effect of the finite bias as a linear voltage drop (i.e., a constant electric field) within the barrier, and we smoothed the potential using a sigmoid function instead of Heaviside steps to avoid sharp transitions between the different parts of the system.

We used a nanowire length of $L_w = 500\,$nm with barriers of length $L_b = 50\,$nm. The local chemical potential in the nanowire is set to $\mu_w = 0.5\,$meV while the zero-bias barrier height is set to $\Delta V_b = 0.3\,$meV. The lead have $\mu_l = 25\,$meV. For the superconductive lead, we set $\Delta = 0.35\,$meV and $\gamma_{Sc} = 0.2\,$meV. To simplify the evaluation of reciprocal conductance, we restrict the elevation angle $\theta \in [-\pi/2, \pi/2]$ while allowing the magnitude $b$ to take negative values. We discretized the Hamiltonian using the finite-differences method with step lengths $a_x = 1\,$nm, then evaluated the scattering matrix $S[\varepsilon, \mathcal{H}(\varepsilon; P)]$ using the `Kwant` package for quantum transport [161]. After evaluation of the $S$ matrix, the conductance is calculated for the CLA case following Eqs. (3.9)-(3.12), while in the nonlinear case, the electric charge current
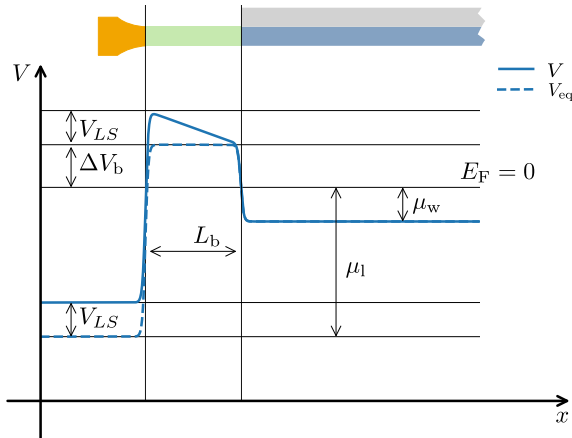


Fig. 3.4: **Sketch of one contact of a three-terminals device.** The monomodal wire (blue, green) is coated with a superconductive shell (gray), which induces a superconducting pairing potential in the central region and fixes the chemical potential due to the high density. Two barriers (quantum point contacts) are introduced on the side (green), while barrier gates can partially control the shape of the potential drop here. Two bias voltages are applied on the left and right leads (yellow) with respect to the grounded superconductor. In the lower panel, we sketch the potential landscape of the system $V(x)$ in the unbiased regime (dashed blue line) and biased one (solid blue line), showing all the quantities used to parametrize the potential landscape.

is calculated by numerical integration of Eq. (3.6).

**Identification of the spin-orbit coupling direction**

We first focus on the newly introduced quantities, reciprocal differential conductances and conductance magnetic asymmetry, and their use for the determination of the spin-orbit coupling direction. To emphasize the effect and maximize $G^{\mathrm{ra}}$, we consider a strongly asymmetric case in which the left barrier is set to $\Delta V_{\mathrm{b},L} = 0.3\,\mathrm{meV}$ while the right barrier is in the open regime $\Delta V_{\mathrm{b},R} = 0$. We also choose to align the Rashba field in the out-of-plane direction $\alpha_R = (0, 0, -10)\,\mathrm{meV\,nm}$ while we set the Dresselhaus energy to $\beta = 5\,\mathrm{meV\,nm}$.

A sweep in Zeeman energy $b$ is shown in Fig. 3.5. We find that $G^{\mathrm{re}}$ is much larger than $G^{\mathrm{ra}}$. By Eqs. (3.33) and (3.34), this indicates that the antisymmetric part of the electron-electron transmission probability dominates over the antisymmetric part of the crossed Andreev reflection probability. Note that in the presence of both mirror symmetry $\mathcal{M}_x$ (inverting the wire direction) and an antiunitary symmetry, the Andreev transmission probabilities are symmetric in energy such that $G^{\mathrm{ra}}_{LR}$ vanishes. For our device, in the presence of only Rashba SOC and a magnetic field oriented in the wire direction, a mirror-symmetric device satisfies an antiunitary symmetry $\mathcal{A} = \mathcal{K}$ and a mirror symmetry $\mathcal{M}_x = \sigma_x \tau_0$. Therefore, a signal in $G^{\mathrm{ra}}_{LR}$ is correlated to the mirror symmetry breaking terms in the device geometry, such as the asymmetric barrier configuration used here, and Dresselhaus spin-orbit coupling $\propto k_x \sigma_x$, breaking both the antiunitary symmetry and the mirror symmetry.
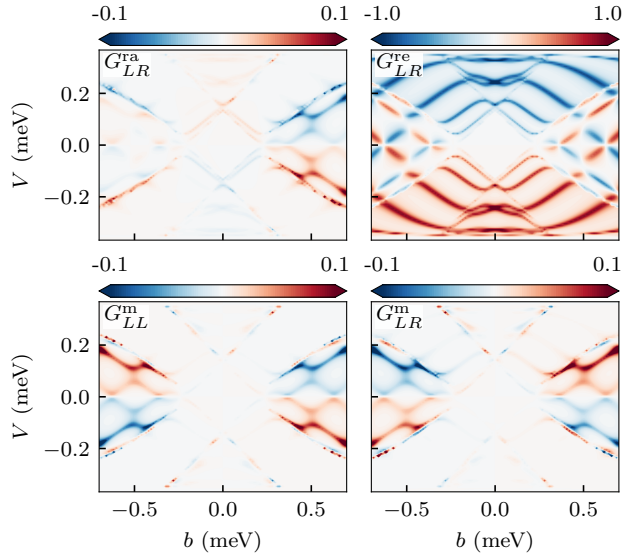


Fig. 3.5: **Reciprocal conductance and conductance magnetic asymmetry in a super-semi nanowire.** We show the typical signature of the reciprocal conductance and conductance magnetic asymmetry [Eqs. (3.33), (3.34), and (3.43)] for a proximitized semiconductor nanowire with Rashba spin-orbit coupling as a function of the Zeeman energy $b$. We set the direction of the magnetic field as $\theta = \frac{\pi}{4}$ and $\phi = 0$.

The reciprocal conductances $G^{\text{ra}}$ and $G^{\text{re}}$ can be used to characterize the spin-orbit coupling of the nanowire. Indeed both are symmetric under reversal of magnetic field only if the system satisfies an antiunitary symmetry that persists at a finite magnetic field. An alternative and easier measurement is the conductance magnetic asymmetry $G^{\text{m}}$, Eq. (3.43), since it requires the combination of only two differential conductances at the same terminal. This quantity vanishes if there is an antiunitary symmetry persisting at a finite magnetic field. Measuring this quantity while rotating the azimuth of the magnetic field allows for the identification of the direction of the generalized spin-orbit coupling vector $\mathbf{e}_\kappa$, as shown in Fig. 3.6.

The zero of the quantity $G^{\text{m}}(\phi = \phi_0) = 0$ is achieved only when the orthogonality condition $\mathbf{b} \cdot \boldsymbol{\kappa} = 0$ is satisfied. Therefore, with the measured set of directions for which $G^{\text{m}} = 0$ it is possible to determine $\mathbf{e}_\kappa$ and its relative angle with the wire direction $\phi_\kappa = \phi_0 - \pi/2$. With this information, it is possible to determine both the direction of the Rashba field and the ratio of the orthogonal Rashba and Dresselhaus SOC. The orthogonal Rashba field $\boldsymbol{\alpha}_\perp$ is oriented in the direction $\mathbf{e}_\kappa \times \mathbf{e}_x$ while the ratio of the two fields is connected to the angle by $\beta/\alpha_\perp = \tan(\phi_\kappa)$.

Note that $G^{\text{m}}(\phi)$ shows a linear behavior in $\phi$ near $\phi_0$ (marked by a change of sign in the neighborhood). In the simulations we noticed an additional zero in the direction $(\phi_\kappa, \theta_\kappa)$ that is $\boldsymbol{\kappa} \times \mathbf{b} = 0$. In this case, $G^{\text{m}}(\phi, \theta)$ has a quadratic behavior in both $\phi$ and $\theta$ in the neighborhood of $(\phi_\kappa, \theta_\kappa)$. Note that $\theta_\kappa = 0$ in the chosen coordinate system.

**Finite-bias effect and dissipation**

Transport symmetries can be also exploited to assess the presence of non-ideal effects and possibly distinguish between them. To illustrate the idea in this example system, we consider the dissipation and finite-bias effect. Indeed, in an ideal system the antisymmetric components of the local and nonlocal electrical differential conductance as a function of bias voltage are opposite to each other, such that $G_\alpha^{\text{sa}}(V) \equiv G_{LL}^{\text{anti}}(V) + G_{LR}^{\text{anti}}(V) = 0$ [c.f. Eq. (3.24)]. This is illustrated in Fig. 3.7.

This symmetry relation is broken by finite-bias effects, dissipation, and Coulomb scattering between quasiparticles. We verify the possibility of distinguishing between finite-bias and dissipation effects by calculating the quantity $G_L^{\text{sa}}$ in presence of these effects. We consider the same system as before in Sec. 3.4 with the only difference of considering symmetric barrier of $\Delta V_{\text{b}} = 30\,\mu\text{eV}$ and we set the Dresselhaus SOC $\beta = 0$.

First, we introduce the finite-bias effect by manually introducing the voltage drop in the barrier regions as shown in Fig. 3.4. The nonlinear differential conductance is then obtained by numerical differentiation of the total current calculated with Eq. (3.6). The comparison of the full-nonlinear theory and the CLA can be seen in Fig. 3.8. It is possible to distinguish two corrections, one general background correction in the local conductance that can be attributed to an increase in the average barrier height as the potential is raised. On top of this, we can identify a shift in the position of the peaks. The effect of a finite bias gets stronger and more evident as the barrier length is increased since the effect of the voltage drop is distributed in a greater area of the device.

To introduce dissipation, we compare two cases: in the first case we consider an additional normal lead acting as a quasiparticle reservoir described by a self-energy $\Sigma_{\text{Sm}}$ of the form Eq. (3.54) with parameter $\gamma_n$ describing the coupling strength between system and reservoir, while in the second case we introduce a soft gap in the superconductor through the parameter

$\Gamma_\nu = \Gamma_{\text{Sc}}$ in the Dynes model for the self-energy $\Sigma_{\text{Sc}}$ of proximity induced superconductivity, Eq. (3.53). Note that the first case has been already assessed in Ref. [150] for local conductance.

We consider two leads such that $\Sigma = \Sigma_{\text{Sc}} + \Sigma_{\text{Sm}}$. In the quasiparticle reservoir case we assume $\Gamma_{\text{Sc}} = 0$ and $\gamma_{\text{Sm}} = 5\,\mu\text{eV}$ while in the soft gap case $\Gamma_{\text{Sc}} = 5\,\mu\text{eV}$ while $\gamma_{\text{Sm}} = 0$.

The left and right plots in the top row of Fig. 3.9 shows, within CLA, the effect of a dissipation term in the wire Hamiltonian (setting $\gamma_{\text{Sm}} = 5\,\mu\text{eV}$, $\Gamma_{\text{Sc}} = 0$) and of inelastic scattering processes in the superconductor modeled with the Dynes model (setting $\gamma_{\text{Sm}} = 0$, $\Gamma_{\text{Sc}} = 5\,\mu\text{eV}$), respectively. The effects of the two dissipation terms are very similar and consistent with the result in Eq. (3.28). Therefore, it is not possible to distinguish between the two effects with this measurement. In the lower plots, nonlinear theory within perfect metallic screening approximation is considered. The effect of finite bias on the symmetry relation appears qualitatively different from dissipation also in this case. It can be described by a background contribution that depends on the sign of the applied voltage together with a localized correction in the position of the peaks. More strikingly, after the topological transition, there is no evident
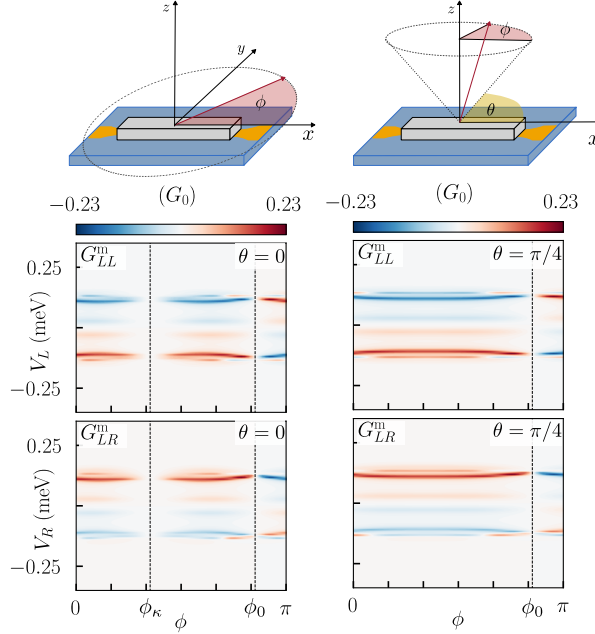


Fig. 3.6: **Identification of the spin-orbit orientation.** We show how local ($G_{LL}^{\text{m}}$) and nonlocal ($G_{LR}^{\text{m}}$) conductance magnetic asymmetry, Eq. (3.43), can be used to identify the spin-orbit coupling orientation by measuring these quantities while rotating the magnetic field, i.e. the angles $(\theta, \phi)$ in the reference frame introduced in Fig. 3.2. Both these quantities vanish linearly when the condition $\mathbf{b}_\perp \times \boldsymbol{\kappa} = 0$ is met. In the case shown, the Rashba spin-orbit coupling $\alpha_R$ is oriented in the $z$-direction and the relative strength of Dresselhaus over Rashba spin-orbit coupling is $\beta/\alpha_\perp = 1/2 = \tan(\phi_\kappa)$. Therefore $G^{\text{m}}$ vanishes only for the plane identified by the angle $\phi_0 = \phi_\kappa + \pi/2$ and is thus observed both in the case of $\theta = 0$ shown in the left panels and the case $\theta = \pi/4$ shown in the right ones.
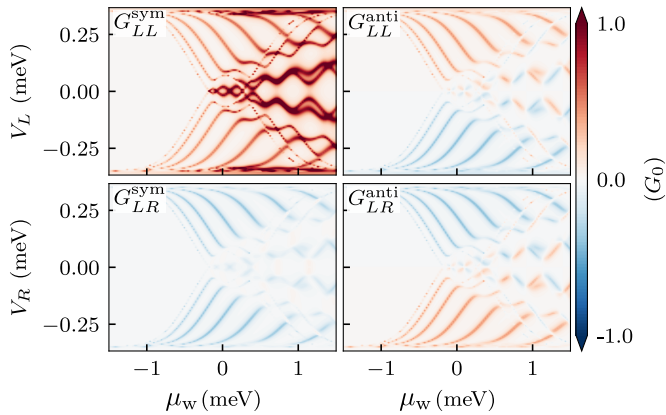
Fig. 3.7: **Symmetric and antisymmetric parts of electric differential conductance.** The antisymmetric parts of local and nonlocal electric conductance are opposite. This corresponds to the symmetry relation $G^{\text{sa}}(V) \equiv G_{LL}^{\text{anti}}(V) + G_{LR}^{\text{anti}}(V) = 0$ in ideal systems. Deviations from this symmetry relation can be used to identify non-ideal effects like dissipation or finite-bias effect.

oscillation in the sign connected to the local BCS charge like in the dissipation case. Therefore measurements of electrical conductance offer the possibility of distinguishing between the effect of finite bias and dissipation. These results are consistent with previous analyses [140, 150].

**Thermoelectric conductance**

The clear advantage of thermoelectric conductance is that temperature-induced charge accumulation, which leads to potential change modification, can be safely ignored in the regime of interest. Therefore it represents an alternative measurement free of problems related to the finite-bias effect. We stress here that by thermoelectric measurements we mean the measurement of the current as a change in the temperature of the leads. We note that for negligible inelastic scattering we expect no local thermalization, such that the device parameters should remain unchanged by the temperatures in the leads.

As in the case of electric differential conductance, we can define local and nonlocal thermoelectric conductance. These satisfy the symmetry relation

$$L_L^{\text{sum}}(\theta) = L_{LL}(\theta_L = \theta) + L_{LR}(\theta_R = \theta) \simeq 0 \tag{3.58}$$

if we restrict the integral over the energy to values below the parent gap region. The latter just introduces a non-exactly balanced background contribution. As can be seen in Fig. 3.10, the interesting features are the lobes with an oscillating sign at low temperatures. These features can be linked to the BCS charge $\langle \tau_z \rangle$ of the Andreev bound states at the end of the wire by a straightforward extension of the derivation using non-local electric conductance presented in Ref. [113].

Finite-bias effects can also affect the procedure for the determination of the spin-orbit coupling outlined in Section 3.4. The same information can be obtained by thermoelectric
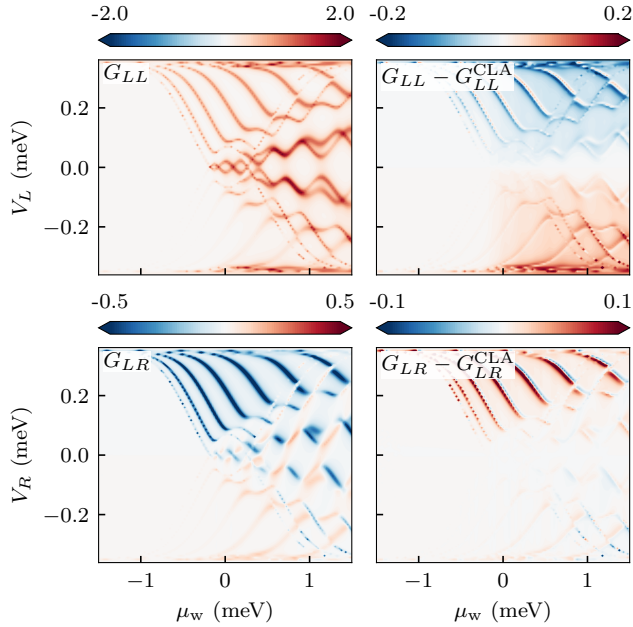
Fig. 3.8: **Electric differential conductance in the symmetric setup calculated with nonlinear theory and correction to differential conductance in CLA.** It is possible to distinguish two contributions. One general background correction in the local conductance that can be attributed to an increase in the average barrier height as the potential is raised. On top of this, we can identify a correction that moves and changes the position of the peaks. The finite-bias effect gets stronger and more evident as the barrier length is increased. In this simulation, $V_{b,L} = 30\,\mu\text{eV}$, $V_{b,R} = 30\,\mu\text{eV}$, $\beta = 0$, while we set the Zeeman field to $\mathbf{b} = (1, 0, 0)\,40\,\mu\text{eV}$.

measurements by evaluating the thermoelectric conductance magnetic asymmetry $L^{\text{m}}$ while rotating the magnetic field as shown in Fig. 3.11. As expected, when the magnetic field lies in the plane orthogonal to the generalized spin-orbit coupling vector $\boldsymbol{\kappa}$, identified by the angle $\phi_0$, we observe a zero in $L^{\text{m}}$. In contrast to the electric conductance combination, $G^m_{\alpha\beta}$, the thermoelectric conductance combination $L^m_{LR}$ displays a quadratic behavior in $\phi$ around $\phi_0$ at the magnetic field angle $\theta = \pi/4$. Also for $L^m$ we observe an additional quadratic zero at $(\phi_\kappa, \theta_\kappa)$, i.e. when $\boldsymbol{\kappa} \times \mathbf{b} = 0$.

## 3.5 Summary

We have explored the limits of local and nonlocal tunneling spectroscopy of hybrid devices within the extended Landauer-Büttiker formalism. We have derived symmetry constraints on the multiterminal conductance matrix that follow from the fundamental microreversibility and particle-hole conjugation in the presence of superconductivity. Our first result shows that the reciprocal conductances $G^{\text{ra}}$ and $G^{\text{re}}$, defined in Eqs. (3.33) and (3.34), can be employed to extract the antisymmetric-in-voltage parts of the individual electron and Andreev transmission

and reflection probabilities.

In the presence of an additional antiunitary symmetry that persists at a finite Zeeman field, a further relation can be derived for the conductance magnetic asymmetry $G^{\mathrm{m}}$ in Eq. (3.43). This relation is particularly useful in the study of spin-orbit coupled semiconductor nanowires proximitized by an $s$-wave superconductor since it allows extracting the ratio between the Rashba and Dresselhaus spin-orbit coupling strength. We have demonstrated this result in an explicit numerical model. This result may be useful for material and device characterization because the characterization of the spin-orbit coupling in proximitized semiconductor devices is an open research question. Future work can study these quantities in a more realistic scenario, modeling the cross-section of the superconductor-semiconductor heterostructure to include multiple transverse modes and the orbital coupling of the magnetic field.
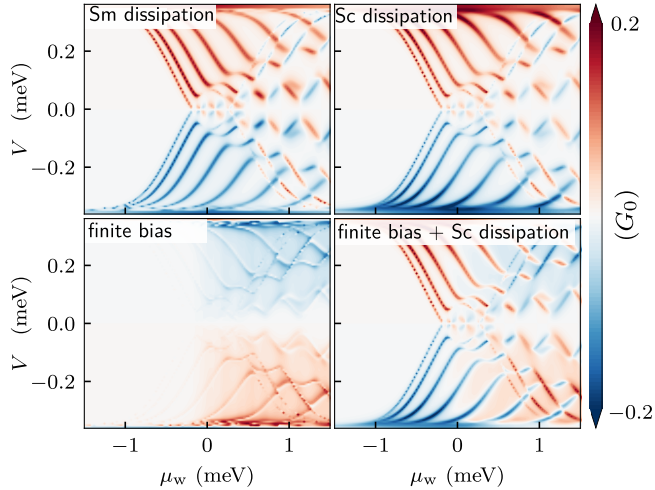


Fig. 3.9: $G_L^{\mathrm{sa}}$ **when different symmetry-breaking mechanisms are introduced.** In the upper plots, two distinct dissipation terms are considered within CLA, in the left $\gamma_{\mathrm{Sm}} = 5\,\mu\mathrm{eV}$ while in the right one $\Gamma_{\mathrm{Sc}} = 5\,\mu\mathrm{eV}$. The lower plots shows the same quantity calculated using the nonlinear theory on the left $\gamma_{\mathrm{Sm}} = 0$ while on the right $\Gamma_{\mathrm{Sc}} = 5\,\mu\mathrm{eV}$.
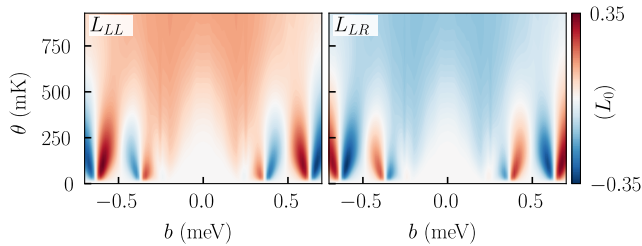


Fig. 3.10: **Local and nonlocal thermoelectric conductance in a proximitized semiconductor nanowire.** The low-temperature lobes with alternating signs can be associated with the BCS charge $\langle \tau_z \rangle$ similarly to the interpretation of $G^{\mathrm{anti}}$.

Furthermore, we have studied the effects of dissipation and the dependence of the electric potential on the bias voltage on the symmetry relations at an explicit model of a proximitized semiconductor nanowire. Generally, these symmetry relations are broken by these non-idealities. However, the two effects yield distinct signatures in the conductance matrix elements and their linear combinations.
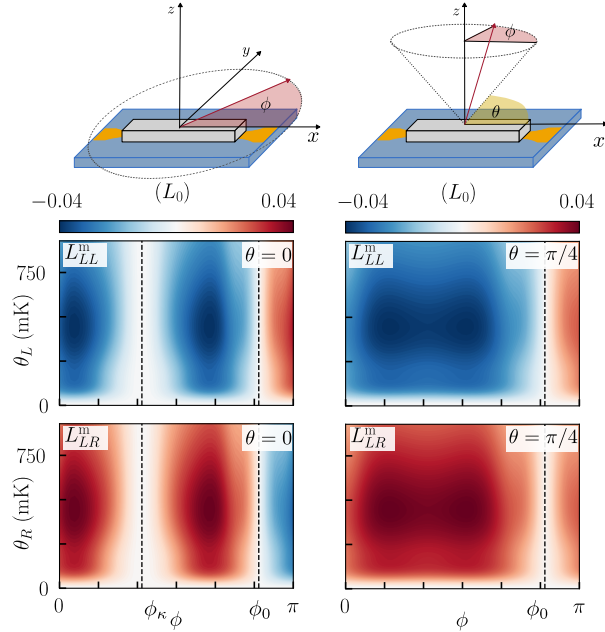


Fig. 3.11: **Identification of the spin-orbit orientation by thermoelectric measurements.** We show how local ($L_{LL}^{\mathrm{m}}$) and nonlocal ($L_{LR}^{\mathrm{m}}$) thermoelectric conductance magnetic asymmetry can be used to identify the spin-orbit coupling orientation by measuring these quantities while rotating the magnetic field, i.e. the angles $(\theta, \phi)$ in the reference frame introduced in Fig. 3.2. Both these quantities vanish when the condition $\mathbf{b}_\perp \times \boldsymbol{\kappa} = 0$ is met. In the case shown, the Rashba spin-orbit coupling $\alpha_R$ is oriented in the $z$-direction while $\beta/\alpha_\perp = \tan(\phi_\kappa) = 1/2$. Therefore $L^{\mathrm{m}}$ vanishes only for the plane identified by the angle $\phi_0 = \phi_\kappa + \pi/2$ and is thus observed both in the case of $\theta = 0$ shown in the left panels and the case $\theta = \pi/4$ shown in the right ones. The parameters are the same as Fig. 3.6.

# Ferromagnetic hybrid heterostructures

At the end of Ch. 1, we outlined the general idea behind the Lutchyn-Oreg proposal of synthetic topological superconductivity in hybrid heterostructures. One limitation of this approach is the requirement of external magnetic fields to induce the topological phase transition. External magnetic fields have several drawbacks. Primarily, it is complicated to separate their effect in spin-space, the Zeeman interaction, from their orbital effects, like the suppression of the superconducting pairing, among others. Secondarily, the topological phase is very sensitive to the relative orientation between the magnetic and the spin-orbit fields. This problem becomes even more evident when considering more complicated geometries featuring several nanowires that cannot be aligned in the same direction. This set strict constraints on the design of experiments, like the ones proposed to demonstrate non-Abelian statistics [42, 162–164], and, ultimately, for topological quantum devices.

Several alternatives to the use of an external magnetic field have been proposed in recent years, like devices based on magnetic flux through full-shell nanowires [165–167], and the phase difference in superconducting junctions [93, 168, 169]. However, these alternatives face challenges with device scaling, including sensitivity to magnetic field direction in the former and difficulty in controlling phase differences among multiple superconductors in the latter.

Magnetic insulators offer an alternative approach to solve the above problems by inducing a local exchange field on the semiconductor through the ferromagnetic proximity effect, eliminating the need for external magnetic fields. This idea has gained momentum from recent developments in the fabrication technology that have enabled the integration of thin layers of the ferromagnetic insulators EuS in the hybrid InAs-Al heterostructures with excellent interface quality [170–172]. This material has also been tested in combination with gold, showing signatures consistent with the presence of Majorana bound states [173]. In addition, experiments in hexagonal nanowires partially covered by overlapping superconductors and ferromagnetic insulator shells showed the appearance of zero-bias conductance peaks [73], and spin-polarized subgap states [174].

The same platform has also been considered for the fabrication of Josephson junctions. Initial experiments have observed a configurable supercurrent reversal in ferromagnetic nanowire-based Josephson junctions [P6]. The subsequent theoretical analysis focused on the possibility of further controlling the current-phase relation in these structures and achieving nonsinusoidal Josephson potentials [P7].

This chapter is devoted to introducing the physics of such *ferromagnetic hybrid heterostructures*. We will briefly introduce ferromagnetic insulators and the ferromagnetic proximity effect in Sec. 4.1, while the main experimental features of the platform are outlined in Sec. 4.2. The applications to topological superconductivity are discussed in Sec. 4.3 and Sec. 4.4. The physics of ferromagnetic hybrid Josephson junctions is investigated first in experiments, Sec. 4.5 and then in an abstract theoretical setting in Sec. 4.6. The chapter is concluded with a summary of the research activity on the topic, Sec. 4.7

## 4.1 Magnetic insulator and magnetic proximity effects

Magnetic insulators are a class of dielectric materials that display a magnetic order. Many transition metal oxides belong to this category, and, in the majority of cases, these materials show an antiferromagnetic order. These materials can be described by spin models that are a generalization of the Heisenberg model. In the case of ferromagnetic insulators, where the

spins tend to align, it is possible to define classical field theories, known as micromagnetic theories, that describe the configuration of the system in terms of a local magnetization vector $\mathbf{M}(\mathbf{r}) = M_s \mathbf{m}(\mathbf{r})$ where $M_s$ is the saturation magnetization, which is homogenous in the material and depends only on the temperature, while $\mathbf{m}(\mathbf{r})$ is the micromagnetic configuration of the system [175–179].

In the following, we will avoid introducing an additional layer of complexity in the description of these systems, and we will simply consider effective models that focus on the effect of the ferromagnetic insulator on the rest of the device. We will seldom refer to the micromagnetic configuration of the ferromagnet, albeit it is important to be aware of this aspect of the system.

Practically, when explicitly included in the model, the ferromagnetic insulator will be treated as a semiconductor with an intrinsic exchange field $\mathbf{h}(\mathbf{r})$ that describes the spin-split conduction band. In other cases, we want to remove the ferromagnetic insulator entirely from the model domain. In this case, we will resort to an *effective exchange field* that arises from the ferromagnetic proximity effect. The definition of such effective fields is not obvious and will be a recurring theme in this chapter.

In the limit of a strongly insulating material, we can imagine that the main interaction is due to the scattering between the electrons of the proximitized material and the localized magnetic moments in the ferromagnet. We can describe the effect of the interface through a Heisenberg-like term

$$H_{\text{FIprox}} = -J^{\text{p}} \sum_i \int \mathrm{d}^3 \mathbf{r} \, \mathbf{S}_i \cdot \mathbf{s}(\mathbf{r}_i) \delta(\mathbf{r} - \mathbf{R}_i) \tag{4.1}$$

which describes the coupling between the spin density of the free electron in a material, $\mathbf{s}$, and the localized spins in the insulator, $\mathbf{S}_i$, considered as fixed classical magnetic moments. The coupling strength $J^{\text{p}}$ is related to the exchange integral between the localized orbitals and the free electron. This coupling strength is different for the conduction band electrons of the ferromagnetic insulator (that is depleted in this case) and the electrons in the proximitized material [180]. In this case, the ferromagnetic insulator does not appear explicitly in the model, but its effect is included in the form of an effective surface exchange field $\mathbf{h}_{\text{eff}}$ that couples to the spin degree of freedom of the electrons. Such an exchange field can be thought proportional to the local micromagnetic configuration of the ferromagnetic insulator and is defined only at the interface of the ferromagnetic insulator with another material.

With this picture in mind, let us move to the case of proximity-coupled ferromagnetic insulator-superconductor heterostructures. After the first experiments [181, 182], a general theory of ferromagnetic proximity effects has been proposed by Millis and Tokuyasu [183, 184]. In particular, Tokuyasu's theory predicts that the effect of the magnetic insulator can be described to some extent by an induced exchange field in the superconductor $\mathbf{h}_{\text{eff}}$. This field decays away from the interface in a length scale comparable to the coherence length of the superconductor. This simple description in terms of an induced exchange field is valid in most cases addressed, and the effects are equivalent to the spin-split superconductor described in Sec. 1.2. Many subsequent experimental works have verified a strong effect of ferromagnetic insulators on thin superconductors that resembles the one of a Zeeman-split superconductor by a strong magnetic field and can thus be adequately described by an effective exchange field [185–187]. Other features of the density of states can be described by additional spin-flip terms that arise from inhomogeneous magnetization pattern, magnetic disorder at

the interfaces [188–190], and also spin-orbit scattering, which, although small, is not always negligible even for low atomic number materials such as Al [191].

## 4.2 The InAs-Al-EuS platform

One of the most successful experimental platforms for the investigation of ferromagnetic proximity effects in superconductors are heterostructures made of aluminum (Al) and europium (Eu) compounds like EuO and EuS. Europium sulfide (EuS) was extensively studied along with other members of the group of magnetic semiconductors known as the europium chalcogenides during the 1960s after europium oxide (EuO) was found to be a ferromagnetic insulator [192, 193]. These early studies revealed that the magnetic properties in these compounds arise from the interaction between the well-localized half-filled $4f$ orbitals of the $Eu^{2+}$ ions and their interactions with the conduction electrons. The electrons in these shells behave as localized spins with a magnetic moment of around 7 $\mu_B$, making EuS one of the few materials that are well described by the Heisenberg model. The low Curie temperature of $T_C = 16.6\,K$ [194, 195] makes it unattractive for potential application in room-temperature electronics, but this is not concerning for scientific exploration in low-temperature physics.

Optical absorption and photoemission measurements determined that the energy gap, $E_g$, between the occupied valence band and the unoccupied conduction band in EuS is 3.1 eV. Photoemission spectroscopy, however, measures 1.7 eV emission line, which is interpreted as the photo-excitation of $4f$ states to the conduction band [196]. In EuS-Al hybrids, a polarization of around 50% of the bare Al gap has been found in experiments [185–187, 197, 198].
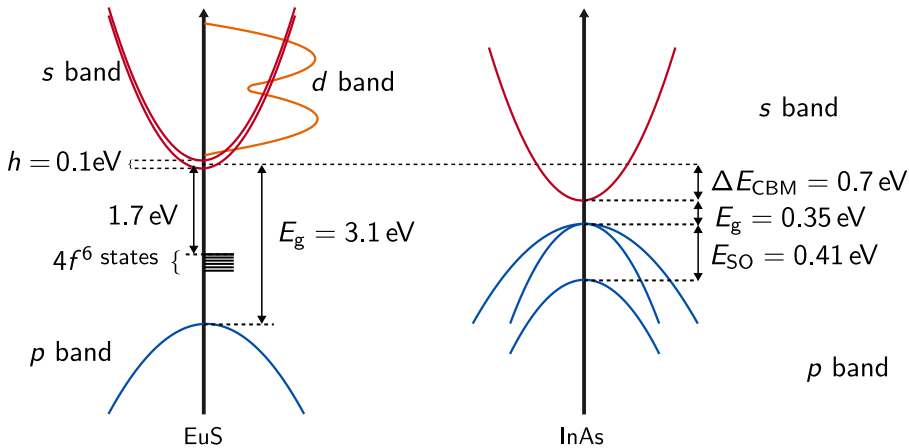


Fig. 4.1: **Band structure of EuS-InAs hybrids.** On the left, a sketch of the band structure of EuS shows the relative position of the conduction and valence bend with respect to the localized $4f^6$ states responsible for the compound's magnetic properties. On the right, a sketch of the band structure of InAs shows the difference in the band gap of the two materials explaining the insulating behavior of EuS at low temperatures.

EuS crystallizes in the face-centered cubic lattice, with a lattice parameter of around 5.97 Å, which has only 1% lattice mismatch with InAs, making it a perfect candidate for epitaxial

growth. Early efforts to integrate EuS with III-V semiconductors were made for spintronics applications, yielding positive results for both GaAs [199–201] and also InAs [171, 193, 202]. A tricsystalline EuS-InAs-Al heterostructure, both in the VLS and SAG nanowires, has been demonstrated two years later [170, 172]. These features a complex epitaxial matching of wurtzite and zinc-blende InAs/rock-salt EuS interfaces as well as rock-salt EuS/face-centered cubic Al interface. The stray field of both VLS and SAG nanowires was studied with SQUID measurements of the stray field. The study reported a strong dominant shape anisotropy, with a stray field pointing along the wire and taking the maximum value at the edge of the wire.

Analysis of the interfacial InAs-EuS band alignment revealed that the Fermi level lays close to the InAs conduction band while being in the band gap of EuS and far from the localized $4f$ states. This causes the EuS to behave as an insulator at the low temperatures considered [170].

The induction of an exchange field in a semiconductor is not an obvious effect because of the low density of carriers. Indeed, suppression of ferromagnetic order in the Eu layers closer to the interface has been detected in InAs-EuS hybrids by both neutron and X-ray reflectivity measurements [170]. This behavior is consistent with microscopic simulations of EuS-InAs interface [203] that predict a low level of induced exchange field. This can be a great obstacle that poses some constraints to the geometry of devices designed to leverage the direct ferromagnetic proximity effect in the semiconductor. However, the spin-polarizing effect in out-of-equilibrium situations in which a current flows *through* the EuS has been reported in experiments [193].

## 4.3 Mechanisms for topological superconductivity

In experiments with ferromagnetic hybrid nanowires, spectroscopic measurements have shown the onset of a zero-bias conductance peak, which has been interpreted as a signature of localized Majorana zero modes at their ends [73]. This signature has been detected only when the Al and the EuS layers overlap, Fig. 4.2(a). Samples with non-overlapping facets, Fig. 4.2(b), have shown no signatures of zero-energy modes. This behavior is in contrast with expectations that the main effect of EuS is to induce an exchange field in the semiconductor. The discrepancy has sparked an intense theoretical discussion of the possible mechanism for topological superconductivity in these structures. In this next section, we will provide an argument against the hypothesis of a superconductor-mediated ferromagnetic proximity effect, subject of Ref. [P1], and we will compare this result with other analyses from other groups.

Because of the lack of evidence of spin-polarization in samples with non-overlapping facets, a direct proximity effect from the EuS to the InAs has to be excluded, or at least, it is not sufficient to induce a topological transition. Another consequence of such a strikingly different behavior is that we can exclude a strong influence of the stray field in the physics of the device. Indeed, we can expect the magnetic fields in the two settings, overlapping and non, to be comparable. For this reason, in the initial interpretation of the results, it was proposed that the proximity mechanism is indirect, meaning that the EuS proximitizes the Al, inducing an exchange field, as this effect has been extensively demonstrated in the past as discussed in the previous section. In turn, the Al induces both superconductivity and an exchange field in the semiconductor InAs, causing the topological transition.

In the following, we compare the two different situations. In the first case, the only ferromagnetic proximity effect in the device is mediated by the superconductor, which is spin-split
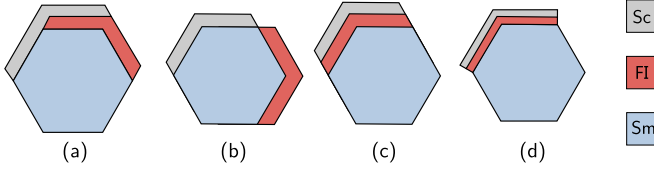
Fig. 4.2: **Cross sections of possible designs for ferromagnetic hybrid hexagonal nanowires.**
The picture shows four different possible arrangements of the superconductor (Sc) and ferromagnetic insulator (FI) on top of a VLS semiconductor nanowire (Sm). The designs with partially overlapping facets in (a) and non-overlapping facets in (b) have been reported in experiments [P6, 73, 170, 172, 174]. The hypothetical setup (c) is shown to display an example situation where the only ferromagnetic proximity effect in the semiconductor is mediated by the superconductor, while the setup with completely overlapping facets in (d) has only been proposed in Ref. [P1]

by the ferromagnetic proximity effect and, in turn, induces both a pairing potential and an effective exchange field in the semiconductor. This case corresponds to the hypothetical situation displayed in Fig. 4.2(c). It has also been considered as the main mechanism in the situation of Fig. 4.2(a), in the case a thick ferromagnetic insulator layer is placed in between the two materials such that the tunneling through the insulator is strongly suppressed.

In the second case, we consider an alternative explanation: a tunneling mechanism that is spin-polarized. This is valid in the case of completely overlapping facets in Fig. 4.2(d) or in partially overlapping, Fig. 4.2(a) when the ferromagnetic insulator is thin.

To assess the validity of these two hypotheses, we now introduce a minimal model for the system. We consider a translation-invariant wire consisting of a single-channel semiconductor coupled to a superconductor shell. The Hamiltonian of the system reads as

$$H = H_{\text{Sm}} + H_{\text{Sc}} + H_{\text{t}}. \tag{4.2}$$

The semiconductor wire is described by

$$H_{\text{Sm}} = \sum_{p_z} \left( \frac{p_z^2}{2m_{\text{Sm}}} - \mu_{\text{Sm}} \right) c_{p_z}^\dagger \sigma_0 c_{p_z} + \alpha_x p_z c_{p_z}^\dagger \sigma_y c_{p_z}, \tag{4.3}$$

where we use the spinors $c_{p_z} = (c_{p_z\uparrow}, c_{p_z\downarrow})$ and $c_{p_z\sigma}$ is the electron annihilation operator in the semiconductor, while $\alpha_x$ is the spin-orbit coupling strength.

The bare Hamiltonian for the superconductor shell is given by

$$H_{\text{Sc}} = \sum_{np_z} \xi_{np_z} a_{np_z}^\dagger \sigma_0 a_{np_z} + a_{np_z}^\dagger \mathbf{h} \cdot \boldsymbol{\sigma} \, a_{np_z} + \left( a_{np_z}^\dagger \boldsymbol{\Delta}_{np_z} i\sigma_y a_{n-p_z}^\dagger + \text{H.c.} \right), \tag{4.4}$$

where $a_{np_z}$ is the electron annihilation operator for the mode $n$ in the superconductor and $\xi_{np_z} = \frac{p_z^2}{2m_{\text{Sc}}} + \varepsilon_n - \mu_{\text{Sc}}$. We neglect the possible superconductive interband coupling, and we assume singlet pairing in the parent superconductor gap matrix $\boldsymbol{\Delta}_{np_z} = \Delta_{0,np_z}\sigma_0$. We model the effect of the ferromagnetic insulator by a homogeneous exchange field $\mathbf{h}$, which we consider to be aligned to the wire.

In our model, we consider a relatively clean superconductor shell with a well-defined distribution of the transverse modes, $\varepsilon_n$, which strongly depends on the device geometry. Depending on the cross-section of the shell, the separation between transverse modes can range from a value larger than the superconducting gap to zero for a bulk superconductor, where the modes above the gap form a continuum. The two regions are coupled by a momentum-conserving tunneling Hamiltonian

$$H_{\mathrm{t}} = \sum_{n p_z} \left( -c_{p_z}^\dagger T_{n p_z} a_{n p_z} + \mathrm{H.c.} \right), \tag{4.5}$$

where the hopping matrix $T_{n p_z} = t_{0,n p_z}\sigma_0 + t_{z,n p_z}\sigma_z$ describes the electron tunneling processes taking place at the interfaces between the two materials.

To analyze the effect of the spin-split superconductor, we analyze the shell self-energy $\Sigma(\omega, n, p_z) = \sum_n T_{n p_z} G_{\mathrm{Sc}}^R(\omega, n, p_z) T_{n p_z}^\dagger$ where the bare superconducting shell retarded Green's function in the basis of time-reversed pairs reads:

$$G_{\mathrm{Sc}}^R(\omega, n, p_z) = \left[ (\omega + i0^+)\tau_0\sigma_0 - \xi_{n p_z}\tau_z\sigma_0 - \Delta_{n p_z}\tau_x\sigma_0 - h_z\tau_0\sigma_z \right]^{-1}, \tag{4.6}$$

As a simplifying assumption, we ignore any back action of the semiconductor on the superconductor as the electron density in the semiconductor is orders of magnitude smaller than the one in the superconductor.

Since we focus on the quantum phase transition characterized by the gap closing, we work with the effective Hamiltonian $H_{\mathrm{eff}} = H_{\mathrm{Sm}} + \tilde{H}_0$ where the induced Hamiltonian is $\tilde{H}_0 = \Sigma(\omega = 0)$. We can split the effective Hamiltonian into three different contributions:

$$\tilde{H}_0 = \sum_{p_z} c_{p_z}^\dagger \tilde{\mu}(p_z)\sigma_0 c_{p_z} + c_{p_z}^\dagger \tilde{h}_z(p_z)\sigma_z c_{p_z} + \left( c_{p_z}^\dagger \tilde{\Delta}_0(p_z) i\sigma_y c_{-p_z}^\dagger + \mathrm{H.c.} \right), \tag{4.7}$$

These three terms describe the shift in the chemical potential, which can be neglected, the induced exchange field, and the induced superconducting gap matrix in the semiconductor. The explicit forms of these contributions are

$$\tilde{h}_z^{(1)}(p_z) = \sum_n \frac{h_z(t_{0,n p_z}^2 + t_{z,n p_z}^2)}{\xi_{n p_z}^2 + \Delta_{0,n p_z}^2 - h_z^2}, \tag{4.8}$$

$$\tilde{h}_z^{(2)}(p_z) = \sum_n \frac{-2\xi_{n p_z} t_{z,n p_z} t_{0,n p_z}}{\xi_{n p_z}^2 + \Delta_{0,n p_z}^2 - h_z^2}, \tag{4.9}$$

$$\tilde{\Delta}_0(p_z) = \sum_n \frac{\Delta_{0,n p_z}(t_{0,n p_z}^2 - t_{z,n p_z}^2)}{\xi_{n p_z}^2 + \Delta_{0,n p_z}^2 - h_z^2}, \tag{4.10}$$

where we have divided the induced exchange field into two contributions $\tilde{h}_z = \tilde{h}_z^{(1)} + \tilde{h}_z^{(2)}$. The first one is proportional to the splitting in the parent superconductor (4.8), while the second one is linked to the spin-asymmetric tunneling amplitude of the barrier $t_z$ (4.9). We assume that the parent superconductor pairing potential is constant along $p_z$ and is also approximately constant for each band, even if different from the bulk value, $\Delta_{0,n p_z} = \Delta_0$.

**Topological superconductivity through indirect exchange coupling**

Under the superconductor-mediated ferromagnetic proximity effect hypothesis, the ferromagnetic insulator induces a spin splitting in the superconductor. The superconductor, in turn, induces superconductivity and an exchange field in the semiconductor. To check the presence of topological phases, we calculate the ratio between the induced exchange field, $\tilde{h}_z$, and the gap, $\tilde{\Delta}_0$. The topological phases appear when the condition in Eq. (1.94) is met, which leads to a closing of the superconducting gap at $p_z = 0$. For this reason, we focus on this point in momentum space in the following. A necessary condition to satisfy the inequality is having $\left|\tilde{h}/\tilde{\Delta}_0\right| > 1$.

Taking the ratio of Eqs. (4.8) and (4.10) for $t_z = 0$, we see that

$$\left|\frac{\tilde{h}_z}{\tilde{\Delta}_0}\right| = \left|\frac{h_z}{\Delta_0}\right| < \frac{1}{\sqrt{2}}, \tag{4.11}$$

so the induced $\left|\tilde{h}/\tilde{\Delta}_0\right|$ ratio in the semiconductor is the same as in the superconductor and thus needs to fulfill the Chandraskear-Clogston limit, Eq. (1.48), otherwise, superconductivity is suppressed in the whole device. This result is independent of the mode distribution in the superconductor within the constant $\Delta_0$ and $t_z$ approximation. If we allow the pairing potential to be different in each mode, the induced $\left|\tilde{h}/\tilde{\Delta}_0\right|$ ratio could take any value in the range of $\left[\min(h_z/\Delta_{0,n}), \max(h_z/\Delta_{0,n})\right]$ depending on the coupling terms $T_n$. For a gapped superconductor, all the modes close to the Fermi level fulfill $\Delta_{0,n} > h_z$. With this constraint, it is still not possible to get topological superconductivity in a semiconductor coupled to a spin-split superconductor through a spin-symmetric tunnel barrier.

We have demonstrated that a spin-split superconductor cannot induce topological superconductivity in a spin-orbit coupled semiconductor by the combined superconducting and magnetic proximity effect. This is in contradiction with the superconductor-mediated ferromagnetic proximity effect hypothesis.

**Spin-dependent tunneling**

We consider now the case of spin-asymmetric tunneling between the superconductor and the semiconductor, taken as momentum independent for simplicity and described by $T = t_0 \sigma_0 + t_z \sigma_z$. As Eqs. (4.8)–(4.10) show the induced terms in the effective Hamiltonian are dependent on the distribution of the transverse modes in the superconductor with respect to the chemical potential. In particular, they decay with the energy difference between the bottom of the superconductor mode and the chemical potential. This means that the modes closer to the semiconductor Fermi energy give the dominant contribution to the induced superconducting pairing and exchange fields at $p_z = 0$.

We first analyze the contribution of an isolated superconductor mode to the effective Hamiltonian, as the ones from the different modes add up. The behavior of the induced term in the effective Hamiltonian is illustrated in Fig. 4.3(a). The two terms of the induced exchange field $h_z^{(1)}$ and $h_z^{(2)}$ sum constructively for occupied modes. Both $\tilde{h}_z$ and $\tilde{\Delta}_0$ decay for $\left|\xi_{n,0}\right| \to \infty$, leading to the existence of an optimal regime where both the induced exchange field and superconducting pairing are maximal and $\left|\tilde{h}_z/\tilde{\Delta}_0\right| > 1$. This is the ideal region for searching for topological superconductivity.
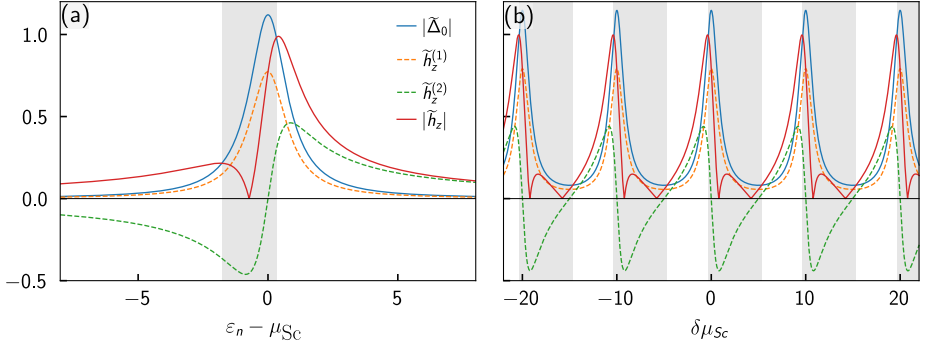
Fig. 4.3: **Induced fields in the effective Hamiltonian.** Induced gap $\tilde{\Delta}_0$ (blue line), exchange field contributions $\tilde{h}_z^{(1)}$ and $\tilde{h}_z^{(2)}$ (dashed lines), and total spin splitting $\tilde{h}_z = \tilde{h}_z^{(1)} + \tilde{h}_z^{(2)}$ (red line) at $p_z = 0$ induced in the semiconductor. (a) Results for a single transverse mode of a spin-split superconductor as a function of the chemical potential in the superconductor, $\mu_{Sc} - \varepsilon_0$. (b) Results for the case of a multimode superconductor as a function of the chemical potential from mid-band $\delta\mu_{Sc}$. The effect of the resonance peaks in $\tilde{h}_z^{(2)}$ cause an oscillation between topologically trivial and nontrivial phases while varying the chemical potential in the superconductor. The area with gray background is topologically trivial, while the one with white background satisfies the condition $\left|\tilde{h}_z\right| > \tilde{\Delta}_0$. Parameters: $\Delta_0 = 1$, $t_0 = 1$, $-t_z = 0.4$, $-h_z = 0.5$ for (a) and (b), and $\delta\varepsilon = 10$ for (b).

In general, a spin-dependent component $t_i$ in the tunneling matrix enhances the collinear component in the exchange field $\tilde{h}_i$, suppressing the non-collinear components in $\tilde{\mathbf{h}}$ and the superconducting gap in the semiconductor. From Eqs. (4.8)–(4.10) we see that $\tilde{\Delta}$ and $\tilde{h}_z^{(1)}$ share the same dependence on the superconductor band structure (they decay as $\sim \xi^{-2}$) while having a different prefactor which depends on the tunneling matrix. Therefore, the spin splitting in the superconductor leads to an enhancement of $\left|\tilde{h}_z\right|$ and provides a first mechanism to induce topological superconductivity in the semiconductor.

In contrast to $\tilde{h}_z^{(1)}$, the second contribution $\tilde{h}_z^{(2)}$ to the induced exchange field in the semiconductor is totally independent of the spin polarization in the parent superconductor. This term depends solely on the spin-asymmetric component of the tunneling Hamiltonian. Moreover, $\tilde{h}_z^{(2)}$ has an energy dependence $\sim \xi^{-1}$, with a sign that depends on the relative position of the mode to the superconductor Fermi energy. Since $\tilde{\Delta}_0$ and $\tilde{h}_z^{(1)}$ decay as $\sim \xi^{-2}$, $\tilde{h}_z^{(2)}$ dominates as the energy difference between the semiconductor and superconductor modes increases. This contribution exhibits a sign change, which leads to a cancellation of $\tilde{h}_z^{(2)}$ in the limit of small energy separation between modes. However, the transverse modes can exhibit a large energy separation in thin superconductors because of quantum confinement effects.

If the separation between transverse modes in the superconductor is large enough, the contribution of the mode closest to the chemical potential dominates over the other ones. We can visualize this system as two coupled one-dimensional wires, where one features both exchange field and superconductivity while the other features only spin-orbit coupling. This case is discussed in detail in Ref. [P1].

In a more realistic scenario, the superconductor features many transverse modes. In

this case, Eqs. (4.8)–(4.10) explain how the induced terms in the semiconductor effective Hamiltonian are determined by the sum of the contributions of each mode. The relative energy of the transverse modes in the superconductor strongly affects the gap polarization in the semiconductor, becoming a critical factor for the appearance of the topological phase. For the systems of interest, the dimensions of the superconductor section vary from a few to hundreds of nanometers. For small lengthscales, the effect of quantum confinement separates the superconductor modes such that it is not possible to treat the density of states like a continuum. Both $\tilde{\Delta}_0$ and $\tilde{h}_z^{(1)}$ have a Lorentzian shape with a full width at half maximum $\Gamma = \sqrt{\Delta_0^2 - h_z^2}$. We can use $\Gamma$ as a reference to distinguish between discrete modes, $\delta\varepsilon \gg \Gamma$, and a continuum distribution of modes, $\delta\varepsilon \ll \Gamma$, where $\delta\varepsilon$ is the average separation of modes. Indeed, if the average energy separation between the transverse modes is $\delta\varepsilon \gtrsim \Gamma$, the resonance peaks do not overlap entirely, and $h_z^{(2)}$ do not completely cancel out. In this case, the net exchange field experienced in the semiconductor will be due to the sum of the contribution of each transverse mode.

To provide a clearer picture, we consider the case where the band structure of the superconductor can be described by perfectly equidistant transverse modes. In this case, $\delta\varepsilon$ is the relative separation between the superconductor modes. This approximation recovers the continuum limit for a two-dimensional system, where we expect a constant density of transverse modes $g_m = (\delta\varepsilon)^{-1}$. We also define $\delta\mu_{\mathrm{Sc}}$ as the relative position of the Fermi energy in the superconductor from the middle of the band.

We consider that, in the relevant energy scale, the band structure of the superconductor can be described by $N_m$ modes distributed in an energy range $E_B$. For simplicity, we will take equidistant modes with energy difference $\delta\varepsilon = E_B/N_m$. This is also consistent with the continuum limit since, for a 2D system, we can expect a constant density of transverse modes $g_m = (\delta\varepsilon)^{-1}$. We also define $\delta\mu_{\mathrm{Sc}}$ as the relative position of the Fermi energy in the superconductor from the middle of the band. We proceed by summing over the modes' contributions following Eqs. (4.8)–(4.10) to derive the value of the induced terms in the effective Hamiltonian. In the limit $N_m = E_B/\delta\varepsilon \gg 1$ we get to

$$\tilde{h}_z^{(1)}(p_z) \simeq \pi g_m \frac{h_z}{\Gamma}(t_0^2 + t_z^2) G\left[\pi g_m \Gamma, \pi g_m \left(\delta\mu - \frac{p_z^2}{2m_{\mathrm{Sc}}^*}\right)\right], \tag{4.12}$$

$$\tilde{h}_z^{(2)}(p_z) \simeq 2\pi g_m t_0 t_z F\left[\pi g_m \Gamma, \pi g_m \left(\delta\mu - \frac{p_z^2}{2m_{\mathrm{Sc}}^*}\right)\right], \tag{4.13}$$

$$\tilde{\Delta}_0(p_z) \simeq -\pi g_m \frac{\Delta_0}{\Gamma}(t_0^2 - t_z^2) G\left[\pi g_m \Gamma, \pi g_m \left(\delta\mu - \frac{p_z^2}{2m_{\mathrm{Sc}}^*}\right)\right], \tag{4.14}$$

where we define the auxiliary functions

$$
\begin{aligned}
F(x,y) &= \frac{\cot(ix+y) - \cot(ix-y)}{2} = \frac{\sin(2y)}{\cosh(2x) - \cos(2y)}, \\
G(x,y) &= i\frac{\cot(ix+y) + \cot(ix-y)}{2} = \frac{\sinh(2x)}{\cosh(2y) - \cos(2x)}.
\end{aligned}
\tag{4.15}
$$

These expressions can be used to derive the induced fields in the effective Hamiltonian. The behavior of the induced terms for $p_z = 0$ is illustrated in Fig. 4.3(b). By varying the chemical

potential in the superconductor, we see an alternation of trivial regions (gray background) and regions where topological superconductivity can appear by tuning $\mu_{\text{Sm}}$ (white background) as the modes cross the Fermi level. Additionally, with a simple linear search for the minimum eigenvalue, find the effective gap shown in Fig. 4.3(b).
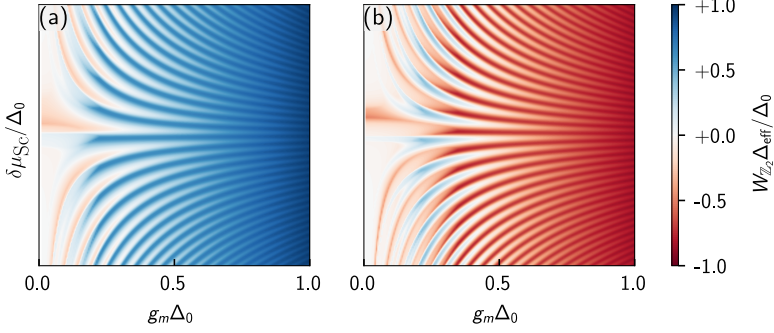


Fig. 4.4: **Phase diagram for the case of a multimode superconductor**. The effective gap in the semiconductor is $|\Delta_{\text{eff}}| = \min_{n,p_z} E_{n,p_z}$, where $E_{n,p_z}$ are the Hamiltonian eigenvalues and sign given by the topological invariant $W_{\mathbb{Z}_2}$. We observe an oscillation between the topological (red) and trivial (blue) phases as we vary the chemical potential measured from the middle of the band $\delta\mu_{\text{Sc}}$. As the density of transverse modes $g_m$ increases, the peaks get closer and overlap until they merge in the continuous limit $g_m \gg (\Delta_0)^{-1}$. In the continuum limit, the system is in a globally trivial or topological phase, depending on the condition in Eq. (4.17). We assume that the chemical potential in the semiconductor is tuned such that $\mu_{\text{Sm}} = -\tilde{\mu}$. Parameters used: $m_{\text{Sc}}^* = 1$, $m_{\text{Sm}}^* = 0.2$, $\alpha_x/\Delta_0 = 20$, $V_z/\Delta_0 = 0.5$, $t_0/\Delta_0 = 1$. For the left panel, we use $t_z/\Delta_0 = 0.4$, while for the right panel, we use $t_z/\Delta_0 = 0.7$.

The limit $g_m \ll 1/\Delta_0$ corresponds to a large superconductor where the effect of quantum confinement becomes completely negligible. This behavior can be realized if the average separation of the transverse modes is such that $\delta\varepsilon \ll \Gamma$. In this limit, the contributions from each mode overlap, leading to a globally trivial or topological phase, depending on the polarization of the spin-filter barrier $t_z/t_0$. A quantitative criterion can be obtained by integrating Eqs. (4.8)–(4.10) over a constant density of transverse modes. In this limit, the term in Eq. (4.9) vanishes, and we get

$$\left|\frac{\tilde{h}_z}{\tilde{\Delta}_0}\right| = \left|\frac{h_z}{\Delta_0}\right| \left|\frac{t_0^2 + t_z^2}{t_0^2 - t_z^2}\right|. \tag{4.16}$$

We note that the spin-dependent tunneling leads to an enhancement of the induced exchange field while reducing the induced superconducting gap. This effect can be used to bring the $h_z/\Delta_0$ ratio above one, closing the gap at $p_z = 0$ and inducing a quantum phase transition to the topological phase. Therefore, the spin-asymmetric tunneling provides a way to overcome the limitation of Eq. (4.11) and to induce a phase transition to the topological phase, Fig. 4.2(a). The topological phase appears for a barrier polarization

$$\frac{t_z}{t_0} > \sqrt{\frac{1 - |h_z/\Delta_0|}{1 + |h_z/\Delta_0|}}. \tag{4.17}$$

As discussed in the previous section, the behavior of the system is strongly dependent on the band structure of the superconductor, which is controlled by the dimension of the superconducting region. If a wide shell is used, the transverse modes of the nanowire will be densely distributed in the energy spectrum. In this case, $\tilde{h}_z^{(2)}$ vanishes, and topological superconductivity can only be induced using the spin-asymmetric tunneling to enhance $\tilde{h}_z^{(1)}$ and suppress $\tilde{\Delta}_0$, Eq. (4.16).

Finally, we note that both nanowires superconductor shell and superconductor layers in 2DEG systems are around 5 nm thick, so we can already expect a measurable effect of quantum confinement in this direction. For this reason, we expect that the resonance effect discussed previously can be measured by scaling down the width of the devices.

To check if the ferromagnetic hybrid nanowire is in this regime, we can estimate the average mode separation by a simple particle in a box model $\delta\varepsilon \simeq \frac{\hbar^2}{2m_{Sc}^*}\frac{\pi^2}{L_{Sc}^2}$, where $L_{Sc}$ refers to the largest dimension of the cross-section of the superconductor shell. Assuming that $\Gamma \sim 100\,\mu eV$, which is in line with the experimental measurements of Al-EuS heterostructures [73, 187], we estimate that, in order to observe well-separated modes, the maximum dimension of the shell should be in the order of 60 nm. In experiments, the facet length is around 60 nm [73]. For this reason, we expect the contributions of the modes in the superconductor to overlap significantly. Previous measurements performed on EuS-Al heterostructures have shown a polarization of around 50% of the gap. In this case, applying (4.17), we can estimate that a spin-dependent barrier with a 58% polarization is enough to cause a topological transition.

**Connection with other works**

Several other groups independently analyzed the same problem in the same period, finding complementary results. These works, all together, allow us to understand the physics of the device in a convincing way and build a comprehensive picture.

The importance of the electrostatic environment has been independently pointed out by three works [204–206]. The conclusions are similar: in general, in the nanowire geometry with non-overlapping facets, the wavefunction is localized near the superconductive shell. This is due to the electrostatic environment that favors the creation of a quantum well near the superconductor, which also acts as a metallic gate. In general, fine-tuning from back and side gates is necessary to push the electron wavefunction close to both the superconductor and ferromagnetic facets to maximize magnetic and superconducting correlations simultaneously. This condition is extremely hard to achieve in the non-overlapping facets, as the ferromagnetic layer is insulating, and thus the wavefunction weight in the region near the interface is small.

The result concerning the impossibility of topological phases by superconductor-mediated exchange field has been extended to generic systems in terms of a more general requirement about the minimal Zeeman field for a topological phase transition [207]. In particular, a necessary condition for the appearance of a topological phase in a nanowire is the presence of a region in the cross-section where the exchange field overcomes the pairing amplitude. This is clearly not the case for a spin-split superconductor symmetrically coupled to a semiconductor. The spin-dependent tunneling barrier, instead, can be seen as a region where this condition applies.

The ferromagnetic hybrid nanowire physics has been explored using a self-consistent treatment of a diffusive superconductor in Ref. [208] with similar results, while in the opposite

limit of clean systems with, it has been proved that an extremely thin superconductor layer could be used to obtain topological phases even in the ferromagnetic insulator-superconductor-semiconductor stack [209], Fig. 4.2(c).

## 4.4 Tunneling design for topological superconductivity

In the previous section, we proved that a hybrid system composed of a spin-split superconductor coupled to a semiconductor nanowire could not be tuned to the topological phase. As an alternative mechanism, we discussed how spin-asymmetric tunneling could be used to overcome this limitation. The spin-dependent tunneling suppresses the induced superconducting pairing potential while enhancing the spin splitting, thus providing a way to reach the topological phase. While this mechanism is unlikely to explain the appearance of a topological phase in nanowires with partially overlapping facets observed in Ref. [73], because of the relatively thick EuS layer used, the concept of spin-dependent coupling can be exploited in the next generation of topological superconducting devices without magnetic field by promoting spin-asymmetric tunneling as the main mechanism. This idea is represented in Fig. 4.2(d), where a thin ferromagnetic insulator layer is used as a spin-filter tunnel barrier. The proposed mechanism is compatible with the currently used hybrid superconductor-semiconductor platforms. Estimating the optimal magnetic barrier length to achieve this polarization is a complicated task. As the barrier gets thicker, we expect a stronger polarization, but at the same time, the coupling between the two systems gets strongly suppressed. Therefore, the optimal barrier length would be determined by the trade-off between a strongly polarizing thick barrier, which suffers low transparency, and a thin transparent barrier with low polarization.

To assess more precisely the design requirements for this idea, we explored further the idea with detailed microscopic simulations in a subsequent paper [P2] where we study ferromagnetic hybrid heterostructures comparing the 2DEG, Fig. 4.5(a), and VLS designs, Fig. 4.5(c). The core idea is that, due to the band alignment properties between materials, shown in Fig. 4.5(b), a quantum well hosting an accumulation layer appears at the semiconductor-ferromagnetic insulator interface. The role of the ferromagnetic insulator layer is two-fold: to induce an exchange field in the quantum well and the superconductor and to act as a spin-polarized barrier for electrons.

### Model

Both two structures can be described by the BdG Hamiltonian

$$
\begin{aligned}
\mathcal{H} = &\left[ \mathbf{k} \cdot \frac{\hbar^2}{2m(\mathbf{r})} \mathbf{k} + E_{\text{CBM}}(\mathbf{r}) - e\varphi(\mathbf{r}) + \frac{1}{2} \left\{ (\boldsymbol{\alpha}_{\text{R}} \times \boldsymbol{\sigma}), \mathbf{k} \right\} \right] \tau_z + \\
&h_x(\mathbf{r})\sigma_x\tau_0 + \Delta(\mathbf{r})\sigma_0\tau_x.
\end{aligned}
\tag{4.18}
$$

We consider a translation invariant system in the $x$-direction such that $\mathbf{k} = (k_x, -i\partial_y, -i\partial_z)$ with $k_x$ being a good quantum number. The model parameters are the effective mass $m$, the conduction-band bottom $E_{\text{CBM}}$, the exchange field $h_x$ (non-zero only in the ferromagnet), and the superconducting pairing potential $\Delta$ (non-zero only in the superconductor domain, taken real). These parameters have a constant value inside each material.
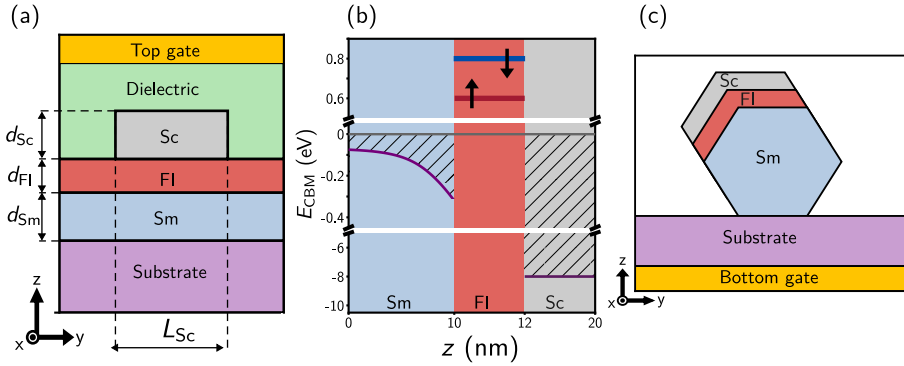
**Fig. 4.5: Geometry and band alignment of ferromagnetic hybrid heterostructures for topo-logical superconductivity.**
(a) semiconductor-ferromagnetic insulator-superconductor 2D heterostructure stacked in the $z$-direction and infinite in the $x$-direction. The substrate is insulating and typically composed of several stacked semiconducting layers. The top gate can be used to confine the wavefunction below the grounded superconductor. The thickness of the ferromagnetic insulator layer $d_{FI}$ is varied to optimize the topological properties. (b) Schematics of the conduction-band bottom along the heterostructure stacking direction for a specific choice of materials (InAs/EuS/Al) and representative geometrical parameters ($d_{Sm} = 10$ nm, $d_{FI} = 2$ nm, $d_{Sc} = 8$ nm and $L_{Sc} = 100$ nm). Red and blue colors represent different spin directions, and the gray dashed line depicts the Fermi level. (c) Sketch of the hexagonal nanowire geometry simulated for comparison. The nanowire is partially covered by a ferromagnetic insulator layer. On top of the ferromagnetic insulator, a grounded superconductor layer is included. The nanowire is gated from below using a back-gate isolated from the wire by a 200 nm thick $SiO_2$ dielectric.

For the planar heterostructure, we use a 10 nm thick layer of InAs as the host of the 2DEG. Usually, the InAs layer is grown on top of an elaborate multilayer semiconductor substrate, used to relax lattice stress and defects. We introduce the substrate in the model by taking a 400 nm-thick layer of $In_{0.25}Ga_{0.75}As$. The superconductor is a stripe 100 nm wide and 8 nm thick of Al. A 8 nm dielectric layer of $HfO_2$ isolates the top gate from the rest of the system. We include in the model an amorphous oxide layer that naturally covers the exposed Al surface to vacuum, which has been shown to be beneficial for the superconducting proximity effect since it significantly enhances the size of the induced gap [74]. The intuitive explanation of this effect is that disorder breaks the conservation of momentum, allowing for a more regular proximity effect. We restrict the disorder to a layer of 2 nm thickness at the outer surface of the superconductor, where we introduce a random on-site potential sampled from a Gaussian distribution with a variance of 1 eV. The remaining parameters are presented in Table 4.2, including typical values for the effective electron mass $m$, Rashba spin-orbit coupling field $\alpha_R$, conduction band minimum $E_{CBM}$, exchange field $h_x$, dielectric constant $\epsilon$, and pairing potential $\Delta$ for each material.

For the VLS nanowire geometry, a hexagonal InAs nanowire of 80 nm width is covered over two facets by a thin EuS layer. The outer facets of the EuS layer are covered in turn by an 8 nm

thick Al layer. The wire is deposited on top of a 200 nm thick $SiO_2$ dielectric and gated from below through a back gate.

We describe the ferromagnetic insulator as a wide-bandgap semiconductor with a spin-split conduction band laying above the Fermi level, as depicted schematically Fig. 4.5(b). This work assumes that the ferromagnet exhibits a homogeneous in-plane magnetization along the $x$-direction and negligible stray fields, consistent with the measured easy-axis in thin EuS [170].

### Numerical methods

We compute the electrostatic potential with the Thomas-Fermi approximation described in Ch. 2 for the conduction band electron only. We take into account the band bending produced at the InAs-EuS interface [172, 206] using a one-site-thick layer of positive fixed charge located at the semiconductor-ferromagnetic insulator interface. Dirichlet boundary conditions are applied to the grounded superconductor stripe, i.e., $V_{Sc} = 0$, and to the top-gate $V_{tg}$. As a result of the electrostatic simulation, the scalar potential $\varphi$ is used to tune the electrochemical potential and to calculate the Rashba spin-orbit field.

After the calculation of the electrostatic interactions, we discretize the continuum Hamiltonian in Eq. (4.18) following a finite differences scheme with a grid of 0.1 nm. We diagonalize the resulting sparse Hamiltonian for different top-gate voltages $V_{tg}$, and longitudinal momenta $k_x$.

We compute the topological invariant using the method introduced in Ref. [205]. We start by defining the winding number as

$$C = \frac{1}{2\pi i} \int_{BZ} dk \, \langle \Phi_k | \partial_k | \Phi_k \rangle \,.$$ (4.19)

| Material | Parameter | Value |
|---|---|---|
| InAs | $m$ | $0.023 m_0$ |
| | $E_{CBM}$ | 0 |
| | $\epsilon_{InAs}$ | $15.5\epsilon_0$ |
| | $\rho_{surf}$ | $2 \cdot 10^{-3} \, e \, nm^{-3}$ |
| Al | $m$ | $m_0$ |
| | $E_{CBM}$ | -8 eV |
| | $\Delta$ | 0.23 meV |
| | $\alpha$ | 0 |
| EuS | $m$ | $0.3 m_0$ |
| | $E_{CBM}$ | 0.7 eV |
| | $h_x$ | 0.1 eV |
| Dielectrics | $\epsilon_{EuS}$ | $10\epsilon_0$ |
| | $\epsilon_{InGaAs}$ | $13.9\epsilon_0$ |
| | $\epsilon_{HfO_2}$ | $25\epsilon_0$ |
| | $\epsilon_{SiO_2}$ | $3.9\epsilon_0$ |

Table 4.1: Parameters used for the simulations of the planar heterostructure.

| Material | Parameter | Value |
|---|---|---|
| InAs | thickness | 10 nm |
| | width | 200 nm |
| Al | thickness | 8 nm |
| | oxidation thickness | 2 nm |
| | width | 100 nm |
| $In_{0.25}Ga_{0.75}As$ | thickness | 400 nm |
| $HfO_2$ | thickness | 8 nm |

Table 4.2: **Geometrical dimensions used in the planar heterostructures.**

where $\Phi_k$ is the many-body wavefunction (a Slater determinant). This can be expressed as

$$C = \frac{1}{2\pi}\text{Arg}\{\det(\mathcal{W})\} = \frac{1}{2\pi}\sum_l \text{Arg}\{\lambda_l\}, \tag{4.20}$$

where $\mathcal{W}$ is the so-called Wilson matrix and $\{\lambda_l\}$ are its eigenvalues. The Wilson matrix can be evaluated as $\mathcal{W} = \prod_{k_l} W_{k_l,k_{l+i}}$ where

$$W_{k_l,k_{l+1}}^{i,j} = \left\langle \Psi^{(i)}(k_l) \middle| \Psi^{(j)}(k_{l+1}) \right\rangle. \tag{4.21}$$

In practice, it is enough to include only the high-symmetry $k$-points in the product inside the Wilson matrix. In our case, these points are $k_z = \{-\pi, 0, \pi\}$, which gives as a result the Wilson matrix $\mathcal{W} = W_{-\pi,0}W_{0,\pi}W_{\pi,-\pi}$. Additionally, since only the non-trivial topological eigenstates provide a non-zero contribution to the winding number, and these states can only emerge close to the Fermi level in the studied system, it is enough to include the closest states to the Fermi level in the Wilson matrix.

While the calculation of the topological invariant precisely characterizes the topological phase diagram, it does not provide an intuitive picture of the behavior of the device. To gain some insight, we map the behavior of each mode of the system to an effective 1D Oreg-Lutchyn model, using effective parameters that characterize each mode.

The approximation assumes the separability of the eigenfunctions into a product of a purely spatial profile $\psi_n(\mathbf{r})$, and a position-independent Nambu spinor $v_n$ for the spin and particle-hole subspaces, i.e., $\Psi_n(\mathbf{r}) \simeq \psi_n(\mathbf{r})v_n$. This approximation is valid for any subgap state when the heterostructure thickness is small compared to the length where the spin and Nambu components change significantly.

The effective Hamiltonian for each transverse mode $n$ is

$$H_{\text{eff},n} = \left(\frac{\hbar^2 k_x^2}{2m_{\text{eff},n}} - \mu_{\text{eff},n} + h_{\text{eff},n}\sigma_x\right)\tau_z + \alpha_{\text{eff},n}k_x\sigma_y\tau_z + \Delta_{\text{eff},n}\sigma_y\tau_y, \tag{4.22}$$
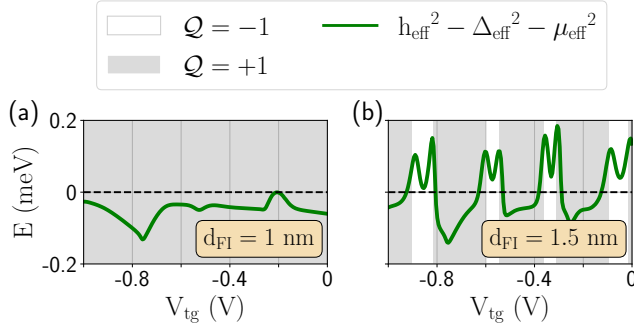
Fig. 4.6: **Topological invariant vs 1D topological criterion.** Topological criterion comparing results from computing the topological invariant (white/gray background for the topological/trivial phases) and the effective 1D model (green line). We show results as a function of the top-gate voltage $V_{tg}$ and for two different ferromagnetic insulator thicknesses (a,b). The remaining parameters are the same as in Fig. 4.9.

where the effective parameters are given by

$$h_{\text{eff},n} \equiv \langle h_x(\mathbf{r})\sigma_0\tau_0\rangle_n = h_0 W_{\text{FI},n}, \tag{4.23}$$

$$\Delta_{\text{eff},n} \equiv \langle \Delta(\mathbf{r})\sigma_0\tau_0\rangle_n = \Delta_0 W_{\text{Sc},n}, \tag{4.24}$$

$$\mu_{\text{eff},n} \equiv \left\langle \left(\partial_x \frac{\hbar^2}{2m(\mathbf{r})}\partial_x + \partial_y \frac{\hbar^2}{2m(\mathbf{r})}\partial_y + E_{\text{CBM}}(\mathbf{r}) - e\varphi(\mathbf{r})\right)\sigma_0\tau_0 \right\rangle_n, \tag{4.25}$$

$$\alpha_{\text{eff},n} \equiv \langle \alpha_z(\mathbf{r})\sigma_0\tau_0\rangle_n, \tag{4.26}$$

$$m_{\text{eff},n}^{-1} \equiv \left\langle \frac{1}{m(\mathbf{r})}\sigma_0\tau_0 \right\rangle_n, \tag{4.27}$$

being $W_{\beta,n} = \int_{\mathbf{r}\in\beta} |\Psi_n(\mathbf{r})|^2\,d\mathbf{r}$ the weight of the wavefunction in the material $\beta$. Here, $h_0$ and $\Delta_0$ are the parent exchange field in the ferromagnetic insulator and parent superconducting gap in the superconductor, correspondingly. For $h_{\text{eff},n}$, we neglect additional contributions arising from the spin-orbit interaction for simplicity. In Fig. 4.6, we compare the value of the topological invariant obtained with the Wilson loop and the one obtained using the effective parameters defined above. In general, there is strong agreement between the two methods, validating the definition of the effective parameters.

### Comparison of electrostatic landscapes in the two geometries

A good understanding of the electrostatic environment is crucially needed for a fragile objective like topological superconductivity, and it reveals fundamental to understanding the different performances of the VLS and 2DEG devices. The cornerstone of the electrostatics in these devices is the strong band-bending at the interface between the semiconductor and the ferromagnetic insulator, able to induce a natural 2DEG in the accumulation layer at the interface. This enhances the topological properties of the device by confining electrons close to the proximitized region.

Confinement in the transversal direction is obtained in different ways: in the VLS nanowire is due to the geometry of the device, while in the 2DEG, a quasi-1D system can be defined by means of electrostatic lateral confinement. This is achieved by applying a negative potential to the top gate that depletes the 2DEG everywhere except underneath the grounded superconductor stripe, which screens the electric field coming from the top gate. This allows controlling the lateral extension of the semiconductor 1D channels. Moreover, the top gate allows for partial control of the local chemical potential in the effective wire.

To illustrate this, we show in Fig. 4.7(a) an example of the electrostatic potential profile across the device's section in a highly-depleted regime (i.e., for a large negative $V_{\text{tg}}$ potential). Electrons are attracted to positive potential regions, meaning that their wavefunction is localized mainly in these regions. As one can appreciate in Fig. 4.7(a), when the top gate depletes the system, the electrostatic potential is only positive inside the semiconductor in the region below the superconductor, due to the screening created by the superconductor stripe. This effect leads to the confinement effect mentioned previously. On the other hand, for positive voltages, the electrostatic potential is positive all across the semiconductor section, and thus, electrons are not only localized beneath the superconductor but spread in the whole structure, like in Fig. 4.7(b). This, in turn, suppresses the semiconductor-superconductor coupling and, consequently, this situation is unfavorable to developing a topological superconducting regime inside the semiconductor.

The electrostatic potential profile across the hexagonal nanowire is shown in Fig. 4.7(c) and (d), together with the planar device's profiles (a,b) for comparison. Fig. 4.7(c) shows the case where the back gate strongly depletes the wire. The electrostatic potential is larger close to the ferromagnetic insulator-superconductor interface due to the band-bending present there. However, the electrostatic potential is positive in the entire upper half of the wire, i.e., up to ~30 nm away from the semiconductor-ferromagnetic insulator interface. Hence, the electron wavefunction will spread all across that region [positive $\phi(\mathbf{r})$], and therefore its localization close to the superconductor will be smaller compared to the planar device. This necessarily leads to a worse hybridization with both the ferromagnetic insulator and the superconductor. For completeness, we show in Fig. 4.7(d) the case where the back gate fills the wire (i.e., positive $V_{\text{bg}}$). In this case, the electrostatic potential is nearly homogeneous across the wire's section, and thus, the hybridization between the semiconductor and the ferromagnetic insulator and superconductor will be almost completely suppressed.

The consequence of the rectangular well that characterizes the planar structure is the regularity in the eigenmode wavefunctions. We show two examples of the wavefunction profile in Fig. 4.8 for the two geometries considered. The four cases correspond to the lowest-energy states in a topological regime. In the 2DEG geometry (a,b), the wavefunction is well localized below the superconductor stripe with a regular nodes distribution, top panels in Fig. 4.8. This is a consequence of the strong vertical confinement imposed by the thin semiconductor layer. In contrast, the wavefunction in the hexagonal nanowire, bottom panels in Fig. 4.8, spreads across the whole cross-section of the wire in some cases [Fig. 4.8(d)], having a significant weight at positions several nanometers away from the semiconductor-ferromagnetic insulator interface. The reduced localization at the interface and the irregular distribution affect the value of the effective superconducting pairing and exchange potential. This results in the reduced topological region, spectral gap, and irregular distribution of the trivial and topological phases in parameter space.

Finally, another consequence of the regular electrostatic potential of the planar design is
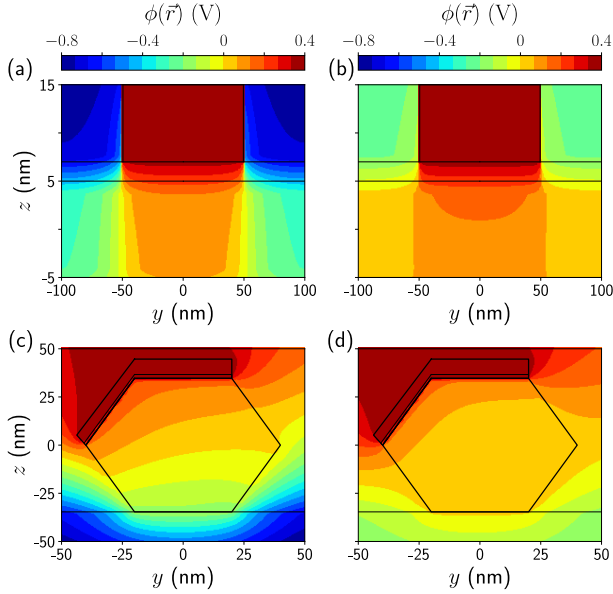
Fig. 4.7: **Electrostatic potential profiles.** (a, b) Electrostatic potential across the planar device's section for two different top gate potentials: (a) $V_{\text{tg}} = -0.8$ V and (b) $V_{\text{tg}} = 0$ V. In (c, d), we show the same profiles but for the hexagonal wire device, for (c) $V_{\text{bg}} = -4$ V and (d) $V_{\text{bg}} = 0$ V. Black lines represent the interfaces between different materials.

that the spin-orbit field ($\sim \mathbf{k} \times \boldsymbol{\alpha}_{\text{R}}$) is mainly oriented in the $y$-direction ($\sim \alpha_{\text{R},z} k_x \sigma_y$), with small components in the $x$ and $z$-directions. Contributing to the predictability of the device behavior.

## Topological superconductivity in the planar heterostructure

The low-energy wavefunctions decay exponentially in the ferromagnetic insulator layer on a length scale approximately given by $\xi_{\text{FI}} = \sqrt{2 E_{\text{CBM,FI}} m_{\text{FI}} / \hbar^2}$, where $E_{\text{CBM,FI}}$ is the conduction band minimum in the ferromagnetic insulator with respect to the Fermi level. For our materials choice $\xi_{\text{FI}} \approx 2.3$ nm. As a consequence, the thickness of the ferromagnetic insulator layer determines the tunneling amplitude between the 2DEG and the superconductor: thicker ferromagnetic insulator layers decouple the 2DEG from the superconductor resulting in a reduction of the superconducting proximity effect, while thinner ones exhibit a reduced induced magnetization in the 2DEG. Hence, an optimal barrier thickness allows for a sufficiently large induced exchange field and pairing potential in the 2DEG to drive the system into the topological regime.

The topological phase transition of the system occurs at a gap closing and reopening when the lowest energy subband crosses zero energy at the $k_x = 0$ high symmetry point. For this reason, in Fig. 4.9 we show the energy spectrum of the system at $k_x = 0$ as a function of the top-gate voltage for three different values of the ferromagnetic insulator thickness ($d_{\text{FI}}$). The white
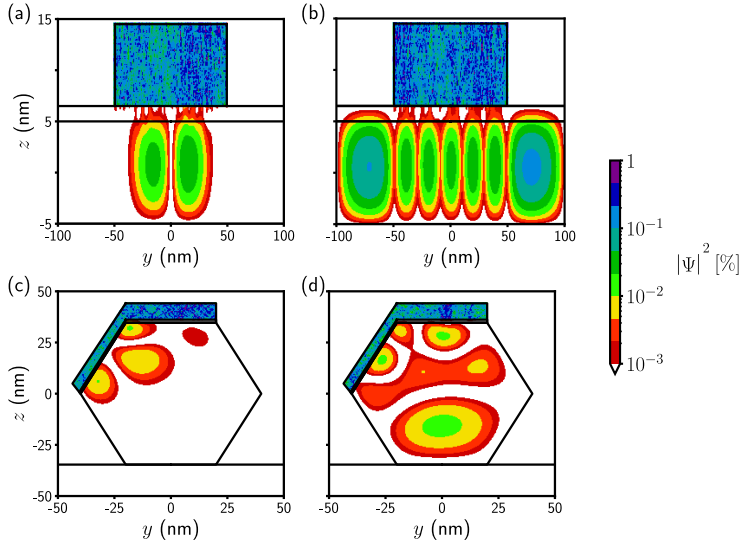
Fig. 4.8: **Wavefunction profiles comparison between the two geometries.** Wavefunction profile of the lowest-energy state in the 2DEG device (a) in a non-trivial topological phase close to pinch-off, $V_{tg} = -850$ mV, and (b) in a trivial phase after several subbands are populated in the wire, and the wavefunction is not localized anymore, $V_{tg} = 300$ mV. We take $d_{FI} = 1.5$ nm, and the rest of the parameters are the same as in Fig. 4.5. In (c,d), we show the same profile but for the hexagonal nanowire device, also (c) in a non-trivial topological regime close to pinch-off, $V_{bg} = -4$ V, and (d) in a different non-trivial phase but after several subbands are occupied in the wire, $V_{bg} = -1$ V.

(gray) background denotes the topological (trivial) phase, determined by the corresponding topological invariant.

The left panels in Fig. 4.9 show the regime where the ferromagnetic insulator is too thin to induce a topological phase transition. The energy spectrum shows low-energy bands localized mainly in the superconductor, represented by the black color in Fig. 4.9(a). In this case, superconductivity dominates the properties of the low-energy modes while in Fig. 4.9(b) we show the effective superconducting pairing amplitude and exchange coupling.. For this thickness, we observe that $h_{eff}$ is mostly below $\Delta_{eff}$, consistent with the system being in the trivial regime as the topological condition $|h_{eff}| \gtrsim \sqrt{\Delta_{eff}^2 + \mu_{eff}^2}$ cannot be fulfilled.

The situation becomes more favorable for ferromagnetic insulator layers of intermediate thickness, middle panels in Fig. 4.9. As a function of $V_{tg}$, the system shows several topological transitions when consecutive subbands cross zero energy. The topological regions are characterized by a non-trivial topological invariant and are marked by a white background in Figs. 4.9(b) and (e). In these regions, the lowest-energy wavefunction has a significant weight in both the superconductor and the semiconductor, as illustrated by the purple line color. The topological transition is associated with an increase of $h_{eff}$, overcoming the value of $\Delta_{eff}$, see Fig. 4.9(e). The small deviations found are due to the approximated character of the effective parameters. We note that, for the optimal range of $d_{FI}$, every subband can be tuned to the

topological regime as $V_{tg}$ is varied, in contrast to the hexagonal wire case where some subbands do not show a topological crossing, see for instance Ref. [205]. This is due to the effective hard-wall confinement of the wavefunction in the thin semiconductor layer in the $z$-direction [see Fig. 4.5(a)], which keeps the wavefunction close to the ferromagnetic insulator- superconductor layers for every subband. As a consequence, the device shows a regular alternation of trivial and topological regions against $V_{tg}$ with comparable spectral gaps. The topological regions thus occupy a larger area in parameters space compared to the hexagonal wire case, where the appearance of the topological regions is more erratic since the wavefunction can spread throughout the wide hexagonal section, sometimes avoiding a good proximity effect with the superconductor-ferromagnetic insulator layers.

The situation of a too-thick ferromagnetic insulator barrier is illustrated in the right panels of Fig. 4.9. A thick barrier hinders tunneling through the ferromagnetic insulator, preventing the hybridization of superconductor and 2DEG states. The reduced hybridization between the two materials can be seen from the shape of the spectrum in Fig. 4.9(c), where the system shows an almost horizontal black line at the superconductor gap ($E \sim 0.23$ meV) and a series of almost vertical lines (orange dots) crossing the gap. This is also manifested in the abrupt transitions of effective parameters in Fig. 4.9(f). When $\Delta_{eff} > h_{eff}$ the ground-state wavefunction is localized mostly in the superconductor and it is essentially independent of the gate voltage, whereas when $\Delta_{eff} < h_{eff}$ it is localized mostly in the semiconductor. We note that the regions with a large effective exchange field also exhibit a suppressed superconducting pairing, consistent with normal gapless states in the semiconductor.
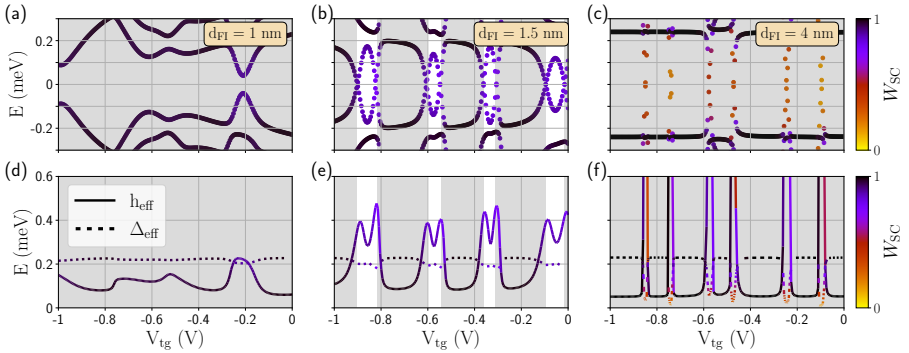


Fig. 4.9: **Topological phase diagrams for different ferromagnetic insulator thicknesses.** Top row: energy spectrum at $k_x = 0$ as a function of the top-gate voltage $V_{tg}$ for a ferromagnetic insulator thickness of (a) $d_{FI} = 1$ nm, (b) $d_{FI} = 1.5$ nm and (c) $d_{FI} = 4$ nm. Colors represent the weight $W_{Sc}$ of each state in the superconducting Al layer. Shaded $V_{tg}$ regions are those characterized by a trivial phase, i.e., $\mathcal{Q} = +1$; while white regions correspond to a topological phase, i.e., $\mathcal{Q} = -1$. Bottom row (d,e,f): effective exchange coupling $h_{eff}$ (solid lines) and superconducting pairing amplitude $\Delta_{eff}$ (dotted lines) for the lowest-energy state in (a), (b), (c).

The properties of a topological superconductor are highly dependent on the value and quality of the topological spectral gap, which we examine now. In Fig. 4.10, we consider a device with $d_{FI} = 1.5$ nm as we sweep $V_{tg}$. We show the energy subbands versus momentum $k_x$ and the spin-resolved density of states (DOS) in three representative situations: before (left

column), at (middle column), and after (right column) the topological transition. Before the transition, Fig. 4.10(a), the heterostructure features a trivial gap and the above-gap states are mostly localized in the superconductor (black color curves). The DOS displays a hard gap around zero energy and the characteristic spin-split superconducting coherence peaks, see red and blue curves in Fig. 4.10(d). From this plot we infer that the induced exchange field in the superconductor is around $100\,\mu$eV ($\sim 50\%$ of the Al gap), consistent with the value found in experiments [187, 197, 198]. A similar peak splitting is found in Figs. 4.10(e,f), i.e., it is independent of the value of the gate potential.

At the topological transition, one subband crosses zero energy at $k_x = 0$, Fig. 4.10(b). It results in a finite DOS inside the superconducting gap, see Fig. 4.10(e). As we increase $V_{tg}$, the superconducting gap reopens in the topological phase, Fig. 4.10(c), accompanied by the onset of Majorana bound states at the ends of a finite-length quasi-1D wire defined by the superconductor stripe (not shown). The hard gap found in Fig. 4.10(f), $E_{min}$, has a typical value of tens to a hundred $\mu$eV. We associate the large topological gaps found in these devices with the electrostatic confinement in the vertical direction. The thin semiconductor layer, together with the top gate tuned to negative values, makes it possible to concentrate the weight of the wavefunction in the region where superconductivity, magnetism, and spin-orbit coupling coexist. This is signaled by the purple color of the lowest-energy subband in Fig. 4.10(c).
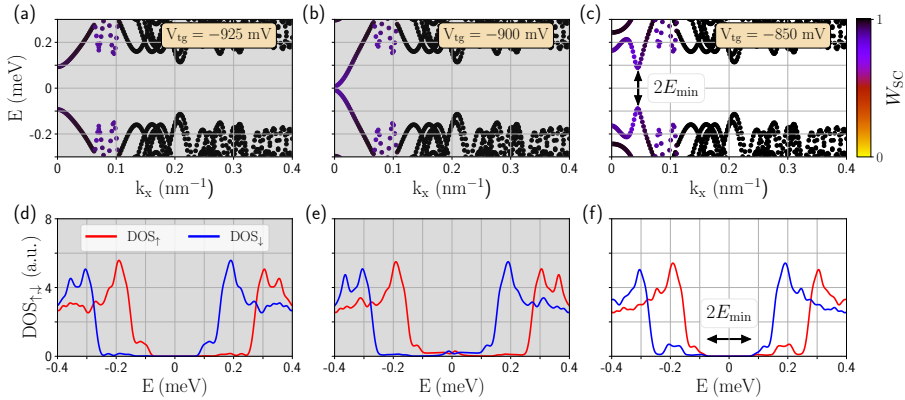


Fig. 4.10: **Topological phase transition and DOS.** Dispersion relation for a device with EuS layer thickness $d_{FI} = 1.5$ nm, and for (a) $V_{tg} = -925$ mV (before the topological transition), (b) $V_{tg} = -900$ mV (at the topological transition), and (c) $V_{tg} = -850$ V (in the middle of the topological phase). In (d-f) we show the spin-resolved integrated DOS of the corresponding plot on the top. Only the (c,f) case is topological, with $E_{min}$ being the topological spectral gap, i.e., the lowest-state energy at $k_x = k_F$.

Finally, we vary the ferromagnetic insulator thickness to extract the optimal range for topological superconductivity, Fig. 4.11. The effective exchange coupling is shown in Fig. 4.11(a) and the effective superconducting pairing in Fig. 4.11(b). The transverse modes considered (depicted with different colors) are the first four lowest-energy subbands that get populated starting from a depleted semiconductor as we increase $V_{tg}$. For each calculated point, we tune $V_{tg}$ to the value where the subband is closer to the Fermi level ($E = 0$), where $h_{eff}$ is maximum, see Fig. 4.9(e,f). Therefore, each point corresponds to a different $V_{tg}$ value. We observe that in

general $h_{\text{eff}}$ increases with $d_{\text{FI}}$ because of the growing weight of the wavefunction inside the ferromagnetic insulator. In contrast, the effective superconducting pairing decreases with the ferromagnetic insulator thickness as the weight of the wavefunction in the superconductor diminishes.

The topological spectral gap is shown in Fig. 4.11(c). It is calculated for the value of $V_{\text{tg}}$ that maximizes $E_{\text{min}}$ for each subband, i.e., well within the topological region. Depending on the transverse mode, its value ranges from tens to a hundred µeV. Note that we have used the bulk superconductor gap for the Al layer, $\Delta_0 = 230\,\text{µeV}$.

Interestingly, for the small semiconductor thickness considered here (10 nm), $E_{\text{m}in}$ is essentially constant with $d_{\text{FI}}$ for every transverse mode. This is again a consequence of the vertical confinement that tends to produce regular topological patterns.

The topological phase can appear when the ferromagnetic insulator magnetization is not aligned with the spin-orbit field, which is oriented fundamentally in the $y$-direction the planar heterostructure, and it is maximized when the magnetization and the spin-orbit field are perpendicular. We note that the planar setup could tolerate in principle an arbitrary misalignment of the exchange field in the $z$-direction since this would still be perpendicular to the spin-orbit term. This is an advantage with respect to schemes relying on magnetic fields, where relatively small perpendicular magnetic fields to the superconductor layer suppress superconductivity due to orbital effects.

### Topological superconductivity in the hexagonal nanowire geometry

The hexagonal nanowire can also be tuned to the topological regime using an electrostatic gate. However, the topological phase appears for reduced and irregular gate-voltage ranges compared to the planar structure in Fig. 4.5. In addition, the topological gap in hexagonal nanowires is typically soft, exhibiting low-energy trivial states. These states are prone to creating quasiparticle excitations poisoning, undermining coherence in the device and being an obstacle to topological superconductivity. We associate the improved topological properties of the presented 2D stacking with the vertical confinement of the 2DEG wavefunction, see Fig. 4.8. In contrast, since the quantum well in hexagonal wires is less confined, the wavefunction can spread several nanometers away from the superconductor-ferromagnetic insulator interface, giving rise to weaker proximity effects. Moreover, due to the smaller wavefunction localization, the effective parameters are highly dependent on the wavefunction profile (or subband) and, consequently, the phase diagram appears to be more irregular than in the planar device. This is evident in Fig. 4.12(a), that shows the energy spectrum at $k_x = 0$ vs the back gate potential while the background color highlights the the topological phase as with a white background and the trivial with a gray one. The topological phases are narrower and appear in a less regular way than the case in the main text. This is related to the fact that some bands cannot be tuned to the topological regime as they cannot be confined to the interesting spatial region where superconductivity and exchange field coexists. Therefore, the nanowire exhibits a reduced parameter space where topology exists compared to the planar structure.

This is also illustrated by the effective parameters, shown in the right panels of Fig. 4.12(b). We note that the exchange field exceeds the superconducting gap for various $V_{\text{tg}}$ values. Some of these crossings are correlated to a dip in $\Delta_{\text{eff}}$, indicating that the wavefunction is not proximitized by the superconductor and the system remains in the trivial regime.
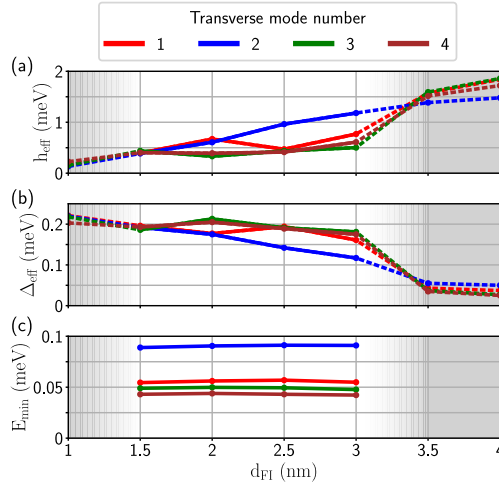
Fig. 4.11: **Effective parameters as a function of ferromagnetic insulator thickness.** (a) Effective ferromagnetic exchange coupling $h_{\text{eff}}$, (b) effective superconducting pairing amplitude $\Delta_{\text{eff}}$, and (c) topological spectral gap $E_{\text{min}} = |E(k_x = k_F)|$ for the first four occupied transverse subbands (in different colors) versus the EuS thickness $d_{\text{FI}}$. We extract these effective parameters when the subband is close to the Fermi level ($E = 0$), and therefore different points necessarily correspond to different $V_{\text{tg}}$ values. Shaded regions and dashed lines represent that the system is characterized by a topologically trivial phase (and therefore there is no spectral gap). The suitable ferromagnetic insulator thickness $d_{\text{FI}}$ for topological superconductivity in the 2D stacking device proposed in this work ranges from ~1.5 to ~3 nm.

Fig. 4.12(c) displays the dispersion relation, while panel (d) the density of states for an instance of the topological region. Notably, the superconducting gap of the wire is significantly reduced with many subgap states close to the Fermi level that make a soft gap. These states are an obstacle for applications and the demonstration of Majorana non-abelian properties. In general, softening of the gap can be attributed to two main effects: the presence of poorly proximitized subgap states in the semiconductor and the back-action of the semiconductor-ferromagnetic insulator on the superconductor that suppresses the pairing. Notice, however, that while both effects can be identified in the nanowire case, the softening of the gap, in this case, can be mainly attributed to states localized in the parent superconductor. This suggests a stronger back-action of the ferromagnetic insulator and semiconductor on the superconductor. This effect appears negligible in the 2DEG case.

Further discussion of the dependence of the effective parameters and topological phase diagram of the planar heterostructure on the geometrical and material parameters can be found in Ref. [P2].
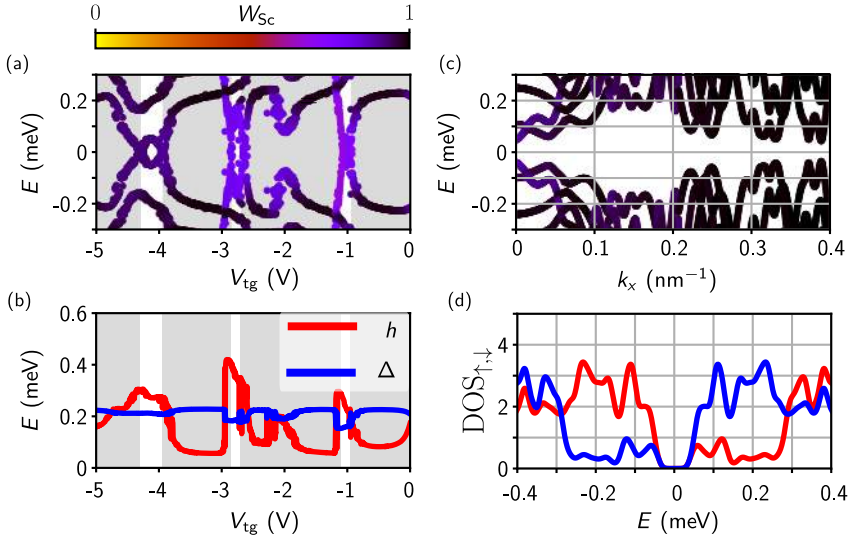
Fig. 4.12: **Results for the hexagonal nanowire.** (a) Energy spectrum at $k_x = 0$ versus the back gate voltage $V_{bg}$ for the hexagonal wire device. Colors represent the weight of each state on the superconducting Al layer $W_{Sc}$. Shaded $V_{tg}$ regions are those characterized by a trivial topological phase, i.e., $\mathcal{Q} = +1$; while the lighter ones correspond to non-trivial ones, i.e., $\mathcal{Q} = -1$. (b) Effective exchange field $h_{eff}$ and superconducting gap $\Delta_{eff}$ for the lowest energy state on the left. (d) Spin-resolved DOS of the corresponding plot on the left.

## 4.5 Ferromagnetic hybrid junctions: experimental investigation

Another application of ferromagnetic hybrid heterostructures is as a platform to fabricate Josephson junctions. In Josephson junctions with insulating weak links, the flow of a dissipationless supercurrent arises from individual Cooper-pair tunneling events, which is typically characterized by a sinusoidal current-phase relation (CPR) [210]. For junctions with high transparency, additional contributions to the supercurrent appear thanks to the simultaneous coherent tunneling of multiple Cooper pairs [48, 211–218]. These tunneling events give rise to higher harmonics in the CPR, leading to deviations from the standard sinusoidal form.

In a simple weak link, the Josephson energy is minimized when the superconducting phases on both sides of the junction are equal. However, when time-reversal symmetry is broken, a phase transition can occur, resulting in an equilibrium state with a relative phase difference of $\pi$. This shift in the macroscopic degree of freedom leads to a phase transition between the so-called 0 and $\pi$ phases [219–222].

Josephson junctions with broken time-reversal symmetry can be tuned to a regime where both the 0 and the $\pi$ phases are metastable with the Josephson potential showing two local minima [223, 224]. In this case, the junction is said to be $0'$ or $\pi'$ regime if the global minimum is at 0 or $\pi$ phase difference. The fundamental harmonic changes sign when moving from $0'$ to $\pi'$ and vanishes at the crossover between the two. At this point, the current is dominated by higher harmonics, causing a nonsinusoidal CPR [225].

The study of such nonsinusoidal CPRs has recently gained significant interest due to potential applications in developing protected superconducting qubits [P5, 226–229] and supercurrent diodes [230–237]. These novel applications of Josephson junctions require not only a static nonsinusoidal CPR but also the ability to control its harmonic content.

In this view, ferromagnetic hybrid junctions can offer a solution to engineer nonsinusoidal current-phase relations. The gate-tunability of charge carriers density in the semiconductor, together with the adjustable magnetization of the ferromagnetic insulator, may provide control over the content of the supercurrent harmonics. We investigate this idea in two research works. The first one, documented in Ref. [P6], is an experimental study of a multi-interferometer device made of ferromagnetic hybrid heterostructures and is the subject of this section. A second study, an exhaustive theoretical investigation of the possibility offered by this platform, is found in Ref. [P7] and summarized in Sec. 4.6.

**Experimental results**

To demonstrate the emergence of $\pi$-junctions in ferromagnetic hybrid nanowires, we studied a multi-interferometer device consisting of ferromagnetic (target) and non-magnetic (reference) wires. The two wires, denoted A and B, were placed next to each other on a Si substrate with 200 nm SiOx capping. The middle and the ends of both wires were connected by *ex situ* Al contacts, forming multiple loops [Fig. 4.13(a)]. The main wire A was comprised of a hexagonal InAs core with epitaxial two-facet EuS and three-facet *in situ* Al shells, with the Al fully covering both EuS facets and one InAs facet. The reference wire B with InAs core and three-facet Al shell did not include EuS. Four junctions, denoted $j_1^F$, $j_2^F$ on the ferromagnetic wire A, and $j_3$, $j_4$ on the reference wire B, were formed by selectively removing $\sim 100$ nm of *in situ* Al in the segments between the ohmic contacts. Top gates were fabricated over all four junctions after the deposition of a thin HfOx dielectric layer, allowing independent electrostatic control of each junction.

The phase across a particular junction relative to a reference junction was measured by depleting the other two junctions, thus forming a single superconducting interferometer. This is further explained in Appendix A. Three triple-hybrid junctions from two different devices were investigated and showed similar results.

We begin by exploring the magnetotransport properties of a single ferromagnetic junction, $j_2^F$, while keeping the other junctions depleted. Four-terminal differential resistance, $R = dV/dI$, of the junction was measured as a function of current bias, $I$, and external magnetic field, $H_\parallel$, applied parallel to wire A, see Figs. 4.13(b) and 4.13(c). Sweeping from negative to positive field, $R(I)$ remains finite and featureless throughout the measured range, except between $\mu_0 H_\parallel = 15$ and 25 mT, where $R(I)$ decreases abruptly for $|I| \lesssim 5$ nA, see Fig. 4.13(b). Reversing the sweep direction of $H_\parallel$ shifts the low-resistance window to around $-20$ mT, Fig. 4.13(c). A similar hysteretic dip in resistance has been reported in uninterrupted EuS/Al bilayer films [238].

We interpret the observed behavior as the recovery of the superconductivity near the coercive field, $H_C$, where the induced magnetization, $\langle M \rangle_\xi$, averaged over the superconducting coherence length, $\xi$, decreases below a critical value $M_C$. To verify this picture, we calculate disorder-averaged $\langle M \rangle_\xi$ using the kinetic random-field Ising model. This quick dive in the extremely interesting physics of magnetic hysteresis is included in Appendix. D. The resulting magnetization curves, see Fig. 4.13(d) are asymmetric around the coercive field. In this regime,
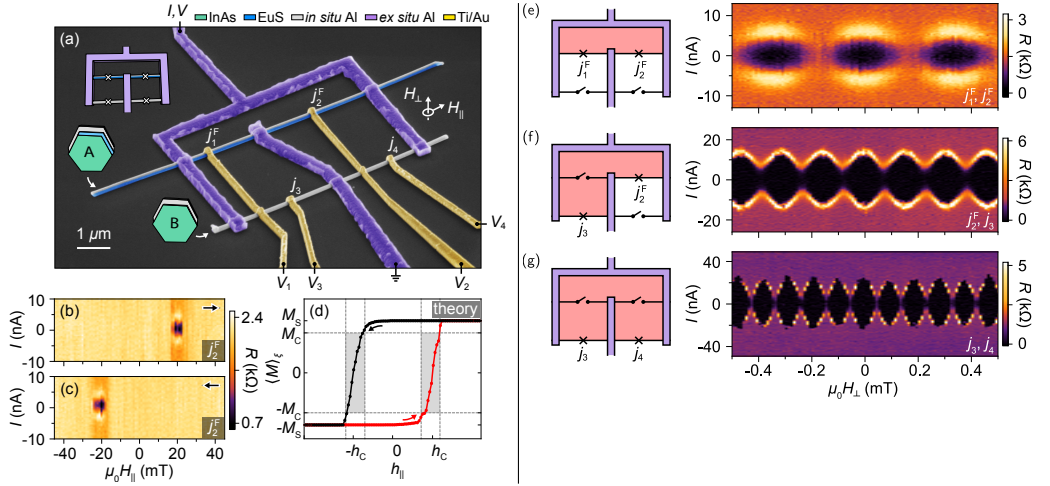
Fig. 4.13: (a) Color-enhanced micrograph of a representative multi-interferometer device comprised of ferromagnetic (target) and non-magnetic (reference) nanowires. The insets show schematic device layout and wire cross-sections. (b) an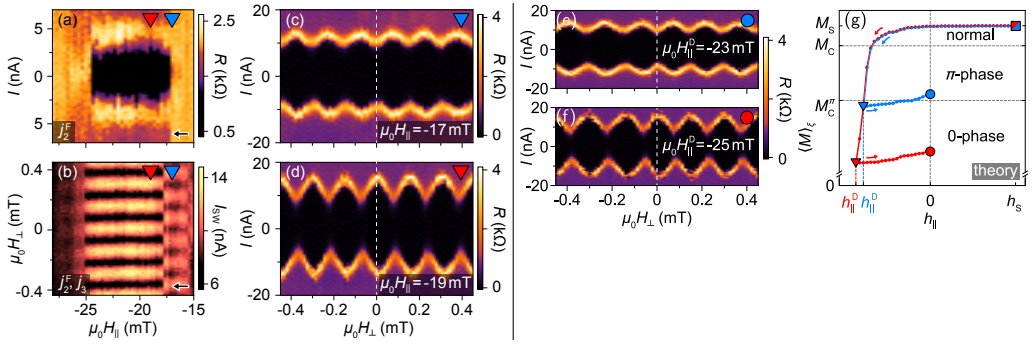d (c) Differential resistance, $R$, as a function of current bias, $I$, and parallel external magnetic field, $H_\parallel$, measured for the $j_2^F$ junction sweeping $H_\parallel$ from (b) negative to positive and (c) positive to negative. $R$ is suppressed in a narrow, sweep-direction dependent window away from $H_\parallel = 0$. (d) Disorder-averaged induced magnetization, $\langle M \rangle_\xi$, calculated using random-field Ising model. $h_\parallel$ is a model parameter representing external magnetic field. The junction superconducts only in a narrow hysteretic window (gray) around the coercive field $\pm h_C$ and is otherwise normal. For the (f), (e), and (g) group, the left panels show schematics of the multi-interferometer device in various open and closed junction configurations with highlighted effective loop areas. while, in the right panels, the corresponding current-phase relations are shown, represented by differential resistance, $R$, measured as a function of current bias, $I$, and flux-threading perpendicular magnetic field, $H_\perp$, for (f) two ferromagnetic, (e) one ferromagnetic and one non-magnetic, and (g) two non-magnetic junctions. All junction configurations show effective-area dependent, periodic switching current modulations in $H_\perp$.

the EuS domain size is shorter than $\xi$, which leads to a reduced $\langle M \rangle_\xi$ compared to the saturation value, $M_S$. Realistic hysteresis curves are typically not as smooth as depicted in Fig. 4.13(d); instead, they display irreversible jumps between discrete magnetization values.

We note that the magnetic junctions in the superconducting state display residual resistance at $I = 0$, which we tentatively attribute to the supercurrent suppression due to the uncertainty in the phase difference across a junction with low Josephson energy [239]. Such phase diffusion can be stabilized by integrating the junction into a superconducting loop [240].

Having established the magnetic-field response of an individual magnetic junction, we next examine the current-phase relations (CPRs) of various junction pairs. To ensure that wire A was superconducting, $\mu_0 H_\parallel$ was first ramped to $-100$ mT and then tuned to 21 mT, close to $H_C$, where $R(I \sim 0)$ is suppressed. Three example measurements of distinct superconducting interferometers, formed by opening either two ferromagnetic, mixed, or non-magnetic

Fig. 4.14: (a) Differential resistance, $R$, of $j_2^F$ as a function of current bias, $I$, and parallel external magnetic field, $H_\parallel$, showing the superconducting window of the junction centered around $-21$ mT. The data were taken with $j_1^F$, $j_3$, and $j_4$ depleted. (b) Switching current, $I_{SW}$, as a function of flux-threading perpendicular magnetic field, $H_\perp$, measured for $j_2^F$ - $j_3$ interferometer at decreasing $H_\parallel$ values. The magnetic junction switches abruptly from $\pi$- to 0-phase around $-18$ mT as $H_\parallel$ is lowered. (c) Current-phase relation measured at $\mu_0 H_\parallel = -17$ mT exhibits $I_{SW}$ minimum at $H_\perp = 0$, suggesting $\pi$-junction. (d) similar to (c) but in the 0-junction regime at $\mu_0 H_\parallel = -19$ mT. All the data were taken after polarizing the wire at $\mu_0 H_\parallel = 100$ mT. (e) Differential resistance, $R$, as a function of current bias, $I$, and flux-threading magnetic field, $H_\perp$, measured for $j_2^F$ - $j_3$ interferometer at zero parallel external field ($H_\parallel = 0$) showing a $\pi$-shifted current-phase relation. The data were taken after polarizing the wire at $\mu_0 H_S = 100$ mT and demagnetizing it at $\mu_0 H_\parallel^D = -23$ mT. (f) Similar to (e) but taken after demagnetizing the wire at $\mu_0 H_\parallel^D = -25$ mT, showing 0-junction behavior. (g) Calculated disorder-averaged induced magnetization, $\langle M \rangle_\xi$, illustrating the experimental demagnetization scheme. After saturating $\langle M \rangle_\xi$, the parameter representing the external magnetic field, $h_\parallel$, is swept to the variable demagnetization value, $h_\parallel^D$, and then back to 0. Depending on $h_\parallel^D$, the junction can either relax to the $\pi$ or 0 phase.

junctions, are displayed in Fig. 4.13(e), (f) and (g). In all three configurations, the device shows periodic switching current, $I_{SW}$, modulations as a function of the flux-threading perpendicular magnetic field, $H_\perp$. The oscillation period changes for different junction combinations due to the different effective loop areas, corresponding to the superconducting flux quantum, $\Phi_0 = h/2e$. The zero-flux offset of the magnet was calibrated using the CPR of the loop with two non-magnetic junctions ($j_3$ and $j_4$).

At $\mu_0 H_\parallel = 21$ mT, $I_{SW}$ is maximal at zero flux ($H_\perp = 0$) for all configurations, indicating a homogeneous superconducting phase across the device. However, we find that the loops with magnetic junctions show characteristic $\pi$-shifted CPRs at the onset of the superconducting window, before $H_C$ is reached (Fig. 4.14). We study the transition between the two regimes in $j_2^F$ by measuring CPRs (using $j_3$ as a reference, while keeping $j_1^F$ and $j_4$ depleted) over a range of $H_\parallel$ spanning the superconducting window [Fig. 4.14(a)]. The deduced evolution of $I_{SW}$ with $H_\perp$ and $H_\parallel$ is shown in Fig. 4.14(b). Outside the superconducting window, $I_{SW}$ is independent of $H_\perp$, indicating that $j_2^F$ is not superconducting. Moving to more negative $H_\parallel$, $j_2^F$ displays a $\pi$-shifted CPR in the range between $-16$ and $-18$ mT, Fig. 4.14(c), but then switches abruptly to a state without a phase shift, Fig. 4.14(d). The average $I_{SW}$ is ~ 10 nA in both cases, but its

modulation amplitude increases from around 3 to 6 nA as the CPR phase switches from $\pi$ to 0, see Figs. 4.14(c) and 4.14(d). The superconducting phase remains unchanged throughout the rest of the superconducting window, whereas the amplitude of $I_{SW}$ oscillations shrinks abruptly at $-25$ mT and once again at $-26$ mT as the supercurrent through $j_2^F$ gets suppressed. This is likely because of the sweep-direction dependent, discrete jumps of $\langle M \rangle_\xi$ through $M_C$. The transition features were qualitatively the same around positive $H_C$, after reversing $H_\parallel$ direction, and did not depend on the gate voltages $V_2$ and $V_3$. The transition-field value shifted by a fraction of a millitesla between different runs, presumably due to the magnetic noise from the stochastic domain switching [241]. Furthermore, the superconducting phase shift of $\pi$ within the superconducting window was observed also for the other two measured ferromagnetic junctions, with $j_1^F$ showing hints of a second $0-\pi$ transition at the end of its superconducting window.

These experimental observations suggest that the $0-\pi$ transition is driven by a discrete flipping of the EuS domains affecting $\langle M \rangle_\xi$ and changing the effective spin splitting of the ABSs in the junction. In Sec. 4.6, a theoretical model to describe in detail how the change in the magnetization drives the 0-$\pi$ transition will be described more in detail.

Finally, we demonstrate experimentally that the $\pi$ phase can be realized at zero external magnetic field by demagnetizing EuS with the following procedure, see Fig. 4.14, right panels. First, a saturating magnetic field, $\mu_0 H_S = +100$ mT, was applied to fully polarize the EuS. The field was then gradually swept through zero to a demagnetizing (negative) value, $H_\parallel^D$, before returning to zero. Carrying out the demagnetization loop for different $H_\parallel^D$ values, we find that $j_2^F$ transitions from $\pi$ to 0 phase as $\mu_0 H_\parallel^D$ is changed from $-23$ to $-25$ mT. This is similar to the behavior observed at the finite external field (Fig. 4.14, left panels), but now measured at $H_\parallel = 0$. Qualitatively the same phenomenology was observed for $j_1^F$. We ascribe this behavior to the $H_\parallel$-controlled EuS domain relaxation into a configuration with the remanent $\langle M \rangle_\xi < M_C$ as $H_\parallel$ is ramped back and forth. The calculated demagnetization loops for two different demagnetization values support this picture, Fig. 4.14(g).

In summary, we have studied the current-phase relation of triple-hybrid Josephson junctions comprised of semiconducting (InAs) nanowires with epitaxial ferromagnetic insulator (EuS) and superconductor (Al) shells. The magnetic junctions showed a $0-\pi$ phase transition within a hysteretic superconducting window in the parallel magnetic field. We interpret the results in the context of magnetic domains and provide a simple theoretical model demonstrating that an induced average magnetization can account for the transition. By demagnetizing the EuS layer, the $\pi$-phase can be realized at zero magnetic field, making the triple-hybrid junctions an attractive component for quantum and classical applications in superconducting circuitry.

## 4.6 Ferromagnetic hybrid junctions: theoretical modeling

In this section we introduce two models aimed at describing ferromagnetic hybrid junctions. The first one is a simple model valid in the limit of a short junction with a single dominant level that was developed to explain the 0–$\pi$ transition in the experiment described in Sec. 4.5. In the subsequent work, Ref. [P7], we broaden the analysis by introducing a continuum model and study other aspect of such system. We sill show that these hybrid materials offer a new way to control the harmonic content of the CPR by combining the gate-tunable charge carriers

density of the semiconductor and the adjustable magnetization of ferromagnetic insulator insets. Additionally, in these devices, both the superconducting pairing and the exchange field are induced through proximity effects in the semiconductor. This allows for unique regimes where the exchange field in the superconductor is below the Chandrasekhar-Clogston limit [17, 18], while in the semiconductor it can exceed the induced pairing potential. As a result, this platform is suited for studying superconductivity under extreme exchange fields that can surpass the induced pairing potential.
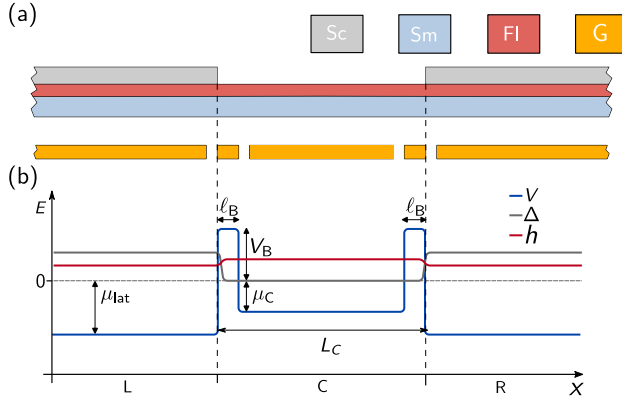


Fig. 4.15: **Josephson junction in a semiconductor-ferromagnet-superconductor device.** Sketch of a ferromagnetic hybrid junction (a) and the continuum model considered in this paper (b). The nanowire divides into three regions: the lateral left (L) and right (R) regions feature proximity-induced superconductivity from the superconductor shells, while in the central (C) region the superconductor is etched. All the regions are subjected to the ferromagnetic proximity effect. The density in the central region and the barriers between the central and the lateral ones can be controlled by gates.

The system we are considering can be conceptually split into three regions: two lateral (L and R), and a central region (C), see Fig. 4.15(a). The superconductor primarily induces a superconducting pairing potential $\Delta(x)$ in the semiconductor through the proximity effect. It also contributes to the electrostatic potential landscape $V(x) = -\mu(x)$. The ferromagnetic insulator induces an exchange field $\mathbf{h}(x)$ in both the superconductor and the semiconductor. Given that both the exchange field and the pairing potential are induced in a semiconductor with controllable charge carrier density, there is not a fixed hierarchy of energy scales, and, in principle, all regimes can be realized in the system. We consider that the exchange field is sufficiently weak in the superconductor such that superconductivity persists. This condition is relaxed in the semiconductor, where the induced exchange field can overcome the induced pairing potential. Therefore, ferromagnetic hybrid junctions allow exploring the parameter space beyond the conventional regime ($\mu \gg \Delta > |\mathbf{h}|$). Note that we do not refer to a particular arrangement of the layers in the lateral region, as different combinations of interfaces, for instance, tripartite arrangement [205, 206] and tunneling arrangement [P1, P2], allows induction of both superconducting pairing and exchange field in the semiconductor.

**Single-level model**

Before proceeding to the numerical results, we introduce a minimal model in which two high carrier density superconducting lateral regions are coupled by a single level in the junction. To describe the transport through the system, we use the Green function formalism, summarized in Ref. [242]. The retarded/advanced (R/A) Green function of the central region is given by

$$\hat{G}_0^{R/A}(\omega) = \left[\hat{g}_0^{-1}(\omega) - \hat{\Sigma}_L^{R/A}(\omega) - \hat{\Sigma}_R^{R/A}(\omega)\right]^{-1}, \tag{4.28}$$

where $\hat{g}_0^{-1}(\omega) = (\omega + \sigma h_C)\hat{\tau}_0 + \varepsilon\hat{\tau}_z$ describes the isolated normal region as a function of the electron energy $\omega$, and $\hat{\Sigma}_\nu^{R/A}$ is the self-energy describing the coupling to the lateral regions $\nu$.

In the wide bandwidth limit, the self-energy of these regions is given by

$$\hat{\Sigma}_\nu^{R/A}(\omega) = \sum_\nu \Gamma_\nu \left[\mathfrak{g}_\nu^{R/A}(\omega)\hat{\tau}_0 + \mathfrak{f}_\nu^{R/A}(\omega)\tau_x e^{\hat{\tau}_y \phi_\nu}\right]. \tag{4.29}$$

Here

$$\mathfrak{g}_\nu^{R/A}(\omega) = -\frac{\omega + \sigma h_\nu \pm i\eta}{\sqrt{\Delta^2 - (\omega + \sigma h_\nu \pm i\eta)^2}}, \qquad \mathfrak{f}_\nu^{R/A}(\omega) = \frac{\Delta}{\sqrt{\Delta^2 - (\omega + \sigma h_\nu \pm i\eta)^2}}, \tag{4.30}$$

and $\eta$ is the Dynes parameter, controlling the width of the superconducting coherent peaks at $\omega = \pm\Delta$, which we take infinitesimal in this case.

In the short junction case, the single electronic level has energy $\varepsilon$ and exchange splitting $h_C$. To determine the ABS spectrum, we search for the poles of the retarded Green's function by solving $\det\left[(G^R)^{-1}\right] = 0$. This results in the complicated expression

$$\left(\omega + \sigma h_C + \sum_\nu \gamma_\nu \frac{\omega + \sigma h_\nu}{\sqrt{\Delta^2 - (\omega + \sigma h_\nu)^2}}\right)^2 = \varepsilon^2 + \left|\sum_\nu \frac{\Delta\gamma_\nu e^{i\phi_\nu}}{\sqrt{\Delta^2 - (\omega + \sigma h_\nu)^2}}\right|^2 \tag{4.31}$$

The expression becomes more compact if we consider $h_R = h_L = h_{lat}$. In this case, the expression simplifies to

$$\left(\omega + \sigma h_C + \sum_\nu \gamma_\nu \frac{\omega + \sigma h_{lat}}{\sqrt{\Delta^2 - (\omega + \sigma h_{lat})^2}}\right)^2 = \varepsilon^2 + \frac{\Delta^2}{\Delta^2 - (\omega + \sigma h_{lat})^2} b^2(\phi) \tag{4.32}$$

where we defined the phase potential

$$b(\phi) = \left|\sum_\nu \gamma_\nu e^{i\phi_\nu}\right|. \tag{4.33}$$

Note that with this minimal simplification, the dependence on the phase is entirely condensed in the function $b(\phi)$.

By defining the total coupling $\gamma = \gamma_L + \gamma_R$ and the transmission as $T = 4\gamma_L\gamma_R/(\gamma_L + \gamma_R)^2$, we get a simplified expression that reads as

$$\frac{\omega + \sigma h_C}{\gamma} + \frac{\omega + \sigma h_{lat}}{\sqrt{\Delta^2 - (\omega + \sigma h_{lat})^2}} = \pm\sqrt{\frac{\varepsilon^2}{\gamma^2} + \frac{\Delta^2}{\Delta^2 - (\omega + \sigma h_{lat})^2}\left[1 - T\sin^2(\phi/2)\right]}. \tag{4.34}$$

The quantum point contact limit, in which the intermediate state in the junction is strongly hybridized with the states in the leads, can be obtained from the above expressions for $\gamma \to \infty$. This results in a generalization of Beenakker's formula [48] for spin-split leads

$$\omega = \pm \Delta \sqrt{1 - T \sin^2(\phi/2)} - \sigma h_{\text{lat}}. \qquad (4.35)$$

We consider the condition where an ABS crosses the Fermi level to get an expression for the critical lines separating the different phases. When a spin-split ABS crosses the Fermi level, its occupation changes and stops contributing to the current. At the same time, the newly occupied ABS provides a current contribution that exactly cancels the one of the same spin ABS. Therefore, the residual current is entirely due to the continuum of states and has a characteristic $\pi$ contribution [P6].

In the case of equal exchange fields in the leads, $h_{\text{L}} = h_{\text{R}} = h_{\text{lat}}$, the Fermi level crossing condition for ABS with spin $\sigma = \pm 1$ is given by the expression

$$\frac{\sigma h_{\text{C}}}{\gamma} + \frac{\sigma h_{\text{lat}}}{\sqrt{\Delta^2 - h_{\text{lat}}^2}} = \pm \sqrt{\frac{\varepsilon^2}{\gamma^2} + \frac{\Delta^2}{\Delta^2 - h_{\text{lat}}^2}[1 - T \sin^2(\phi/2)]}, \qquad (4.36)$$

where $\gamma = \gamma_{\text{L}} + \gamma_{\text{R}}$ is the tunnel rate to the leads and $T = 4\gamma_{\text{L}}\gamma_{\text{R}}/(\gamma_{\text{L}} + \gamma_{\text{R}})^2$ is the transparency of the junction. When a spin-split ABS crosses the Fermi level at $\phi = \pi$, a metastable $\pi$ phase appears, marking the transition from 0 to $0'$. When such a crossing happens for $\phi = 0$, the 0 phase becomes completely unstable, marking the $\pi'$ to $\pi$ transition. Finally, the $0'$ to $\pi'$ critical line can be approximated by $\phi = \pi/2$.

## Continuum model

As an alternative model for the system, we consider a continuum model represented by an Hamiltonian is $H = \frac{1}{2} \int \psi^\dagger \mathcal{H} \psi$, where the Bogoliubov-de Gennes (BdG) Hamiltonian $\mathcal{H}$ in the Nambu spinor basis $\psi^\dagger = \begin{pmatrix} \psi_\uparrow^\dagger & \psi_\downarrow^\dagger & -\psi_\downarrow & \psi_\uparrow \end{pmatrix}$ is

$$\mathcal{H} = \left[ \frac{\hbar^2 k_x}{2m^*} - \mu \right] \tau_z + \mathbf{h} \cdot \boldsymbol{\sigma} + \Delta \tau_+ + \Delta^\dagger \tau_- + \mathcal{H}_{\text{SOC}}. \qquad (4.37)$$

Here, $k_x = -i\partial_x$ is the momentum operator (we consider a single mode in the junction), $m^*$ is the effective mass, and $\sigma_j$ and $\tau_j$ are the Pauli matrices in the spin and particle-hole space, respectively. The spin-orbit coupling Hamiltonian $\mathcal{H}_{\text{SOC}}$ is given in Eq. (4.43) and discussed in Sec. 4.6.

The proximity-induced exchange field $\mathbf{h}$ is due to the coupling to the ferromagnetic insulator and, in principle, can be spatially inhomogeneous due to the micromagnetic configuration. The magnitude of the $\mathbf{h}$ field can also vary due to a nonuniform coupling strength. Moreover, recent theoretical investigations of ferromagnetic InAs-Al-EuS nanowires showed that the electrostatic environment is crucial in modulating the effect of the EuS on the InAs [P2, 205, 206], suggesting that, in principle, it is possible to tune the induced exchange field electrostatically.

In this work, we consider that the exchange field $\mathbf{h}$ takes a constant value $\mathbf{h}_j$ in each of the three regions $i \in \{\text{L, C, R}\}$. We will call collectively L and R lateral regions, with an exchange field

$\mathbf{h}_\text{L} = \mathbf{h}_\text{R} = \mathbf{h}_\text{lat}$. In the following, we will use $\mathbf{h}_\text{all}$ when considering a homogeneous value for the exchange field. We use the same notation for the chemical potential $\mu$ of the three regions. In addition, we introduce potential barriers with height $V_\text{B}$ at the interfaces between the central and the lateral regions, tuning the system from the open ($V_\text{B} = 0$) to the quantum dot regimes ($V_\text{B} \gg -\mu_\text{lat}$). The induced pairing potential is $\Delta_j = \Delta_{0,j} e^{i\phi_j}$ with the modulus $\Delta_{0,j}$ taking finite value only in the L and R regions while the superconducting phase difference between the two leads is $\phi = \phi_\text{R} - \phi_\text{L}$.

In all the simulations we use realistic parameters for InAs-Al-EuS heterostructures, taking $\Delta_0 = 0.250\,\text{meV}$ and effective mass $m^* = 0.026\,m_e$. We consider a nanowire of total length including both the lateral and central regions of $\ell_\text{W} = 3\,\mu\text{m}$. To obtain numerical results, we discretize the Hamiltonian using a finite-differences scheme with a lattice spacing of $a = 2\,\text{nm}$ implemented using the KWANT package [161]. We focus on the short junction limit, and we consider a central region of length $\ell_\text{C} = 180\,\text{nm}$, such that the quantization energy is comparable to the other energy scales. We fix the chemical potential in the lateral regions to be $\mu_\text{L} = \mu_\text{R} = 16\,\Delta = 4\,\text{meV}$. Directly solving for the quasiparticle spectrum of the continuum model allows treating on equal footing the current carried by Andreev bound states (ABSs) and the quasi-continuum of states above the gap. Usually, the continuum current is subdominant, except for strong exchange fields, where its contribution is comparable to or even larger than the ABS one [P6, 243–246].

As shown in Ch. 1, the supercurrent in a Josephson junction is an equilibrium phenomenon that can be described by a function $E_\text{J}(\phi)$, called Josephson potential or phase dispersion relation. This can be evaluated from the quasiparticle spectrum, assuming that the quasiparticles are in thermal equilibrium and calculating the free energy at a fixed phase

$$E_\text{J}(\phi) = -k_\text{B}T_\text{p} \ln \text{tr}\, e^{-\frac{H}{k_\text{B}T_\text{p}}} = -k_\text{B}T_\text{p} \sum_n \ln\left[2\cosh\left(\frac{\omega_n(\phi)}{2k_\text{B}T_\text{p}}\right)\right], \tag{4.38}$$

where $\omega_n$ is the quasiparticle spectrum, $k_\text{B}$ is the Boltzmann constant and $T_\text{p}$ is the quasiparticle temperature [6]. From $E_\text{J}$, the CPR is calculated through the thermodynamic relation

$$\langle I \rangle = \frac{2e}{\hbar}\frac{\partial E_\text{J}(\phi)}{\partial \phi}. \tag{4.39}$$

The maximum current that can flow in the junction in equilibrium is called critical current, $I_\text{c}$, while we define the critical phase, $\phi_\text{c}$, as the phase where this is reached

$$I_\text{c} = |I(\phi_\text{c})|, \qquad \phi_\text{c} \equiv \text{argmax}_{\phi \in [0,\pi]}\left|I(\phi)\right|, \tag{4.40}$$

where we restricted the maximum to $[0,\pi]$ in the reciprocal case. We define the quantity $I_0 \equiv 2e\Delta/\hbar$ as the relevant current scale that has the numerical value $I_0 = 122\,\text{nA}$ for Al. The sign of $I(\phi_\text{c})$ defines the direction of the supercurrent at the critical phase.

It is useful to decompose the phase dispersion in its harmonic components

$$E_\text{J}(\phi) = F_0 + \sum_{k=1}^{\infty}\left[C_k \cos(k\phi) + S_k \sin(k\phi)\right], \tag{4.41}$$

since each $E_\text{J}$ harmonic corresponds to the tunneling of multiplets of Cooper pairs between the two superconducting regions. To see this, it is necessary to understand the phase in Eq. (4.41)

101

as an operator and rewrite the expression in the charge basis by interpreting $\exp(ik\phi)$ as a translation operator. Neglecting the constant term, the result is

$$\mathcal{H}_J = \sum_n \sum_k \frac{C_k + iS_k}{2} |n+k\rangle\langle n| + \text{H.c.} \tag{4.42}$$

where $|n\rangle$ is the state with a difference of $n$ Cooper pairs in the two leads. In this way, it is easy to see how the terms $\cos(k\phi)$ mediate the tunneling of $k$ Cooper pairs.

If time-reversal and inversion symmetries are not simultaneously broken, the Josephson junction is reciprocal and $E_J(\phi) = E_J(-\phi)$. It subsequently results in the absence of the $S_k$ components, for this reason, called anomalous. These components are necessary for $\phi_0$ junctions and the diode effects. Assuming all the components $\{C_k\}$ with $k > 2$ are negligible, if $|C_1| \geq 4C_2$ the only minima of the Josephson potential are located at $\phi = 0$ and $\pi$. For $|C_1| < 4C_2$, minima can be found at $\phi = \pm\arctan\left(C_1/\sqrt{16C_2^2 - C_1^2}\right)$. This case, dubbed $\pm\phi_0$-junction, does not require an inversion-symmetry breaking mechanism [247].
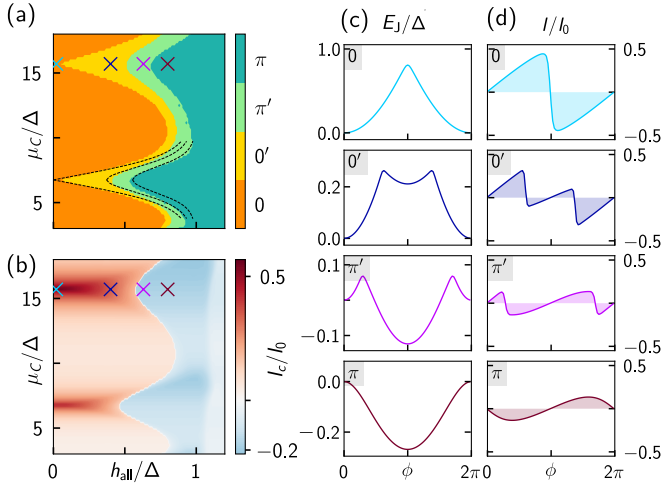


Fig. 4.16: **Phase diagram in the quantum dot regime.** (a) Phase diagram, and (b) critical current for a system in the dot regime as a function of the chemical potential in the central region, $\mu_C$, and the exchange field, $h_{\text{all}}$, considered homogeneous in the heterostructure. The dashed lines are an overlay of the analytical model in Eq.(4.36) where we selected $\varepsilon = 16\,\Delta$ and $\gamma = 0.2\,\Delta$. (c) and (d) show the Josephson potential and the CPR for some selected points in the parameter space [crosses in (a) and (b)]. Parameters for the continuum BdG model: $\mu_{\text{lat}} = 4\,\text{meV}$, $V_b = 3\,\text{meV}$.

## Results

### Quantum dot regime

The quantum dot regime is reached when large barriers at the edge of the central region are introduced, see Fig. 4.15. In this regime, electrons are confined in the central region. This work

does not consider the electrostatic repulsion in the central region (Coulomb blockade). We expect the mean-field picture to be valid for large exchange fields, and the Coulomb repulsion will enhance the exchange field in the central region. The quantum dot regime is optimal for the electrostatic controllability of the $0 - \pi$ transition. When the quantum dot levels align with the chemical potential in the leads, the $\pi$ phase appears at low exchange fields, and the critical line takes the form $h_C \propto \varepsilon$, see Fig. 4.16(c). In this regime, $I_c$ is maximal when the dot levels align with the chemical potential of the leads, as shown in Fig. 4.16(b). The critical lines converge to the spectral gap closing point, $h = \Delta$, in the off-resonance condition. The phase diagram can be understood using the single-level model, which predicts the hyperbolic critical lines [see the dashed lines in Fig. 4.16(a)]. The Josephson potential and CPRs on resonance are shown in Figs. 4.16(c) and (d). The fundamental harmonic dominates the junction properties in both the 0 and the $\pi$ phases (top and bottom panels). In contrast, high-harmonic contributions become important in the $0'$ and $\pi'$ phases because of the double minima Josephson potential.

To better understand the harmonic composition of the Josephson energy, we present the lowest harmonic components of the CPR in Fig. 4.17. For a small value of the exchange field, in the 0 and $0'$ phases, the harmonic component coefficients show a peak corresponding to an energy level in the quantum dot aligning with the Fermi level of the lateral regions. These peaks have widths that decrease for higher-order components, allowing the relative strength of the first two harmonics, $\delta C_{21} = |C_2| - |C_1|$, to be tuned by slightly changing the energy of the quantum dot levels electrostatically. In contrast, the sensitivity of $E_J$ to the chemical is almost negligible in the $\pi$ phase and the suppression of $C_2$ is significant, resulting in a sinusoidal CPR, as shown in Fig. 4.16(d). When the system is tuned to the vicinity of the $0'-\pi'$ transition, the fundamental harmonic is suppressed, leading to a regime dominated by the second harmonic and a double-well Josephson potential.

**Open regime**

In contrast to the quantum dot regime, the open regime shows a weak dependence on chemical potential, except close to the edge of the band ($\mu = 0$), Fig. 4.18 (a). The open regime shows a $\pi$ phase for $h_{all} > \Delta$, as predicted by the analytic expression in Eq. (4.36). The system shows extended metastable $0'$ and $\pi'$ regions compared to the quantum dot regime. In the open regime, the transition happens for $h_{all} = \Delta/\sqrt{1 - T/2}$. This critical line coincides with the zero-temperature paramagnetic limit for superconductors for $T = 1$. It means that this regime cannot be achieved in materials with intrinsic superconductivity. Instead, semiconductor-superconductor devices are ideal for reaching the $\pi'$ and $\pi$ regimes. At the $0'-\pi'$ transition point, the CPR is dominated by the $\sin(2\phi)$ term, leading to a Josephson potential with two equivalent minima within the $\phi \in [0, \pi]$ range. We note that the robustness against local fluctuations in $\mu_C$ is a unique feature of the open regime. The other two transitions lines, for $0-0'$ and $\pi-\pi'$, are also almost independent of the chemical potential once $\mu_C \gtrsim 10$, taking place at $h_{all} = 0$ and $h_{all} = \Delta\sqrt{1-T}$. Since the higher harmonic components are dictated mainly by the lowest ABS, the main effect of increasing temperatures is a reduction of the metastable $0'$ and $\pi'$ regions.

The open and dot regimes have different advantages and disadvantages for practical applications of ferromagnetic hybrid junctions as a $\cos(2\phi)$ Josephson element. The open regime is insensitive to noise in the gate voltage but requires a relatively high exchange field $h_{all} \simeq \Delta/\sqrt{2}$ for the second harmonic to dominate. Increasing the barriers, and so moving toward the dot regime, lowers the required exchange field toward to the theoretical limit $h_{all} \simeq 0$ at the price of
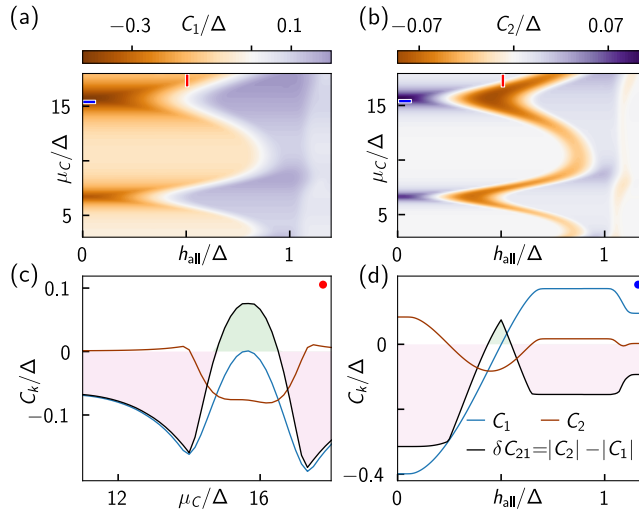
Fig. 4.17: **Harmonic components in the dot regime.** Fundamental (a) and second (b) harmonic for a ferromagnetic junction in the dot regime. The transition from $0$ to $\pi$ appears close to the gap closing ($h/\Delta = 1$) for a detuned dot, while near resonance the $\pi$ phase can appear at lower magnetic fields. In the regions of the metastable phases, a strong $C_2$ component can be observed while the $C_1$ component vanishes. In panels (c) and (d), we show two cuts of the harmonic components [blue and red ticks in (a) and (b)]. For constant $h_{\text{all}}$ the $C_k$ components show a peak when a dot level crosses the Fermi level of the leads, but the width is increasingly smaller for higher harmonics. For constant $\mu_C$, the CPR show a sinusoidal behavior until the system reaches the $0$–$\pi$ transition, where the second harmonic dominates. The parameters are equal to those in Fig. 4.16.

a higher sensitivity to gate noise. It also allows electrostatic control of the harmonic content. Indeed, when the $C_2$ component approaches its maximum location, $C_1$ vanishes linearly. This opens up the possibility of introducing a gate-controllable $\cos(\phi)$ component. Additionally, the ability to change from a dot to an open regime is controlled by the electrostatic environment, allowing to tune the system between the two regimes.

**Inhomogeneous exchange field**

The exchange field in the lateral and central regions affects CPR differently. To reveal this difference, we now analyze the case where the exchange field in the central ($h_C$) and lateral regions ($h_R = h_L = h_{\text{lat}}$) have different values while being still aligned in the same direction, Fig. 4.19. In the case of small magnetization in the lateral regions ($h_{\text{lat}} \sim 0$), we find that a strong polarization in the central one $h_C \gg \Delta$ is needed to induce the transition to the $\pi$ state in the open regime.

The exchange field strength necessary to induce a $0$–$\pi$ transition crucially depends on other parameters of the system. In particular, longer junctions and low density in the central region are associated with transitions at lower fields. The length dependence can be understood using a semiclassical model, where $h_C$ adds an extra phase accumulated by quasiparticles in
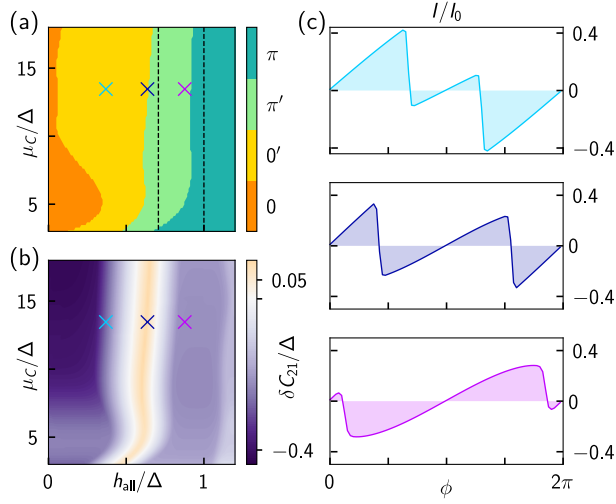
Fig. 4.18: **Open regime.** (a) Phase diagram and (b) difference between the second and first CPR harmonic component for a ferromagnetic hybrid junction in the open regime. The overlaid dashed lines are the prediction of the analytic model in the $\gamma \to \infty$ limit and $T = 1$. The sensitivity of the phase boundaries to $\mu_C$ is strongly suppressed in this limit, while the phase space occupied by $0'$ and $\pi'$ phases is increased. Parameters: $\mu_{lat} = 4\,\text{meV}$, $\ell_B = 0\,\text{nm}$.

a round-trip between the leads. This phase is proportional to $h_C \ell_C$ product, explaining why longer junctions exhibit switches from the 0 to the $\pi$ phase at lower exchange field values. In addition, it leads to a periodic pattern of 0 and $\pi$ phases along the $h_C$ axis. A similar effect can be obtained by reducing $\mu_C$, which reduces the Fermi velocity.

A sharp transition from 0 to $\pi$ can also be obtained near gap closing ($|h_{lat}| = \Delta$). In this case, the transition is associated with a strong reduction in the magnitude of $I_c$. This behavior can be understood using the simplified one-level model in Eq. (4.36), which provides an approximate expression for the critical lines of the BdG model. The fact that the $0-\pi$ transition is associated with a decrease of critical current only in the case of gap closing can be potentially used to infer the dominant mechanism in experiments.

**Spin-orbit coupling in the semiconductor**

So far, we have neglected the effect of spin-obit coupling. Here, we consider a simple model for linear spin-orbit coupling that, for a quasi-1D system, takes the form

$$\mathcal{H}_{SOC} = k_x [\alpha_z \sigma_y + \beta \sigma_x] \tau_z = k_x [\boldsymbol{\kappa} \cdot \sigma] \tau_z, \qquad (4.43)$$

where we defined a spin-orbit coupling vector $\boldsymbol{\kappa} = (\beta_x, \alpha_z, 0)$. In the simplest setup, $\alpha_z$ arises from the Rashba field and $\beta$ from the Dresselhaus term. We note that the distinction between the two terms is artificial in a one-dimensional model, as the two terms can be mapped onto each other by a unitary transformation

$$U = \exp(-i\theta/2\sigma_z \tau_0), \qquad (4.44)$$
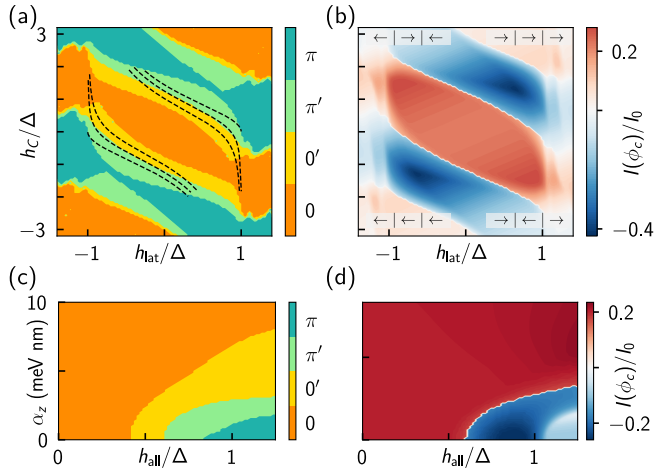
Fig. 4.19: **Effect of inhomogeneous exchange field and spin-orbit coupling.** Phase diagram (a) and critical current (b) for a ferromagnetic hybrid junction with an inhomogeneous exchange field. The overlaid dashed lines are the prediction of the single-level model, Eq. (4.36). The system shows the alternation of 0 and $\pi$ phases as a function of $h_C$ with sharp transitions. A transition from 0 to $\pi$ can also be obtained by gap closing ($h/\Delta = 1$). Phase diagrams (c) and critical current (d) of the ferromagnetic hybrid junction in the presence of spin-orbit coupling such that $\boldsymbol{\kappa} \cdot \mathbf{h} = 0$. Spin-orbit coupling leads to general suppression of the $\pi$ phase and the expansion of the metastable phases. Parameters: $\mu_C = 1\,\mathrm{meV}$, $\mu_{\mathrm{lat}} = 4\,\mathrm{meV}$, $\ell_B = 0\,\mathrm{nm}$.

that is a rotation in spin space around the $z$ axis by an angle $\theta$, potentially inhomogeneous in space. Using $\theta = \arctan(\beta/\alpha_z)$, we can always remove the term proportional to $\sigma_x$ and align the spin-orbit vector in the $y$ direction. This transformation, however, also rotates the exchange field. This result illustrates the equivalence between inhomogeneous spin-orbit fields and exchange fields.

We first focus on the homogeneous spin-orbit situation, displayed in Fig. 4.19 (c) and (d). Although spin-orbit coupling splits the Fermi surface, Cooper pairs do not acquire a finite momentum unless time-reversal symmetry is broken. Thus, the oscillation between triplet and singlet components is absent, and it is impossible to obtain a $\pi$ phase. At a finite magnetic field, the Rashba term couples the two spin-split ABSs reopening the gap, unless the field aligns with the spin-orbit vector $\boldsymbol{\kappa}$. The effect on the CPR of a transverse Rashba field is a substantial reduction of the $\pi$ regions and an enlargement of the metastable phases. When the exchange field $\mathbf{h}$ is instead aligned with $\boldsymbol{\kappa}$, the spin-rotation symmetry is unbroken. This allows for $\pi$ phases, but simultaneously, the system remains gapless for $h > \Delta$.

Anomalous Josephson effects can occur when a spin-orbit coupling vector is aligned with a magnetic field [248]. However, it is not observed in the homogeneous case as the combination of various spin-rotation symmetry-breaking effects is necessary for its manifestation [249]. This can occur, for instance, due to finite spin-splitting with a non-zero component in both the junction direction and the transverse one [250], or multiple modes that can hybridize [251]. The presence of anomalous currents in similar systems has been considered in Refs. [252, 253].
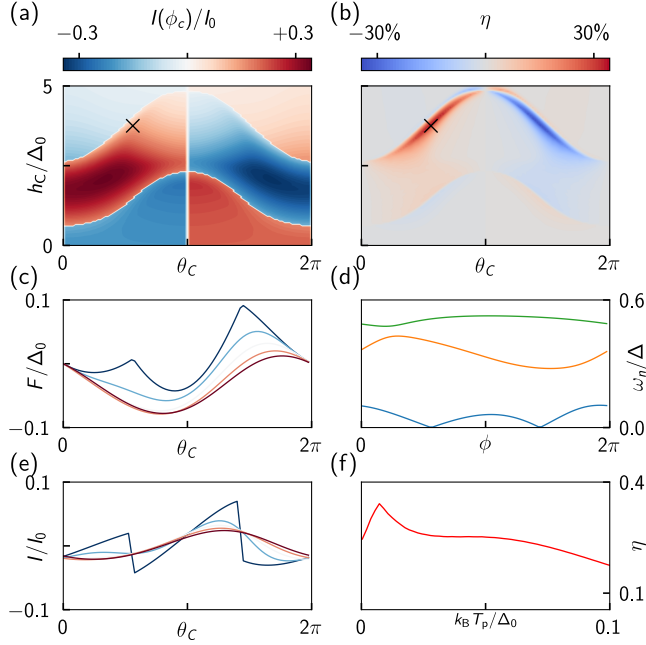
Fig. 4.20: **Non-reciprocal behavior.** We introduce a spin-orbit coupling $\kappa = 2\,\text{nm eV}$, misaligned with an angle $\theta_C$ between the central and the lateral regions. Panel (a) shows the current at the critical phase, while the diode efficiency is shown in (b). (c) The Josephson potential and (e) CPR for a specific point of the parameter space [black cross in (a)] are displayed for increasing temperature. Non-reciprocal behavior shows a non-monotonic temperature dependence, evident in panel (f). This can be explained by the ABS spectrum [panel (d)] that comprises a reciprocal lowest state. Therefore, increasing the temperature suppresses the reciprocal contribution increasing the efficiency. Parameters: $\mu_C = 1\,\text{meV}$, $\mu_{\text{lat}} = 4\,\text{meV}$, $\ell_B = 0\,\text{nm}$, $h_{\text{lat}} = 0.8\Delta$, $\kappa = 2\,\text{meV nm}$.

The spin-orbit field depends on the local electrostatic environment. For this reason, the spin-orbit direction can have different magnitudes and directions in different regions of the ferromagnetic hybrid junction. We consider this situation in Fig. 4.20. The spin-orbit direction is misaligned in the central region by an angle $\theta_C$ with respect to the lateral ones, while we consider a homogeneous exchange field. Since the Rashba field is proportional to the electric field, this scenario might appear in Josephson junctions due to a varying electrostatic environment. This is equivalent to a homogeneous spin-orbit coupling field and a misaligned exchange field in the three regions. In this case, the CPR shows a non-reciprocal behavior, $I(\phi) \neq I(-\phi)$, due to the presence of anomalous $\sin(k\phi)$ terms in the Josephson potential. The non-reciprocal supercurrent has been recently reported in superconductor-semiconductor nanowires [237]. We now define the critical phase as $\phi_c \equiv \text{argmax}_{[0,2\pi]} |I|$. To measure the non-reciprocal behavior, we also define the diode efficiency as $\eta \equiv [\max(I) + \min(I)]/[\max(I) - \min(I)]$. For the parameters considered, the efficiency can be as high as 30% in the region close to the $0-\pi$ transition. For this point, the CPR shows a characteristic form $I(\phi) \sim \sin(\phi - \phi_0) +$

$\cos(2\phi)$.

The rectification effect exhibits a non-monotonic temperature dependence $\eta(T_p)$ that shows a maximum at finite temperature. This can be explained by the ABS spectrum, see Fig. 4.20 (d): the lowest state is dominated by the $\cos(n\phi)$ contribution, with a weak non-reciprocal behavior. The first excited state has a predominant $\sin(\phi)$ contribution. Therefore, increasing the temperature increases the non-reciprocal supercurrent contribution through an interference process of the different CPR harmonics [236]. At higher temperatures, more states become populated, washing out the contribution from the harmonics and leading to a sinusoidal CPR, Fig. 4.20(e).

**Interpretation of the experiment**

The results of the analysis suggest that the ferromagnetic hybrid junction explored in the experiment reported are in an intermediate regime between the dot and the open regime. No substantial sensitivity to gate voltage has been reported, signaling that the levels in the central region are strongly hybridized with the lateral region states. Since the open regime requires higher exchange fields to reach the $\pi$ phase, this also suggests a strong ferromagnetic proximity effect from the magnetic insulator. Moreover, the presence of the $\pi$ phase put some limits on the strength of the spin-orbit coupling in the structure.

## 4.7 Summary of the research activity

Ferromagnetic hybrid heterostructures offer new avenues for supercurrent spintronics, superconducting circuitry, and quantum information processing. In this chapter, we presented some advancements in this field. The research activity started by reviewing the theory of ferromagnetic proximity effects in superconductors and semiconductors and studying how this applies to the systems of interest.

We started the activity by analyzing the results on topological superconductivity presented in Ref. [73]. We proposed an argument against the idea that the indirect proximity effect of a spin-split superconductor can be the dominant mechanism in this structure, Sec. 4.3 and Ref. [P1]. We then proposed an alternative mechanism based on spin-polarized tunneling. The thin ferromagnetic insulator acts as a spin-filter barrier for electrons tunneling through, inducing a sufficiently large exchange field that gives rise to a topological transition in the tripartite heterostructure.

We detailed this idea with accurate numerical simulations in Sec. 4.4 and Ref. [P2]. We have proposed a planar heterostructure for topological superconductivity using a thin ferromagnetic insulator between a 2DEG and a superconductor. In this geometry, superconducting stripes define quasi-1D wires that can be gated from the top, avoiding bottom gates that might be ineffective due to the rather thick substrates needed to create high-quality semiconducting heterostructures. We compared this geometry with the hexagonal nanowire one finding significant improvements with respect to previous hexagonal nanowire geometries, where these gaps were only possible by fine-tuning side gates to push the wavefunction sufficiently close to the ferromagnetic insulator-superconductor layers. We associate this behavior with the vertical confinement of the wavefunction for thin semiconductor layers. Most importantly, this vertical confinement also helps to create a rather regular phase diagram, with topological

and trivial phases appearing at controlled values of the top-gate potential. Experimentally, this is an advantageous property since it permits searching for the topological phase in a predictable manner rather than randomly scanning parameters, as is typically the case with hexagonal nanowires. The proposed stacking allows to define and control of complex networks of topological superconductor wires. The presented planar structure requires no magnetic field to reach the topological phase, allowing for different orientations of the effective wires. This opens the door to experimentally access a new set of problems, including multi-terminal junctions for braiding experiments and unconventional Josephson junctions.

In the second part of this chapter, we focused on ferromagnetic hybrid junctions. We first analyzed the results of experiments, subject of Ref. [P6]. We show that junctions can experience a magnetization-induced $0–\pi$ transition, identified by supercurrent reversal. The junction is configurable through the application of external fields that change the micromagnetic configuration of the ferromagnet. We presented a simple model able to explain the $0–\pi$ transition in such systems. The induced exchange field in the semiconductor can overcome the induced pairing potential without causing a transition to the normal state. This results in spin-polarized Andreev bound states with opposite spin crossing the Fermi level, leading to the $0–\pi$ phase transition and supercurrent reversal.

We then broaden the scope of the theoretical investigation to first analyze the controllability of the transition by means of an electrostatic gate and the possibility of higher harmonics in the current-phase relation becoming dominant close to the $0–\pi$ transition, where the supercurrent changes sign. In the dot regime (weak coupling to the leads), the $\pi$ depends on the relative position of the dot levels with respect to the leads' chemical potential. In case the junction is tuned into the open regime (large coupling to the leads), the onset of the $\pi$ phase is less sensitive to changes in chemical potential. We find that the spin-orbit coupling increases the coexisting region between 0 and $\pi$ phases with considerable amplitudes of higher-harmonic components. Finally, we find that non-collinear spin-orbit coupling in the junction, due to a varying electrostatic environment, results in a supercurrent rectification effect whose efficiency peaks around $0–\pi$ transition.

The tunability of the harmonic content of CPRs is relevant for a number of applications, including superconducting diodes [230–237], ferromagnetic transmon qubits [254], and parity-protected qubits [P5, 226–229]. In this context, ferromagnetic junctions in the open regime are a promising option thanks to their robustness to fluctuations in the charge environment.

# Parity-protected superconducting qubits

*Never trust a computer you can't throw out a window.*

*– Steve Wozniak (apocryphal)*

This chapter explores an alternative platform for quantum information processing, *superconducting qubits*. Superconducting qubits have emerged as one of the leading platforms for building quantum computers due to their scalability, long coherence times, and compatibility with existing fabrication technologies. In superconducting qubits, electromagnetic modes of superconducting circuits store the quantum information. The most widespread type of superconducting qubit is the transmon [255], a highly promising platform for noisy intermediate-scale quantum (NISQ) devices [256] and error-corrected quantum computers [257–260]. Among the most attractive features of the transmon circuit are its reproducibility, insensitivity to charge noise-induced dephasing, and coherence times that have seen steady improvements over the past decade [261].

The subject of this chapter are *Parity-Protected superconducting Qubits* (PPQ) [226, 227, 229, 262–264]. PPQs rely on special Josephson elements that only permit the tunneling of pairs of Cooper-pairs. Such circuit elements can be realized utilizing ferromagnetic hybrid junctions, introduced in the last part of Ch. 4, where the phase dispersion can be tuned to a pure $\cos(2\phi)$ component. Alternatively, similar behavior can be obtained with SQUID-based devices featuring superinductors [226] or nonsinusoidal Josephson junction, as discussed in Appendix A.

Similar to the transmon qubit, the two nearly-degenerate ground states of the PPQ have a nearly flat charge dispersion, which makes them insensitive to charge-noise-induced dephasing. Differently from the transmon, PPQs exhibit *intrinsic protection* to errors. The two-qubit states also have disjoint support since they carry opposite Cooper-pair parity. This disjoint support prevents relaxation errors between the computational states if the qubit-environment coupling conserves the Cooper-pair parity.

As is often the case, intrinsic protection comes with the drawback of more complicated quantum state control. Considerable efforts have been devoted to developing a gate set for protected superconducting qubits [265–267]. While there is ample room for improvement, we can envision a different mode to utilize PPQ and, in general, protected superconducting qubits. Protected qubits can be a component of an *heterogeneous quantum architecture*. With this word, we mean integrating protected qubits as memory elements in a conventional transmon-based quantum computing architecture. In such heterogeneous architecture, the qubit state is stored on the protected qubit during idle times and transferred to the transmon qubits for fast, high-fidelity operations using the full machinery of well-established high-fidelity transmon operation.

After introducing superconducting qubits in Sec. 5.1, this chapter presents transmons (Sec 5.2), and PPQs (Sec. 5.3), as a special case of *generalized k-transmons* (Sec. 5.4). Finally, Sec. 5.5 discusses the coupling of the two PPQs with flux-tunable transmons, including possible errors affecting the scheme.

## 5.1   Introduction to superconducting qubits

Consider a device formed by a Josephson junction that connects two superconducting islands placed very close to each other. While the Josephson junction allows for a dissipationless current to flow, the current causes the building of a charge dipole between the two islands. This dipole will tend to restore the original charge configuration, leading to oscillatory behavior.

The effect of the charge dipole can be described by introducing a capacitance $C$ that is the sum of the junction's intrinsic capacitance and any shunting capacitance added to the circuit. The Hamiltonian term for the dipole contribution reads as

$$H_C = 4E_C(n - n_g)^2 , \tag{5.1}$$

where $n$ is the difference in the number of Cooper pairs in the two islands, $E_C = e^2/2C$ is the charging energy, while $n_g$ is the static charge. This is induced by a biasing gate, that is controllable, as well as uncontrollable background charges and unpaired electrons that fluctuate on some large time scale. The contribution originating from unpaired electrons is discrete and changes by $\pm 1/2$ upon a quasiparticle tunneling across the junction; the background charge instead may vary continuously [268]. The charge operator in Eq. 5.1 is connected to the phase difference operator by the canonical commutation relation $[\phi, n] = i$. Consequently, it can be expressed as a differential operator, $n = i\partial/\partial\phi$.

We can write the Hamiltonian as the sum of the Josephson energy and the charging energy resulting in

$$H = 4E_C(n - n_g)^2 - \sum_k E_{Jk} \cos(k\phi). \tag{5.2}$$

As discussed in the previous chapter, each harmonic in the decomposition of the Josephson potential corresponds to the tunneling of multiplets of Cooper pairs. A way to visualize this decomposition is by rewriting the expression in the charge basis and interpreting $\exp(ik\phi)$ as a translation operator. The result is

$$\begin{aligned} H_J &= \sum_k E_{J,C_k} \cos(k\phi) + E_{J,S_k} \sin(k\phi) \\ &= \sum_n \sum_k \frac{E_{J,C_k} + iE_{J,S_k}}{2} |n + k\rangle \langle n| + \text{h.c.} \end{aligned} \tag{5.3}$$

where $|n\rangle$ is the state with a difference of $n$ Cooper pairs in the two leads. In this way, it is easy to see how, e.g., a term $\cos(2\phi)$ mediates the tunneling of pairs of Cooper pairs. In the next section, we will consider the case where there is a single dominant harmonic in the Josephson potential while the other harmonics, if present, act as perturbations. We will call this kind of system generalized transmon. The transmon is the case for a dominant fundamental harmonic, a $\cos(\phi)$ potential, the PPQ has a dominant $\cos(2\phi)$ term, while a generalized $k$-transmon has a dominant $k$th component.

## 5.2 Transmons

The transmon, proposed in 2007 as an improved version of the Cooper pair box qubit [255], is currently the most common type of superconducting qubits [269]. Its circuit model can be seen as an LC resonator where the linear inductance has been substituted with a nonlinear Josephson junction. This nonlinearity makes it possible to control specific states since each transition will have a different frequency. At a practical level, it is realized by shunting the Josephson junction with a large capacitor to reduce the charging energy.

The transmon Hamiltonian reads as

$$H = 4E_C(n_t - n_g)^2 - E_J \cos(\phi_t). \tag{5.4}$$

The fundamental quantity that describes the behavior of the system is the ratio $E_J/E_C$. As shown in Fig. 5.1(a), the sensitivity to the offset charge decreases as $E_J/E_C$ increases. This is the fundamental characteristic that determines the excellent performance of this quantum device since charge noise is the least controllable noise source.
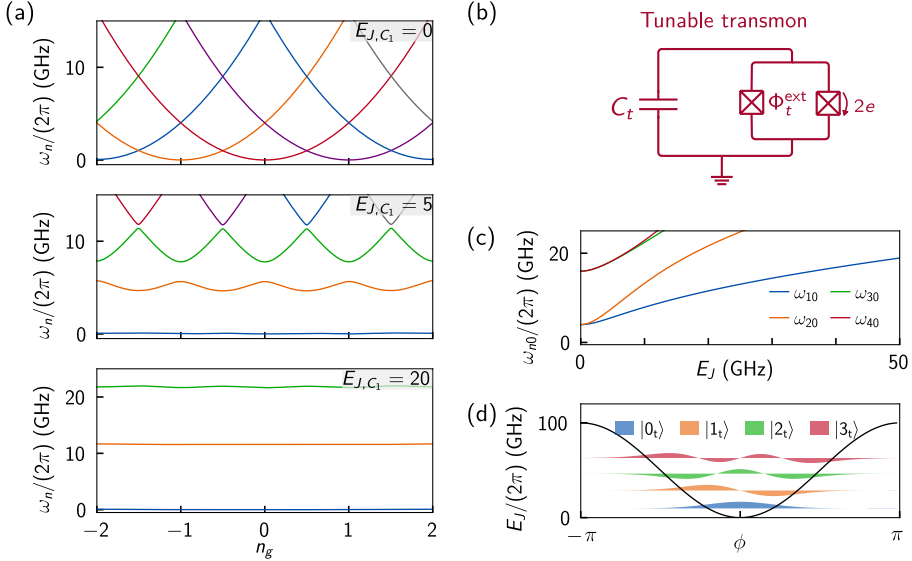


Fig. 5.1: **Transmon qubit.** (a) Charge dispersion for a transmon qubit for increasing value of $E_J$. For $E_J = 0$, there is one parabola for each integer value of $n_g$. The introduction of a finite $E_J$ opens gaps at the crossing point of the parabola. A large $E_J/E_C$ ratio flattens the charge dispersion relation, determining the insensitivity to charge noise. ($E_C = 1$ GHz) (b) Circuit diagram of a tunable transmon circuit. The use of a SQUID in place of the Josephson junction makes it possible to control the effective Josephson energy of the transmon b varying the external flux $\Phi_t^{\text{ext}}$. (c) Levels energy difference for a transmon as a function of $E_J$. (d) The four lower eigenstates of a transmon in phase space on top of the Josephson potential (black line).

Using the approximation scheme we will introduce in Sec. 5.4, it is possible to prove that the energy difference between level $|1_t\rangle$ and $|0_t\rangle$, and between $|2_t\rangle$ and $|1_t\rangle$ are

$$\omega_{10} \simeq \omega + \alpha$$
$$\omega_{21} \simeq \omega + 2\alpha$$

(5.5)

where we define the frequency $\omega = \sqrt{8E_J/E_C}$ and the anharmonicity $\alpha = -E_C$

The transmon has a negative anharmonicity, causing the inter-level separation to decrease climbing the energy ladder. The anharmonicity makes it possible to manipulate a single pair of levels without the risk of causing undesired transitions. To provide a reference, $\omega_{10}$ is usually in the range 3-6 GHz, while $\alpha$ is around 100-300 MHz [269].

Transmons come in two versions: fixed-frequency and tunable-frequency. Fixed-frequency transmons have a resonant frequency determined during their fabrication process and cannot be changed. In contrast, tunable-frequency transmons use a SQUID instead of a Josephson

junction, which allows for control of the resonant frequency. As discussed in Appendix. A, in the case of junctions with sinusoidal CPR, the effective phase dispersion of the SQUID is

$$E_J = E_{J,\Sigma} \sqrt{\cos^2(\phi^e) + d^2 \sin^2(\phi^e)} \tag{5.6}$$

where $E_{J,\Sigma} = E_{J1} + E_{J2}$ and $d = (\gamma - 1)(\gamma + 1)$ with $\gamma = E_{J2}/E_{J1}$. In this case, the $E_J$ parameter of the circuit is tuned by the flux that pierces the mesh between the two junctions.

In flux-tunable transmons, two-qubit gates can be achieved using a direct capacitive coupling between the qubits without the need for a resonator. In this small introduction, we have not discussed the implementation of single and two-qubit gates in flux-tunable transmons. They are not necessary to understand the coupling scheme in Sec. 5.5 and are extensively discussed in the literature, like Ref. [269].

## 5.3 Parity-protected qubits

In PPQs, the standard Josephson junction in the transmon is substituted with a special $\cos(2\phi)$ junction that is dominated by the second harmonic, as shown in the circuit in Fig. 5.2(b). This special Josephson element only permits the tunneling of pairs of Cooper pairs. As a consequence, the Cooper-pair parity is a conserved quantity, and the eigenstates of the Hamiltonian are composed of only even or only odd states. In phase space, the eigenstates wavefunctions are symmetric and anti-symmetric combinations of states that are localized in the 0- and $\pi$-valleys of the Josephson potential, see Fig. 5.2(d).

The charge dispersion of this quantum device is shown in Fig. 5.2(a): as in the case of the transmon, the Josephson junction opens gaps in the spectrum, but this time it preserves the crossings between the parabolas of different Cooper pair parity sectors. The remaining spectrum shows a periodicity of $2n$. For odd values of $n_g$, the two states in each pair swap, while for half-integer values, they are degenerate.

Due to this disjoint support of the charge space wavefunctions, $\langle 0_p | \mathcal{O} | 1_p \rangle = 0$ for any operator $\mathcal{O}$ that preserves the Cooper-pair parity, which is the condition for protection against parity-preserving relaxation errors [263]. As $E_J$ increases, the energy separation between the states in the pair decreases exponentially, see Fig. 5.2(c).

### Single-qubit gates

For implementing single-qubits gates, we consider the generalized circuit for a PPQ depicted in Fig. 5.3(a). The circuit comprises not only a $\cos(2\phi_p)$ element for the tunneling of pairs of Cooper pairs but also a $\cos(\phi_p)$ and $\sin(\phi_p)$ element that describes the tunneling of single Cooper-pairs. The Hamiltonians for these additional circuit elements are given by,

$$\begin{aligned} H^x &= -\varepsilon^x \cos(\phi_p), \\ H^y &= -\varepsilon^y \sin(\phi_p), \end{aligned} \tag{5.7}$$

While both additional circuit elements permit single Cooper-pair tunnelings and temporarily lift the qubit protection, they are typically tuned by different control parameters, depending on the experimental implementation of the PPQ [226, 227]. For example, if the PPQ is realized in a nanowire Josephson interferometer, as the one discussed in Appendix. A, then the sinusoidal
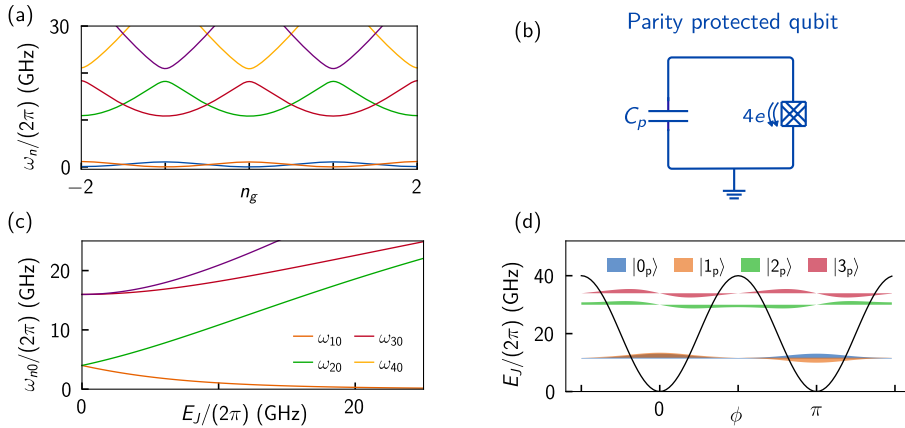
Fig. 5.2: **Parity-protected qubit.** (a) Charge dispersion relation of a PPQ. Note how the eigenstates are $2n_g$-periodic. (b) Circuit description of a PPQ. (c) Levels energy difference for a PPQ as a function of $E_J$. Note that, in this case, $\omega_{10}$ decreases with the Josephson energy and becomes degenerate in the high $E_J/E_C$ limit. The same happens for level $|2_p\rangle$ and $|3_p\rangle$. (d) The four lower eigenstates of a PPQ in phase space on top of the Josephson potential (black line). In the high $E_J/E_C$ limit, these states can be seen as the bonding and anti-bonding superposition of the levels of two harmonic wells.

term arises if the interferometer junctions are tuned out of balance by local gate electrodes. In contrast, the cosinusoidal term arises when the interferometer magnetic flux is biased away from half flux quantum [227, 229]. In the case of the ferromagnetic hybrid junction, described in Sec. 4.5 and 4.6, both of them can be controlled through electrostatic gating.

We now project the Hamiltonians $H_p + H^x$ and $H_p + H^y$ onto the computational subspace of the PPQ. The resulting qubit Hamiltonians read,

$$H_{\text{eff}}^x = \delta\omega_p \cos(\pi n_{g,p})\,\sigma_p^z/2 + \delta h^x \sigma_p^x,$$
$$H_{\text{eff}}^y = \delta\omega_p \cos(\pi n_{g,p})\,\sigma_p^z/2 + \delta h^y \sin(\pi n_{g,p})\,\sigma_p^y. \tag{5.8}$$

From this result, we see that the $\cos(\phi_p)$ and $\sin(\phi_p)$ elements induce rotations around the $x$- and $y$-axis of the Bloch sphere. The respective matrix elements are given by $\delta h^x = \langle 0_p|H^x|1_p\rangle$ and $\delta h^y \sin(\pi n_{g,p}) = \langle 0_p|H^y|1_p\rangle$. The dependence of these matrix elements on the offset charge $n_{g,p}$ is shown in Fig. 5.3(b). Since we can reach any point on the Bloch sphere through a combined rotation around the $x$- and $y$-axis, we conclude that the free time evolution of the Hamiltonians in Eq. (5.8) can implement a complete set of single-qubit gates. However, we also emphasize that these single-qubit gates break the Cooper-pair parity conservation so that the PPQ is prone to relaxation errors during the operation time of the single-qubit gates.

## 5.4 $k$-transmon and harmonic approximation

The transmon and the parity-protected qubit can be seen as a special case of a more *generalized transmon*, or *k-transmon*. We define the *k*-transmon as a Cooper pair box where the Josephson
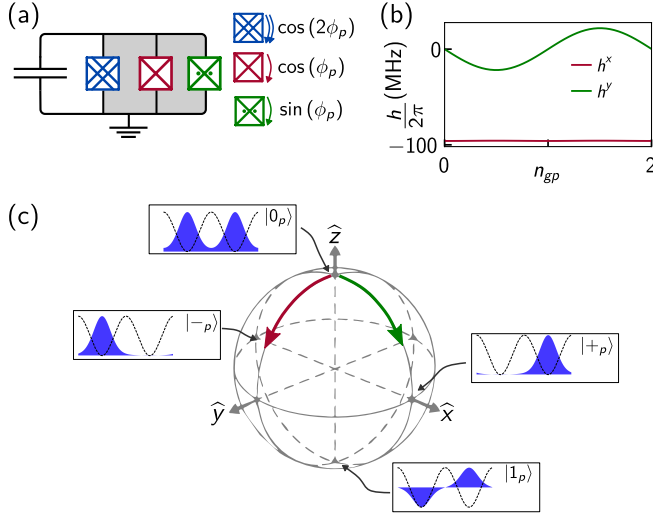
Fig. 5.3: **Single-qubit gates.** (a) A generalized PPQ circuit with three circuits elements; a $\cos(2\phi_p)$ element (blue), a $\cos(\phi_p)$ element (red), and a $\sin(\phi_p)$ element (green). No magnetic flux is threading the gray areas of the circuit. (b) Dependence of the matrix element $h^x$ (resulting from the $\cos(\phi_p)$ element) and $h^y$ (resulting from the $\sin(\phi_p)$ element) as a function of $n_{g,p}$. The system parameters are $(E_{J,p}, E_{C,p}) = 2\pi(2.7, 0.18)\,\mathrm{GHz}$ and $(\varepsilon_x/E_{J,p}, \varepsilon_y/E_{J,p}) = (0.04, 0.2)$. (c) The $\cos(\phi_p)$ element induces rotations around the $x$-axis of the Bloch sphere (red arrow). The $\sin(\phi_p)$ element induces rotations around the $y$-axis of the Bloch sphere. The wavefunctions of the PPQ in the $z$-basis ($|0_p\rangle, |1_p\rangle$) and in the $x$-basis ($|+_p\rangle, |-_p\rangle$) are shown schematically.

potential is dominated by only the $k$-th harmonic component with a Hamiltonian that reads as

$$H^{(k)} = 4E_C\left(i\frac{\partial}{\partial\phi} - n_g\right)^2 - E_{J,C_k}\cos(k\phi). \tag{5.9}$$

Such a hypothetical device is not suitable to work as a qubit, as the ground state is $k$-fold degenerate. But it could be used as an element of a circuit for quantum simulations.

This Hamiltonian is amenable to an approximate analytical treatment. First of all, the offset charge can always be removed by the unitary transformation $U = e^{in_g\phi}$ resulting in the Hamiltonian

$$H = -4E_C\frac{\partial^2}{\partial\phi^2} - E_{J,C_k}\cos(k\phi). \tag{5.10}$$

and in a modified boundary condition

$$\psi(\phi + 2\pi) = e^{i2n_g\pi}\psi(\phi). \tag{5.11}$$

In the ideal transmon limit $E_J/E_C \to \infty$, the ground state is $k$-degenerate, and the low energy states are localized in the minimum of the Josephson potential $E_J$ that are located at

points $\phi_j^k = 2\pi j/k$. We can expand the potential around these minima

$$V_J/E_{Jk} = \cos(k\phi) \simeq 1 - k^2 \frac{\left(\phi - \overline{\phi}\right)^2}{2} + k^4 \frac{\left(\phi - \overline{\phi}\right)^4}{24} + o(\phi^6)$$ (5.12)

and, for small fluctuations near the minimum, we can use the quadratic approximation and rewrite the Hamiltonian as an anharmonic oscillator

$$H_k^j = +4E_C n^2 + E_{Jk} \frac{k^2}{2}(\phi - \phi_k^j)^2 + H_{\mathrm{nl}}.$$ (5.13)

where $H_{\mathrm{nl}}$ contains the higher order terms. We then rescale the Hamiltonian by introducing the parameter $\xi$ and the rescaled coordinates $\tilde{n} = n/\xi$ and $\tilde{\phi} = \xi\phi$. In this way, the commutation relation $[\tilde{\phi}, \tilde{n}] = i$ is preserved. Using $\xi^{(k)} = \sqrt[4]{8E_C/k^2 E_{J,C_k}}$ the Hamiltonian becomes

$$H_k^j = \omega^{(k)} \left( \frac{\tilde{n}^2}{2} + \frac{\tilde{\phi}^2}{2} \right) + H_{nl}$$ (5.14)

with the frequency $\omega^{(k)} = \sqrt{8k^2 E_{J,C_k}/E_C}$.

The eigenfunctions of these harmonic oscillators read as

$$\psi_{jn}^{(k)}(\phi) = \frac{1}{\sqrt{2^n n!}} \left[ \frac{(\xi^{(k)})^2}{\pi} \right]^{1/4} e^{-\frac{[\xi^{(k)}(\phi - \phi_j)]^2}{2}} H_n \left[ \xi^{(k)}(\phi - \phi_j) \right].$$ (5.15)

and can be used as a basis to project the full Hamiltonian.

We start by considering the quartic term in $H_{\mathrm{nl}}$: by defining $a = (\tilde{\phi} + i\tilde{n})/\sqrt{2}$ we can write the Hamiltonian for the well as

$$H = \omega^{(k)} a^\dagger a - \frac{E_C}{12} \left( a + a^\dagger \right)^4$$ (5.16)

that is the Hamiltonian of a Duffing oscillator. A first-order perturbation study provides the anharmonic correction to the eigenstates energies

$$\omega_j = \omega^{(1)} n - \frac{E_C}{12}(6n^2 + 6n + 3).$$ (5.17)

We now proceed by modeling the system as a collection of coupled Duffing oscillators. By defining the annihilation operator $a_j$ for an excitation in the valley $j$, we can write the effective Hamiltonian as

$$\tilde{H}^{(k)} = \sum_{j=1}^{k} \left[ \omega^{(k)} a_j^\dagger a_j + \frac{\alpha^{(k)}}{2} a_j^\dagger a_j^\dagger a_j a_j + t^{(k)}(a_j^\dagger a_{j+1} + \mathrm{H.c.}) \right] + t^{(k)} \left( e^{i n_g 2\pi} a_k^\dagger a_1 + \mathrm{H.c.} \right).$$ (5.18)

where we can approximate the internal nearest neighbor hopping amplitude as

$$t_{nn'}^{(k)} = \left\langle jn \middle| H^{(k)} \middle| (j+1)n' \right\rangle.$$ (5.19)

By translation invariance, this integral does not depend on $j$ as long the hopping is in the unit cell. However, there is an additional phase when the hopping term involves states in two adjacent charge sectors. For example, in the case of a 4-transmon, the hopping energy would read as

$$\tilde{H}^{(4)} = t^{(4)} \begin{pmatrix} 0 & 1 & 0 & e^{in_g 2\pi} \\ 1 & 0 & 1 & 0 \\ 0 & 1 & 0 & 1 \\ e^{-in_g 2\pi} & 0 & 1 & 0 \end{pmatrix} \tag{5.20}$$

Then the dispersion relation for the low-energy subspace of a $k$-transmon in the harmonic approximation reads

$$\varepsilon_j(n_g) = 2t^{(k)} \cos\left[\frac{2\pi}{k}(j + n_g)\right]. \tag{5.21}$$

For the conventional transmon, the $|0\rangle$ and $|1\rangle$ states have different energy given by the two lowest energy states with a gap $\omega^{(1)}$

$$H^{(1)} = +\omega^{(1)}\frac{\sigma_z}{2} - \sigma_x t_{01}^{(1)}\cos(2\pi n_g) \tag{5.22}$$

while for the parity-protected qubit

$$H^{(2)} = t_{00}^{(2)}\left[\cos(n_g 2\pi)\sigma_x + \sin(n_g 2\pi)\sigma_y\right] \tag{5.23}$$

The spectrum of a 4-transmon is displayed in Fig. 5.4(a). The spectrum resemble the one of the PPQ, but this time the gap is opened only between the parabola corresponding to states that belong to a charge congruent modulo 4. As a result, there are subspaces formed by 4 states that oscillate with periodicity $4n$.
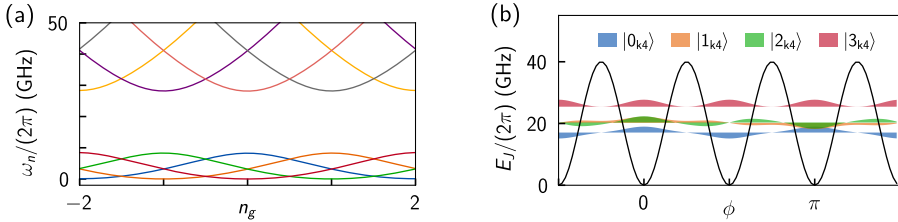


Fig. 5.4: **Energy levels of a 4-transmon.** (a) Charge dispersion relation of a 4-transmon. (b) Wavefunctions of a 4-transmon.

## 5.5 Heterogeneous quantum architecture

As depicted in Fig. 5.5(a), we consider a direct capacitively coupling between a frequency-tunable transmon qubit and a PPQ, realized by a capacitively-shunted $\cos(2\phi)$ Josephson element for the tunneling of pairs of Cooper-pairs. The individual Hamiltonians of the transmon, $H_t$, and of the PPQ, $H_p$, are given by,

$$\begin{aligned} H_t &= 4E_{C,t}(n_t - n_{g,t})^2 - E_{J,t}\cos(\phi_t), \\ H_p &= 4E_{C,p}(n_p - n_{g,p})^2 - E_{J,p}\cos(2\phi_p). \end{aligned} \tag{5.24}$$
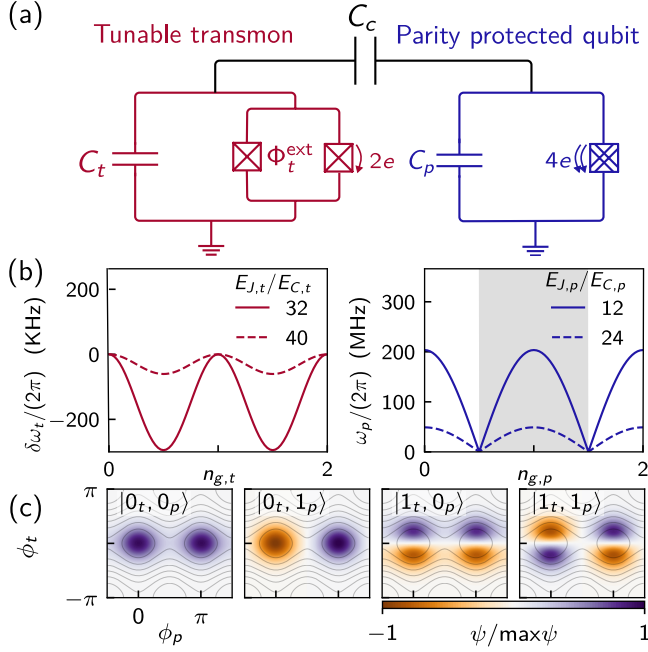
Fig. 5.5: **Heterogeneous qubit setup.** (a) A frequency-tunable transmon (red) coupled to a PPQ (blue) realized by a capacitively-shunted tunneling element for pairs of Cooper-pairs (Josephson junction symbol with double lines). The two qubits are coupled via a coupling capacitance $C_c$. (b) Zoom-in on the charge dispersion relation for the transmon (left panel) and the PPQ (right panel). In the gray area, the ground (first excited) state carries odd (even) Cooper-pair parity. In the white area, the order is inverted. (c) Wavefunctions of the decoupled system ($C_c = 0$). The system parameters are $(E_{J,t}, E_{J,p}, E_{C,t}, E_{C,p}) = 2\pi (10, 3, 0.25, 0.25)\,\text{GHz}$.

Here, $(n_t, \phi_t)$ and $(n_p, \phi_p)$ denote Cooper-pair charge and phase degrees of freedom of the transmon and PPQ. Moreover, $E_{J,t}$ is the transmon Josephson energy and $E_{J,p}$ is the two-Cooper-pair tunneling amplitude of the PPQ. The charging energies of the two qubit circuits are $E_{C,t} = e^2/2C_t$ and $E_{C,p} = e^2/2C_p$ with the shunt capacitances $C_t$ and $C_p$.

Both Hamiltonians in Eq. (5.24) can be diagonalized exactly by rewriting the eigenvalue problems as Mathieu equations. For the transmon [255], the energy splitting between the ground and first-excited state, which form the qubit basis $|0_t\rangle$ and $|1_t\rangle$, is $\omega_t = \sqrt{8E_{J,t}E_{C,t}} + \delta\omega_t$ with $\delta\omega_t \propto \exp(-\sqrt{8E_{J,t}/E_{C,t}})\cos(2\pi n_{g,t})$ for $E_{J,t} \gg E_{C,t}$, see the left panel of Fig. 5.5(b). For the PPQ [226], the qubit basis is given by the two lowest-energy states with even and odd Cooper-pair parity, $|0_p\rangle$ and $|1_p\rangle$. These states have an exponentially suppressed energy splitting, $\omega_p \propto \exp(-\sqrt{2E_{J,p}/E_{C,p}})|\cos(\pi n_{g,p})|$ for $E_{J,p} \gg E_{C,p}$, see the right panel of Fig. 5.5(b). Unlike the transmon, the PPQ is thus a low-frequency qubit with the computational states exhibiting an exact degeneracy if $\cos(\pi n_{g,p}) = 0$ and a near-degeneracy otherwise. However, like the transmon, the energy splitting of the PPQ is insensitive to variations in $n_{g,p}$ if $E_{J,p} \gg E_{C,p}$, which ensures insensitivity to charge noise dephasing.

Having introduced the two decoupled qubit circuits with the associated computational
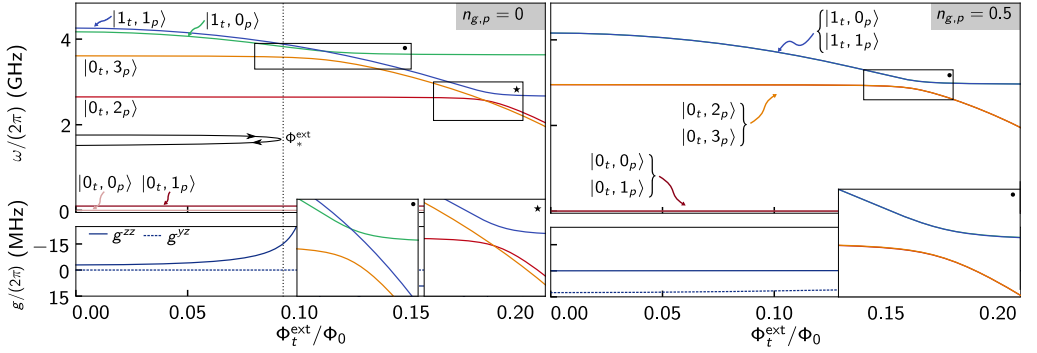
Fig. 5.6: **Low-energy spectrum of the hybrid qubit setup and CZ$_\phi$ gate.** The left panel shows the low-energy spectrum of the hybrid qubit setup for $n_{g,p} = 0$ and $(E_{J,t}, E_{J,p}, E_{C,t}, E_{C,p}, E_{C,c}) = 2\pi(12, 2.7, 0.2, 0.15, 0.025)$ GHz as a function of the external flux $\Phi_{\text{ext}}$ of the tunable transmon. The CZ$_\phi$ gate is realized by a rapid excursion from $\Phi_{\text{ext}} = 0$ to the vicinity of the $|1_t, 0_p\rangle \leftrightarrow |0_t, 3_p\rangle$ anti-crossing at $\Phi_{\text{ext}} = \Phi_{\text{ext}}^*$. The bottom panel shows the coupling strengths, $g^{yz}$ and $g^{zz}$, upon approaching the anti-crossing. The right panel shows the same but for $n_{g,p} = 0.5$. Each shown energy level is now exactly two-fold degenerate.

subspace $\mathcal{P}_0 = \{|1_t, 1_p\rangle, |1_t, 0_p\rangle, |0_t, 1_p\rangle, |0_t, 0_p\rangle\}$, we proceed by coupling the qubits via a standard capacitive coupling (see also Fig. 5.5a) corresponding to a coupling Hamiltonian given by

$$H_c = 4E_{C,c}(n_p - n_{g,p})(n_t - n_{g,t}). \tag{5.25}$$

Here, $E_{C,c} = e^2 C_c/(C_p C_t)$ with the coupling capacitance $C_c$. In summary, the full Hamiltonian of our setup is $H = H_p + H_t + H_c$. In the next section, we will derive the effective qubit interaction due to this direct capacitive coupling.

To motivate the derivation of the effective qubit interaction, we first recall the case of two capacitively coupled transmon qubits, $t1$ and $t2$, which are both 'high-frequency' qubits. In this example, the capacitive coupling mediates a $\sigma_{t1}^y \sigma_{t2}^y$ interaction when projected onto the computational subspace and a $\sigma_{t1}^z \sigma_{t2}^z$ interaction due to the mixing of computational and non-computational states [269]. In our setup, which involves the coupling of a 'high-frequency' transmon qubit and a 'low-frequency' PPQ, we will show that the couplings to non-computational states will play an even more essential role. To anticipate this result, we note that the coupling Hamiltonian of Eq. (5.25) at $n_{g,p} = 0$ vanishes exactly when projected onto the computational subspace, $\langle s_t, s_p'|H_c|s_t'', s_p'''\rangle = 0$ for any two states $|s_t, s_p'\rangle, |s_t'', s_p'''\rangle$ in $\mathcal{P}_0$ since $\langle 0_t|n_t|0_t\rangle = \langle 1_t|n_t|1_t\rangle = 0$ and $\langle 0_p|n_p|1_p\rangle = 0$. A direct coupling within the computational subspace is thus fully absent at $n_{g,p} = 0$ and any qubit interaction, if present, is necessarily mediated by virtual transitions through non-computational states.

### Special case: $n_{g,p} = 0$

To identify the origin of such virtual transitions, we initially compare two special cases with the offset charge on the PPQ set to either $n_{g,p} = 0$ or $n_{g,p} = 0.5$. Starting with the $n_{g,p} = 0$ case, we show the low-energy spectrum as a function of external magnetic flux $\Phi_t^{\text{ext}}$ of the tunable

transmon in Fig. 5.6(a). The spectrum comprises not only the four qubit levels of $\mathcal{P}_0$ but also two additional levels corresponding to the $|0_t, 2_p\rangle$ and $|0_t, 3_p\rangle$ state of the uncoupled system. Interestingly, the *non-computational* states exhibit two anti-crossings with the *computational* states, $|1_t, 1_p\rangle \leftrightarrow |0_t, 2_p\rangle$ and $|1_t, 0_p\rangle \leftrightarrow |0_t, 3_p\rangle$, at certain values of external flux. These anti-crossings arise because the respective couplings preserve the Cooper-pair parity on the PPQ. On the other hand, anti-crossing between $|1_t, 0_p\rangle \leftrightarrow |0_t, 2_p\rangle$ and $|1_t, 1_p\rangle \leftrightarrow |0_t, 3_p\rangle$ are absent from the spectrum in Fig. 5.6(a), as such couplings violate the Cooper-pair parity conservation on the PPQ. We will now show that in the vicinity of the two anti-crossings, virtual transitions in-and-out of the computational subspace are enhanced and, consequently, can induce a sizable effective qubit interaction between the transmon and the PPQ.

For computing the effective qubit interaction at $n_{g,p} = 0$, we initially project our setup Hamiltonian $H$ onto the four qubit states of $\mathcal{P}_0$ and on the additional $|0_t, 2_p\rangle$ and $|0_t, 3_p\rangle$ states. This yields the following low-energy Hamiltonian,

$$H_{\text{low}}^{(n_{g,p}=0)} = \begin{pmatrix} \omega_{11} & 0 & 0 & 0 & \lambda' & 0 \\ 0 & \omega_{10} & 0 & 0 & 0 & -\lambda'' \\ 0 & 0 & \omega_{01} & 0 & 0 & 0 \\ 0 & 0 & 0 & \omega_{00} & 0 & 0 \\ \lambda' & 0 & 0 & 0 & \omega_{02} & 0 \\ 0 & -\lambda'' & 0 & 0 & 0 & \omega_{03} \end{pmatrix}. \tag{5.26}$$

Here, the frequency of the the $|s_t, s'_p\rangle$ state in the uncoupled system is denoted by $\omega_{ss'} = \omega_{t,s}(\Phi_t^{\text{ext}}) + \omega_{p,s'}$. Moreover, the coupling matrix elements are given by $\lambda' = \langle 1_t, 1_p | H_c | 0_t, 2_p\rangle$ and $\lambda'' = \langle 1_t, 0_p | H_c | 0_t, 3_p\rangle$, where we picked a wavefunction gauge for which $(\lambda', \lambda'')$ are real-valued. We point out that the low-energy Hamiltonian of Eq. (5.26) is different from the one of capacitively-coupled transmons [269], because the conservation of Cooper-pair parity prohibits a coupling of the $|0_t, 1_p\rangle$ to the $|1_t, 0_p\rangle$ state. Also, for two coupled transmons only the highest energy computational state exhibits crossing with non-computational states. In our case, the two computational states, $|1_t, 0_p\rangle$ and $|1_t, 1_p\rangle$, both cross with non-computational states, albeit at different values of external flux.

Next, we integrate out the non-computational states to second order in $\lambda'$ and $\lambda''$ by a Schrieffer-Wolff transformation. Provided that $\lambda'^2 \ll |\omega_{02} - \omega_{11}|$ and $\lambda''^2 \ll |\omega_{03} - \omega_{10}|$, we find that the effective qubit Hamiltonian reads,

$$H_{\text{eff}}^{(n_{g,p}=0)} = \left(\omega_t + \frac{g_+^{zz}}{2}\right)\frac{\sigma_t^z}{2} + \left(\omega_p + \frac{g_-^{zz}}{2}\right)\frac{\sigma_p^z}{2} + g_-^{zz}\frac{\sigma_t^z}{2}\frac{\sigma_p^z}{2},$$
$$g_\pm^{zz} = \frac{\lambda'^2}{\omega_{11} - \omega_{02}} \pm \frac{\lambda''^2}{\omega_{10} - \omega_{03}}, \tag{5.27}$$

where $\omega_{p/t} = \omega_{p/t,1} - \omega_{p/t,0}$ denote the bare qubit frequencies. The key insight from Eq. (5.27) is that the interaction between the two qubits is of $\sigma_p^z \sigma_t^z$ type. As anticipated, this interaction arises from a two-step perturbative sequence involving virtual transitions in-and-out of the $|0_t, 2_p\rangle$ and $|0_t, 3_p\rangle$ state. For example, in a perturbative sequence close to the $|1_t, 1_p\rangle \leftrightarrow |0_t, 2_p\rangle$ anti-crossing, the system exhibits a first virtual transition from the computational state $|1_t, 1_p\rangle$ to the non-computational state $|0_t, 2_p\rangle$ and, subsequently, a second virtual transition back to $|1_t, 1_p\rangle$. Such a sequence preserves the state of the transmon, which explains why the

interaction is $\propto \sigma_t^z$. The dependence of the interaction on $\sigma_p^z$ arises because the coupling Hamiltonian of Eq. (5.25) preserves the Cooper-pair parity.

**Special case: $n_{g,p} = 0.5$**

Having derived the qubit interaction at $n_{g,p} = 0$, we want to compare the results of Eq. (5.27) with the $n_{g,p} = 0.5$ case. We therefore plot the low-energy spectrum at $n_{g,p} = 0.5$ in Fig. 5.6(b). Unlike in the previous case, we find that each depicted energy level exhibits an exact two-fold degeneracy, corresponding to opposite Cooper-pair parity sectors. This finding is consistent with our results of Fig. 5.5(b), where we pointed out that the levels on the uncoupled PPQ are exactly degenerate at $n_{g,p} = 0.5$. In particular, the anti-crossings $|1_t,1_p\rangle \leftrightarrow |0_t,2_p\rangle$ and $|1_t,0_p\rangle \leftrightarrow |0_t,3_p\rangle$ occur now at the same value of external flux and overlap exactly. Couplings between $|1_t,0_p\rangle \leftrightarrow |0_t,2_p\rangle$ and $|1_t,1_p\rangle \leftrightarrow |0_t,3_p\rangle$ remain absent (they are forbidden since the states belong to a different parity sector). We will now show that this new scenario at $n_{g,p} = 0.5$ will lead to a different effective qubit Hamiltonian compared to Eq. (5.27).

We begin again by projecting the setup Hamiltonian $H$ onto the qubit subspace $\mathcal{P}_0$ and onto the states $|0_t,2_p\rangle$ and $|0_t,3_p\rangle$. The resulting low-energy Hamiltonian reads,

$$H_{\text{low}}^{(n_{g,p}=0.5)} = \begin{pmatrix} \omega_{11} & 0 & -i\eta & 0 & \lambda & 0 \\ 0 & \omega_{10} & 0 & i\eta & 0 & -\lambda \\ i\eta & 0 & \omega_{01} & 0 & 0 & 0 \\ 0 & -i\eta & 0 & \omega_{00} & 0 & 0 \\ \lambda & 0 & 0 & 0 & \omega_{02} & 0 \\ 0 & -\lambda & 0 & 0 & 0 & \omega_{03} \end{pmatrix}. \tag{5.28}$$

Here, we have $\lambda = \langle 1_t,1_p|H_c|0_t,2_p\rangle = -\langle 1_t,0_p|H_c|0_t,3_p\rangle$ and

$$\eta = i\langle 1_t,1_p|H_c|0_t,1_p\rangle = -i\langle 1_t,0_p|H_c|0_t,0_p\rangle$$

in a wavefunction gauge for which $(\lambda,\eta)$ are real-valued. By inserting the coupling Hamiltonian in the expressions for the matrix elements, we note that $\eta \propto \langle s_p|n_p|s_p\rangle - n_{g,p}$. In the previous case when $n_{g,p} = 0$, we had $\langle s_p|n_p|s_p\rangle = 0$ and, consequently, $\eta$ vanished. In the present case when $n_{g,p} = 0.5$ and $E_{J,p} \gtrsim E_{C,p}$, we have $\langle s_p|n_p|s_p\rangle \neq n_{g,p}$ so that $\eta$ is finite yet gets successively smaller upon increasing $E_{J,p}$. In particular, when $E_{J,p} \gg E_{C,p}$, we have $\langle s_p|n_p|s_p\rangle \to n_{g,p}$ so that the contribution of $\eta$ to the low-energy Hamiltonian is negligible. Lastly, we note that due to the degeneracy of the PPQ levels, $\omega_{p,0} = \omega_{p,1}$ and $\omega_{p,2} = \omega_{p,3}$. Hence, the frequencies of the hybrid setup satisfy $\omega_{11} = \omega_{10}$, $\omega_{01} = \omega_{00}$, and $\omega_{02} = \omega_{03}$.

We now proceed by integrating out the effects of the non-computational states, $|0_t,2_p\rangle$ and $|0_t,3_p\rangle$, with a Schrieffer-Wolff transformation. The resulting effective Hamiltonian is of the form,

$$H_{\text{eff}}^{(n_{g,p}=0.5)} = \left(\omega_t + \frac{g_+^{zz}}{2}\right)\frac{\sigma_t^z}{2} + g^{yz}\sigma_t^y\sigma_p^z,$$
$$g^{yz} = \eta, \tag{5.29}$$

Contrasting this result with Eq. (5.27), we note that both terms $\propto \sigma_p^z$ and $\propto \sigma_t^z\sigma_p^z$ have vanished because $\omega_p = 0$ and $g_-^{zz} = 0$. As a result, the effective qubit interaction is *not* of $\sigma_t^z\sigma_p^z$ but rather

of $\sigma_t^y \sigma_p^z$ type. The physical origin of the interaction at $n_{g,p} = 0.5$ is different from the $n_{g,p} = 0$ case, since it arises directly from the finite matrix elements of the charge operators of the parity-protected qubit and the transmon qubits. The non-computational states induce only a renormalization of the transmon frequency through the $g_+^{zz}$ contribution in the coefficient of $\sigma_t^z$.

**General case**

So far, we have seen that the capacitive coupling between the transmon and the parity-protected qubit induces a qubit interaction that is substantially different for $n_{g,p} = 0$ and $n_{g,p} = 0.5$. In a last step, we want to interpolate between those two representative cases. This interpolation is achieved by studying the dependence on the offset charge $n_{g,p}$ of the various matrix elements. Since the procedure for obtaining the effective interaction is otherwise identical to the special cases, we only note that for generic values of $n_{g,p}$ the effective Hamiltonian acquires both a $\sigma_t^z \sigma_p^z$ and a $\sigma_t^y \sigma_p^z$ interaction term,

$$H_{\text{eff}}^{(n_{g,p})} = \left(\omega_t + \frac{g_+^{zz}}{2}\right)\frac{\sigma_t^z}{2} + \left(\omega_p + \frac{g_-^{zz}}{2}\right)\frac{\sigma_p^z}{2} + g^y \sigma_t^y$$
$$+ g_-^{zz}\frac{\sigma_t^z}{2}\frac{\sigma_p^z}{2} + g^{yz}\sigma_t^y\sigma_p^z. \tag{5.30}$$

While $g_\pm^{zz}$ are defined as in Eq. (5.27), the definition of $g^{yz}$ is now slightly generalized to $g^{yz} = (\eta' + \eta'')/2$ with $\eta' = i\langle 1_t, 1_p | H_c | 0_t, 1_p\rangle$ and $\eta'' = -i\langle 1_t, 0_p | H_c | 0_t, 0_p\rangle$. The transition from a pure $\sigma_t^z \sigma_p^z$ at $n_{g,p} = 0$ to a pure $\sigma_t^y \sigma_p^z$ at $n_{g,p} = 0.5$ is gradual. As for the the dependence on the transmon offset charge, we remark that in the deep-transmon regime, $E_{J,t} \gg E_{C,t}$, the qubit interaction is almost independent of $n_{g,t}$.

So far, we have derived the effective qubit interaction and have demonstrated that it depends on the anti-crossings with the non-computational states, $|0_t, 2_p\rangle$ and $|0_t, 3_p\rangle$. To realize the respective anti-crossings, we note that it is essential that,

$$\omega_{02} < \omega_{10}. \tag{5.31}$$

The transmon energy levels are approximated by $\omega_{t,n} \approx \sqrt{8E_{J,t}E_{C,t}}(n+1/2) - E_{J,t}$ while the PPQ energy levels by $\frac{\omega_{p,2}+\omega_{p,3}}{2} \approx 2\sqrt{8E_{J,p}E_{C,p}} - 4E_{J,p}$. Neglecting the anharmonicity corrections on both qubits, we find that the necessary condition in Eq. (5.31) simplifies to $2\sqrt{E_{J,p}E_{C,p}} < \sqrt{E_{J,t}E_{C,t}}$. This condition is satisfied for the parameters chosen in Fig. 5.6.

**CZ gate**

We will now use the effective Hamiltonian for the hybrid PPQ/transmon setup to implement a controlled-phase gate ($\text{CZ}_\phi$), which will preserve the Cooper-pair parity irrespective of the detailed pulse sequence. In addition, we will also discuss a complete set of single-qubit gates realized by controllably driving the system in-and-out of protection. In combination with the $\text{CZ}_\phi$ gate, these single-qubit gates will permit the coherent state transfer, a SWAP operation, between the transmon and PPQ.

For deriving the $\text{CZ}_\phi$ gate protocol, we initially move to the frame that rotates with the bare qubit frequencies, $\tilde{H}_{\text{eff}}^{(n_{g,p})} = U^\dagger(t) H_{\text{eff}}^{(n_{g,p})} U(t) - iU^\dagger(t)\dot{U}(t)$ with $U(t) = e^{i(\omega_t \sigma_t^z + \omega_p \sigma_p^z)t/2}$. Within

this rotating frame, the effective Hamiltonian reads,

$$
\begin{aligned}
\tilde{H}_{\text{eff}}^{(n_{g,p})} &= \frac{g_+^{zz}}{2}\frac{\sigma_t^z}{2} + \frac{g_-^{zz}}{2}\frac{\sigma_p^z}{2} + g_-^{zz}\frac{\sigma_t^z}{2}\frac{\sigma_p^z}{2} \\
&\quad + [-i\,e^{i\omega_t t}(g^{yz}\sigma_t^+\sigma_p^z + g^y\sigma_t^+) + \text{H.c.}],
\end{aligned}
\tag{5.32}
$$

where we introduced $\sigma^\pm = (\sigma^x \pm i\sigma^y)/2$. We note that the terms $\propto g^{yz}\sigma_t^\pm\sigma_p^z$ and $\propto g^y\sigma_t^\pm$ vanish if $n_{g,p} = 0$. In this situation, the free evolution of the effective Hamiltonian can implement a $\text{CZ}_\phi^{10}$ gate. For executing this $\text{CZ}_\phi^{10}$ gate, we carry out a rapid excursion from $\Phi_t^{\text{ext}} \approx 0$ to a flux $\Phi_t^{\text{ext}} \approx \Phi_*^{\text{ext}}$ close to the anti-crossing $\left|1_t, 0_p\right\rangle \leftrightarrow \left|0_t, 3_p\right\rangle$. We then let the system evolve freely for a time $t_* = \phi$. This free evolution gives rise to a rotation in the space of $\left|1_t, 0_p\right\rangle$ and $\left|0_t, 3_p\right\rangle$. After the time $t_*$, the $\left|1_t, 0_p\right\rangle$ state will have acquired a finite phase factor and we rapidly return to the idle configuration at $\Phi_t^{\text{ext}} \approx 0$. Because $g_-^{zz} \approx -g_+^{zz}$ near the anti-crossing, the result of this rapid excursion is a $\text{CZ}_\phi^{10}$ gate of the form,

$$
\begin{aligned}
\text{CZ}_\phi^{10} &= |0_t\rangle\langle 0_t| \otimes \mathsf{I}_p + |1_t\rangle\langle 1_t| \otimes \mathsf{P}_p \\
\mathsf{P}_p &= e^{-i\phi}|0_p\rangle\langle 0_p| + |1_p\rangle\langle 1_p|
\end{aligned}
\tag{5.33}
$$

Unlike for the case of two capacitively coupled transmons $t1$ and $t2$, we remark that the phase factor is not acquired by the $|1_{t1}, 1_{t2}\rangle$ state but by the $\left|1_t, 0_p\right\rangle$ state. Also, as announced at the beginning of this section, we highlight that the Cooper-pair parity is preserved for the full duration of the $\text{CZ}_\phi^{10}$ gate.

In the protocol for the $\text{CZ}_\phi^{10}$ gate, we have assumed that the offset charge on the PPQ is gate-tuned to $n_{g,p} = 0$. Such a tuning is beneficial as it maximizes the coefficient of the $\sigma_t^z\sigma_p^z$ terms, thereby allowing for improved gate speed. Furthermore, the tuning should always be achievable because higher levels of the PPQ are strongly offset charge sensitive and can be used for adjusting $n_{g,p}$. However, the fine-tuning to $n_{g,p} = 0$ is not essential for the gate protocol. To see this, we note that the terms $\propto g^{yz}\sigma_t^\pm\sigma_p^z$ and $\propto g^y\sigma_t^\pm$ in Eq. (5.32), which appear when $n_{g,p}$ is detuned from zero, share a fast-oscillating prefactor $\propto e^{i\omega_t t}$. This fast-oscillating prefactor suggests that such terms are average to zero when invoking a 'rotating-wave approximation'. For making this argument more precise, we have integrated out the fast-oscillating terms to second order in $g^y$ and $g^{yz}$ with a time-dependent Schrieffer-Wolff transformation [270, 271]. The resulting modified effective Hamiltonian reads

$$
\begin{aligned}
\tilde{H}_{\text{eff}}^{(n_{g,p})}(t) &\approx \left(\frac{g_+^{zz}}{2} + \frac{4[\tilde{g}^y(t)^2 + \tilde{g}^{yz}(t)^2]}{\omega_t}\right)\frac{\sigma_t^z}{2} + \frac{g_-^{zz}}{2}\frac{\sigma_p^z}{2} \\
&\quad + \left(g_-^{zz} + \frac{16\tilde{g}^y(t)\tilde{g}^{yz}(t)}{\omega_t}\right)\frac{\sigma_t^z}{2}\frac{\sigma_p^z}{2},
\end{aligned}
\tag{5.34}
$$

with $\tilde{g}(t) = g\sin(\omega_t t/2)$. Provided that $g^y \ll \omega_t$ and $g^{yz} \ll \omega_t$, we see that the correction terms to the effective Hamiltonian are indeed negligibly small. For the realistic parameters chosen in Fig. 5.6, we have $g^y/(2\pi) = 345\,\text{kHz}$ and $g^{yz}/(2\pi) = 3.88\,\text{MHz}$ if $n_{g,p} = 0.1$.

## CNOT and SWAP gate

We now combine the proposed method for single-qubit gates with the $CZ_\phi^{10}$ (with $\phi = \pi$) gate to realize a $CNOT_{tp}$ gate with the transmon as control and the PPQ as target by the gate sequence,

$$CNOT_{tp} = \quad = \quad \boxed{Y_{\frac{\pi}{2}}} \boxed{CZ^{10}} \boxed{Y_{-\frac{\pi}{2}}} \tag{5.35}$$

A $CNOT_{pt}$ gate that uses the PPQ as control and the transmon as target is similarly given by $CNOT_{pt} = H_t \cdot H_p \cdot CNOT_{tp} \cdot H_t \cdot H_p$ with the Hadamards, $H_{t/p} = (\sigma_{t/p}^x + \sigma_{t/p}^z)/\sqrt{2}$. Most notably, the $CNOT_{tp}$ and $CNOT_{pt}$ gate can now be combined to realize a $SWAP = CNOT_{tp} \cdot CNOT_{pt} \cdot CNOT_{tp}$ operation. The SWAP operation enables the *coherent* transfer of quantum information between the transmon and the PPQ. Interestingly, this coherent state transfer also gives a novel read-out method for the PPQ by swapping the quantum information onto the transmon and performing the read-out on the latter.

### Possible errors

In the previous sections, we have focused on deriving a scheme for a $CZ_\phi$ gate within our hybrid qubit setup. For our scheme, we have assumed that the Cooper-pair parity on the PPQ is conserved during the gate operation time. An interesting question is if the gate protocol modifies if errors due to *unintentional* single Cooper-pair tunneling terms, as given by Eq. (5.7), are present on the PPQ?

To address this question, we consider the PPQ at its $n_{g,p} = 0$ operation point for optimal gate-speed. We initially consider an error term, $H^y = -\varepsilon^y \sin(\phi_p)$, with an amplitude $\varepsilon^y$ that is small compared to the remaining energy scales of the setup. This $\sin(\phi_p)$ error arises in a PPQ realized by a nanowire Josephson interferometer if the two interferometers junctions are not in balance [229]. Due to the error term, we find that the low-energy Hamiltonian of Eq. (5.26) changes to,

$$H_{\text{low}}^{(n_{g,p}=0)} \rightarrow \begin{pmatrix} \omega_{11} & 0 & 0 & 0 & \lambda' & 0 \\ 0 & \omega_{10} & 0 & 0 & 0 & -\lambda'' \\ 0 & 0 & \omega_{01} & 0 & 0 & \kappa \\ 0 & 0 & 0 & \omega_{00} & \kappa & 0 \\ \lambda' & 0 & 0 & \kappa & \omega_{02} & 0 \\ 0 & -\lambda'' & \kappa & 0 & 0 & \omega_{03} \end{pmatrix}. \tag{5.36}$$

Here, we introduced the real-valued matrix element $\kappa = \langle 0_t, 1_p | H^y | 0_t, 3_p \rangle = \langle 0_t, 0_p | H^y | 0_t, 2_p \rangle$. Moreover, in accordance with Eq. (5.8), couplings of states with opposite Cooper-pair parity within the qubit subspace $\mathcal{P}_0$ are found to be absent at $n_{g,p} = 0$, .

Next, we integrate out the non-computational states, $|0_t, 2_p\rangle$ and $|0_t, 3_p\rangle$, with a Schrieffer-Wolff transformation and move to the rotating frame of the bare qubit frequencies. The effective rotating frame Hamiltonian of Eq. (5.32) then modifies to,

$$\tilde{H}_{\text{eff}}^{(n_{g,p}=0)} \rightarrow \frac{g_+^{zz}}{2} \frac{\sigma_t^z}{2} + \frac{g_-^{zz}}{2} \frac{\sigma_p^z}{2} + g_-^{zz} \frac{\sigma_t^z}{2} \frac{\sigma_p^z}{2} \tag{5.37a}$$
$$+ (e^{i(\omega_p+\omega_t)t} g^{++} \sigma_t^+ \sigma_p^+ + e^{i(\omega_t-\omega_p)t} g^{+-} \sigma_t^+ \sigma_p^- + \text{H.c.}),$$

with the coefficients,

$$g^{++} = \frac{\kappa \lambda'}{2(\omega_{11} - \omega_{02})}, \quad g^{+-} = \frac{\kappa \lambda''}{2(\omega_{03} - \omega_{10})}. \tag{5.37b}$$

It is now instructive to compare this result to the case of two capactively coupled transmons, $t1$ and $t2$, near the operation point of the iSWAP gate [269]. In the latter case, the effective Hamiltonian comprises similar terms, $\propto \sigma_{t1}^+ \sigma_{t2}^-$ and $\propto \sigma_{t1}^+ \sigma_{t2}^+$, that are 'rotating' with a factor $e^{i(\omega_{t1} - \omega_{t2})t}$ and 'counter-rotating' with a factor $e^{i(\omega_{t1} + \omega_{t2})t}$, respectively. For $\omega_{t1} \approx \omega_{t2}$, the 'counter-rotating' terms, which are fast-oscillating, average to zero within a 'rotating-wave approximation'. Only the 'rotating' terms, which oscillate slowly, are thus retained in the effective qubit Hamiltonian. In our case, the situation is very different. Because $\omega_t \gg \omega_p$, both factors, $e^{i(\omega_t + \omega_p)t}$ and $e^{i(\omega_t - \omega_p)t}$, are fast-oscillating. Within a 'rotating-wave approximation', we thus expect that both error terms average to zero.

To formalize this 'rotating-wave approximation' argument, we integrate out the fast-oscillating terms with a time-dependent Schrieffer-Wolff transformation. To second order in $g^{++}$ and $g^{+-}$, we find that

$$\begin{aligned}
\tilde{H}_{\text{eff}}^{(n_{g,p})} \approx &\left( \frac{g_+^{zz}}{2} + \frac{2[\tilde{g}^{xx}(t) - \tilde{g}^{yy}(t)]^2}{\omega_t} \right) \frac{\sigma_t^z}{2} \\
&+ \left( \frac{g_-^{zz}}{2} + \frac{2[\tilde{g}^{xx}(t) - \tilde{g}^{yy}(t)]^2}{\omega_t} \right) \frac{\sigma_p^z}{2} \\
&+ \left( g_-^{zz} - \frac{4[\tilde{g}^{xx}(t) + \tilde{g}^{yy}(t)]^2}{\omega_t} \right) \frac{\sigma_t^z}{2} \frac{\sigma_p^z}{2},
\end{aligned} \tag{5.38}$$

with $\tilde{g}(t) = g \sin(\omega_t t / 2)$. From this expression for the effective rotating-frame Hamiltonian, we conclude that the mitigation of the effects of $\sin(\phi_p)$ errors requires us to operate the setup in the regime when $g^{xx} \ll \omega_t$ and $g^{yy} \ll \omega_t$.

It is now interesting to compare our results for $\sin(\phi_p)$ errors with $\cos(\phi_p)$ errors that are described by an error term $H^x = -\varepsilon^x \cos(\phi_p)$ in the Hamiltonian. Such an error term can arise in an implementation of the PPQ with a nanowire Josephson interferometer if the external flux that threading the interferometer loop is detuned from half flux quantum [229]. In this situation, the low-energy Hamiltonian of Eq. (5.26) modifies to,

$$H_{\text{low}}^{(n_{g,p}=0)} \rightarrow \begin{pmatrix} \omega_{11} & \delta h^x & 0 & 0 & \lambda' & 0 \\ \delta h^x & \omega_{10} & 0 & 0 & 0 & -\lambda'' \\ 0 & 0 & \omega_{01} & \delta h^x & 0 & 0 \\ 0 & 0 & \delta h^x & \omega_{00} & 0 & 0 \\ \lambda' & 0 & 0 & 0 & \omega_{02} & \chi \\ 0 & -\lambda'' & 0 & 0 & \chi & \omega_{03} \end{pmatrix}, \tag{5.39}$$

with the matrix element $\chi = \langle 0_t, 2_p | H^y | 0_t, 3_p \rangle$. Importantly, we see that the $\cos(\phi_p)$ errors do not lead to off-diagonal terms that couple the matrix blocks representing the qubit subspace $\mathcal{P}_0$ and the non-computational subspace $\{|0_t, 2_p\rangle, |0_t, 3_p\rangle\}$. Consequently, we note that the $\cos(\phi_p)$ errors primarily induce the mixing of opposite-parity states on the PPQ as described by $H_{\text{eff}}^x$ in Eq. (5.8).
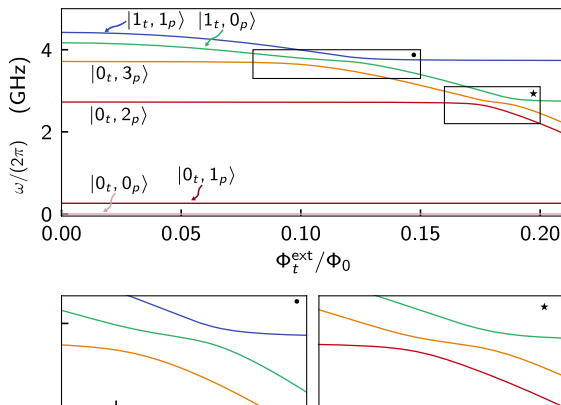
Fig. 5.7: **Effect of a cosine error in the PPQ.** Low-energy spectrum of the hybrid qubit setup for $n_{g,p} = 0$ and $(E_{J,t}, E_{J,p}, E_{C,t}, E_{C,p}, E_{C,c}) = 2\pi(12, 2.7, 0.2, 0.15, 0.025)\,\text{GHz}$ as a function of the external flux $\Phi_{\text{ext}}$ of the tunable transmon in the presence of an error term $H^x = \varepsilon^x \cos(\phi_p)$ with $\varepsilon^x = 0.05 E_{J,p}$. The error term introduces additional anticrossings between states belonging to the same pair.

In summary, we have found that the nature of $\sin(\phi_p)$ errors and $\cos(\phi_p)$ errors is different in our hybrid qubit. While the $\sin(\phi_p)$ errors lead primarily to additional two-qubit interactions that become less relevant in the limit when $g^{xx} \ll \omega_t$ and $g^{yy} \ll \omega_t$, the $\cos(\phi_p)$ errors lead primarily to additional single-qubit terms. Finding strategies of mitigating such flux errors, for example by concatenating multiple imperfect PPQs [229, 272], is an important open challenge of the field.

**Errors on the transmon qubit**

Besides the possible errors on the PPQ, it is essential to note that the performance of the $\text{CZ}_\phi^{10}$ gate in our hybrid setup can also be affected by errors on the transmon qubit. One source of such errors is $1/f$ flux noise [273, 274], which can give rise to fluctuations in the transmon qubit frequency, $\omega_t(\Phi_t^{\text{ext}})$, and thus induce qubit dephasing. In its idle configuration at $\Phi_t^{\text{ext}} = 0$, the flux-tunable transmon is always first-order protected against flux noise, $\partial \omega_t / \partial \Phi_t^{\text{ext}} = 0$ at $\Phi_t^{\text{ext}} = 0$. However, when tuning transmon away from $\Phi_t^{\text{ext}}$ to realize the $\text{CZ}_\phi^{10}$ gate it becomes susceptible to flux noise, because (in general) $\partial \omega_t / \partial \Phi_t^{\text{ext}} \neq 0$ when $\Phi_t^{\text{ext}} \neq 0$. In this section, we would like to understand how our proposed $\text{CZ}_\phi^{10}$ gate performs in the presence of realistic $1/f$ flux noise amplitudes, which are of the order of a few $\mu\Phi_0$ at $1\,\text{Hz}$ [275].

As a starting point of our analysis, we assume that the PPQ is in its protected regime, as described by $H_p$ in Eq. (5.24), and tuned to $n_{g,p} = 0$ for optimal gate speed. Following our previously outlined protocol, the $\text{CZ}_\phi^{10}$ gate is then realized via a rapid excursion from the idle configuration at $\Phi_t^{\text{ext}} = 0$ to a flux $\Phi_t^{\text{ext}} = \Phi_*^{\text{ext}}$ close to the anti-crossing $|1_t, 0_p\rangle \leftrightarrow |0_t, 3_p\rangle$ and back. We parametrize this excursion within the time interval $[0, t_* + t_r]$ through the following
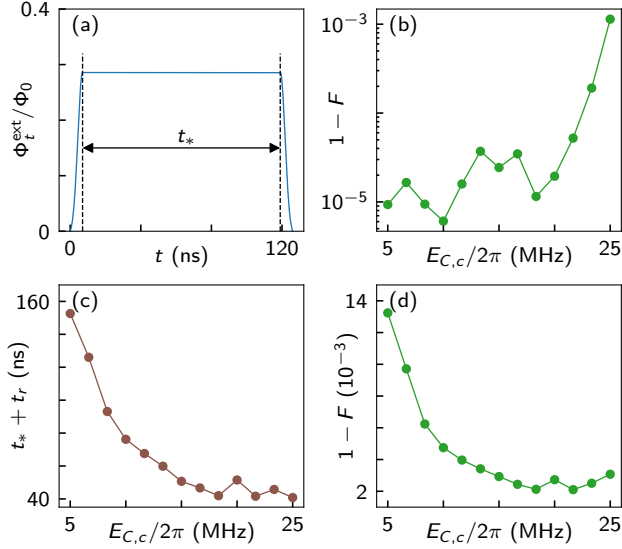
Fig. 5.8: **Performance of the CZ$_{\text{ffi}}^{\mathbf{10}}$ gate.** (a) A typical flux pulse, $\Phi_t^{\text{ext}}(t)$, for the CZ$_\phi^{10}$ gate as described by Eq. (5.40). The wait time near the anti-crossing $\left|1_t, 0_p\right\rangle \leftrightarrow \left|0_t, 3_p\right\rangle$ is $t_*$. The ramp up/down time of the flux pulse is $t_r/2$. (b) Optimized gate error, $1 - F$, in the absence of $1/f$ flux noise and qubit relaxation errors obtained from Eq. (5.41) versus the coupling capacitance, $E_{C,c}$. The system parameters are $(E_{J,t}, E_{J,p}, E_{C,t}, E_{C,p}) = 2\pi(12, 2.7, 0.2, 0.15)\,\text{GHz}$ and $n_{g,p} = 0$. (c) Optimized gate time, $t_* + t_r$, versus the coupling capacitance, $E_{C,c}$. The system parameters are the same as in (b). (d) Optimized gate error, $1 - F$, in the presence of $1/f$ flux noise and qubit relaxation errors obtained from Eq. (5.45), as a function of the coupling capacitance, $E_{C,c}$. The system parameters are the same as in (b). The noise parameters are $\Gamma_1^{(\text{even})} = \Gamma_1^{(\text{odd})} = 1/T_1$ with $T_1 = 20\,\mu\text{s}$ [273]. Moreover, $A_{1/f,\Phi} = 5\,\mu\Phi_0$ [275] and $\lambda_{1/f} = 4$, [276].

pulse shape [277],

$$\Phi_t^{\text{ext}}(t) = \Phi_*^{\text{ext}} \begin{cases} C(e^{-f(t)} - 1), & t > \frac{t_r}{2} + t_* \\ C(e^{-f(t-t_*)} - 1), & t < \frac{t_r}{2} \\ 1, & \text{else.} \end{cases} \tag{5.40}$$

Here, $t_r/2$ denotes the rise/decay time of the pulse and $t_*$ is the wait time near the anti-crossing. Moreover, we have introduced the constant $C = 1/(e^{-A/4} - 1)$ and the function $f(t) = At(t - t_r)/t_r^2$ with the parameter $A$ that sets the curvature of the rising/decaying pulse. An example of the pulse shape is shown in Fig. 5.8(a).

   With the help of Eq. (5.40), it is instructive to first look into errors of the unitary time evolution. To assess the importance of such unitary errors, we numerically solve $i\partial_t U(t) = \tilde{H}_{\text{low}}^{(n_{g,p}=0)}(\Phi_t^{\text{ext}}(t))U(t)$, where $\tilde{H}_{\text{low}}^{(n_{g,p}=0)}$ is represented in the rotating frame of the bare frequencies at $\Phi_t^{\text{ext}} = 0$, and project the resulting time-evolution operator, $U(t_r + t_*)$, onto the computational subspace. The projected operator is (in general) non-unitary due to leakage to the non-computational states and of the form $U_c = \text{diag}[a_{11}e^{i\phi_{11}}, a_{10}e^{i\phi_{10}}, 1, 1]$. For comparing $U_c$ to the CZ$_\phi^{10}$ gate, we apply a single-qubit Z operation, yielding $U_c' = U_Z U_c$ with

$U_Z = \text{diag}[e^{-i\phi_{11}}, e^{-i\phi_{11}}, 1, 1]$. We then use $U'_c$ to compute the gate fidelity [278, 279],

$$F = [\text{Tr}(U'^\dagger_c U'_c) + |\text{Tr}(U^\dagger_{\text{CZ}^{10}_\phi} U'_c)|^2]/20, \tag{5.41}$$

where $U_{\text{CZ}^{10}_\phi} = \text{diag}[1, e^{-i\phi}, 1, 1]$. In our simulations, we have focused on $\phi = \pi$ and optimized over the pulse parameters ($\Phi^{\text{ext}}_*, A, t_r, t_*$). The resulting gate errors, $1 - F$, and gate times are shown in Fig. 5.8(b) and (c) versus the coupling charging energy, $E_{C,c}$. While the gate time is reduced for stronger couplings, we find that the gate errors increases upon increasing $E_{C,c}$. We attribute this increase in $1 - F$ to an increase in both the phase error, $e^{i(\phi_{10} - \phi_{11})} \neq -1$, and the error due to leakage to non-computational states, $a_{11} \neq 1$ or $a_{10} \neq 1$.

Having discussed the effect of errors in the unitary time evolution, we now proceed by analyzing the performance of the $\text{CZ}^{10}_\phi$ gate in the presence of incoherent errors, including $1/f$ flux noise. To determine the time-evolution of the density matrix in the presence of $1/f$ flux noise, we follow the approach of [280] and consider a phenomenological master equation of the form,

$$\begin{aligned} \partial_t \rho = &[\tilde{H}^{(n_{g,p}=0)}_{\text{low}}, \rho] + \mathcal{D}[L_{1,t}]\rho + \mathcal{D}[L_{1,p}]\rho \\ &+ \mathcal{D}[L^{(10)}_\varphi(t)]\rho + \mathcal{D}[L^{(11)}_\varphi(t)]\rho, \end{aligned} \tag{5.42}$$

where $\mathcal{D}[L]\rho = L\rho L^\dagger - (L^\dagger L\rho + \rho L^\dagger L)/2$.

For the time-dependent collapse operators accounting for $1/f$ flux noise, we use,

$$\begin{aligned} L^{(10)}_\varphi(t) &= 2\sqrt{t}\,\Gamma^{(10)}_\varphi(t)\,|1_t, 0_p\rangle\langle 1_t, 0_p|, \\ L^{(11)}_\varphi(t) &= 2\sqrt{t}\,\Gamma^{(11)}_\varphi(t)\,|1_t, 1_p\rangle\langle 1_t, 1_p|, \end{aligned} \tag{5.43}$$

with the $1/f$ flux noise dephasing rates,

$$\Gamma^{(ss')}_\varphi(t) = \lambda_{1/f} \left| \frac{\partial \omega_{ss'}}{\partial \Phi^{\text{ext}}_t}(t) \right| A_{1/f,\Phi}. \tag{5.44}$$

Here, $\lambda_{1/f}$ is a dimensionless numerical prefactor and $A_{1/f,\Phi}$ denotes the amplitude of the $1/f$ flux noise power spectral density, $S(\omega) = 2\pi A^2_{1/f,\Phi}/|\omega|$. We have assumed, again for simplicity, that the dephasing arises primarily from the flux-dependence of the $|1_t, 0_p\rangle$ and $|1_t, 1_p\rangle$ levels.

To estimate the gate error, $1 - F$, in the presence of $1/f$ flux noise and the decay channels, we follow closely the procedure in [279]: For a given initial state, $|\psi_0\rangle$, we first compute the time evolution of the density matrix, $\rho$, from Eq. (5.42) using the QuTip package [281]. Subsequently, we compute the state-dependent gate fidelity,

$$F_\rho = \text{Tr}[\rho \rho_{\text{ideal}}]. \tag{5.45}$$

Here, $\rho_{\text{ideal}} = |\psi_{\text{ideal}}\rangle\langle\psi_{\text{ideal}}|$ with $|\psi_{\text{ideal}}\rangle = U^\dagger_Z U_{\text{CZ}^{10}_\phi}|\psi_0\rangle$ and $U_Z$ is obtained from the calculation of the unitary error. We repeat this procedure for 36 initial two-qubit states obtained by combining the single-qubit states $\{|0_{t/p}\rangle, |1_{t/p}\rangle, (|0_{t/p}\rangle \pm |1_{t/p}\rangle)/\sqrt{2}, (|0_{t/p}\rangle \pm i|1_{t/p}\rangle)/\sqrt{2}\}$. By averaging the resulting values for $1 - F_\rho$, we arrive at an estimate for $1 - F$.

Our results from the aforementioned procedure are shown in Fig. 5.8(d) for a typical set of system and noise parameters. We find that the gate error depends strongly on the magnitude

of the coupling charging energy, $E_{C,c}$. For smaller capacitive couplings, $E_{C,c}/2\pi = 5\,\mathrm{MHz}$, corresponding to longer gate times, 152ns, we find a rather substantial reduction of the fidelity to $F \approx 98.6\%$. In contrast, for stronger couplings, $E_{C,c}/2\pi = 20\,\mathrm{MHz}$, the shorter gate times, 51ns, reduce the exposure to low-frequency flux noise and the decay channels. As a result, the theoretical gate fidelity can reach $F \approx 99.7\%$, which is comparable to entangling gates between transmons [261]. However, we acknowledge that additional factors may further degrade the theoretical gate fidelity values in experiments. For example, it is to be expected that the effects of $1/f$ flux noise become more acute when many qubits are operated on the same chip. In this scenario, realizing accurate qubit calibration and high-fidelity gate operations will become more difficult. An interesting challenge for future works will be to further optimize gate protocols for hybrid PPQ-transmon devices, for example, by using dynamical decoupling techniques [282] or optimal control [283].

# 6

## Conclusion and outlook

The research work presented in this thesis has focused on modeling hybrid nanoelectronic devices for quantum information processing. Chapter 1 provided an introduction to the theory of superconductivity, focusing on the aspects that are relevant for analyzing hybrid heterostructures.

In Chapter 2, we have introduced modeling tools for the electrostatic landscape. After presenting the Schrödinger-Poisson formulation, we moved to orbital-free approaches. The widespread Thomas-Fermi method is often applied outside its range of validity, in particular, closer to interfaces. To achieve a more accurate description of the density profile in these cases, we introduced the extended Thomas-Fermi method that includes a gradient correction of the kinetic energy functional, significantly increasing the precision of the density profile near interfaces while keeping a minimal increase in the computational cost. We closed the chapter with an outline of the physics of spin-orbit coupling in semiconductor nanostructures.

Chapter 3 is a detailed introduction to the scattering formalism for describing transport phenomena in hybrid superconducting devices. The original results concerned the possibility of leveraging microscopic and geometrical symmetries to extract additional information from the differential conductance matrix. By considering new quantities defined as the differences of elements of the differential conductance matrix, we have shown how to distinguish dissipation from non-linear electrostatic effect, and we explored the interplay of spin-orbit coupling and Zeeman splitting, revealing a strategy to identify the spin-orbit coupling direction.

Chapter 4 discussed some research related to extending the hybrid heterostructure platform with ferromagnetic insets. We started by introducing the basic phenomenology of the ferromagnetic proximity effect and the material platform used in experiments. In the second part of the chapter, we discussed the applications of this platform to topological superconducting devices, first discussing the interplay of proximity effects in the system and then presenting a new planar heterostructure for topological nanowires. The last part of the chapter discussed Josephson junctions made with ferromagnetic hybrid heterostructures. After having presented the result of an experiment and proposed an interpretative model, we expanded the model to thoroughly investigate the variety of regimes that can be available for these devices, including $0$–$\pi$ transitions, higher-harmonic current-phase relations, and superconducting diode effects.

Chapter 5 of this thesis explored a potential application of the unconventional Josephson junction to superconducting quantum computing. Specifically, it introduced parity-protected qubits and demonstrated a possible way to create heterogeneous quantum architectures by combining them with tunable transmons. By tuning the external flux on the transmon, it is shown that non-computational states can mediate an entangling gate that preserves the Cooper-pair parity, regardless of the specific pulse sequence used. In addition to enabling coherent state transfer, the proposed entangling gate exhibits similarities with a controlled-phase gate in conventional capacitively coupled transmon qubits. These findings suggest that standard high-precision two-qubit calibration protocols may be repurposed for the operation of hybrid qubit devices.

The findings of this thesis investigate the potential of hybrid nanoelectronic devices as the next technological node in the field of quantum information processing. Hybrid heterostructures not only hold promise as a platform for studying non-abelian anyons in topological phases of matter for fundamental research and topological quantum computation. It also has the potential for applications beyond these fields. A future aim is to further explore the versatility of these devices, with a focus on creating new electronic elements in conventional superconducting circuits, like supercurrent rectifiers, in order to showcase their potential for

future technological innovations and as a research tool to investigate exotic phases of matter.

The major challenge facing future developments of this platform is the need for greater control and reproducibility in experimental results. To overcome this challenge, new theoretical investigations that focus on the microscopic modeling of interfaces are probably the necessary ingredient needed to provide a deeper physical understanding and predictive capabilities for experimental efforts. In addition, large-scale simulations are required to address the interplay between different devices and to integrate the technology into more complex experiments. This thesis presents work aimed at advancing in these directions, including the development of a formalism for transport measurement and the orbital-free electrostatic approach.

The addition of ferromagnetic insets is an interesting extension of the platform, but it is associated with a great increase in the overall complexity. It is not yet clear how big is the challenge of making these devices controllable. However, they will allow the implementation of many new ideas concerning the investigation of the interplay of superconductivity and ferromagnetism,

The application of hybrid heterostructures in superconducting quantum computing showcases their versatility and potential for future technological advancements. Whether this variation of the platform will reach similar popularity is yet to be seen.

Looking ahead, there is much room for further research in this field. One possible avenue is to explore the impact of different materials. Additionally, the potential for these devices in other areas of quantum information processing, such as quantum communication and quantum sensing, can be explored.

# SQUIDs

A superconducting quantum interference device (SQUID) is a circuit made of two Josephson junctions in parallel. By piercing the loop with a magnetic field, it is possible to control the supercurrent flowing in the SQUID by virtue of quantum interference effects. SQUIDs made of sinusoidal Josephson junction are usually employed as magnetometers with very high sensitivity.

In this Appendix, we consider a generic SQUID made of nonsinusoidal Josephson junctions that can be realized using hybrid heterostructures. Let us consider a SQUID made of two junctions with generic Josephson potential $E_{JL}(\phi_L)$ and $E_{JR}(\phi_R)$, Fig A.1(a). The total energy of the interferometer can be written as

$$E_J(\phi_L, \phi_R) = E_{JL}(\phi_L) + E_{JR}(\phi_R) = E_{JL}(\phi + \phi^e) + E_{JR}(\phi - \phi^e) \tag{A.1}$$

where we have defined the average phase $\phi = (\phi_L + \phi_R)/2$, while following Aharonov-Bohm quantization we get $\phi_L - \phi_R = \phi^e = 2\pi \Phi^{ext}/\Phi_0$.
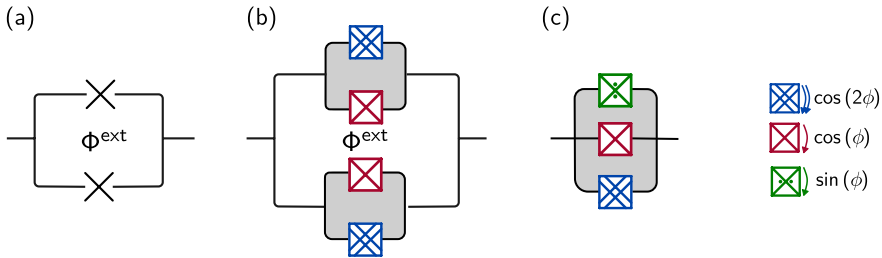


Fig. A.1: **SQUID made with nonsinusoidal Josephson junctions.** (a) SQUID made with non-sinusoidal Josephson junctions. (b) Circuit model with ideal Josephson elements (up to the second order). The gray area means that the total flux in the mesh is fixed to zero. (c) Circuit model of the effective Josephson potential at the two ends of the SQUID.

The total current flowing in the SQUID is given by $I(\phi) = \partial E_J/\partial \phi = \partial E_{JL}/\partial \phi + \partial E_{JR}/\partial \phi$. Suppose that one of the two junctions, for example, the left junction, has a significantly higher critical current than the other. The total critical current of the SQUID is then reached for a $\phi_c$ that satisfies $\partial I_L/\partial \phi = -\partial I_R/\partial \phi \simeq 0$. This means that the critical phase at which the

transition takes place is always close to the critical phase of the dominant junction, $\phi_c \approx \phi_{cL}$. Consequently, the critical current as a function of the external field is

$$I_c(\phi^e) \approx I_{cL} + I(\phi_{cL} - 2\phi^e). \tag{A.2}$$

This explains how studying the critical current of a SQUID with one dominant junction can be used to inspect the CPR of the other junction.

Now, as is often the case, let us assume that only the first two harmonics provide non-negligible contributions to the Josephson potential.

$$E_{JL}(\phi_L) = \sum_{k=1,2} E_{JLk} \cos(k\phi L), \quad E_{JR}(\phi_R) = \sum_{k=1,2} E_{JRk} \cos(k\phi R) \tag{A.3}$$

The total energy can be written as

$$
\begin{aligned}
E_J =\ & E_{J\Sigma 1} \sqrt{\cos^2(\phi^e/2) + d_1^2 \sin^2(\phi^e/2)} \cos(\phi - \phi_{o1}) \\
& + E_{J\Sigma 2} \sqrt{\cos^2(\phi_p^{ext}) + d_2^2 \sin^2(\phi^e)} \cos(2\phi - 2\phi_{o2})
\end{aligned} \tag{A.4}
$$

where $E_{J\Sigma k} = E_{JLk} + E_{JRk}$ while $d_k = (E_{JLk} - E_{JRk})/(E_{JLk} + E_{JRk})$. Finally, the phase offsets are

$$\phi_{o1} = \arctan[(d_1 \tan(\phi^e/2)] \tag{A.5}$$
$$\phi_{o2} = \arctan[d_2 \tan(\phi^e)]. \tag{A.6}$$

To obtain a $\cos(2\phi)$ element, one should set the external phase $\phi_e = \pi$ while tuning the transparencies to cancel the Josephson energy asymmetry in the first Harmonic $d_1 = 0$.

For what concerns the use of the interferometer in a PPQ, the $\sin(\phi)$ and $\cos(\phi)$ perturbation can be implemented by introducing some asymmetry $d_1 \neq 0$. This reintroduces the first harmonic in the phase dispersion relation. To determine what kind of perturbation we are introducing, we first apply a gauge transformation to get rid of the phase offset in the second harmonic term and then expand the cosine term. The result read as

$$
\begin{aligned}
E_{Jp} =\ & E_{J\Sigma 1} \sqrt{\cos^2(\phi^e/2) + d_1^2 \sin^2(\phi^e/2)} \big[\cos(\phi)\cos(\phi_{o2} - \phi_{o1}) + \sin(\phi)\sin(\phi_{o2} - \phi_{o1})\big] \\
& + E_{J\Sigma 2} \sqrt{\cos^2(\phi_p^{ext}) + d_2^2 \sin^2(\phi^e)} \cos(2\phi).
\end{aligned} \tag{A.7}
$$

This demonstrate how, by tuning the external phase, one can control the rotation axis on the Bloch sphere in the case the SQUID is used as an element of a PPQ.

# Semiconductor-metal boundary condition in the ETF method

As is briefly described in the method presentation, the treatment of the interfaces between metals and semiconductors is an open problem [284]. Moreover, the electron density shows a strong dependence on the thickness of thin metallic films that afflicts heterostructures when placed in contact with clean metallic films [75]. Usually, the electrostatic problem of the charge distribution in the metal is not taken into account, and metallic parts are assumed neutral by assigning a Dirichlet boundary condition at the surface [74, 75]. We will consider the problem starting with a complete treatment of the semiconductor-metal interface and discuss the issues of this solution. Next, we will search for an approximate solution able to reproduce the important physical behavior of the electrostatics in the semiconductor.

## Complete treatment

A complete treatment of the semiconductor-metal interface can be formulated by assuming that $\psi^2$ represents the conduction band electron density in both the semiconductor and the metal. We denote by $E_{F,M}$ the bulk Fermi energy of the metal defined as $E_{F,M} = \frac{\hbar^2 k_F^2}{2m}$. We define $E_W$ as the difference between the Fermi energy of the metal and the conduction band minimum of the semiconductor such that the local CBM takes the form

$$E_{\mathrm{CBM}}(\mathbf{r}) = -E_{\mathrm{W}}\mathbf{1}_{\mathrm{Sm}}(\mathbf{r}) - E_{F,M}\mathbf{1}_{\mathrm{M}}(\mathbf{r}),$$ (B.1)

where $\mathbf{1}_{\Omega_i}$ is the indicator function of region $\Omega_i$.

In addition, since in the metal the Fermi energy lies in the conduction band, the equilibrium bulk electron density needs to be compensated by a positive background that we assumed homogeneous and equal to

$$\rho_{\mathrm{fx}} = \rho_{\mathrm{M}}\mathbf{1}_M(\mathbf{r}), \qquad \rho_{\mathrm{M}} = \frac{e}{3\pi^2}\left(\frac{2mE_{F,M}}{\hbar^2}\right)^{3/2},$$ (B.2)

such that a homogeneous metallic system is neutral at equilibrium with an electron density equal to the one predicted by the Thomas-Fermi model. However, there are issues with this model when it is applied to a semiconductor-metal system. Since $\psi^2$ is the electron density in both materials, there will be a huge jump in its value at the interface, violating the assumption of slowly varying electron density.

**Effective boundary treatment**

Since a complete model of the semiconductor-metal interface is not available and the boundary conditions for the ETF method are unknown, we explored the possibility of finding an effective way to treat the semiconductor-metal boundary.

A first approach consists in excluding the metal from the NLSE. In this way, $\psi^2$ models the electron density only in the semiconductor, and the problem reduces to finding an effective boundary condition by trial and error. We tested three options. If the interface is not transparent, setting the density at the interface to zero $\psi(\partial\Omega_M) = 0$ can be an acceptable boundary condition even in the metallic case. Alternatively, if we assume that the metal is not perturbed at all, we can impose that the density should continuously go to the unperturbed metal density at the interface $\psi(\partial\Omega_M) = \sqrt{n_M}$. Finally, we tried a Neumann boundary condition by fixing the change in electron density to zero at the semiconductor-metal interface $\partial\psi(\partial\Omega_M) = 0$.

These approaches cannot be applied if the metal has to be included, for example because it is a floating part. In this case, we found that a mixed TF and ETF approach can be used, where we solve for the electron density in both the semiconductor and the metal, but we allow $\lambda_{vW}$ to vary in space. The idea of promoting $\lambda_{vW}$ to an inhomogeneous field has already been considered in more traditional application fields of OFDFT [285, 286].

Since metals have an extremely large electron density compared to that of the semiconductor, there will be an extremely large electron density gradient at the very interface. Since the vW-correction of the energy functional is proportional to the absolute value of this gradient squared, the vW-term will be extremely large here and, thus, essentially penalize the energy functional, trying to remove the abrupt change in electron density. However, this abrupt change in electron density at the semiconductor-metal interface is what we would expect of the system and should thus not be removed. A solution to this could be to change $\lambda_{vW}$ through the stack to diminish the correction where we expect large gradients. We dubbed this method $\lambda_{vW}$-sweep. In the metal, we expect an extremely large electron density (when compared to the semiconductor) that is only weakly perturbed by being in contact with a semiconductor. Changes are thus slow in space on the length scale of the Fermi wavelength, and the electron density in the metal can be effectively described by the TF method, i.e., assigning $\lambda_{vW} \simeq 0$ in the metal while using a finite $\lambda_{vW}$ in the semiconductor. This circumvents the problem of assigning a boundary condition to the interface. In the bulk of the semiconductor we use $\lambda_{vW} = 1/9$, and, in the aluminum, we set $\lambda_{vW}$ to zero (for convergence reasons we use a small but non-zero $\lambda_{vW}$ of $2 \cdot 10^{-8}$).
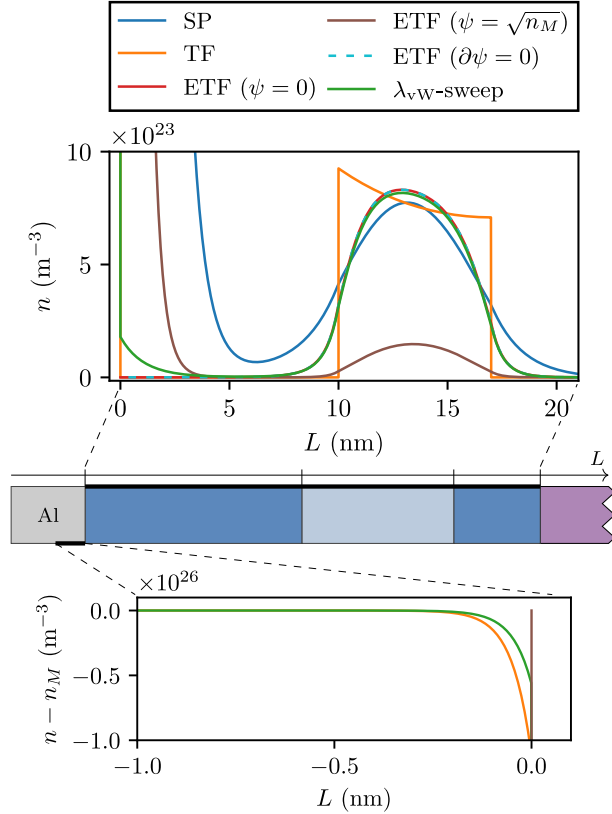
Fig. B.1: **Comparison of different ways to treat the semiconductor-metal interface.** We simulate the semiconductor stack in Fig. 2.2 (a), with a 5 nm layer of aluminum on top. The upper plot shows the electron density in the semiconducting stack, while the lower one shows the electron density in the metal. Six different ways of treating the semiconductor-metal interface are simulated: Three ETF simulations with different boundary conditions at the interface ($\psi = 0$, $\psi = \sqrt{n_{Al}}$, and $\partial\psi = 0$), one TF simulation, one SP simulation that is solved only in the semiconductor, and one ETF simulation where the value of $\lambda_{vW}$ is swept such that it is 1/9 in the semiconductor and 0 in the metal.

# Additional material on superconducting qubits

## C.1 Time-independent effective Hamiltonians

In this section of the Appendix, we give details on the derivation of the time-independent effective Hamiltonians for the coupled qubit setup as presented in Sec. 5.5. As a starting point, we project the setup Hamiltonian $H$ onto

$$\{\left|0_t, 0_p\right\rangle, \left|1_t, 0_p\right\rangle, \left|0_t, 1_p\right\rangle, \left|1_t, 1_p\right\rangle, \left|0_t, 2_p\right\rangle, \left|0_t, 3_p\right\rangle\},$$

which corresponds to the relevant low-energy states of the uncoupled Hamiltonian $H_0$. The resulting projected Hamiltonian is given by $H_{\text{low}}^{(n_{g,p})} = H_{\text{low}}^{(0)} + H_{\text{low}}^{(1)} + H_{\text{low}}^{(2)}$ with,

$$H_{\text{low}}^{(0)} = \begin{pmatrix} \omega_{11} & 0 & 0 & 0 & 0 & 0 \\ 0 & \omega_{10} & 0 & 0 & 0 & 0 \\ 0 & 0 & \omega_{01} & 0 & 0 & 0 \\ 0 & 0 & 0 & \omega_{00} & 0 & 0 \\ 0 & 0 & 0 & 0 & \omega_{02} & 0 \\ 0 & 0 & 0 & 0 & 0 & \omega_{03} \end{pmatrix}, \tag{C.1}$$

$$H_{\text{low}}^{(1)} = \begin{pmatrix} 0 & 0 & -i\eta' & 0 & 0 & 0 \\ 0 & 0 & 0 & i\eta'' & 0 & 0 \\ i\eta' & 0 & 0 & 0 & 0 & 0 \\ 0 & -i\eta'' & 0 & 0 & 0 & 0 \\ 0 & 0 & 0 & 0 & 0 & 0 \\ 0 & 0 & 0 & 0 & 0 & 0 \end{pmatrix}, \tag{C.2}$$

$$H_{\text{low}}^{(2)} = \begin{pmatrix} 0 & 0 & 0 & 0 & \lambda' & 0 \\ 0 & 0 & 0 & 0 & 0 & -\lambda'' \\ 0 & 0 & 0 & 0 & 0 & 0 \\ 0 & 0 & 0 & 0 & 0 & 0 \\ \lambda' & 0 & 0 & 0 & 0 & 0 \\ 0 & -\lambda'' & 0 & 0 & 0 & 0 \end{pmatrix}. \tag{C.3}$$

Here we have chosen a gauge of the wavefunctions in the uncoupled system such that $\langle 2_p|n_p|1_p\rangle$, $\langle 3_p|n_p|0_p\rangle$, and $\langle 0_t|n_t|1_t\rangle$ are purely imaginary-valued. As a result of this gauge

choice, the following quantities are real-valued,

$$
\begin{aligned}
\lambda' &= \left\langle 1_t, 1_p | H_c | 0_t, 2_p \right\rangle, \\
-\lambda'' &= \left\langle 1_t, 0_p | H_c | 0_t, 3_p \right\rangle, \\
-i\eta' &= \left\langle 1_t, 1_p | H_c | 0_t, 1_p \right\rangle, \\
i\eta'' &= \left\langle 1_t, 0_p | H_c | 0_t, 0_p \right\rangle.
\end{aligned}
\tag{C.4}
$$

Next, we integrate out the effects of the non-computational states $\{|0_t, 2_p\rangle, |0_t, 3_p\rangle\}$ by means of a Schrieffer-Wolff transformation [287, 288]. As the generator of the Schrieffer-Wolff transformation, we use

$$
S = \begin{pmatrix}
0 & 0 & 0 & 0 & -\Omega'/\lambda' & 0 \\
0 & 0 & 0 & 0 & 0 & \Omega''/\lambda'' \\
0 & 0 & 0 & 0 & 0 & 0 \\
0 & 0 & 0 & 0 & 0 & 0 \\
\Omega'/\lambda' & 0 & 0 & 0 & 0 & 0 \\
0 & -\Omega''/\lambda'' & 0 & 0 & 0 & 0
\end{pmatrix}
\tag{C.5}
$$

with

$$
\Omega' = \frac{\lambda'^2}{\omega_{11} - \omega_{02}} \quad \text{and} \quad \Omega'' = \frac{\lambda''^2}{\omega_{10} - \omega_{03}}.
\tag{C.6}
$$

We note that the generator satisfies $[H_{\text{low}}^{(0)}, S] = -H_{\text{low}}^{(2)}$. To second order in $\lambda'$ and $\lambda''$, the Schrieffer-Wolff generator produces an effective Hamiltonian $H_{\text{eff}}^{(n_{g,p})} = H_{\text{low}}^{(0)} + H_{\text{low}}^{(1)} + [H_{\text{low}}^{(2)}, S]/2$. Evaluating this expression yields,

$$
H_{\text{eff}}^{(n_{g,p})} = \left(\omega_t + \frac{g_+^{zz}}{2}\right)\frac{\sigma_t^z}{2} + \left(\omega_p + \frac{g_-^{zz}}{2}\right)\frac{\sigma_p^z}{2} + g_-^{zz}\frac{\sigma_t^z}{2}\frac{\sigma_p^z}{2} + g_t^y \sigma_t^y + g^{yz}\sigma_t^y \sigma_p^z
\tag{C.7}
$$

with

$$
\begin{aligned}
g_\pm^{zz} &= \Omega' \pm \Omega'', \\
g^{yz} &= (\eta' + \eta'')/2, \\
g_t^y &= (\eta' - \eta'')/2.
\end{aligned}
\tag{C.8}
$$

## C.2 Effective Hamiltonians for the time evolution

In this section of the Appendix, we give details on the derivation of the effective Hamiltonian in Sec. 5.5 that approximates the time evolution of our heterogeneous qubit system.

### Time-dependent Schrieffer-Wolff transformation

As a starting point, we briefly review the time-dependent version of the Schrieffer-Wolff transformation. Given some time-dependent effective Hamiltonian $H(t)$, the time-dependent

Schrieffer-Wolff transformation generates an effective Hamiltonian $H_{\text{eff}}(t)$ via a unitary transformation with a time-dependent generator $S(t)$ with $S(t) = -S(t)^{\dagger}$. By using the Baker-Campbell-Haussdorf formula, we can formulate the action of the time-dependent Schrieffer-Wolff unitary transformation on the Hamiltonian $H(t)$ as,

$$
\begin{aligned}
H_{\text{eff}}(t) - i\partial_t &\equiv e^{-S(t)}(H(t) - i\partial_t)e^{S(t)} \\
&= (H(t) - i\partial_t) + [H(t) - i\partial_t, S(t)] + \frac{1}{2}\left[[H(t) - i\partial_t, S(t)], S(t)\right] + \dots \\
&= H(t) - i\partial_t + [H(t), S(t)] - i\dot{S}(t) + \frac{1}{2}\left[[H(t), S(t)], S(t)\right] - \frac{i}{2}\left[\dot{S}(t), S(t)\right] + \dots
\end{aligned}
\tag{C.9}
$$

Next, we choose the time-dependent Hamiltonian to be of the specific form,

$$
H(t) = H^{(0)} + \xi H^{(2)}(t).
\tag{C.10}
$$

Here, $H^{(0)}$ is a time-independent unperturbed Hamiltonian and $H^{(2)}(t)$ is a time-dependent perturbation. The parameter $\xi$ is an aid to count the order in perturbation theory and can be set to $\xi = 1$ at the end of the derivation. Besides specifying the form of the time-dependent Hamiltonian, we also require that the generator of the time-dependent Schrieffer-Wolff transformation satisfies the following differential equation,

$$
\xi H^{(2)}(t) + \left[H^{(0)}, S(t)\right] - i\dot{S}(t) = 0.
\tag{C.11}
$$

Using these two conditions on the time-independent Hamiltonian and the generator $S(t)$, we find that the expression for the effective Hamiltonian $H_{\text{eff}}(t)$ can be simplified to,

$$
\begin{aligned}
H_{\text{eff}}(t) - i\partial_t &= H(t) - i\partial_t + [H(t), S(t)] - i\dot{S}(t) + \frac{1}{2}\left[[H(t), S(t)], S(t)\right] - \frac{i}{2}\left[\dot{S}(t), S(t)\right] + \dots \\
&= H^{(0)} - i\partial_t + \frac{1}{2}\left[\xi H^{(2)}(t), S(t)\right] + \frac{1}{2}\left[\left[\xi H^{(2)}(t), S(t)\right], S(t)\right] + \dots
\end{aligned}
\tag{C.12}
$$

We now proceed by assuming that the generator $S(t)$ can be expanded in a perturbative series,

$$
S(t) = \xi S_1(t) + \xi^2 S_2(t) + \cdots
\tag{C.13}
$$

Inserting this series into the expression for the effective Hamiltonian $H_{\text{eff}}$ and only retaining terms up to order $\xi^2$, we find that,

$$
H_{\text{eff}}(t) - i\partial_t = H^{(0)} - i\partial_t + \frac{\xi^2}{2}\left[H^{(2)}(t), S_1(t)\right] + \mathcal{O}(\xi^3)
\tag{C.14}
$$

Finally, we set $\xi = 1$ and arrive at the following form of the effective Hamiltonian,

$$
H_{\text{eff}}(t) - i\partial_t \equiv H^{(0)} - i\partial_t + \frac{1}{2}\left[H^{(2)}(t), S_1(t)\right]
\tag{C.15}
$$

## Rotating frame for the heterogeneous qubit setup

We now want to apply the time-dependent Schrieffer-Wolff transformation to our heterogeneous qubit setup. For that purpose, it is helpful to initially move to a rotating reference frame, which is achieved by separating the full qubit entangling Hamiltonian into $H_{\mathrm{eff}}^{(n_{gp})} = H^{(0)} + H^{(2)}$ with

$$
\begin{aligned}
H^{(0)} &= \left(\omega_t + \frac{g_+^{zz}}{2}\right)\frac{\sigma_t^z}{2} + \left(\omega_p + \frac{g_-^{zz}}{2}\right)\frac{\sigma_p^z}{2} + +g_-^{zz}\frac{\sigma_t^z}{2}\frac{\sigma_p^z}{2}, \\
H^{(2)} &= g_t^y \sigma_t^y + g_{tp}^{yz}\sigma_t^y\sigma_p^z,
\end{aligned}
\tag{C.16}
$$

and applying the following time-dependent unitary transformation,

$$
U(t) = e^{i(\omega_t\sigma_t^z + \omega_p\sigma_p^z)t/2}.
\tag{C.17}
$$

This transformation yields the qubit entangling Hamiltonian in the frame that rotates at the bare qubit frequencies with components,

$$
\begin{aligned}
\tilde{H}^{(0)} &= U^\dagger(t)H^{(0)}U(t) - iU^\dagger(t)\dot{U}(t) = \frac{g_+^{zz}}{2}\frac{\sigma_t^z}{2} + \frac{g_-^{zz}}{2}\frac{\sigma_p^z}{2} + g_-^{zz}\frac{\sigma_t^z}{2}\frac{\sigma_p^z}{2}, \\
\tilde{H}^{(2)}(t) &= U^\dagger(t)H^{(2)}U(t) - iU^\dagger(t)\dot{U}(t) = \\
&\quad g^y\sin(\omega_t t)\sigma_t^x + g^y\cos(\omega_t t)\sigma_t^y + g^{yz}\sin(\omega_t t)\sigma_t^x\sigma_p^z + g^{yz}\cos(\omega_t t)\sigma_t^y\sigma_p^z.
\end{aligned}
\tag{C.18}
$$

## Time-dependent Schrieffer-Wolff transformation for heterogeneous qubit setup

We now want to perform a time-dependent Schrieffer-Wolff transformation that eliminates the fast-oscillating terms, $\propto e^{\pm i\omega_t t}$, in $\tilde{H}^{(2)}(t)$ to second order in $g^y$ and $g^{yz}$. We, therefore, introduce the following Schrieffer-Wolff generator,

$$
S_1(t) = \begin{pmatrix} 0 & 0 & f_1(t) & 0 \\ 0 & 0 & 0 & f_2(t) \\ -f_1(t)^* & 0 & 0 & 0 \\ 0 & -f_2(t)^* & 0 & 0 \end{pmatrix}
\tag{C.19}
$$

with the functions,

$$
\begin{aligned}
f_1(t) &= \frac{-2i(g^y + g^{yz})(e^{-i(g_-^{zz}+g_+^{zz})t/2} - e^{i\omega_t t})}{g_-^{zz} + g_+^{zz} + 2\omega_t}, \\
f_2(t) &= \frac{2i(g^y - g^{yz})(e^{i(g_-^{zz}-g_+^{zz})t/2} - e^{i\omega_t t})}{g_-^{zz} - g_+^{zz} - 2\omega_t}
\end{aligned}
\tag{C.20}
$$

This generator satisfies,

$$
S_1(t) = -S_1(t)^\dagger, \quad \tilde{H}^{(2)}(t) + \left[\tilde{H}^{(0)}, S_1(t)\right] - i\dot{S}_1(t) = 0, \quad \text{and} \quad S_1(0) = 0.
\tag{C.21}
$$

Moreover, the generator allows us to compute the effective correction term to $\tilde{H}^{(0)}(t)$ to second order in $g^y$ and $g^{yz}$,

$$
\frac{1}{2}\left[\tilde{H}^{(2)}(t), S_1(t)\right] = \begin{pmatrix} h_1(t) & 0 & 0 & 0 \\ 0 & h_2(t) & 0 & 0 \\ 0 & 0 & -h_1(t) & 0 \\ 0 & 0 & 0 & -h_2(t) \end{pmatrix},
\tag{C.22}
$$

with the functions

$$
\begin{aligned}
h_1(t) &= \frac{4(g^y + g^{yz})^2 \sin\big([g_-^{zz} + g_+^{zz} + 2\omega_t]\, t/4\big)^2}{g_-^{zz} + g_+^{zz} + 2\omega_t}\,, \\
h_2(t) &= -\frac{4(g^y - g^{yz})^2 \sin\big([g_-^{zz} - g_+^{zz} - 2\omega_t]\, t/4\big)^2}{g_-^{zz} - g_+^{zz} - 2\omega_t}\,.
\end{aligned}
\tag{C.23}
$$

Provided that $\omega_t \gg g_\pm^{zz}$, we neglect the terms in the denominators and sine functions that are $\propto g_\pm^{zz}$. When then add the correction term to $\tilde{H}^{(0)}(t)$, which yields the full effective Hamiltonian,

$$
\begin{aligned}
\tilde{H}_{\text{eff}}^{(n_{g,p})}(t) \approx & \left( \frac{g_+^{zz}}{2} + \frac{4[(g^y)^2 + (g^{yz})^2]\sin(\omega_t t/2)^2}{\omega_t} \right) \frac{\sigma_t^z}{2} \\
& + \frac{g_-^{zz}}{2}\frac{\sigma_p^z}{2} + \left( g^{zz} + \frac{16 g^y g^{yz} \sin(\omega_t t/2)^2}{\omega_t} \right) \frac{\sigma_t^z}{2}\frac{\sigma_p^z}{2}.
\end{aligned}
\tag{C.24}
$$

This concludes our derivation of the effective Hamiltonian for the time evolution of our heterogeneous qubit setup.

## C.3   More details on the possible errors

In this section of the Appendix, we provide details on the derivation of the effective Hamiltonians that account for the presence of $\sin(\phi_p)$ error terms in our heterogeneous qubit setup.

First, we note that the derivations for the effective Hamiltonians *with* the $\sin(\phi_p)$ error terms are very similar to the derivations for the effective Hamiltonians *without* $\sin(\phi_p)$ the error terms. Since the latter derivations have been discussed in great detail in the previous sections of the Appendix, we will focus only on the main modifications.

### Time-independent effective Hamiltonian

For deriving the time-independent effective Hamiltonian of Eq. (15), we note that the low-energy Hamiltonian at $n_{g,p} = 0$ is given by $H_{\text{low}}^{(n_{g,p}=0)} = H_{\text{low}}^{(0)} + H_{\text{low}}^{(2)}$ with,

$$
H_{\text{low}}^{(0)} = \begin{pmatrix} \omega_{11} & 0 & 0 & 0 & 0 & 0 \\ 0 & \omega_{10} & 0 & 0 & 0 & 0 \\ 0 & 0 & \omega_{01} & 0 & 0 & 0 \\ 0 & 0 & 0 & \omega_{00} & 0 & 0 \\ 0 & 0 & 0 & 0 & \omega_{02} & 0 \\ 0 & 0 & 0 & 0 & 0 & \omega_{03} \end{pmatrix}, \quad H_{\text{low}}^{(2)} = \begin{pmatrix} 0 & 0 & 0 & 0 & \lambda' & 0 \\ 0 & 0 & 0 & 0 & 0 & -\lambda'' \\ 0 & 0 & 0 & 0 & 0 & \kappa \\ 0 & 0 & 0 & 0 & \kappa & 0 \\ \lambda' & 0 & 0 & \kappa & 0 & 0 \\ 0 & -\lambda'' & \kappa & 0 & 0 & 0 \end{pmatrix}.
\tag{C.25}
$$

Here, the matrix element $\kappa = \langle 0_t, 1_p | H^y | 0_t, 3_p \rangle = \langle 0_t, 0_p | H^y | 0_t, 2_p \rangle$ is real-valued (in the same gauge as the one used in the first section of the Appendix) and accounts for the presence of the $\sin(\phi_p)$ error terms.

Next, we write down the generator of the Schrieffer-Wolff transformation,

$$S = \begin{pmatrix} 0 & 0 & 0 & 0 & -\Omega'/\lambda' & 0 \\ 0 & 0 & 0 & 0 & 0 & \Omega''/\lambda'' \\ 0 & 0 & 0 & 0 & 0 & \Gamma' \\ 0 & 0 & 0 & 0 & \Gamma'' & 0 \\ \Omega'/\lambda' & 0 & 0 & -\Gamma'' & 0 & 0 \\ 0 & -\Omega''/\lambda'' & -\Gamma' & 0 & 0 & 0 \end{pmatrix} \tag{C.26}$$

with

$$\Gamma' = \frac{\kappa}{\omega_{03} - \omega_{01}} \quad \text{and} \quad \Gamma'' = \frac{\kappa}{\omega_{02} - \omega_{00}}, \tag{C.27}$$

The generator satisfies $[H_{\text{low}}^{(0)}, S] = -H_{\text{low}}^{(2)}$ and yields the effective Hamiltonian, $H_{\text{eff}}^{(n_{g,p}=0)} = H_{\text{low}}^{(0)} + [H_{\text{low}}^{(2)}, S]/2$. Projected onto the qubit subspace $\mathcal{P}_0$, the effective Hamiltonian evaluates to,

$$H_{\text{eff}}^{(n_{g,p}=0)} \approx \left(\omega_t + \frac{g_+^{zz}}{2}\right) \frac{\sigma_t^z}{2} + \left(\omega_p + \frac{g_-^{zz}}{2}\right) \frac{\sigma_p^z}{2} + g_-^{zz} \frac{\sigma_t^z}{2} \frac{\sigma_p^z}{2} + g^{xx} \sigma_t^x \sigma_p^x + g^{yy} \sigma_t^y \sigma_p^y \tag{C.28}$$

with the coefficients,

$$g^{xx} = \frac{\kappa}{4} \left(\frac{\lambda'}{\omega_{11} - \omega_{02}} + \frac{\lambda''}{\omega_{03} - \omega_{10}}\right), \quad g^{yy} = \frac{\kappa}{4} \left(\frac{\lambda'}{\omega_{02} - \omega_{11}} + \frac{\lambda''}{\omega_{03} - \omega_{10}}\right). \tag{C.29}$$

Here, we have dropped terms $\propto 1/(\omega_{01} - \omega_{03})$ and $\propto 1/(\omega_{00} - \omega_{02})$ due to the large separation of the respective energy levels.

**Time-dependent effective Hamiltonian**

For deriving the time-dependent effective Hamiltonian of Eq. (16), we transform the effective Hamiltonian, $H_{\text{eff}}^{(n_{g,p}=0)}$, to the frame that rotates with the bare qubit frequencies. The rotating-frame Hamiltonian is of the form $\tilde{H}^{(0)} + \tilde{H}^{(2)}(t)$ with the two contributions,

$$\tilde{H}^{(0)} = \frac{1}{4} \begin{pmatrix} g_+^{zz} + 2g_-^{zz} & 0 & 0 & 0 \\ 0 & g_+^{zz} - 2g_-^{zz} & 0 & 0 \\ 0 & 0 & -g_+^{zz} & 0 \\ 0 & 0 & 0 & -g_+^{zz} \end{pmatrix}, \tag{C.30}$$

$$\tilde{H}^{(2)}(t) = \begin{pmatrix} 0 & 0 & 0 & h_1 \\ 0 & 0 & h_2 & 0 \\ 0 & h_3 & 0 & 0 \\ h_4 & 0 & 0 & 0 \end{pmatrix}, \quad \begin{aligned} h_1 &= (g^{xx} - g^{yy})e^{i(\omega_t+\omega_p)t}, \\ h_2 &= (g^{xx} + g^{yy})e^{i(\omega_t-\omega_p)t}, \\ h_3 &= (g^{xx} + g^{yy})e^{-i(\omega_t-\omega_p)t}, \\ h_4 &= (g^{xx} - g^{yy})e^{-i(\omega_t+\omega_p)t}, \end{aligned} \tag{C.31}$$

We now introduce the generator of the time-dependent Schrieffer-Wolff transformation,

$$S_1(t) = \begin{pmatrix} 0 & 0 & 0 & f_1(t) \\ 0 & 0 & f_2(t) & 0 \\ 0 & -f_2(t)^* & 0 & 0 \\ -f_1(t)^* & 0 & 0 & 0 \end{pmatrix}, \tag{C.32}$$

with the functions,

$$
\begin{aligned}
f_1(t) &= \frac{2(g^{xx} - g^{yy})(e^{-i(g^{zz}_- + g^{zz}_+)t/2} - e^{i(\omega_t + \omega_p)t})}{g^{zz}_- + g^{zz}_+ + 2(\omega_p + \omega_t)}, \\
f_2(t) &= -\frac{2(g^{xx} + g^{yy})(e^{i(g^{zz}_- - g^{zz}_+)t/2} - e^{i(\omega_t - \omega_p)t})}{g^{zz}_- - g^{zz}_+ + 2(\omega_p - \omega_t)}.
\end{aligned}
\tag{C.33}
$$

This generator satisfies,

$$
S_1(t) = -S_1(t)^\dagger, \quad \tilde{H}^{(2)}(t) + \left[\tilde{H}^{(0)}, S_1(t)\right] - i\dot{S}_1(t) = 0, \quad \text{and} \quad S_1(0) = 0.
\tag{C.34}
$$

The generator yields the effective Hamiltonian, $\tilde{H}^{(n_{g,p}=0)}_{\text{eff}}(t) = \tilde{H}^{(0)} + [\tilde{H}^{(2)}(t), S_1(t)]/2$, which evaluates to,

$$
\begin{aligned}
\tilde{H}^{(n_{g,p}=0)}_{\text{eff}}(t) \approx &\left(\frac{g^{zz}_+}{2} + \frac{2(g^{xx} - g^{yy})^2 \sin(\omega_t t/2)^2}{\omega_t}\right)\frac{\sigma^z_t}{2} + \\
&\left(\frac{g^{zz}_-}{2} + \frac{2(g^{xx} - g^{yy})^2 \sin(\omega_t t/2)^2}{\omega_t}\right)\frac{\sigma^z_p}{2} \\
&+ \left(g^{zz}_- - \frac{4(g^{xx} + g^{yy})^2 \sin(\omega_t t/2)^2}{\omega_t}\right)\frac{\sigma^z_t}{2}\frac{\sigma^z_p}{2}.
\end{aligned}
\tag{C.35}
$$

This concludes our derivation of the effective Hamiltonians presented in Sec. 5.5.

## C.4 Numerical Schrieffer-Wolff transformation

In this section of the Appendix, we provide more details on the theory and application of the Schrieffer-Wolff transformation for the coupled qubits problem. The numerical Schrieffer-Wolff method is used in the text to derive the 6-levels effective Hamiltonians integrating out the effect of high-energy levels.

Let us consider the Hamiltonian of the coupled system $H = H_0 + H_c$ with $H_0 = H_t \otimes \mathbb{I} + \mathbb{I} \otimes H_p$ being the decoupled system Hamiltonian and $H_c$ the capacitive coupling Hamiltonian. The Hilbert space of the system can be decomposed as $\mathcal{H} = \mathcal{P}_0 \oplus \mathcal{Q}_0 = \mathcal{P} \oplus \mathcal{Q}$ where $\mathcal{P}_0$ and $\mathcal{P}$ are the low energy Hilbert spaces of the decoupled and coupled system. The computational space of the system is identified by $\mathcal{P}_0$. For this reason, we are interested in finding a unitary $U \in \text{End}(\mathcal{H})$ that maps the low-energy subspace of the interacting Hamiltonian $\mathcal{P}$ to the one of the uncoupled one $\mathcal{P}_0$. In other words, defining $P$ and $P_0$ the orthogonal projectors on the low-energy subspaces

$$
P = \sum_i^d |\psi_i\rangle\langle\psi_i|
\tag{C.36}
$$

$$
P_0 = \sum_i^d |\psi_i^0\rangle\langle\psi_i^0|
\tag{C.37}
$$

where $|\psi_i\rangle$ and $|\psi_i^0\rangle$ are, respectively, the coupled and decoupled system eigenstates and $d = 4$, we are seeking a unitary $U$ that satisfies

$$
UPU^\dagger = P_0 \quad \Rightarrow \quad UP = P_0 U.
\tag{C.38}
$$

This is achieved by the Schrieffer-Wolff transformation [287].

One way to see this is as a direct rotation that can be written as the square root of the product of the two reflections

$$U = \sqrt{\mathcal{M}_{\mathcal{P}_0}\mathcal{M}_{\mathcal{P}}} = \sqrt{(P_0 - Q_0)(P - Q)} = \sqrt{(2P_0 - \mathbb{I})(2P - \mathbb{I})} \tag{C.39}$$

where $Q$ and $Q_0$ are the orthogonal projectors to the high-energy subspaces and $\mathcal{M}_j$ are the reflections upon the lower energy subspaces.

The low energy Hamiltonian is then:

$$H_{\text{eff}} = P_0 U H U^\dagger P_0 = U P H P U^\dagger \tag{C.40}$$

An efficient way to tackle the problem numerically is the procedure developed in [289, 290] that we will now discuss. Since the final objective is the effect of the Schrieffer-Wolff transformation only in the low-energy sector, we can focus on the following operator product

$$P_0 U = U P = \sum_{ij} A_{ij} \left|\psi_i^0\right\rangle\left\langle\psi_j\right| = A \tag{C.41}$$

where $A \in \text{Hom}(\mathcal{P}_0, \mathcal{P})$ is a rank $d$ operator. For later use, we introduce also the rank $d$ operator $B \in \text{Hom}(\mathcal{P}_0, \mathcal{P})$ defined as $B = P_0 P$. Since both the operators belongs to $\text{Hom}(\mathcal{P}_0, \mathcal{P})$, $P_0$ acts as a left identity and $P$ is a right identity. Moreover, $A$ and $B$ are related, indeed

$$(UP)^2 = (P_0 A P)^2 = P_0 A P P_0 A P = P_0 A B^\dagger A P = A B^\dagger A \tag{C.42}$$

at the same time

$$(UP)^2 = P_0 U^2 P = P_0 (P_0 - Q_0)(P - Q) P = P_0 P = B \tag{C.43}$$

and therefore $A B^\dagger A = B$. Using singular values decomposition, we can decompose $B = W \Sigma V^\dagger$ where $W$ and $V$ are unitaries and $\Sigma$ is a diagonal matrix. The equation $A B^\dagger A = B$ is then solved by $A = W V^\dagger$.

In a practical implementation, by starting with the Hamiltonian $H_0$ and $H$ in whatever basis, we can calculate the incomplete low-energy $d$-dimensional orthogonal eigenbasis $V_0$ and $V$ ($n \times d$ matrices) with eigenvalue matrices $W_0$ and $W$ ($d \times d$ diagonal matrices) by using the Lanczos algorithm. With these, we can calculate $B = V_0^\dagger V$, that is a dimension $d$ matrix and perform SVD to calculate the unitary $A$. The effective low-energy Hamiltonian in the computational basis is then $H_{\text{eff}} = A W A^\dagger$. The drawback of this method is that we lose the information on the dressed states that is encoded in the matrix $U$.

**Smooth gauge for parametric sweeps**

The purpose of the Schrieffer-Wolff transformation is to derive an effective Hamiltonian $H_{\text{eff}}$ written in the basis of the unperturbed system $H_0$. Since $H_{\text{eff}}$ is not an observable of the system, the effective Hamiltonian derived is not unique, but it depends on the choice of the gauge for the unperturbed eigenstates $\{|\psi_i^0\rangle\}$. This means that it is crucial to fix a smooth gauge when sweeping over a parameter that appear also in the unperturbed Hamiltonian $H_0$. Notice that when numerical diagonalization is employed, control over the global phase of the eigenvectors is not guaranteed. Therefore a smooth gauging algorithm needs to be applied after the diagonalization.

In the case addressed in this paper, we are free to fix the gauge of the two qubits independently since they are decoupled in $H_0$. In the case, the charge offsets $n_{g,t}$ and $n_{g,p}$ are both zero, it is possible to fix the gauge consistently by imposing that the wavefunction is real at a reference point. A convenient choice is represented by picking $\phi = 0$ for $|0_p\rangle$, $|1_p\rangle$ and $|0_t\rangle$ and $\phi = \pi/4$ for $|1_t\rangle$.

We use a smooth gauge fixing procedure to keep a smooth gauge fixing during the sweep of the offset charge. We first discretize the $n_{g,i}$ axes in a set of $N$ points in the interval $[0, k]$ where $k$ is 1 for the transmon and 2 for the parity qubit. We will assume a homogeneous discretization with inter-site distance $\Delta n = k/(N-1)$ for simplicity. First, an arbitrary gauge fixing, like the one described in the previous paragraph, is applied for the wavefunction at point $i = 0$. Next, for each wavefunction, we impose that the overlap integral with the previous point is real. In other words, we calculate the fixing phase $\beta_i$ as

$$\beta_{n,i} = \sum_{j=0}^{i-1} \operatorname{Im}\ln \left\langle \psi_{n,j}^0 \middle| \psi_{n,j+1}^0 \right\rangle \tag{C.44}$$

and then the wavefunctions are updated as $\left|\tilde{\psi}_{n,i}^0\right\rangle = e^{-i\beta_{n,i}} \left|\tilde{\psi}_{n,i}^0\right\rangle$. This is possible because we have assumed that the index $n$ identifies corresponding eigenstates at different indexes $i$. In other words, if the index $n$ orders the states by the energy, we are assuming that there are no level crossings in the charge-Brillouin zone. This is not true for the parity qubit, but in this case, we have labeled by $n = 0, 1$ the even and odd lowest states that can be identified, for example, by comparing the amplitude at $\phi = 0$.

A more general method is available for the case when it is not possible to easily identify corresponding eigenstates at different values of the parameters. In that case, the application of an additional unitary point-by-point is necessary.

## C.5  Additional results on the energy levels

In this section of the Appendix, we provide additional details on the energy spectrum of the two-qubit system and the design principles of a heterogeneous qubit.

We recall that, for the transmon, it is possible to approximate the distribution of the eigenvalues by expanding the transmon Hamiltonian to the fourth order. In this way, the Hamiltonian is mapped to a quantum Duffing oscillator [255]. This gives the following approximate spectrum for the transmon:

$$E_{t,m} = -E_{J,t} + \sqrt{8E_{C,t}E_{J,t}}(m + 1/2) - \frac{E_{C,t}}{12}\left(6m^2 + 6m + 3\right). \tag{C.45}$$

A similar approach can be used to model the parity-protected qubit in the transmon regime by treating it as a double Duffing oscillator. We can expand the potential in the two wells as

$$V(\phi) = E_{J,p}\cos\left(2\phi - \pi/4\right) = -E_{J,p} + 4E_{j,p}\frac{(\phi - \phi_l)^2}{2} - 16E_{j,p}\frac{(\phi - \phi_l)^4}{24} + o(\phi^5) \tag{C.46}$$

with $\phi_L = \pm\pi/4$. Next, we introduce a hopping amplitude between the two wells. For simplicity, we consider allowed only hoppings between the same energy levels in the left and right well,

i.e., $t_{mm'} = t_m \delta_{mm'}$. Therefore, the approximate Hamiltonian is

$$H = \sum_{l=L,R} \left[ \omega_p a_l^\dagger a_l - E_{j,p} - \frac{E_{C,p}}{3}(a_l + a_l^\dagger)^4 \right] + \sum_m \left[ t_m \left( 1 + e^{i2\pi n_{g,p}} \right)(a_L^\dagger)^m (a_R)^m \right] \qquad \text{(C.47)}$$

where $\omega_p = 2\sqrt{8E_{j,p}E_{C,p}}$. The eigenvalues of the Hamiltonian can be calculated by first-order perturbation theory using the number basis $\{|m_L m_R\rangle\}$.

The double Duffing oscillator spectrum is composed of pairs of states located around the mean value

$$\mu_{n,n+1} = \frac{E_n + E_{n+1}}{2} \simeq -E_{J,p} + 2\sqrt{8E_{C,p}E_{J,p}}\left(\frac{n}{2} + 1/2\right) - 4\frac{E_{C,p}}{12}\left(6\left(\frac{n}{2}\right)^2 + 6\frac{n}{2} + 3\right), \qquad \text{(C.48)}$$

for even $n$, with a splitting $\delta_{n,n+1} = E_{n+1} - E_n \simeq \frac{t_n}{2}\cos(\pi n_{g,p})$. Each state belongs to either the even or odd parity sector. In the regime $-0.5 < n_{g,p} < 0.5$ the order of the states is *even, odd, odd, even, ...*, while in the regime $0.5 < n_{g,p} < 1.5$ is *odd, even, even, odd, ...*. In the PPQ, the $E_{J,p}/E_{C,p}$ ratio has a twofold role. On the one hand, higher ratios reduce the splitting between pair of states (i.e, $\omega_{p,1}$ and $\delta\omega_{23} = \omega_{p,2} - \omega_{p,3}$) on the other hand increase the separation between the pairs of states (*i.e.* $\mu_{p,23}$).

At the optimal point $n_{g,p} = 0$, states $|0_t, 2_p\rangle$ belongs to the odd sector while $|0_t, 3_p\rangle$ belongs to the even sector. This pair of states show a splitting $\propto |\cos(\pi n_{g,p})|$ and the mean is located approximately at energy $\mu_{p,23} = (\omega_{p,2} + \omega_{p,3})/2 \simeq 2\sqrt{8E_{C,p}E_{J,p}} - 4E_{C,p}$. Depending on the parameters of the system, the pair of states can be placed above the $|1_t, 0_p\rangle\,|1_t, 1_p\rangle$ pair (when $\mu_{p,23} \gtrsim \omega_{t,1}$) or below (when $\mu_{p,23} \lesssim \omega_{t,1}$). In the presence of a sizable splitting of the pair, the situation in which one of the two states lies below and one above is also possible. To obtain a controllable coupling, it is necessary that at least one of the two excited states lies below the pair of computational states. For this reason, the choice of parameters is crucial. For this reason, the approximate condition

$$\sqrt{8E_{C,t}E_{J,t}} - E_{C,t} > 2\sqrt{8E_{C,p}E_{J,p}} - 4E_{C,p} \qquad \text{(C.49)}$$

has to be satisfied.

# Hystersis curves with kinetic random field Ising model

In the reported measurements, for each ramp, we observe a transition from the normal phase (N) to the $\pi$ phase, then to the 0 phase, and then to the normal phase. However, by comparing the textbook example of hysteresis curves, one would expect a sequence of transition like N-$\pi$-0-$\pi$-N. We attribute the missing second $\pi$ transition to the asymmetric hysteresis curves that is characteristic of granular ferromagnetic samples. The hysteresis curves in these cases show a strong Barkhausen noise [291], also known as crackling noise [292]. Indeed, since the relevant magnetization for the switching, $\langle M \rangle_\xi$, is an average over a small number of magnetic grains, the crackling noise is likely to play a role.

To qualitatively explain the mechanism, we employ a kinetic random field Ising model [293–295]. We represent a magnetic insulator region of size $\xi^2$ such that the average magnetization is representative of $\langle M \rangle_\xi$. We estimated that the magnetic insulator's grain size is around one order of magnitude smaller than the coherence length. For this reason, we consider a $10 \times 10$ grid with periodic boundary conditions. As simplified assumptions, we assume each grain contains approximately the same number of spins and that the only directions allowed are collinear with the wire direction, such that the configuration can be represented by an Ising spins $\{S_i\}$.

The Hamiltonian of such a system read as

$$H = -\frac{1}{2} \sum_{ij} J_{ij} S_i S_j - \sum_i f_i S_i - \sum_i h_\parallel S_i \,, \tag{D.1}$$

where we further assume that the exchange coupling $J_{ij} = 1$ for nearest neighbors and zero otherwise. The random field $f_i \sim \mathcal{N}(\mu = 0, \sigma^2 = 1.2)$ is introduced to model grain anisotropy and $b$ is the external field.

We equip the model with a Glauber dynamic, this dissipative dynamic mimics the contact with a bath at temperature $T$ [296]. At each step, select a spin at random, we calculate the energy difference with the flipped spin $\Delta E$, accept the change with probability

$$p = \frac{1}{2} \left[ 1 - \tanh\left(\frac{\Delta E}{2T}\right) \right] \,. \tag{D.2}$$

To simplify the picture, we set $T = 0$ and look at the athermal dynamics. This dynamic guarantees that, for each $h_\parallel$, the system moves to one of the closest metastable minima, mimicking the dynamic of the magnetic material that hinders major reconfigurations.
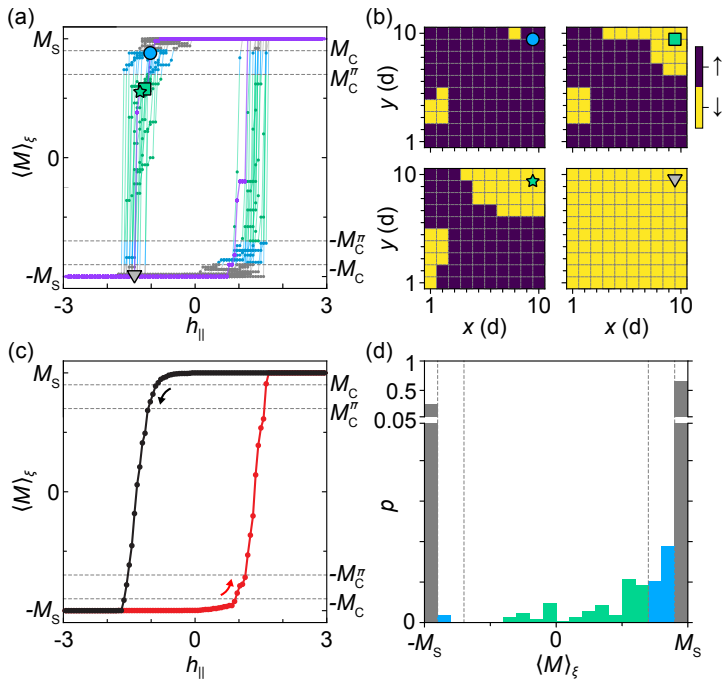
Fig. D.1: **Model of magnetization dynamics using a kinetic random field Ising model.** (a) Average magnetization, $\langle M \rangle_\xi$, as a function of the external magnetic field, $h_\parallel$, calculated using kinetic random-field Ising model [see Eq. (D.1)] for 20 disorder realizations of a grid of $10 \times 10$ magnetic grains. $M_S$ is magnetization saturation value. $M_C$ and $M_C^\pi$ are arbitrarily-chosen critical-magnetization values. (b) Four magnetic-domain configurations of the grid taken from a selected down-sweep realization highlighted in (a) at equidistantly spaced $h_\parallel$ values. (c) Disorder-averaged $\langle M \rangle_\xi$ as a function of $h_\parallel$, deduced from the 20 realizations shown in (a). (d) Histogram of the 20 down-sweep traces in (a) representing the probability, $p$, for the grid to have a particular $\langle M \rangle_\xi$ value.

We initialize the grid in a fully spin-polarized configuration ($S_i = -1$) and sweep $h_\parallel$ from -3 to 3 and back, allowing the system to evolve for 4000 iterations at each step. The results of 20 different $f_i$ realizations are shown in Fig. D.1(a). In a typical scenario, a few domains flip after $h_\parallel$ passes through 0, causing small changes in $\langle M \rangle_\xi$, which is followed by an abrupt domain-flip avalanche resulting in a fully polarized grid, see Fig. D.1(b). The disorder-average hysteresis curve shown in Fig. D.1(c) further illustrates how $\langle M \rangle_\xi$ first decreases smoothly as $h_\parallel$ is changed, but then jumps through 0 and inverts abruptly around the coercive field. This asymmetry can be further illustrated by considering the probability, $p$, for the grid to have a certain $\langle M \rangle_\xi$ value. Figure D.1(c) shows a histogram of $\langle M \rangle_\xi$ take from the 20 down-sweeps in Fig. D.1(a). To put these results into the context of our experiment, we introduce two critical magnetization values: $|M_C| = 0.9 \langle M \rangle_\xi$, below which the system is superconducting, and $|M_C^\pi| = 0.7 \langle M \rangle_\xi$, above which the system is in the $\pi$ phase. Based on these findings, it is apparent that the probability of the $\pi$-phase formation is higher at the onset compared to the end of the superconducting

window. The asymmetry of the hysteresis curve around the coercive field is presumably the reason for the observed $\pi$ phase at the onset of the superconducting window but not at the end. Note that the above argument does not depend on the specific value of $M_C^\pi$ and $M_C$ but rather on the general asymmetry of the hysteresis curve.

# Semiclassical analysis of a long junction

The more conventional regime is described by the energy scale hierarchy $\mu \gtrsim \Delta \gtrsim h$ in the lateral regions and $\mu \gtrsim h$ in the central one. In this case, the device behaves substantially as a superconductor-ferromagnetic metal-superconductor junction. For long junctions with a sufficiently high density and small polarization, a semiclassical model can approximately describe the behavior. This assumption is not met in the system studied by the numerical model. Nevertheless, this approach provides a clearer qualitative picture of the physics of this system. We follow the steps of Refs. [48, 211] including a spin splitting oriented in the wire direction with magnitudes $h_{\mathrm{L}}$ and $h_{\mathrm{R}}$. Later we include a spin-splitting field in the central region captured by the magnetic phase $\Phi_M$.

The discrete spectrum is obtained by solving the equation

$$\det[1 - S_{\mathrm{C}}(\varepsilon)S_A(\varepsilon)] = 0 \tag{E.1}$$

where $S_A$ is the scattering matrix at the interfaces while $S_{\mathrm{C}}$ is the scattering matrix for the transmission through the central region. We use the basis $\psi^{\mathrm{in}} = \left(c_+^e(0)\, c_-^e(\ell_{\mathrm{C}})\, c_-^h(0)\, c_+^h(\ell_{\mathrm{C}})\right)$ and $\psi^{\mathrm{out}} = \left(c_-^e(0)\, c_+^e(\ell_{\mathrm{C}})\, c_+^h(0)\, c_-^h(\ell_{\mathrm{C}})\right)$ such that $S_{\mathrm{C}}\psi^{\mathrm{in}} = \psi^{\mathrm{out}}$ and $S_A\psi^{\mathrm{out}} = \psi^{\mathrm{in}}$.

For $\varepsilon < \Delta$, we can assume that no normal reflection happens at the interface between the central and lateral regions if the interfaces are clean. In this case, the Andreev reflection matrix takes the form

$$S_A = \begin{pmatrix} 0 & s_A^{eh} \\ s_A^{he} & 0 \end{pmatrix}. \tag{E.2}$$

where the submatrices are

$$s_A^{eh} = \begin{pmatrix} e^{-i\arccos[(\varepsilon+\sigma h_{\mathrm{L}})/\Delta]}\, e^{+i\phi/2} & 0 \\ 0 & e^{-i\arccos[(\varepsilon+\sigma h_{\mathrm{R}})/\Delta]}\, e^{-i\phi/2} \end{pmatrix}, \tag{E.3}$$

$$s_A^{he} = \begin{pmatrix} e^{-i\arccos[(\varepsilon+\sigma h_{\mathrm{L}})/\Delta]}\, e^{-i\phi/2} & 0 \\ 0 & e^{-i\arccos[(\varepsilon+\sigma h_{\mathrm{R}})/\Delta]}\, e^{+i\phi/2} \end{pmatrix}, \tag{E.4}$$

For the central region, we assume a general scattering matrix that is block-diagonal in the electron-hole subspaces:

$$S_{\mathrm{C}} = \begin{pmatrix} s_N^{ee} & 0 \\ 0 & s_N^{hh} \end{pmatrix}, \tag{E.5}$$

where the two scattering matrices are related.

Using the property $\det\begin{pmatrix} A & B \\ C & D \end{pmatrix} = \det\left(AD - ACA^{-1}B\right)$ we eliminate the particle-hole blocks to simplify Eq. (E.1) to

$$\det\left(1 - s_A^{he} s_N^{ee} s_A^{eh} s_N^{hh}\right) = 0. \tag{E.6}$$

To proceed, we need to introduce some specific assumptions on the form of $S_C$. For a clean system, we can assume a free propagation that, in Andreev approximation, results in a scattering matrix with the form

$$s_N^{ee} = \exp\left(i\frac{\pi}{2}\frac{\varepsilon + \sigma h_C}{E_T}\right)\begin{pmatrix} 0 & 1 \\ 1 & 0 \end{pmatrix} \tag{E.7}$$

where we defined the Thouless energy $E_T = \frac{\pi}{2}\frac{\hbar v_F}{L_C}$. This results in an equation for the bound states

$$\pi\frac{\varepsilon + \sigma h_C}{E_T} \pm \phi - \sum_{\text{lat}=L,R}\arccos\left(\frac{\varepsilon + \sigma h_{\text{lat}}}{\Delta}\right) = 2\pi n. \tag{E.8}$$

If we take the exchange field in the lateral regions to be equal $h_L = h_R = h_{\text{lat}}$, this simplifies to

$$\frac{\pi}{2}\frac{\varepsilon}{E_T} + \sigma\Phi_M \pm \frac{\phi}{2} - \arccos\left(\frac{\varepsilon + \sigma h_{\text{lat}}}{\Delta}\right) = \pi n, \tag{E.9}$$

where we defined the magnetic phase $\Phi_M \equiv \frac{\pi}{2}\frac{h_C}{E_T} = \frac{h_C \ell_C}{\hbar v_F}$. In the case of a short central region, we can neglect the spin-independent phase shift in the central region and get the simplified relation

$$\varepsilon_{0,\sigma} = \pm\Delta\cos\left(\pm\frac{\phi}{2} + \sigma\Phi_M\right) - \sigma h_{\text{lat}} \tag{E.10}$$

In the case of a low-density regime, the conduction-band polarization $h_C/\mu_C$ can reach high values and exceed one at the transition to a half-metallic regime.
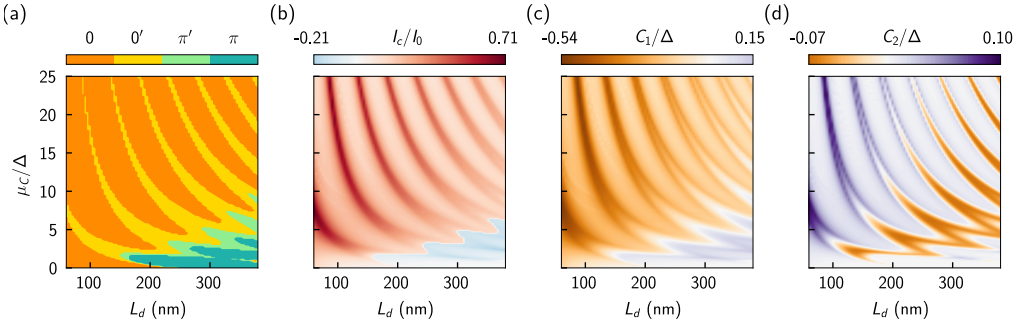


Fig. E.1: **Analysis of a ferromagnetic hybrid junction of various lengths.** The plots show the phase diagram, (a), the critical current, (b), and the value of the first two harmonic components of the Josephson potential, (c) and (d), as a function of the chemical potential and length of the central region. Parameters: $h_{\text{lat}} = 0$, $h_C = 0.1875\,\text{meV}$, $\mu_C = 3.125\,\text{meV}$ $\mu_{\text{lat}} = 1.25\,\text{meV}$, $V_B = 0.5\,\text{meV}$.

The presence of inhomogeneities in the chemical potential or exchange field causes the breakdown of quasiclassical Andreev solutions that manifests in the hybridization of the

solutions of Eq. E.8 and the opening of sizable gaps in the spectrum [297, 298]. Some features of this simple model can be connected to the results of the non-linearized BdG model displayed in Fig. E.1. Even in the short superconductor-normal metal-superconductor junction limit ($\ell_C \ll \xi$), the junction length modulates the magnetic phase acquired in the transport in the normal region. Systems with a longer normal region show an alternation of 0 and $\pi$ phases together with $0'$ and $\pi'$ regions. The phase diagram shows a series of $\pi$ regions with a $\frac{\ell_C}{\mu_C^a} \sim b$ shapes, with $a$ and $b$ constants. This can be understood on the basis of the semiclassical result where the effect of the ferromagnetic insulator in the central region enters the ABSs spectrum through the magnetic phase $\Phi_M = \frac{\pi}{2} h_C \ell_C \left( \frac{2\mu_C}{m*} \right)^{-1/2}$. Therefore changing the density can have effects similar to changing the length of the junction.

# Bibliography

[P1]    A. Maiani, R. S. Souto, M. Leijnse, and K. Flensberg. "Topological superconductivity in semiconductor–superconductor–magnetic insulator heterostructures". In: *Physical Review B* 103.10 (Mar. 2021), p. 104508. DOI: 10.1103/physrevb.103.104508.

[P2]    S. D. Escribano, A. Maiani, M. Leijnse, K. Flensberg, Y. Oreg, A. L. Yeyati, E. Prada, and R. S. Souto. "Semiconductor-ferromagnet-superconductor planar heterostructures for 1D topological superconductivity". In: *npj Quantum Materials* 7.81 (Aug. 2022). DOI: 10.1038/s41535-022-00489-9.

[P3]    W. Svejstrup, A. Maiani, K. V. Hoogdalem, and K. Flensberg. "Orbital-free approach for large-scale electrostatic simulations of quantum nanoelectronics devices". In: *Semiconductor Science and Technology* 38.4 (Feb. 2023), p. 045004. DOI: 10.1088/1361-6641/acbb9a.

[P4]    A. Maiani, M. Geier, and K. Flensberg. "Conductance matrix symmetries of multiterminal semiconductor-superconductor devices". In: *Physical Review B* 106.10 (Sept. 2022), p. 104516. DOI: 10.1103/physrevb.106.104516.

[P5]    A. Maiani, M. Kjaergaard, and C. Schrade. "Entangling Transmons with Low-Frequency Protected Superconducting Qubits". In: *PRX Quantum* 3.3 (Aug. 2022), p. 030329. DOI: 10.1103/prxquantum.3.030329.

[P6]    D. Razmadze, R. S. Souto, L. Galletti, A. Maiani, Y. Liu, P. Krogstrup, C. Schrade, A. Gyenis, C. M. Marcus, and S. Vaitiekėnas. "Supercurrent reversal in ferromagnetic hybrid nanowire Josephson junctions". In: *Physical Review B* 107.8 (Feb. 2023), p. l081301. DOI: 10.1103/physrevb.107.1081301.

[P7]    A. Maiani, K. Flensberg, M. Leijnse, C. Schrade, S. Vaitiekėnas, and R. S. Souto. "Non-sinusoidal current-phase relations in semiconductor-superconductor-ferromagnetic insulator devices". Feb. 2023. arXiv: 2302.04267.

[1]    H. Bruus and K. Flensberg. *Many-body quantum theory in condensed matter physics. an introduction.* 2nd ed. Oxford: Oxford University Press, 2004. ISBN: 0198566336.

[2]    H. Haug and A.-P. Jauho. *Quantum Kinetics in Transport and Optics of Semiconductors.* Vol. 123. Solid-State Sciences. Berlin, Heidelberg: Springer Berlin Heidelberg, 2008. ISBN: 978-3-540-73561-8. DOI: 10.1007/978-3-540-73564-9.

[3]    N. Bogoliubov. "On the theory of superfluidity". In: *Journal of Physics* 11.1 (1947), p. 23.

[4] P. G. de Gennes. *Superconductivity of Metals and Alloys*. 1st ed. Boca Raton: CRC Press, Mar. 1989. DOI: 10.1201/9780429497032.

[5] L. P. Gor'kov. "On the energy spectrum of superconductors". In: *Sov. Phys. JETP* 7.505 (1958), p. 158.

[6] I. Kosztin, Š. Kos, M. Stone, and A. J. Leggett. "Free energy of an inhomogeneous superconductor: A wave-function approach". In: *Physical Review B* 58.14 (Oct. 1998), pp. 9365–9384. ISSN: 0163-1829. DOI: 10.1103/PhysRevB.58.9365.

[7] M. Sigrist. "Introduction to Unconventional Superconductivity". In: *AIP Conference Proceedings*. AIP, 2005. DOI: 10.1063/1.2080350.

[8] T. Kita. *Statistical Mechanics of Superconductivity*. London: Springer London, Limited, 2015. ISBN: 9784431554059. DOI: 10.1007/978-4-431-55405-9.

[9] J.-X. Zhu. *Bogoliubov-de Gennes Method and Its Applications*. Springer International Publishing, 2016. DOI: 10.1007/978-3-319-31314-6.

[10] M. Stone and S.-B. Chung. "Fusion rules and vortices in $p_x + ip_y$ superconductors". In: *Physical Review B* 73.1 (Jan. 2006), p. 014505. DOI: 10.1103/physrevb.73.014505.

[11] G. Eilenberger. "Transformation of Gorkov's equation for type II superconductors into transport-like equations". In: *Zeitschrift für Physik A Hadrons and nuclei* 214.2 (Apr. 1968), pp. 195–213. DOI: 10.1007/bf01379803.

[12] K. D. Usadel. "Generalized diffusion equation for superconducting alloys". In: *Physical Review Letters* 25.8 (Aug. 1970), pp. 507–509. ISSN: 0031-9007. DOI: 10.1103/physrevlett.25.507.

[13] W. Belzig, F. K. Wilhelm, C. Bruder, G. Schön, and A. D. Zaikin. "Quasiclassical Green's function approach to mesoscopic superconductivity". In: *Superlattices and Microstructures* 25.5-6 (May 1999), pp. 1251–1288. DOI: 10.1006/spmi.1999.0710.

[14] M. Tinkham. *Introduction to Superconductivity. Second Edition*. 2nd ed. New York: Dover Publications, Incorporated, 2004. ISBN: 9780486134727.

[15] P. W. Anderson. "Knight Shift in Superconductors". In: *Physical Review Letters* 3.7 (Oct. 1959), pp. 325–326. DOI: 10.1103/physrevlett.3.325.

[16] W. A. Roshen and J. Ruvalds. "Spin susceptibility in superconductors". In: *Physical Review B* 28.3 (Aug. 1983), pp. 1329–1331. DOI: 10.1103/physrevb.28.1329.

[17] B. S. Chandrasekhar. "A note on the maximum critical field of high-field superconductors". In: *Applied Physics Letters* 1.1 (Sept. 1962), pp. 7–8. ISSN: 0003-6951. DOI: 10.1063/1.1777362.

[18] A. M. Clogston. "Upper Limit for the Critical Field in Hard Superconductors". In: *Physical Review Letters* 9.6 (Sept. 1962), pp. 266–267. DOI: 10.1103/physrevlett.9.266.

[19] T. T. Heikkilä, M. Silaev, P. Virtanen, and F. S. Bergeret. "Thermal, electric and spin transport in superconductor/ferromagnetic-insulator structures". In: *Progress in Surface Science* 94.3 (2019). ISSN: 0079-6816. DOI: 10.1016/j.progsurf.2019.100540.

[20] K. Maki and T. Tsuneto. "Pauli Paramagnetism and Superconducting State". In: *Progress of Theoretical Physics* 31.6 (June 1964), pp. 945–956. ISSN: 0033-068X. DOI: 10.1143/ptp.31.945.

[21] G. Sarma. "On the influence of a uniform exchange field acting on the spins of the conduction electrons in a superconductor". In: *Journal of Physics and Chemistry of Solids* 24.8 (Aug. 1963), pp. 1029–1032. ISSN: 0022-3697. DOI: 10.1016/0022-3697(63)90007-6.

[22] P. Wójcik. "Thickness-Dependent Oscillations of the Critical Magnetic Field Induced by the Quantum Size Effect in Superconducting Nanofilms". In: *Journal of Superconductivity and Novel Magnetism* 28.2 (Aug. 2014), pp. 339–343. DOI: 10.1007/s10948-014-2676-z.

[23] P. Fulde and R. A. Ferrell. "Superconductivity in a Strong Spin-Exchange Field". In: *Physical Review* 135.3A (Aug. 1964), A550–A563. DOI: 10.1103/physrev.135.a550.

[24] A. I. Larkin and Y. N. Ovchinnikov. "Nonuniform state of superconductors". In: *Soviet Physics-JETP* 20.3 (1965), pp. 762–762.

[25] M. Sato and Y. Ando. "Topological superconductors: a review". In: *Reports on Progress in Physics* 80.7 (May 2017), p. 076501. DOI: 10.1088/1361-6633/aa6ac7.

[26] A. W. W. Ludwig. "Topological phases: classification of topological insulators and superconductors of non-interacting fermions, and beyond". In: *Physica Scripta* T168 (Dec. 2015), p. 014001. DOI: 10.1088/0031-8949/2015/t168/014001.

[27] C.-K. Chiu, J. C. Teo, A. P. Schnyder, and S. Ryu. "Classification of topological quantum matter with symmetries". In: *Reviews of Modern Physics* 88.3 (Aug. 2016), p. 035005. ISSN: 1539-0756. DOI: 10.1103/revmodphys.88.035005.

[28] X.-G. Wen. "Colloquium: Zoo of quantum-topological phases of matter". In: *Reviews of Modern Physics* 89.4 (Dec. 2017), p. 041004. DOI: 10.1103/revmodphys.89.041004.

[29] A. Altland and M. R. Zirnbauer. "Nonstandard symmetry classes in mesoscopic normal-superconducting hybrid structures". In: *Physical Review B* 55.2 (Jan. 1997), pp. 1142–1161. DOI: 10.1103/physrevb.55.1142.

[30] A. P. Schnyder, S. Ryu, A. Furusaki, and A. W. W. Ludwig. "Classification of topological insulators and superconductors in three spatial dimensions". In: *Physical Review B* 78.19 (Nov. 2008), p. 195125. DOI: 10.1103/physrevb.78.195125.

[31] S. Ryu, A. P. Schnyder, A. Furusaki, and A. W. W. Ludwig. "Topological insulators and superconductors: tenfold way and dimensional hierarchy". In: *New Journal of Physics* 12.6 (June 2010), p. 065010. DOI: 10.1088/1367-2630/12/6/065010.

[32] B. A. Bernevig and T. L. Hughes. *Topological Insulators and Topological Superconductors*. Vol. 55. 4. Princeton: Princeton University Press, Apr. 2013, pp. 353–354. DOI: 10.1515/9781400846733.

[33] N. Read and D. Green. "Paired states of fermions in two dimensions with breaking of parity and time-reversal symmetries and the fractional quantum Hall effect". In: *Physical Review B* 61.15 (Apr. 2000), pp. 10267–10297. DOI: 10.1103/physrevb.61.10267.

[34] A. Y. Kitaev. "Unpaired Majorana fermions in quantum wires". In: *Physics-Uspekhi* 44.10S (2001), pp. 131–136. ISSN: 1468-4780. DOI: 10.1070/1063-7869/44/10s/s29.

[35] M. Leijnse and K. Flensberg. "Introduction to topological superconductivity and Majorana fermions". In: *Semiconductor Science and Technology* 27.12 (Nov. 2012), p. 124003. DOI: 10.1088/0268-1242/27/12/124003.

[36] J. Alicea. "New directions in the pursuit of Majorana fermions in solid state systems". In: *Reports on Progress in Physics* 75.7 (June 2012), p. 076501. DOI: 10.1088/0034-4885/75/7/076501.

[37] S. D. Sarma, M. Freedman, and C. Nayak. "Majorana zero modes and topological quantum computation". In: *npj Quantum Information* 1.1 (Oct. 2015). DOI: 10.1038/npjqi.2015.1.

[38] R. Aguado. "Majorana quasiparticles in condensed matter". In: *La Rivista del Nuovo Cimento* 40 (Oct. 2017), pp. 523–593. ISSN: 0393697X, 0393697X. DOI: 10.1393/ncr/i2017-10141-9.

[39] K. Laubscher and J. Klinovaja. "Majorana bound states in semiconducting nanostructures". In: *Journal of Applied Physics* 130.8 (Aug. 2021), p. 081101. DOI: 10.1063/5.0055997.

[40] P. Marra. "Majorana nanowires for topological quantum computation". In: *Journal of Applied Physics* 132.23 (Dec. 2022), p. 231101. DOI: 10.1063/5.0102999.

[41] D. A. Ivanov. "Non-Abelian Statistics of Half-Quantum Vortices in p-wave Superconductors". In: *Physical Review Letters* 86.2 (Jan. 2001), pp. 268–271. DOI: 10.1103/physrevlett.86.268.

[42] J. Alicea, Y. Oreg, G. Refael, F. von Oppen, and M. P. A. Fisher. "Non-Abelian statistics and topological quantum information processing in 1D wire networks". In: *Nature Physics* 7.5 (Feb. 2011), pp. 412–417. DOI: 10.1038/nphys1915.

[43] P. G. de Gennes. "Boundary Effects in Superconductors". In: *Reviews of Modern Physics* 36.1 (Jan. 1964), pp. 225–237. DOI: 10.1103/revmodphys.36.225.

[44] B. Pannetier and H. Courtois. "Andreev Reflection and Proximity effect". In: *Journal of Low Temperature Physics* 118.5/6 (2000), pp. 599–615. DOI: 10.1023/a:1004635226825.

[45] T. M. Klapwijk. "Proximity Effect From an Andreev Perspective". In: *Journal of Superconductivity* 17.5 (Oct. 2004), pp. 593–611. DOI: 10.1007/s10948-004-0773-0.

[46] W. L. McMillan. "Tunneling Model of the Superconducting Proximity Effect". In: *Physical Review* 175.2 (Nov. 1968), pp. 537–542. DOI: 10.1103/physrev.175.537.

[47] T. D. Stanescu and S. D. Sarma. "Proximity-induced low-energy renormalization in hybrid semiconductor-superconductor Majorana structures". In: *Physical Review B* 96.1 (July 2017), p. 014510. DOI: 10.1103/physrevb.96.014510.

[48] C. W. J. Beenakker. "Universal limit of critical-current fluctuations in mesoscopic Josephson junctions". In: *Physical Review Letters* 67.27 (Dec. 1991), pp. 3836–3839. DOI: 10.1103/physrevlett.67.3836.

[49] L. P. Gor'kov and E. I. Rashba. "Superconducting 2D System with Lifted Spin Degeneracy: Mixed Singlet-Triplet State". In: *Physical Review Letters* 87.3 (July 2001), p. 037004. DOI: 10.1103/physrevlett.87.037004.

[50]   L. Fu and C. L. Kane. "Superconducting Proximity Effect and Majorana Fermions at the Surface of a Topological Insulator". In: *Physical Review Letters* 100.9 (Mar. 2008), p. 096407. DOI: 10.1103/physrevlett.100.096407.

[51]   R. M. Lutchyn, J. D. Sau, and S. D. Sarma. "Majorana Fermions and a Topological Phase Transition in Semiconductor-Superconductor Heterostructures". In: *Physical Review Letters* 105.7 (7 Aug. 2010), p. 077001. DOI: 10.1103/physrevlett.105.077001.

[52]   Y. Oreg, G. Refael, and F. von Oppen. "Helical Liquids and Majorana Bound States in Quantum Wires". In: *Physical Review Letters* 105.17 (Oct. 2010), p. 177002. ISSN: 0031-9007. DOI: 10.1103/physrevlett.105.177002.

[53]   J. Alicea. "Majorana fermions in a tunable semiconductor device". In: *Physical Review B* 81.12 (Mar. 2010), p. 125318. DOI: 10.1103/physrevb.81.125318.

[54]   J. D. Sau, R. M. Lutchyn, S. Tewari, and S. D. Sarma. "Generic New Platform for Topological Quantum Computation Using Semiconductor Heterostructures". In: *Physical Review Letters* 104.4 (Jan. 2010), p. 040502. DOI: 10.1103/physrevlett.104.040502.

[55]   S. Tewari and J. D. Sau. "Topological Invariants for Spin-Orbit Coupled Superconductor Nanowires". In: *Physical Review Letters* 109.15 (Oct. 2012), p. 150408. DOI: 10.1103/physrevlett.109.150408.

[56]   R. M. Lutchyn, E. P. A. M. Bakkers, L. P. Kouwenhoven, P. Krogstrup, C. M. Marcus, and Y. Oreg. "Majorana zero modes in superconductor–semiconductor heterostructures". In: *Nature Reviews Materials* 3.5 (May 1, 2018), pp. 52–68. ISSN: 2058-8437. DOI: 10.1038/s41578-018-0003-1.

[57]   K. Flensberg, F. von Oppen, and A. Stern. "Engineered platforms for topological superconductivity and Majorana zero modes". In: *Nature Reviews Materials* 6.10 (July 2021), pp. 944–958. DOI: 10.1038/s41578-021-00336-6.

[58]   V. Mourik, K. Zuo, S. M. Frolov, S. R. Plissard, E. P. A. M. Bakkers, and L. P. Kouwenhoven. "Signatures of Majorana Fermions in Hybrid Superconductor-Semiconductor Nanowire Devices". In: *Science* 336.6084 (May 2012), pp. 1003–1007. DOI: 10.1126/science.1222360.

[59]   M. T. Deng, C. L. Yu, G. Y. Huang, M. Larsson, P. Caroff, and H. Q. Xu. "Anomalous Zero-Bias Conductance Peak in a Nb–InSb Nanowire–Nb Hybrid Device". In: *Nano Letters* 12.12 (Nov. 2012), pp. 6414–6419. DOI: 10.1021/nl303758w.

[60]   A. Das, Y. Ronen, Y. Most, Y. Oreg, M. Heiblum, and H. Shtrikman. "Zero-bias peaks and splitting in an Al–InAs nanowire topological superconductor as a signature of Majorana fermions". In: *Nature Physics* 8.12 (Nov. 2012), pp. 887–895. DOI: 10.1038/nphys2479.

[61]   L. P. Rokhinson, X. Liu, and J. K. Furdyna. "The fractional a.c. Josephson effect in a semiconductor–superconductor nanowire as a signature of Majorana particles". In: *Nature Physics* 8.11 (Sept. 2012), pp. 795–799. DOI: 10.1038/nphys2429.

[62]   H. O. H. Churchill, V. Fatemi, K. Grove-Rasmussen, M. T. Deng, P. Caroff, H. Q. Xu, and C. M. Marcus. "Superconductor-nanowire devices from tunneling to the multichannel regime: Zero-bias oscillations and magnetoconductance crossover". In: *Physical Review B* 87.24 (June 2013), p. 241401. DOI: 10.1103/physrevb.87.241401.

[63]  M. T. Deng, S. Vaitiekėnas, E. B. Hansen, J. Danon, M. Leijnse, K. Flensberg, J. Nygård, P. Krogstrup, and C. M. Marcus. "Majorana bound state in a coupled quantum-dot hybrid-nanowire system". In: *Science* 354.6319 (Dec. 2016), pp. 1557–1562. DOI: 10.1126/science.aaf3961.

[64]  Ö. Gül, H. Zhang, F. K. de Vries, J. van Veen, K. Zuo, V. Mourik, S. Conesa-Boj, M. P. Nowak, D. J. van Woerkom, M. Quintero-Pérez, M. C. Cassidy, A. Geresdi, S. Koelling, D. Car, S. R. Plissard, E. P. A. M. Bakkers, and L. P. Kouwenhoven. "Hard Superconducting Gap in InSb Nanowires". In: *Nano Letters* 17.4 (Apr. 2017), pp. 2690–2696. DOI: 10.1021/acs.nanolett.7b00540.

[65]  A. Grivnin, E. Bor, M. Heiblum, Y. Oreg, and H. Shtrikman. "Concomitant opening of a bulk-gap with an emerging possible Majorana zero mode". In: *Nature Communications* 10.1 (Apr. 2019). DOI: 10.1038/s41467-019-09771-0.

[66]  S. Vaitiekėnas, A. Whiticar, M.-T. Deng, F. Krizek, J. Sestoft, C. Palmstrøm, S. Marti-Sanchez, J. Arbiol, P. Krogstrup, L. Casparis, and C. Marcus. "Selective-Area-Grown Semiconductor-Superconductor Hybrids: A Basis for Topological Networks". In: *Physical Review Letters* 121.14 (Oct. 2018), p. 147701. ISSN: 1079-7114. DOI: 10.1103/physrevlett.121.147701.

[67]  J. Shabani, M. Kjaergaard, H. J. Suominen, Y. Kim, F. Nichele, K. Pakrouski, T. Stankevic, R. M. Lutchyn, P. Krogstrup, R. Feidenhans'l, S. Kraemer, C. Nayak, M. Troyer, C. M. Marcus, and C. J. Palmstrøm. "Two-dimensional epitaxial superconductor-semiconductor heterostructures: A platform for topological superconducting networks". In: *Physical Review B* 93.15 (Apr. 2016), p. 155402. DOI: 10.1103/physrevb.93.155402.

[68]  M. Kjaergaard, F. Nichele, H. J. Suominen, M. P. Nowak, M. Wimmer, A. R. Akhmerov, J. A. Folk, K. Flensberg, J. Shabani, C. J. Palmstrøm, and C. M. Marcus. "Quantized conductance doubling and hard gap in a two-dimensional semiconductor–superconductor heterostructure". In: *Nature Communications* 7.1 (Sept. 2016). DOI: 10.1038/ncomms12841.

[69]  H. Suominen, M. Kjaergaard, A. Hamilton, J. Shabani, C. Palmstrøm, C. Marcus, and F. Nichele. "Zero-Energy Modes from Coalescing Andreev States in a Two-Dimensional Semiconductor-Superconductor Hybrid Platform". In: *Physical Review Letters* 119.17 (Oct. 2017), p. 176805. DOI: 10.1103/physrevlett.119.176805.

[70]  F. Nichele, A. C. Drachmann, A. M. Whiticar, E. C. O'Farrell, H. J. Suominen, A. Fornieri, T. Wang, G. C. Gardner, C. Thomas, A. T. Hatke, P. Krogstrup, M. J. Manfra, K. Flensberg, and C. M. Marcus. "Scaling of Majorana Zero-Bias Conductance Peaks". In: *Physical Review Letters* 119.13 (Sept. 2017), p. 136803. DOI: 10.1103/physrevlett.119.136803.

[71]  A. Fornieri, A. M. Whiticar, F. Setiawan, E. Portolés, A. C. C. Drachmann, A. Keselman, S. Gronin, C. Thomas, T. Wang, R. Kallaher, G. C. Gardner, E. Berg, M. J. Manfra, A. Stern, C. M. Marcus, and F. Nichele. "Evidence of topological superconductivity in planar Josephson junctions". In: *Nature* 569.7754 (Apr. 2019), pp. 89–92. DOI: 10.1038/s41586-019-1068-8.

[72]  W. Mayer, J. Yuan, K. S. Wickramasinghe, T. Nguyen, M. C. Dartiailh, and J. Shabani. "Superconducting proximity effect in epitaxial Al-InAs heterostructures". In: *Applied Physics Letters* 114.10 (Mar. 2019), p. 103104. DOI: 10.1063/1.5067363.

[73] S. Vaitiekėnas, Y. Liu, P. Krogstrup, and C. M. Marcus. "Zero-bias peaks at zero magnetic field in ferromagnetic hybrid nanowires". In: *Nature Physics* 17.1 (Sept. 2020), pp. 43–47. ISSN: 1745-2473. DOI: 10.1038/s41567-020-1017-3.

[74] G. W. Winkler, A. E. Antipov, B. van Heck, A. A. Soluyanov, L. I. Glazman, M. Wimmer, and R. M. Lutchyn. "Unified numerical approach to topological semiconductor-superconductor heterostructures". In: *Physical Review B* 99.24 (June 2019), p. 245408. ISSN: 2469-9969. DOI: 10.1103/physrevb.99.245408.

[75] A. E. Mikkelsen, P. Kotetes, P. Krogstrup, and K. Flensberg. "Hybridization at Superconductor-Semiconductor Interfaces". In: *Physical Review X* 8.3 (Aug. 2018), p. 031040. ISSN: 2160-3308. DOI: 10.1103/physrevx.8.031040.

[76] A. E. Antipov, A. Bargerbos, G. W. Winkler, B. Bauer, E. Rossi, and R. M. Lutchyn. "Effects of Gate-Induced Electric Fields on Semiconductor Majorana Nanowires". In: *Physical Review X* 8.3 (3 Aug. 2018), p. 031041. DOI: 10.1103/physrevx.8.031041.

[77] J. Robertson. "Band offsets, Schottky barrier heights, and their effects on electronic devices". In: *Journal of Vacuum Science and Technology A: Vacuum, Surfaces, and Films* 31.5 (Sept. 2013), p. 050821. ISSN: 0734-2101. DOI: 10.1116/1.4818426.

[78] P. Armagnat, A. Lacerda-Santos, B. Rossignol, C. Groth, and X. Waintal. "The self-consistent quantum-electrostatic problem in strongly non-linear regime". In: *SciPost Physics* 7.3 (Sept. 2019), p. 031. ISSN: 2542-4653. DOI: 10.21468/scipostphys.7.3.031.

[79] P. Hohenberg and W. Kohn. "Inhomogeneous Electron Gas". In: *Physical Review* 136.3B (Nov. 1964), B864–B871. ISSN: 0031-899X. DOI: 10.1103/physrev.136.b864.

[80] R. M. Dreizler and E. K. U. Gross. *Density Functional Theory*. Berlin, Heidelberg: Springer Berlin Heidelberg, 1990. ISBN: 978-3-642-86107-9. DOI: 10.1007/978-3-642-86105-5.

[81] E. Engel and R. M. Dreizler. *Density Functional Theory*. Theoretical and Mathematical Physics. Berlin, Heidelberg: Springer Berlin Heidelberg, 2011. ISBN: 978-3-642-14089-1. DOI: 10.1007/978-3-642-14090-7.

[82] T. A. Wesolowski and Y. A. Wang. *Recent Progress in Orbital-free Density Functional Theory*. WORLD SCIENTIFIC, Sept. 2012. DOI: 10.1142/8633.

[83] V. V. Karasiev, D. Chakraborty, and S. B. Trickey. "Progress on New Approaches to Old Ideas: Orbital-Free Density Functionals". In: *Many-Electron Approaches in Physics, Chemistry and Mathematics*. Springer International Publishing, 2014, pp. 113–134. DOI: 10.1007/978-3-319-06379-9_6.

[84] W. C. Witt, B. G. del Rio, J. M. Dieterich, and E. A. Carter. "Orbital-free density functional theory for materials research". In: *Journal of Materials Research* 33.7 (Jan. 2018), pp. 777–795. DOI: 10.1557/jmr.2017.462.

[85] W. Kohn and L. J. Sham. "Self-Consistent Equations Including Exchange and Correlation Effects". In: *Physical Review* 140.4A (Nov. 1965), A1133–A1138. DOI: 10.1103/physrev.140.a1133.

[86]  A. Pöschl, A. Danilenko, D. Sabonis, K. Kristjuhan, T. Lindemann, C. Thomas, M. J. Manfra, and C. M. Marcus. "Nonlocal signatures of hybridization between quantum dot and Andreev bound states". In: *Physical Review B* 106.16 (Oct. 2022), p. l161301. DOI: 10.1103/physrevb.106.l161301.

[87]  A. Pöschl, A. Danilenko, D. Sabonis, K. Kristjuhan, T. Lindemann, C. Thomas, M. J. Manfra, and C. M. Marcus. "Nonlocal conductance spectroscopy of Andreev bound states in gate-defined InAs/Al nanowires". In: *Physical Review B* 106.24 (Dec. 2022), p. l241301. DOI: 10.1103/physrevb.106.l241301.

[88]  M. Brack and R. K. Bhaduri. *Semiclassical Physics*. CRC Press, Mar. 2018. DOI: 10.1201/9780429502828.

[89]  D. J. W. Geldart and G. Gumbs. "Convergence properties as a function of spatial dimensionality of gradient expansions for the ground-state energy of an inhomogeneous electron gas". In: *Physical Review B* 33.4 (4 Feb. 1986), pp. 2820–2823. DOI: 10.1103/physrevb.33.2820.

[90]  L. J. Bartolotti and K. Flurchick. "An Introduction to Density Functional Theory". In: *Reviews in Computational Chemistry*. Vol. 7. John Wiley & Sons, Inc., Jan. 2007, pp. 187–216. ISBN: 9780470125847. DOI: 10.1002/9780470125847.ch4.

[91]  W. Jones and W. H. Young. "Density functional theory and the von Weizsacker method". In: *Journal of Physics C* 4.11 (Aug. 1971), pp. 1322–1330. ISSN: 0022-3719. DOI: 10.1088/0022-3719/4/11/007.

[92]  L.-W. Wang and M. P. Teter. "Kinetic-energy functional of the electron density". In: *Physical Review B* 45.23 (June 1992), pp. 13196–13220. DOI: 10.1103/physrevb.45.13196.

[93]  A. Banerjee, O. Lesser, M. A. Rahman, H. R. Wang, M. R. Li, A. Kringhøj, A. M. Whiticar, A. C. C. Drachmann, C. Thomas, T. Wang, M. J. Manfra, E. Berg, Y. Oreg, A. Stern, and C. M. Marcus. "Signatures of a topological phase transition in a planar Josephson junction". Jan. 10, 2022. arXiv: 2201.03453 [cond-mat.mes-hall].

[94]  M. Levinshtein, S. Rumyantsev, and M. Shur. *Handbook Series on Semiconductor Parameters*. World Scientific Publishing, 1996. DOI: 10.1142/2046.

[95]  I. Vurgaftman, J. R. Meyer, and L. R. Ram-Mohan. "Band parameters for III-V compound semiconductors and their alloys". In: *Journal of Applied Physics* 89.11 (June 2001), pp. 5815–5875. ISSN: 0021-8979. DOI: 10.1063/1.1368156.

[96]  J. Robertson. "High dielectric constant oxides". In: *The European Physical Journal Applied Physics* 28.3 (Dec. 2004), pp. 265–291. DOI: 10.1051/epjap:2004206.

[97]  M. Brack. "Extended Thomas-Fermi Model at Finite Temperature". In: *Physical Review Letters* 53.2 (July 1984), pp. 119–122. DOI: 10.1103/physrevlett.53.119.

[98]  J. Bartel, M. Brack, and M. Durand. "Extended Thomas-Fermi theory at finite temperature". In: *Nuclear Physics A* 445.2 (Nov. 1985), pp. 263–303. DOI: 10.1016/0375-9474(85)90071-5.

[99]  P. Krogstrup, N. L. B. Ziino, W. Chang, S. M. Albrecht, M. H. Madsen, E. Johnson, J. Nygård, C. M. Marcus, and T. S. Jespersen. "Epitaxy of semiconductor–superconductor nanowires". In: *Nature Materials* 14.4 (Jan. 2015), pp. 400–406. DOI: 10.1038/nmat4176.

[100] R. Winkler. *Spin-Orbit Coupling Effects in Two-Dimensional Electron and Hole Systems*. Berlin, Heidelberg: Springer Berlin Heidelberg, 2003. ISBN: 9783540366164. DOI: 10. 1007/b13586.

[101] G. Dresselhaus. "Spin-Orbit Coupling Effects in Zinc Blende Structures". In: *Physical Review* 100.2 (Oct. 1955), pp. 580–586. DOI: 10.1103/physrev.100.580.

[102] W.-T. Wang, C. L. Wu, S. F. Tsay, M. H. Gau, I. Lo, H. F. Kao, D. J. Jang, J.-C. Chiang, M.-E. Lee, Y.-C. Chang, C.-N. Chen, and H. C. Hsueh. "Dresselhaus effect in bulk wurtzite materials". In: *Applied Physics Letters* 91.8 (Aug. 2007), p. 082110. DOI: 10.1063/1. 2775038.

[103] X. Zhang, J. Liu, and F. Liu. "Topological Superconductivity Based on Antisymmetric Spin–Orbit Coupling". In: *Nano Letters* 22.22 (Nov. 2022), pp. 9000–9005. DOI: 10.1021/ acs.nanolett.2c03213.

[104] T. Campos, P. E. F. Junior, M. Gmitra, G. M. Sipahi, and J. Fabian. "Spin-orbit coupling effects in zinc-blende InSb and wurtzite InAs nanowires: Realistic calculations with multiband $\vec{k} \cdot \vec{p}$ method". In: *Physical Review B* 97.24 (June 2018), p. 245402. ISSN: 2469-9950. DOI: 10.1103/physrevb.97.245402.

[105] S. D. Escribano, A. L. Yeyati, and E. Prada. "Improved effective equation for the Rashba spin-orbit coupling in semiconductor nanowires". In: *Physical Review Research* 2.3 (Aug. 2020), p. 033264. DOI: 10.1103/physrevresearch.2.033264.

[106] L. Hofstetter, S. Csonka, J. Nygård, and C. Schönenberger. "Cooper pair splitter realized in a two-quantum-dot Y-junction". In: *Nature* 461.7266 (Oct. 2009), pp. 960–963. ISSN: 0028-0836. DOI: 10.1038/nature08432.

[107] L. Hofstetter, S. Csonka, A. Baumgartner, G. Fülöp, S. d'Hollosy, J. Nygård, and C. Schönenberger. "Finite-Bias Cooper Pair Splitting". In: *Physical Review Letters* 107.13 (Sept. 2011), p. 136801. ISSN: 0031-9007. DOI: 10.1103/physrevlett.107.136801.

[108] J. Schindele, A. Baumgartner, and C. Schönenberger. "Near-Unity Cooper Pair Splitting Efficiency". In: *Physical Review Letters* 109.15 (Oct. 2012), p. 157002. ISSN: 0031-9007. DOI: 10.1103/physrevlett.109.157002.

[109] J. Schindele, A. Baumgartner, R. Maurand, M. Weiss, and C. Schönenberger. "Nonlocal spectroscopy of Andreev bound states". In: *Physical Review B* 89.4 (Jan. 2014), p. 045422. ISSN: 1098-0121. DOI: 10.1103/physrevb.89.045422.

[110] G. Wang, T. Dvir, N. van Loo, G. P. Mazur, S. Gazibegovic, G. Badawy, E. P. A. M. Bakkers, L. P. Kouwenhoven, and G. de Lange. "Nonlocal measurement of quasiparticle charge and energy relaxation in proximitized semiconductor nanowires using quantum dots". In: *Physical Review B* 106.6 (Aug. 2022), p. 064503. DOI: 10.1103/physrevb.106. 064503.

[111] A. M. Lobos and S. D. Sarma. "Tunneling transport in NSN Majorana junctions across the topological quantum phase transition". In: *New Journal of Physics* 17.6 (July 2015), p. 065010. ISSN: 1367-2630. DOI: 10.1088/1367-2630/17/6/065010.

[112] T. Ö. Rosdahl, A. Vuik, M. Kjaergaard, and A. R. Akhmerov. "Andreev rectifier: A nonlocal conductance signature of topological phase transitions". In: *Physical Review B* 97.4 (Jan. 2018), p. 045421. ISSN: 2469-9969. DOI: 10.1103/physrevb.97.045421.

[113]  J. Danon, A. B. Hellenes, E. B. Hansen, L. Casparis, A. P. Higginbotham, and K. Flensberg. "Nonlocal Conductance Spectroscopy of Andreev Bound States: Symmetry Relations and BCS Charges". In: *Physical Review Letters* 124.3 (Jan. 2020), p. 036801. ISSN: 1079-7114. DOI: 10.1103/physrevlett.124.036801.

[114]  D. Puglia, E. A. Martinez, G. C. Ménard, A. Pöschl, S. Gronin, G. C. Gardner, R. Kallaher, M. J. Manfra, C. M. Marcus, A. P. Higginbotham, and L. Casparis. "Closing of the induced gap in a hybrid superconductor-semiconductor nanowire". In: *Physical Review B* 103.23 (June 2021), p. 235201. ISSN: 2331-8422. DOI: 10.1103/physrevb.103.235201.

[115]  G. C. Mènard, G. L. R. Anselmetti, E. A. Martinez, D. Puglia, F. K. Malinowski, J. S. Lee, S. Choi, M. Pendharkar, C. J. PalmstrÃ¸m, K. Flensberg, C. M. Marcus, L. Casparis, and A. P. Higginbotham. "Conductance-Matrix Symmetries of a Three-Terminal Hybrid Device". In: *Physical Review Letters* 124.3 (Jan. 2020), p. 036802. ISSN: 1079-7114. DOI: 10.1103/physrevlett.124.036802.

[116]  D. I. Pikulin, B. van Heck, T. Karzig, E. A. Martinez, B. Nijholt, T. Laeven, G. W. Winkler, J. D. Watson, S. Heedt, M. Temurhan, V. Svidenko, R. M. Lutchyn, M. Thomas, G. de Lange, L. Casparis, and C. Nayak. "Protocol to identify a topological superconducting phase in a three-terminal device". Mar. 22, 2021. DOI: 10.48550/ARXIV.2103.12217. arXiv: 2103.12217 [cond-mat.mes-hall].

[117]  B. Sbierski, M. Geier, A.-P. Li, M. Brahlek, R. G. Moore, and J. E. Moore. "Identifying Majorana vortex modes via nonlocal transport". In: *Physical Review B* 106.3 (July 2022), p. 035413. DOI: 10.1103/physrevb.106.035413.

[118]  S. Ikegaya, Y. Asano, and D. Manske. "Anomalous Nonlocal Conductance as a Fingerprint of Chiral Majorana Edge States". In: *Physical Review Letters* 123.20 (Nov. 2019), p. 207002. ISSN: 1079-7114. DOI: 10.1103/physrevlett.123.207002.

[119]  P. Wójcik, D. Sticlet, P. Szumniak, and M. P. Nowak. "Helical and topological phase detection based on nonlocal conductance measurements in a three-terminal junction". In: *Physical Review B* 104.12 (Sept. 2021), p. 125410. ISSN: 2469-9950. DOI: 10.1103/physrevb.104.125410.

[120]  A. R. Akhmerov, J. P. Dahlhaus, F. Hassler, M. Wimmer, and C. W. J. Beenakker. "Quantized Conductance at the Majorana Phase Transition in a Disordered Superconducting Wire". In: *Physical Review Letters* 106.5 (Jan. 2011), p. 057001. DOI: 10.1103/physrevlett.106.057001.

[121]  H. Pan, J. D. Sau, and S. D. Sarma. "Three-terminal nonlocal conductance in Majorana nanowires: Distinguishing topological and trivial in realistic systems with disorder and inhomogeneous potential". In: *Physical Review B* 103.1 (Jan. 2021), p. 014513. ISSN: 2469-9969. DOI: 10.1103/physrevb.103.014513.

[122]  M. Leijnse. "Thermoelectric signatures of a Majorana bound state coupled to a quantum dot". In: *New Journal of Physics* 16.1 (Jan. 2014), p. 015029. ISSN: 1367-2630. DOI: 10.1088/1367-2630/16/1/015029.

[123]  A. Banerjee, O. Lesser, M. Rahman, C. Thomas, T. Wang, M. Manfra, E. Berg, Y. Oreg, A. Stern, and C. Marcus. "Local and Nonlocal Transport Spectroscopy in Planar Josephson Junctions". In: *Physical Review Letters* 130.9 (Feb. 2023), p. 096202. DOI: 10.1103/physrevlett.130.096202.

[124]  E. A. Martinez, A. Pöschl, E. B. Hansen, M. A. Y. van de Poll, S. Vaitiekenas, A. P. Higginbotham, and L. Casparis. "Measurement circuit effects in three-terminal electrical transport measurements". Apr. 6, 2021. arXiv: 2104.02671 [cond-mat.mes-hall].

[125]  A. Banerjee, M. Geier, M. A. Rahman, D. S. Sanchez, C. Thomas, T. Wang, M. J. Manfra, K. Flensberg, and C. M. Marcus. "Control of Andreev Bound States Using Superconducting Phase Texture". In: *Physical Review Letters* 130.11 (Mar. 2023), p. 116203. DOI: 10.1103/physrevlett.130.116203.

[126]  M. Buttiker. "Capacitance, admittance, and rectification properties of small conductors". In: *Journal of Physics: Condensed Matter* 5.50 (Dec. 1993), pp. 9361–9378. ISSN: 0953-8984. DOI: 10.1088/0953-8984/5/50/017.

[127]  T. Christen and M. BÃ¼ttiker. "Gauge-invariant nonlinear electric transport in mesoscopic conductors". In: *Europhysics Letters (EPL)* 35.7 (Sept. 1996), pp. 523–528. ISSN: 0295-5075. DOI: 10.1209/epl/i1996-00145-8.

[128]  D. Sánchez and L. Serra. "Thermoelectric transport of mesoscopic conductors coupled to voltage and thermal probes". In: *Physical Review B* 84.20 (Nov. 2011), p. 201307. ISSN: 1098-0121. DOI: 10.1103/physrevb.84.201307.

[129]  D. Sánchez and R. López. "Scattering Theory of Nonlinear Thermoelectric Transport". In: *Physical Review Letters* 110.2 (Jan. 2013), p. 026804. ISSN: 0031-9007. DOI: 10.1103/physrevlett.110.026804.

[130]  K. Yamamoto and N. Hatano. "Thermodynamics of the mesoscopic thermoelectric heat engine beyond the linear-response regime". In: *Physical Review E* 92.4 (Oct. 2015), p. 042165. ISSN: 1550-2376. DOI: 10.1103/physreve.92.042165.

[131]  J. Wang, Y. Wei, H. Guo, Q.-f. Sun, and T.-h. Lin. "Nonlinear transport theory for hybrid normal-superconducting devices". In: *Physical Review B* 64.10 (Aug. 2001), p. 104508. ISSN: 1550-235X. DOI: 10.1103/physrevb.64.104508.

[132]  J. Meair and P. Jacquod. "Scattering theory of nonlinear thermoelectricity in quantum coherent conductors". In: *Journal of Physics: Condensed Matter* 25.8 (Jan. 2013), p. 082201. ISSN: 0953-8984. DOI: 10.1088/0953-8984/25/8/082201.

[133]  S. Y. Hwang, D. Sánchez, M. Lee, and R. López. "Magnetic-field asymmetry of nonlinear thermoelectric and heat transport". In: *New Journal of Physics* 15.10 (Oct. 2013), p. 105012. DOI: 10.1088/1367-2630/15/10/105012.

[134]  C. Texier and J. Mitscherling. "Nonlinear conductance in weakly disordered mesoscopic wires: Interaction and magnetic field asymmetry". In: *Physical Review B* 97.7 (7 Feb. 2018), p. 075306. ISSN: 2469-9969. DOI: 10.1103/physrevb.97.075306.

[135]  A. R. Hernández and C. H. Lewenkopf. "Nonlinear electronic transport in nanoscopic devices: nonequilibrium Green's functions versus scattering approach". In: *The European Physical Journal B* 86.4 (Apr. 2013), pp. 1–11. ISSN: 1434-6028. DOI: 10.1140/epjb/e2013-31089-1.

[136]  A. Vuik, D. Eeltink, A. R. Akhmerov, and M. Wimmer. "Effects of the electrostatic environment on the Majorana nanowire devices". In: *New Journal of Physics* 18.3 (Mar. 2016), p. 033013. ISSN: 1367-2630. DOI: 10.1088/1367-2630/18/3/033013.

[137] F. Dominguez, J. Cayao, P. San-Jose, R. Aguado, A. L. Yeyati, and E. Prada. "Zero-energy pinning from interactions in Majorana nanowires". In: *npj Quantum Materials* 2.1 (Mar. 2017). DOI: 10.1038/s41535-017-0012-0.

[138] B. D. Woods, T. D. Stanescu, and S. D. Sarma. "Effective theory approach to the Schrödinger-Poisson problem in semiconductor Majorana devices". In: *Physical Review B* 98.3 (July 2018), p. 035428. ISSN: 2469-9950. DOI: 10.1103/physrevb.98.035428.

[139] S. D. Escribano, A. L. Yeyati, and E. Prada. "Interaction-induced zero-energy pinning and quantum dot formation in Majorana nanowires". In: *Beilstein Journal of Nanotechnology* 9.1 (Aug. 2018), pp. 2171–2180. ISSN: 2190-4286. DOI: 10.3762/bjnano.9.203.

[140] A. Melo, C.-X. Liu, P. Rożek, T. Ã.-r. Rosdahl, and M. Wimmer. "Conductance asymmetries in mesoscopic superconducting devices due to finite bias". In: *SciPost Physics* 10.2 (Feb. 2021), p. 037. ISSN: 2542-4653. DOI: 10.21468/scipostphys.10.2.037.

[141] G. E. Blonder, M. Tinkham, and T. M. Klapwijk. "Transition from metallic to tunneling regimes in superconducting microconstrictions: Excess current, charge imbalance, and supercurrent conversion". In: *Physical Review B* 25.7 (Apr. 1982), pp. 4515–4532. ISSN: 0163-1829. DOI: 10.1103/physrevb.25.4515.

[142] Y. Takane and H. Ebisawa. "Conductance Formula for Mesoscopic Systems with a Superconducting Segment". In: *Journal of the Physical Society of Japan* 61.5 (May 1992), pp. 1685–1690. DOI: 10.1143/jpsj.61.1685.

[143] M. P. Anantram and S. Datta. "Current fluctuations in mesoscopic systems with Andreev scattering". In: *Physical Review B* 53.24 (June 1996), pp. 16390–16402. ISSN: 1098-0121. DOI: 10.1103/physrevb.53.16390.

[144] S. Datta, P. F. Bagwell, and M. P. Anantram. *Scattering Theory of Transport for Mesoscopic Superconductors*. ECE Technical Reports 107. Purdue University, Jan. 1996.

[145] G. B. Lesovik and I. A. Sadovskyy. "Scattering matrix approach to the description of quantum electron transport". In: *Physics-Uspekhi* 54.10 (Oct. 2011), pp. 1007–1059. ISSN: 1063-7869. DOI: 10.3367/ufne.0181.201110b.1041.

[146] P. N. Butcher. "Thermal and electrical transport formalism for electronic microstructures with many terminals". In: *Journal of Physics: Condensed Matter* 2.22 (June 1990), pp. 4869–4878. ISSN: 0953-8984. DOI: 10.1088/0953-8984/2/22/008.

[147] G. B. Lesovik and G. Blatter. "Nonlinear transport through NS junctions due to imperfect Andreev reflection". In: *Journal of Experimental and Theoretical Physics Letters* 68.7 (Oct. 1998), pp. 599–605. ISSN: 0021-3640. DOI: 10.1134/1.567914.

[148] M. Leadbeater and C. J. Lambert. "Symmetry breaking in the tunnelling conductance of a superconducting vortex". In: *Journal of Physics: Condensed Matter* 8.24 (June 1996), pp. L345–L352. ISSN: 0953-8984. DOI: 10.1088/0953-8984/8/24/002.

[149] I. Martin and D. Mozyrsky. "Nonequilibrium theory of tunneling into a localized state in a superconductor". In: *Physical Review B* 90.10 (Sept. 2014), p. 100508. ISSN: 1098-0121. DOI: 10.1103/physrevb.90.100508.

[150] C.-X. Liu, J. D. Sau, and S. D. Sarma. "Role of dissipation in realistic Majorana nanowires". In: *Physical Review B* 95.5 (Feb. 2017), p. 054502. ISSN: 2469-9950. DOI: 10.1103/physrevb.95.054502.

[151]  G. B. Lesovik, A. L. Fauchère, and G. Blatter. "Nonlinearity in normal-metal–superconductor transport: Scattering-matrix approach". In: *Physical Review B* 55.5 (Feb. 1997), pp. 3146–3154. ISSN: 1098-0121. DOI: 10.1103/physrevb.55.3146.

[152]  N. R. Claughton and C. J. Lambert. "Thermoelectric properties of mesoscopic superconductors". In: *Physical Review B* 53.10 (Mar. 1996), pp. 6605–6612. ISSN: 0163-1829. DOI: 10.1103/physrevb.53.6605.

[153]  G. Michałek, M. Urbaniak, B. R. Bułka, T. Domański, and K. I. Wysokiński. "Local and nonlocal thermopower in three-terminal nanostructures". In: *Physical Review B* 93.23 (June 2016), p. 235440. ISSN: 2469-9969. DOI: 10.1103/physrevb.93.235440.

[154]  J. Matthews, F. Battista, D. Sánchez, P. Samuelsson, and H. Linke. "Experimental verification of reciprocity relations in quantum thermoelectric transport". In: *Physical Review B* 90.16 (Oct. 2014), p. 165428. ISSN: 1550-235X. DOI: 10.1103/physrevb.90.165428.

[155]  S. G. den Hartog, C. M. A. Kapteyn, B. J. van Wees, T. M. Klapwijk, and G. Borghs. "Transport in MultiTerminal Normal-Superconductor Devices: Reciprocity Relations, Negative and Nonlocal Resistances, and Reentrance of the Proximity Effect". In: *Physical Review Letters* 77.24 (Dec. 1996), pp. 4954–4957. ISSN: 0031-9007. DOI: 10.1103/physrevlett.77.4954.

[156]  P. Jacquod, R. S. Whitney, J. Meair, and M. Bü̈ttiker. "Onsager relations in coupled electric, thermoelectric, and spin transport: The tenfold way". In: *Physical Review B* 86.15 (Oct. 2012), p. 155118. ISSN: 1098-0121. DOI: 10.1103/physrevb.86.155118.

[157]  F. Herman and R. Hlubina. "Microscopic interpretation of the Dynes formula for the tunneling density of states". In: *Physical Review B* 94.14 (Oct. 2016), p. 144508. ISSN: 2469-9969. DOI: 10.1103/physrevb.94.144508.

[158]  F. Herman and R. Hlubina. "Thermodynamic properties of Dynes superconductors". In: *Physical Review B* 97.1 (Jan. 2018), p. 014517. ISSN: 2469-9969. DOI: 10.1103/physrevb.97.014517.

[159]  D. Kavický and R. Hlubina. "Dynes-like superconductivity in thin Al films in parallel magnetic fields". In: *Physical Review B* 102.1 (July 2020), p. 014508. ISSN: 2469-9950. DOI: 10.1103/physrevb.102.014508.

[160]  F. Dittes. "The decay of quantum systems with a small number of open channels". In: *Physics Reports* 339.4 (Dec. 2000), pp. 215–316. ISSN: 0370-1573. DOI: 10.1016/s0370-1573(00)00065-x.

[161]  C. W. Groth, M. Wimmer, A. R. Akhmerov, and X. Waintal. "Kwant: A software package for quantum transport". In: *New Journal of Physics* 16.6 (June 2014), p. 063065. ISSN: 1367-2630. DOI: 10.1088/1367-2630/16/6/063065.

[162]  D. Aasen, M. Hell, R. V. Mishmash, A. Higginbotham, J. Danon, M. Leijnse, T. S. Jespersen, J. A. Folk, C. M. Marcus, K. Flensberg, and J. Alicea. "Milestones Toward Majorana-Based Quantum Computing". In: *Physical Review X* 6.3 (Aug. 2016), p. 031016. DOI: 10.1103/physrevx.6.031016.

[163] T. Karzig, C. Knapp, R. M. Lutchyn, P. Bonderson, M. B. Hastings, C. Nayak, J. Alicea, K. Flensberg, S. Plugge, Y. Oreg, C. M. Marcus, and M. H. Freedman. "Scalable designs for quasiparticle-poisoning-protected topological quantum computation with Majorana zero modes". In: *Physical Review B* 95.23 (June 2017), p. 235305. DOI: 10.1103/physrevb.95.235305.

[164] C. Beenakker. "Search for non-Abelian Majorana braiding statistics in superconductors". In: *SciPost Physics Lecture Notes* (Aug. 2020). DOI: 10.21468/scipostphyslectnotes.15.

[165] S. Vaitiekėnas, G. W. Winkler, B. van Heck, T. Karzig, M.-T. Deng, K. Flensberg, L. I. Glazman, C. Nayak, P. Krogstrup, R. M. Lutchyn, and C. M. Marcus. "Flux-induced topological superconductivity in full-shell nanowires". In: *Science* 367.6485 (Mar. 2020). ISSN: 1095-9203. DOI: 10.1126/science.aav3392.

[166] F. Peñaranda, R. Aguado, P. San-Jose, and E. Prada. "Even-odd effect and Majorana states in full-shell nanowires". In: *Physical Review Research* 2.2 (May 2020), p. 023171. DOI: 10.1103/physrevresearch.2.023171.

[167] M. Valentini, F. Peñaranda, A. Hofmann, M. Brauns, R. Hauschild, P. Krogstrup, P. San-Jose, E. Prada, R. Aguado, and G. Katsaros. "Nontopological zero-bias peaks in full-shell nanowires induced by flux-tunable Andreev states". In: *Science* 373.6550 (July 2021), pp. 82–88. DOI: 10.1126/science.abf1513.

[168] F. Pientka, A. Keselman, E. Berg, A. Yacoby, A. Stern, and B. I. Halperin. "Topological Superconductivity in a Planar Josephson Junction". In: *Physical Review X* 7.2 (May 2017), p. 021032. DOI: 10.1103/physrevx.7.021032.

[169] M. Hell, M. Leijnse, and K. Flensberg. "Two-Dimensional Platform for Networks of Majorana Bound States". In: *Physical Review Letters* 118.10 (Mar. 2017), p. 107701. DOI: 10.1103/physrevlett.118.107701.

[170] Y. Liu, S. Vaitiekėnas, S. Martì-Sánchez, C. Koch, S. Hart, Z. Cui, T. Kanne, S. A. Khan, R. Tanta, S. Upadhyay, M. E. Cachaza, C. M. Marcus, J. Arbiol, K. A. Moler, and P. Krogstrup. "Semiconductor–Ferromagnetic Insulator–Superconductor Nanowires: Stray Field and Exchange Field". In: *Nano Letters* 20.1 (Nov. 2019), pp. 456–462. DOI: 10.1021/acs.nanolett.9b04187.

[171] N. V. Blümel, A. Goschew, Y. A. Shokr, and P. Fumagalli. "Growth-mode investigation of epitaxial EuS on InAs(100)". In: *AIP Advances* 9.3 (Mar. 2019), p. 035016. DOI: 10.1063/1.5080123.

[172] Y. Liu, A. Luchini, S. Martì-Sánchez, C. Koch, S. Schuwalow, S. A. Khan, T. Stankevič, S. Francoual, J. R. L. Mardegan, J. A. Krieger, V. N. Strocov, J. Stahn, C. A. F. Vaz, M. Ramakrishnan, U. Staub, K. Lefmann, G. Aeppli, J. Arbiol, and P. Krogstrup. "Coherent Epitaxial Semiconductor–Ferromagnetic Insulator InAs/EuS Interfaces: Band Alignment and Magnetic Structure". In: *ACS Applied Materials & Interfaces* 12.7 (Dec. 2019), pp. 8780–8787. DOI: 10.1021/acsami.9b15034.

[173] S. Manna, P. Wei, Y. Xie, K. T. Law, P. A. Lee, and J. S. Moodera. "Signature of a pair of Majorana zero modes in superconducting gold surface states". In: *Proceedings of the National Academy of Sciences* 117.16 (Apr. 2020), pp. 8775–8782. DOI: 10.1073/pnas.1919753117.

[174]  S. Vaitiekėnas, R. S. Souto, Y. Liu, P. Krogstrup, K. Flensberg, M. Leijnse, and C. M. Marcus. "Evidence for spin-polarized bound states in semiconductor–superconductor–ferromagnetic insulator islands". In: *Physical Review B* 105.4 (Jan. 2022), p. l041304. ISSN: 2469-9950. DOI: 10.1103/physrevb.105.l041304.

[175]  R. S. Alex Hubert. *Magnetic Domains. The Analysis of Magnetic Microstructures*. Berlin, Heidelberg: Springer Berlin Heidelberg, 1998. ISBN: 978-3-540-85054-0. DOI: 10.1007/978-3-540-85054-0.

[176]  A. Aharoni. *Introduction to the theory of ferromagnetism*. Oxford: Oxford University Press, 2000, p. 319. ISBN: 0198508085.

[177]  C. Abert. "Micromagnetics and spintronics: models and numerical methods". In: *The European Physical Journal B* 92.6 (June 2019). DOI: 10.1140/epjb/e2019-90599-6.

[178]  G. D. Fratta, C. B. Muratov, F. N. Rybakov, and V. V. Slastikov. "Variational Principles of Micromagnetics Revisited". In: *SIAM Journal on Mathematical Analysis* 52.4 (Jan. 2020), pp. 3580–3599. DOI: 10.1137/19m1261365.

[179]  L. Exl, D. Suess, and T. Schrefl. "Micromagnetism". In: *Handbook of Magnetism and Magnetic Materials*. Springer International Publishing, 2021, pp. 1–44. DOI: 10.1007/978-3-030-63101-7_7-1.

[180]  G.-X. Miao and J. S. Moodera. "Spin manipulation with magnetic semiconductor barriers". In: *Physical Chemistry Chemical Physics* 17.2 (2015), pp. 751–761. DOI: 10.1039/c4cp04599h.

[181]  P. M. Tedrow, J. E. Tkaczyk, and A. Kumar. "Spin-Polarized Electron Tunneling Study of an Artificially Layered Superconductor with Internal Magnetic Field: EuO-Al". In: *Physical Review Letters* 56.16 (Apr. 1986), pp. 1746–1749. DOI: 10.1103/physrevlett.56.1746.

[182]  J. E. Tkaczyk and P. M. Tedrow. "Magnetic proximity effect at a superconductor–rare-earth oxide interface". In: *Journal of Applied Physics* 61.8 (Apr. 1987), pp. 3368–3370. DOI: 10.1063/1.338774.

[183]  A. Millis, D. Rainer, and J. A. Sauls. "Quasiclassical theory of superconductivity near magnetically active interfaces". In: *Physical Review B* 38.7 (Sept. 1988), pp. 4504–4515. DOI: 10.1103/physrevb.38.4504.

[184]  T. Tokuyasu, J. A. Sauls, and D. Rainer. "Proximity effect of a ferromagnetic insulator in contact with a superconductor". In: *Physical Review B* 38.13 (Nov. 1988), pp. 8823–8833. ISSN: 0163-1829. DOI: 10.1103/physrevb.38.8823.

[185]  C. Ren, J. Trbovic, R. L. Kallaher, J. G. Braden, J. S. Parker, S. von Molnár, and P. Xiong. "Measurement of the spin polarization of the magnetic semiconductor EuS with zero-field and Zeeman-split Andreev reflection spectroscopy". In: *Physical Review B* 75.20 (May 2007), p. 205208. DOI: 10.1103/physrevb.75.205208.

[186]  M. J. Wolf, C. Sürgers, G. Fischer, and D. Beckmann. "Spin-polarized quasiparticle transport in exchange-split superconducting aluminum on europium sulfide". In: *Physical Review B* 90.14 (Oct. 2014), p. 144509. DOI: 10.1103/physrevb.90.144509.

[187]   E. Strambini, V. N. Golovach, G. D. Simoni, J. S. Moodera, F. S. Bergeret, and F. Giazotto. "Revealing the magnetic proximity effect in EuS/Al bilayers through superconducting tunneling spectroscopy". In: *Physical Review Materials* 1.5 (Oct. 2017), p. 054402. ISSN: 2475-9953. DOI: 10.1103/physrevmaterials.1.054402.

[188]   D. A. Ivanov, Y. V. Fominov, M. A. Skvortsov, and P. M. Ostrovsky. "Effective spin-flip scattering in diffusive superconducting proximity systems with magnetic disorder". In: *Physical Review B* 80.13 (Oct. 2009), p. 134501. DOI: 10.1103/physrevb.80.134501.

[189]   A. Hijano, S. Ilić, M. Rouco, C. González-Orellana, M. Ilyn, C. Rogero, P. Virtanen, T. T. Heikkilä, S. Khorshidian, M. Spies, N. Ligato, F. Giazotto, E. Strambini, and F. S. Bergeret. "Coexistence of superconductivity and spin-splitting fields in superconductor/ferromagnetic insulator bilayers of arbitrary thickness". In: *Physical Review Research* 3.2 (May 2021), p. 023131. DOI: 10.1103/physrevresearch.3.023131.

[190]   A. Hijano, V. N. Golovach, and F. S. Bergeret. "Quasiparticle density of states and triplet correlations in superconductor/ferromagnetic-insulator structures across a sharp domain wall". In: *Physical Review B* 105.17 (May 2022), p. 174507. DOI: 10.1103/physrevb.105.174507.

[191]   N. Poli, J. P. Morten, M. Urech, A. Brataas, D. B. Haviland, and V. Korenivski. "Spin Injection and Relaxation in a Mesoscopic Superconductor". In: *Physical Review Letters* 100.13 (Apr. 2008), p. 136601. DOI: 10.1103/physrevlett.100.136601.

[192]   B. T. Matthias, R. M. Bozorth, and J. H. V. Vleck. "Ferromagnetic Interaction in EuO". In: *Physical Review Letters* 7.5 (Sept. 1961), pp. 160–161. DOI: 10.1103/physrevlett.7.160.

[193]   R. L. Kallaher. "Electron Tunneling Transport Across Heterojunctions Between Europium Sulfide and Indium Arsenide". en. PhD thesis. 2007.

[194]   W. Müller and W. Nolting. "Temperature-dependent quasiparticle band structure of the ferromagnetic semiconductor EuS". In: *Physical Review B* 66.8 (Aug. 2002), p. 085205. DOI: 10.1103/physrevb.66.085205.

[195]   W. Müller and W. Nolting. "Ferromagnetic EuS films: Magnetic stability, electronic structure, and magnetic surface states". In: *Physical Review B* 69.15 (Apr. 2004), p. 155425. DOI: 10.1103/physrevb.69.155425.

[196]   D. E. Eastman, F. Holtzberg, and S. Methfessel. "Photoemission Studies of the Electronic Structure of EuO, EuS, EuSe, And GdS". In: *Physical Review Letters* 23.5 (Aug. 1969), pp. 226–229. DOI: 10.1103/physrevlett.23.226.

[197]   X. Hao, J. S. Moodera, and R. Meservey. "Thin-film superconductor in an exchange field". In: *Physical Review Letters* 67.10 (Sept. 1991), pp. 1342–1345. DOI: 10.1103/physrevlett.67.1342.

[198]   M. Rouco, S. Chakraborty, F. Aikebaier, V. N. Golovach, E. Strambini, J. S. Moodera, F. Giazotto, T. T. Heikkilä, and F. S. Bergeret. "Charge transport through spin-polarized tunnel junction between two spin-split superconductors". In: *Physical Review B* 100.18 (Nov. 2019), p. 184501. DOI: 10.1103/physrevb.100.184501.

[199]   C. Ren, J. Trbovic, P. Xiong, and S. von Molnár. "Zeeman splitting in ferromagnetic Schottky barrier contacts based on doped EuS". In: *Applied Physics Letters* 86.1 (Jan. 2005), p. 012501. DOI: 10.1063/1.1842857.

[200] J. Trbovic, C. Ren, P. Xiong, and S. von Molnár. "Spontaneous spin-filter effect across EuS/GaAs heterojunction". In: *Applied Physics Letters* 87.8 (Aug. 2005), p. 082101. DOI: 10.1063/1.2034089.

[201] J. Trbovic. "Spin-Polarized Transport Across EUS/III-V Semiconductor Heterostructure Interfaces". en. PhD thesis. 2006.

[202] A. Goschew, J. Griesmar, and P. Fumagalli. "Epitaxial growth of EuS on InAs(100) and InP(100)". In: *Thin Solid Films* 625 (Mar. 2017), pp. 106–110. DOI: 10.1016/j.tsf.2017.01.059.

[203] M. Yu, S. Moayedpour, S. Yang, D. Dardzinski, C. Wu, V. S. Pribiag, and N. Marom. "Dependence of the electronic structure of the EuS/InAs interface on the bonding configuration". In: *Physical Review Materials* 5.6 (June 2021), p. 064606. DOI: 10.1103/physrevmaterials.5.064606.

[204] B. D. Woods and T. D. Stanescu. "Electrostatic effects and topological superconductivity in semiconductor-superconductor-magnetic insulator hybrid wires". In: *Physical Review B* 104.19 (Nov. 2021), p. 195433. DOI: 10.1103/physrevb.104.195433.

[205] S. D. Escribano, E. Prada, Y. Oreg, and A. L. Yeyati. "Tunable proximity effects and topological superconductivity in ferromagnetic hybrid nanowires". In: *Physical Review B* 104.4 (July 2021), p. l041404. DOI: 10.1103/physrevb.104.l041404.

[206] C.-X. Liu, S. Schuwalow, Y. Liu, K. Vilkelis, A. L. R. Manesco, P. Krogstrup, and M. Wimmer. "Electronic properties of InAs/EuS/Al hybrid nanowires". In: *Physical Review B* 104.1 (July 2021), p. 014516. ISSN: 2469-9950. DOI: 10.1103/physrevb.104.014516.

[207] K. Pöyhönen, D. Varjas, M. Wimmer, and A. Akhmerov. "Minimal Zeeman field requirement for a topological transition in superconductors". In: *SciPost Physics* 10.5 (May 2021). DOI: 10.21468/scipostphys.10.5.108.

[208] A. Khindanov, J. Alicea, P. Lee, W. S. Cole, and A. E. Antipov. "Topological superconductivity in nanowires proximate to a diffusive superconductor–magnetic-insulator bilayer". In: *Physical Review B* 103.13 (Apr. 2021), p. 134506. DOI: 10.1103/physrevb.103.134506.

[209] J. Langbehn, S. A. González, P. W. Brouwer, and F. von Oppen. "Topological superconductivity in tripartite superconductor-ferromagnet-semiconductor nanowires". In: *Physical Review B* 103.16 (Apr. 2021), p. 165301. DOI: 10.1103/physrevb.103.165301.

[210] A. A. Golubov, M. Y. Kupriyanov, and E. Il'ichev. "The current-phase relation in Josephson junctions". In: *Reviews of Modern Physics* 76.2 (Apr. 2004), pp. 411–469. ISSN: 0034-6861. DOI: 10.1103/RevModPhys.76.411.

[211] P. F. Bagwell. "Suppression of the Josephson current through a narrow, mesoscopic, semiconductor channel by a single impurity". In: *Physical Review B* 46.19 (1992), pp. 12573–12586. ISSN: 0163-1829. DOI: 10.1103/PhysRevB.46.12573.

[212] I. Sochnikov, L. Maier, C. A. Watson, J. R. Kirtley, C. Gould, G. Tkachov, E. M. Hankiewicz, C. Brüne, H. Buhmann, L. W. Molenkamp, and K. A. Moler. "Nonsinusoidal Current-Phase Relationship in Josephson Junctions from the 3D Topological Insulator HgTe". In: *Physical Review Letters* 114.6 (Feb. 2015), p. 066801. DOI: 10.1103/physrevlett.114.066801.

[213]   C. D. English, D. R. Hamilton, C. Chialvo, I. C. Moraru, N. Mason, and D. J. Van Har-
        lingen. "Observation of nonsinusoidal current-phase relation in graphene Josephson
        junctions". In: *Physical Review B* 94.11 (Sept. 2016), p. 115435. DOI: 10.1103/physrevb.
        94.115435.

[214]   G. Nanda, J. L. Aguilera-Servin, P. Rakyta, A. Kormányos, R. Kleiner, D. Koelle, K. Watan-
        abe, T. Taniguchi, L. M. K. Vandersypen, and S. Goswami. "Current-Phase Relation of
        Ballistic Graphene Josephson Junctions". In: *Nano Letters* 17.6 (May 2017), pp. 3396–
        3401. DOI: 10.1021/acs.nanolett.7b00097.

[215]   E. M. Spanton, M. Deng, S. Vaitiekėnas, P. Krogstrup, J. Nygård, C. M. Marcus, and K. A.
        Moler. "Current–phase relations of few-mode InAs nanowire Josephson junctions". In:
        *Nature Physics* 13.12 (Aug. 2017), pp. 1177–1181. DOI: 10.1038/nphys4224.

[216]   F. Schindler, Z. Wang, M. G. Vergniory, A. M. Cook, A. Murani, S. Sengupta, A. Y. Kasumov,
        R. Deblock, S. Jeon, I. Drozdov, H. Bouchiat, S. Guéron, A. Yazdani, B. A. Bernevig, and
        T. Neupert. "Higher-order topology in bismuth". In: *Nature Physics* 14.9 (July 2018),
        pp. 918–924. DOI: 10.1038/s41567-018-0224-7.

[217]   M. Kayyalha, A. Kazakov, I. Miotkowski, S. Khlebnikov, L. P. Rokhinson, and Y. P. Chen.
        "Highly skewed current–phase relation in superconductor–topological insulator–superconductor
        Josephson junctions". In: *npj Quantum Materials* 5.1 (Jan. 2020). DOI: 10.1038/
        s41535-020-0209-5.

[218]   F. Nichele, E. Portolés, A. Fornieri, A. M. Whiticar, A. C. C. Drachmann, S. Gronin, T.
        Wang, G. C. Gardner, C. Thomas, A. T. Hatke, et al. "Relating Andreev Bound States and
        Supercurrents in Hybrid Josephson Junctions". In: *Physical Review Letters* 124.22 (June
        2020), p. 226801. DOI: 10.1103/physrevlett.124.226801.

[219]   L. N. Bulaevskii, V. V. Kuzii, and A. A. Sobyanin. "Superconducting system with weak
        coupling to the current in the ground state". In: *JETP letters* 25.7 (1977), pp. 290–294.

[220]   A. V. Rozhkov, D. P. Arovas, and F. Guinea. "Josephson coupling through a quantum
        dot". In: *Physical Review B* 64.23 (Nov. 2001), p. 233301. DOI: 10.1103/physrevb.64.
        233301.

[221]   J. A. Van Dam, Y. V. Nazarov, E. P. A. M. Bakkers, S. De Franceschi, and L. P. Kouwenhoven.
        "Supercurrent reversal in quantum dots". In: *Nature* 442.7103 (Aug. 2006), pp. 667–670.
        DOI: 10.1038/nature05018.

[222]   R. Delagrange, R. Weil, A. Kasumov, M. Ferrier, H. Bouchiat, and R. Deblock. "0-$\pi$
        quantum transition in a carbon nanotube Josephson junction: universal phase depen-
        dence and orbital degeneracy". In: *Physical Review B* 93.19 (May 2016), p. 195437. DOI:
        10.1103/physrevb.93.195437.

[223]   Z. Radović, L. Dobrosavljević-Grujić, and B. Vujičić. "Coexistence of stable and metastable
        0 and pi states in Josephson junctions". In: *Physical Review B* 63.21 (May 2001), p. 214512.
        DOI: 10.1103/physrevb.63.214512.

[224]   H. Sellier, C. Baraduc, F. Lefloch, and R. Calemczuk. "Half-integer shapiro steps at the
        0-pi crossover of a ferromagnetic josephson junction". In: *Physical Review Letters* 92.25
        (June 2004), p. 257005. DOI: 10.1103/physrevlett.92.257005.

[225] M. Houzet, V. Vinokur, and F. Pistolesi. "Superharmonic Josephson relation at 0-pi junction transition". In: *Physical Review B* 72.22 (Dec. 2005), p. 220506. DOI: 10.1103/physrevb.72.220506.

[226] W. C. Smith, A. Kou, X. Xiao, U. Vool, and M. H. Devoret. "Superconducting circuit protected by two-Cooper-pair tunneling". In: *npj Quantum Information* 6.1 (Jan. 2020). DOI: 10.1038/s41534-019-0231-2.

[227] T. Larsen, M. Gershenson, L. Casparis, A. Kringhøj, N. Pearson, R. McNeil, F. Kuemmeth, P. Krogstrup, K. Petersson, and C. Marcus. "Parity-Protected Superconductor-Semiconductor Qubit". In: *Physical Review Letters* 125.5 (July 2020), p. 056801. DOI: 10.1103/physrevlett.125.056801.

[228] G.-L. Guo, H.-B. Leng, Y. Hu, and X. Liu. "0-pi qubit with one Josephson junction". In: *Physical Review B* 105.18 (May 2022), p. l180502. DOI: 10.1103/physrevb.105.1180502.

[229] C. Schrade, C. M. Marcus, and A. Gyenis. "Protected Hybrid Superconducting Qubit in an Array of Gate-Tunable Josephson Interferometers". In: *PRX Quantum* 3.3 (July 2022), p. 030303. DOI: 10.1103/prxquantum.3.030303.

[230] M. A. Silaev, A. Y. Aladyshkin, M. V. Silaeva, and A. S. Aladyshkina. "The diode effect induced by domain-wall superconductivity". In: *Journal of Physics: Condensed Matter* 26.9 (Feb. 2014), p. 095702. DOI: 10.1088/0953-8984/26/9/095702.

[231] T. Yokoyama, M. Eto, and Y. V. Nazarov. "Anomalous Josephson effect induced by spin-orbit interaction and Zeeman effect in semiconductor nanowires". In: *Physical Review B* 89 (19 May 2014), p. 195407. DOI: 10.1103/PhysRevB.89.195407.

[232] K. Halterman, M. Alidoust, R. Smith, and S. Starr. "Supercurrent diode effect, spin torques, and robust zero-energy peak in planar half-metallic trilayers". In: *Physical Review B* 105 (10 Mar. 2022), p. 104508. DOI: 10.1103/PhysRevB.105.104508.

[233] S. Ilić and F. Bergeret. "Theory of the Supercurrent Diode Effect in Rashba Superconductors with Arbitrary Disorder". In: *Physical Review Letters* 128.17 (Apr. 2022), p. 177001. DOI: 10.1103/physrevlett.128.177001.

[234] S. Ili ć, P. Virtanen, T. T. Heikkilä, and F. S. Bergeret. "Current Rectification in Junctions with Spin-Split Superconductors". In: *Physical Review Applied* 17.3 (Mar. 2022), p. 034049. DOI: 10.1103/physrevapplied.17.034049.

[235] M. Davydova, S. Prembabu, and L. Fu. "Universal Josephson diode effect". In: *Science Advances* 8.23 (June 2022). DOI: 10.1126/sciadv.abo0309.

[236] R. S. Souto, M. Leijnse, and C. Schrade. "Josephson Diode Effect in Supercurrent Interferometers". In: *Physical Review Letters* 129.26 (Dec. 2022), p. 267702. DOI: 10.1103/physrevlett.129.267702.

[237] G. P. Mazur, N. van Loo, D. van Driel, J. Y. Wang, G. Badawy, S. Gazibegovic, E. P. A. M. Bakkers, and L. P. Kouwenhoven. "The gate-tunable Josephson diode". Nov. 25, 2022. arXiv: 2211.14283 [cond-mat.supr-con].

[238]   B. Li, N. Roschewsky, B. A. Assaf, M. Eich, M. Epstein-Martin, D. Heiman, M. Münzenberg, and J. S. Moodera. "Superconducting Spin Switch with Infinite Magnetoresistance Induced by an Internal Exchange Field". In: *Physical Review Letters* 110.9 (Feb. 2013), p. 097001. DOI: 10.1103/physrevlett.110.097001.

[239]   W.-S. Lu, K. Kalashnikov, P. Kamenov, T. J. DiNapoli, and M. E. Gershenson. "Phase Diffusion in Low-EJ Josephson Junctions at Milli-Kelvin Temperatures". In: *Electronics* 12.2 (Jan. 2023), p. 416. DOI: 10.3390/electronics12020416.

[240]   D. F. Sullivan, S. K. Dutta, M. Dreyer, M. A. Gubrud, A. Roychowdhury, J. R. Anderson, C. J. Lobb, and F. C. Wellstood. "Asymmetric superconducting quantum interference devices for suppression of phase diffusion in small Josephson junctions". In: *Journal of Applied Physics* 113.18 (May 2013), p. 183905. DOI: 10.1063/1.4804057.

[241]   E. Puppin. "Statistical Properties of Barkhausen Noise in Thin Fe Films". In: *Physical Review Letters* 84.23 (June 2000), pp. 5415–5418. DOI: 10.1103/physrevlett.84.5415.

[242]   A. Martìn-Rodero and A. L. Yeyati. "Josephson and Andreev transport through quantum dots". In: *Advances in Physics* 60.6 (Dec. 2011), pp. 899–958. DOI: 10.1080/00018732.2011.624266.

[243]   A. Krichevsky, M. Schechter, Y. Imry, and Y. Levinson. "Spectrum and thermodynamic currents in one-dimensional Josephson elements". In: *Physical Review B* 61.5 (Feb. 2000), pp. 3723–3733. DOI: 10.1103/physrevb.61.3723.

[244]   A. Levchenko, A. Kamenev, and L. Glazman. "Singular length dependence of critical current in superconductor/normal-metal/superconductor bridges". In: *Physical Review B* 74.21 (Dec. 2006), p. 212509. DOI: 10.1103/physrevb.74.212509.

[245]   C. Benjamin, T. Jonckheere, A. Zazunov, and T. Martin. "Controllable pi junction in a Josephson quantum-dot device with molecular spin". In: *The European Physical Journal B* 57.3 (June 2007), pp. 279–289. DOI: 10.1140/epjb/e2007-00167-6.

[246]   B. Bujnowski, D. Bercioux, F. Konschelle, J. Cayssol, and F. S. Bergeret. "Andreev spectrum of a Josephson junction with spin-split superconductors". In: *EPL (Europhysics Letters)* 115.6 (Sept. 2016), p. 67001. DOI: 10.1209/0295-5075/115/67001.

[247]   E. Goldobin, D. Koelle, R. Kleiner, and A. Buzdin. "Josephson junctions with second harmonic in the current-phase relation: Properties of $\phi$ junctions". In: *Physical Review B* 76.22 (Dec. 2007), p. 224523. DOI: 10.1103/physrevb.76.224523.

[248]   A. Buzdin. "Direct coupling between magnetism and superconducting current in the josephson $\phi 0$ junction". In: *Physical Review Letters* 101.10 (Sept. 2008), p. 107005. DOI: 10.1103/physrevlett.101.107005.

[249]   A. Rasmussen, J. Danon, H. Suominen, F. Nichele, M. Kjaergaard, and K. Flensberg. "Effects of spin-orbit coupling and spatial symmetries on the Josephson current in SNS junctions". In: *Physical Review B* 93.15 (Apr. 2016), p. 155406. DOI: 10.1103/physrevb.93.155406.

[250]   J. Baumard, J. Cayssol, A. Buzdin, and F. S. Bergeret. "Interplay between superconductivity and spin-dependent fields in nanowire-based systems". In: *Physical Review B* 101.18 (May 2020), p. 184512. DOI: 10.1103/physrevb.101.184512.

[251]   A. Zazunov, R. Egger, T. Jonckheere, and T. Martin. "Anomalous Josephson Current through a Spin-Orbit Coupled Quantum Dot". In: *Physical Review Letters* 103.14 (Oct. 2009), p. 147004. DOI: 10.1103/physrevlett.103.147004.

[252]   M. Cheng and R. M. Lutchyn. "Josephson current through a superconductor/semiconductor-nanowire/superconductor junction: Effects of strong spin-orbit coupling and Zeeman splitting". In: *Physical Review B* 86.13 (Oct. 2012), p. 134522. DOI: 10.1103/physrevb.86.134522.

[253]   K. N. Nesterov, M. Houzet, and J. S. Meyer. "Anomalous Josephson effect in semiconducting nanowires as a signature of the topologically nontrivial phase". In: *Physical Review B* 93.17 (May 2016), p. 174502. DOI: 10.1103/physrevb.93.174502.

[254]   H. G. Ahmad, V. Brosco, A. Miano, L. D. Palma, M. Arzeo, D. Montemurro, P. Lucignano, G. P. Pepe, F. Tafuri, R. Fazio, and D. Massarotti. "Hybrid ferromagnetic transmon qubit: Circuit design, feasibility, and detection protocols for magnetic fluctuations". In: *Physical Review B* 105.21 (June 2022), p. 214522. DOI: 10.1103/physrevb.105.214522.

[255]   J. Koch, T. M. Yu, J. Gambetta, A. A. Houck, D. I. Schuster, J. Majer, A. Blais, M. H. Devoret, S. M. Girvin, and R. J. Schoelkopf. "Charge-insensitive qubit design derived from the Cooper pair box". In: *Physical Review A* 76.4 (Oct. 2007), p. 042319. DOI: 10.1103/physreva.76.042319.

[256]   J. Preskill. "Quantum Computing in the NISQ era and beyond". In: *Quantum* 2 (Aug. 2018), p. 79. DOI: 10.22331/q-2018-08-06-79.

[257]   C. K. Andersen, A. Remm, S. Lazar, S. Krinner, N. Lacroix, G. J. Norris, M. Gabureac, C. Eichler, and A. Wallraff. "Repeated quantum error detection in a surface code". In: *Nature Physics* 16.8 (June 2020), pp. 875–880. DOI: 10.1038/s41567-020-0920-y.

[258]   J. F. Marques, B. M. Varbanov, M. S. Moreira, H. Ali, N. Muthusubramanian, C. Zachariadis, F. Battistel, M. Beekman, N. Haider, W. Vlothuizen, A. Bruno, B. M. Terhal, and L. DiCarlo. "Logical-qubit operations in an error-detecting surface code". In: *Nature Physics* 18.1 (Dec. 2021), pp. 80–86. DOI: 10.1038/s41567-021-01423-9.

[259]   S. Krinner, N. Lacroix, A. Remm, A. D. Paolo, E. Genois, C. Leroux, C. Hellings, S. Lazar, F. Swiadek, J. Herrmann, G. J. Norris, C. K. Andersen, M. Müller, A. Blais, C. Eichler, and A. Wallraff. "Realizing repeated quantum error correction in a distance-three surface code". In: *Nature* 605.7911 (May 2022), pp. 669–674. DOI: 10.1038/s41586-022-04566-8.

[260]   Z. Chen, K. J. Satzinger, J. Atalaya, A. N. Korotkov, A. Dunsworth, D. Sank, C. Quintana, M. McEwen, R. Barends, P. V. Klimov, S. Hong, C. Jones, A. Petukhov, D. Kafri, S. Demura, B. Burkett, C. Gidney, A. G. Fowler, A. Paler, H. Putterman, I. Aleiner, F. Arute, K. Arya, R. Babbush, J. C. Bardin, A. Bengtsson, A. Bourassa, M. Broughton, B. B. Buckley, D. A. Buell, N. Bushnell, B. Chiaro, R. Collins, W. Courtney, A. R. Derk, D. Eppens, C. Erickson, E. Farhi, B. Foxen, M. Giustina, A. Greene, J. A. Gross, M. P. Harrigan, S. D. Harrington, J. Hilton, A. Ho, T. Huang, W. J. Huggins, L. B. Ioffe, S. V. Isakov, E. Jeffrey, Z. Jiang, K. Kechedzhi, S. Kim, A. Kitaev, F. Kostritsa, D. Landhuis, P. Laptev, E. Lucero, O. Martin, J. R. McClean, T. McCourt, X. Mi, K. C. Miao, M. Mohseni, S. Montazeri, W. Mruczkiewicz, J. Mutus, O. Naaman, M. Neeley, C. Neill, M. Newman, M. Y. Niu, T. E. O'Brien, A.

Opremcak, E. Ostby, B. Pató, N. Redd, P. Roushan, N. C. Rubin, V. Shvarts, D. Strain, M. Szalay, M. D. Trevithick, B. Villalonga, T. White, Z. J. Yao, P. Yeh, J. Yoo, A. Zalcman, H. Neven, S. Boixo, V. Smelyanskiy, Y. Chen, A. Megrant, and J. Kelly. "Exponential suppression of bit or phase errors with cyclic error correction". In: *Nature* 595.7867 (July 2021), pp. 383–387. DOI: 10.1038/s41586-021-03588-y.

[261] M. Kjaergaard, M. E. Schwartz, J. Braumüller, P. Krantz, J. I.-J. Wang, S. Gustavsson, and W. D. Oliver. "Superconducting Qubits: Current State of Play". In: *Annual Review of Condensed Matter Physics* 11.1 (Mar. 2020), pp. 369–395. DOI: 10.1146/annurev-conmatphys-031119-050605.

[262] A. Gyenis, P. S. Mundada, A. D. Paolo, T. M. Hazard, X. You, D. I. Schuster, J. Koch, A. Blais, and A. A. Houck. "Experimental Realization of a Protected Superconducting Circuit Derived from the 0-pi Qubit". In: *PRX Quantum* 2.1 (Mar. 2021), p. 010339. DOI: 10.1103/prxquantum.2.010339.

[263] A. Gyenis, A. D. Paolo, J. Koch, A. Blais, A. A. Houck, and D. I. Schuster. "Moving beyond the Transmon: Noise-Protected Superconducting Quantum Circuits". In: *PRX Quantum* 2.3 (Sept. 2021), p. 030101. DOI: 10.1103/prxquantum.2.030101.

[264] W. Smith, M. Villiers, A. Marquet, J. Palomo, M. Delbecq, T. Kontos, P. Campagne-Ibarcq, B. Douçot, and Z. Leghtas. "Magnifying Quantum Phase Fluctuations with Cooper-Pair Pairing". In: *Physical Review X* 12.2 (Apr. 2022), p. 021002. DOI: 10.1103/physrevx.12.021002.

[265] P. Brooks, A. Kitaev, and J. Preskill. "Protected gates for superconducting qubits". In: *Physical Review A* 87.5 (May 2013), p. 052306. DOI: 10.1103/physreva.87.052306.

[266] A. R. Klots and L. B. Ioffe. "Set of holonomic and protected gates on topological qubits for a realistic quantum computer". In: *Physical Review B* 104.14 (Oct. 2021), p. 144502. DOI: 10.1103/physrevb.104.144502.

[267] M. Abdelhafez, B. Baker, A. Gyenis, P. Mundada, A. A. Houck, D. Schuster, and J. Koch. "Universal gates for protected superconducting qubits using optimal control". In: *Physical Review A* 101.2 (Feb. 2020), p. 022321. DOI: 10.1103/physreva.101.022321.

[268] L. Glazman and G. Catelani. "Bogoliubov quasiparticles in superconducting qubits". In: *SciPost Physics Lecture Notes* (June 2021). DOI: 10.21468/scipostphyslectnotes.31.

[269] P. Krantz, M. Kjaergaard, F. Yan, T. P. Orlando, S. Gustavsson, and W. D. Oliver. "A quantum engineer's guide to superconducting qubits". In: *Applied Physics Reviews* 6.2 (June 2019), p. 021318. ISSN: 1931-9401. DOI: 10.1063/1.5089550.

[270] M. Eckstein, J. H. Mentink, and P. Werner. "Designing spin and orbital exchange Hamiltonians with ultrashort electric field transients". Mar. 9, 2017. arXiv: 1703.03269 [cond-mat.str-el].

[271] A. Petrescu, C. L. Calonnec, C. Leroux, A. Di Paolo, P. Mundada, S. Sussman, A. Vrajitoarea, A. A. Houck, and A. Blais. "Accurate methods for the analysis of strong-drive effects in parametric gates". July 6, 2021. arXiv: 2107.02343 [quant-ph].

[272] M. T. Bell, J. Paramanandam, L. B. Ioffe, and M. E. Gershenson. "Protected Josephson Rhombus Chains". In: *Physical Review Letters* 112.16 (Apr. 2014), p. 167001. DOI: 10.1103/physrevlett.112.167001.

[273]   M. Hutchings, J. Hertzberg, Y. Liu, N. Bronn, G. Keefe, M. Brink, J. M. Chow, and B. Plourde. "Tunable Superconducting Qubits with Flux-Independent Coherence". In: *Physical Review Applied* 8.4 (Oct. 2017), p. 044003. DOI: 10.1103/physrevapplied.8.044003.

[274]   J. M. Martinis and A. Megrant. "UCSB final report for the CSQ program: Review of decoherence and materials physics for superconducting qubits". Oct. 21, 2014. DOI: 10.48550/ARXIV.1410.5793. arXiv: 1410.5793 [quant-ph].

[275]   J. Braumüller, L. Ding, A. P. Vepsäläinen, Y. Sung, M. Kjaergaard, T. Menke, R. Winik, D. Kim, B. M. Niedzielski, A. Melville, J. L. Yoder, C. F. Hirjibehedin, T. P. Orlando, S. Gustavsson, and W. D. Oliver. "Characterizing and Optimizing Qubit Coherence Based on SQUID Geometry". In: *Physical Review Applied* 13.5 (May 2020), p. 054079. DOI: 10.1103/physrevapplied.13.054079.

[276]   A. Kou, W. Smith, U. Vool, R. Brierley, H. Meier, L. Frunzio, S. Girvin, L. Glazman, and M. Devoret. "Fluxonium-Based Artificial Molecule with a Tunable Magnetic Moment". In: *Physical Review X* 7.3 (Aug. 2017), p. 031037. DOI: 10.1103/physrevx.7.031037.

[277]   Y. Chen, C. Neill, P. Roushan, N. Leung, M. Fang, R. Barends, J. Kelly, B. Campbell, Z. Chen, B. Chiaro, A. Dunsworth, E. Jeffrey, A. Megrant, J. Mutus, P. O'Malley, C. Quintana, D. Sank, A. Vainsencher, J. Wenner, T. White, M. R. Geller, A. Cleland, and J. M. Martinis. "Qubit Architecture with High Coherence and Fast Tunable Coupling". In: *Physical Review Letters* 113.22 (Nov. 2014), p. 220502. DOI: 10.1103/physrevlett.113.220502.

[278]   L. H. Pedersen, N. M. Møller, and K. Mølmer. "Fidelity of quantum operations". In: *Physics Letters A* 367.1-2 (July 2007), pp. 47–51. DOI: 10.1016/j.physleta.2007.02.069.

[279]   H. Xiong, Q. Ficheux, A. Somoroff, L. B. Nguyen, E. Dogan, D. Rosenstock, C. Wang, K. N. Nesterov, M. G. Vavilov, and V. E. Manucharyan. "Arbitrary controlled-phase gate on fluxonium qubits using differential ac Stark shifts". In: *Physical Review Research* 4.2 (Apr. 2022), p. 023040. DOI: 10.1103/physrevresearch.4.023040.

[280]   N. Didier, E. A. Sete, J. Combes, and M. P. da Silva. "ac Flux Sweet Spots in Parametrically Modulated Superconducting Qubits". In: *Physical Review Applied* 12.5 (Nov. 2019), p. 054015. DOI: 10.1103/physrevapplied.12.054015.

[281]   J. R. Johansson, P. D. Nation, and F. Nori. "QuTiP: An open-source Python framework for the dynamics of open quantum systems". In: *Computer Physics Communications* 183.8 (Aug. 2012), pp. 1760–1772. DOI: 10.1016/j.cpc.2012.02.021.

[282]   B. Pokharel, N. Anand, B. Fortman, and D. A. Lidar. "Demonstration of Fidelity Improvement Using Dynamical Decoupling with Superconducting Qubits". In: *Physical Review Letters* 121.22 (Nov. 2018), p. 220502. DOI: 10.1103/physrevlett.121.220502.

[283]   T. Propson, B. E. Jackson, J. Koch, Z. Manchester, and D. I. Schuster. "Robust Quantum Optimal Control with Trajectory Optimization". In: *Physical Review Applied* 17.1 (Jan. 2022), p. 014036. DOI: 10.1103/physrevapplied.17.014036.

[284]   W. Mönch. *Semiconductor Surfaces and Interfaces*. Springer Series in Surface Sciences. Berlin, Heidelberg: Springer Berlin Heidelberg, 2001, pp. 339–345. ISBN: 978-3-642-08748-6. DOI: 10.1007/978-3-662-04459-9.

[285]  M. L. Plumer and D. J. W. Geldart. "Non-local approximations to the kinetic energy functional". In: *Journal of Physics C* 16.4 (Feb. 1983), pp. 677–689. DOI: 10.1088/0022-3719/16/4/014.

[286]  M. L. Plumer and M. J. Stott. "Approximate kinetic energy functionals for atoms in extended systems". In: *Journal of Physics C* 18.21 (July 1985), pp. 4143–4163. DOI: 10.1088/0022-3719/18/21/011.

[287]  S. Bravyi, D. P. DiVincenzo, and D. Loss. "Schrieffer–Wolff transformation for quantum many-body systems". In: *Annals of Physics* 326.10 (Oct. 2011), pp. 2793–2826. DOI: 10.1016/j.aop.2011.06.004.

[288]  M. J. Rančić, S. Hoffman, C. Schrade, J. Klinovaja, and D. Loss. "Entangling spins in double quantum dots and Majorana bound states". In: *Physical Review B* 99.16 (Apr. 2019), p. 165306. DOI: 10.1103/physrevb.99.165306.

[289]  G. Consani and P. A. Warburton. "Effective Hamiltonians for interacting superconducting qubits: local basis reduction and the Schrieffer–Wolff transformation". In: *New Journal of Physics* 22.5 (May 2020), p. 053040. DOI: 10.1088/1367-2630/ab83d1.

[290]  M. Hita-Pérez, G. Jaumà, M. Pino, and J. J. Garcìa-Ripoll. "Three-Josephson junctions flux qubit couplings". In: *Applied Physics Letters* 119.22 (Nov. 2021), p. 222601. DOI: 10.1063/5.0069530.

[291]  H. Barkhausen. "Zwei mit Hilfe der neuen Verstärker entdeckte Erscheinungen". In: *Physikalische Zeitschrift* 20.17 (1919), pp. 401–403.

[292]  J. P. Sethna, K. A. Dahmen, and C. R. Myers. "Crackling noise". In: *Nature* 410.6825 (Mar. 2001), pp. 242–250. DOI: 10.1038/35065675.

[293]  J. P. Sethna, K. Dahmen, S. Kartha, J. A. Krumhansl, B. W. Roberts, and J. D. Shore. "Hysteresis and hierarchies: Dynamics of disorder-driven first-order phase transformations". In: *Physical Review Letters* 70.21 (May 1993), pp. 3347–3350. DOI: 10.1103/physrevlett.70.3347.

[294]  O. Perković, K. Dahmen, and J. P. Sethna. "Avalanches, Barkhausen Noise, and Plain Old Criticality". In: *Physical Review Letters* 75.24 (Dec. 1995), pp. 4528–4531. DOI: 10.1103/physrevlett.75.4528.

[295]  J. P. Sethna, K. A. Dahmen, and O. Perkovic. "Random-Field Ising Models of Hysteresis". In: ed. by I. D. M. Giorgio Bertotti. June 2004. Chap. 2. arXiv: cond-mat/0406320 [cond-mat.mtrl-sci].

[296]  R. J. Glauber. "Time-Dependent Statistics of the Ising Model". In: *Journal of Mathematical Physics* 4.2 (Feb. 1963), pp. 294–307. DOI: 10.1063/1.1703954.

[297]  J. Cayssol and G. Montambaux. "Exchange-induced ordinary reflection in a single-channel superconductor-ferromagnet-superconductor junction". In: *Physical Review B* 70.22 (Dec. 2004), p. 224520. DOI: 10.1103/physrevb.70.224520.

[298]  J. Cayssol and G. Montambaux. "Incomplete Andreev reflection in a clean SFS junction". In: *Journal of Magnetism and Magnetic Materials* 300.1 (May 2006), pp. 94–97. DOI: 10.1016/j.jmmm.2005.10.040.